The Development and Characterization of Advanced Nodes for the TLM Method

by

Vladica Trenkić, Dipl. Ing.

Thesis submitted to the University of Nottingham
for the degree of Doctor of Philosophy, November 1995

Abstract

Propagation of electromagnetic waves in three-dimensional (3D) space is studied using the Transmission-Line Modelling (TLM) method. The theoretical foundation, generalization and more advanced versions of the symmetrical condensed node (SCN), a basic structure for 3D TLM modelling, are presented.

A unified approach to the derivation of TLM schemes capable of modelling non-uniform anisotropic materials on an arbitrarily graded mesh is introduced. The parameters and the scattering properties for a general symmetrical condensed node (GSCN) constructed from link lines with arbitrary characteristic impedances and up to six stubs are described.

For the first time in 3D TLM modelling it is shown that stubs can be removed completely from the SCN, whilst still allowing general inhomogeneous problems to be modelled. This development, described as the symmetrical super-condensed node (SSCN), contributes significant reductions in memory storage and computer run-time in TLM simulations.

In order to assess accuracy and numerical dispersion in the various TLM schemes based on the GSCN, dispersion relations are studied. A general approach for the analytical expansion of the general dispersion relation is introduced, enabling the derivation of dispersion relations in algebraic form for all currently available nodes.

Based on the results obtained from the dispersion analysis, work aimed at constructing an optimal node is described. A class of adaptable symmetrical condensed nodes (ASCN) is derived, with superior propagation characteristics compared to other known TLM nodes.

Acknowledgements

Firstly, I would like to thank my supervisors, Prof. Christos Christopoulos and Dr. Trevor Benson for their help and support during the course of this work. I am greatful for their continuous assistance and was particularly impressed with their great ability to recognize situations when to direct me and when to let me go my own way. I would also like to thank Dr. Jon Herring for help with 'getting started' with three-dimensional TLM and for numerous discussions on many aspects of the topic. I am also in debt to my colleagues in the Numerical Modelling Group, who have given helpful advice and much practical help during the project.

The work presented here was financially supported by the Engineering and Physical Science Research Council (EPSRC) which I acknowledge with gratitude. Support was also received from the National Physical Laboratory (NPL) in the United Kingdom. The funds provided helped me to attend several scientific conferences worldwide which proved to be of enormous benefit to my work. During these events I had helpful discussions with other TLM researchers, in particular with Prof. Wolfgang Hoefer, Dr. Fred German, Dr. Michael Krumpholz, Mr. David Johns, Ms. Qi Zhang and Mr. Leonardo de Menezes, which I acknowledge with great pleasure.

Finally, I wish to thank all my friends for their considerable encouragement, support and patience, especially during the write up stage of the work.

Many thanks to my parents for their continuous support and understanding.

* * *

Неизмерно хвала мојим родитељима на подршци и разумевању.

Contents

List of main symbols

$a, b \ldots n$	scattering coefficients
c	speed of light
e	base of natural logarithm
f	frequency
i, j, k	dummy indices
j	$\sqrt{-1}$
$\vec{k}$	wave vector
k	propagation constant
m	number of coefficients
n	time step prefix
t	time
$\hat{t}$	discrete time coordinate
p, q, r	space coordinates
v	wave velocity
v_l	pulse velocity on line
v_g	group velocity
v_p	phase velocity
w	weighting factor
x, y, z	space coordinates
$\hat{x}, \hat{y}, \hat{z}$	discrete space coordinates
B_i, C_i	polynomial coefficients
C	capacitance
E	electric field
G	conductance
H	magnetic field
$\mathbf{I}$	identity matrix
I	current
L	inductance
M	numb. of MUL operations
N	number of node ports
$\mathbf{P}$	connection matrix
$\mathcal{P}, \mathcal{Q}$	polynomials
Q	electric charge
R	resistance
$\mathbf{S}$	scattering matrix
$\mathbf{S}_n$	normalized scatt. matrix
V	total voltage
V^i	incident voltage pulse
V^r	reflected voltage pulse
$\vec{X}$	eigenvector
$\mathbf{Y}$	addmitance matrix
Y	characteristic admittance
Z	characteristic impedance
β	phase constant
δf	frequency error
δk	propagation error
$\overline{\delta k}$	normalized error
$\overline{\delta k}_{\max +}$	maximum positive error
$\overline{\delta k}_{\max -}$	maximum negative error
$\overline{\delta k}_t$	total error range
ε	dielectric permittivity
$\overline{\overline{\varepsilon}}$	permittivity tensor
ε_0	permittivity of free-space
ε_r	relative permittivity

η	phase shift	σ_e	electric conductivity
η_x, η_y, η_z	mixed coordinates	σ_m	magnetic conductivity
θ	phase shift	φ	angle
ϑ	angle	χ	phase shift
λ	wavelength	ψ	eigenvalue
λ	eigenvalue	ω	angular frequency
μ	magnetic permeability	Δt	time step
$\overline{\overline{\mu}}$	permeability tensor	$\Delta t_{\max}$	maximum time step
μ_0	permeability of free-space	Δl	node spacing
μ_r	relative permeability	Δl	equivalent cubic cell
ξ	phase shift	Δx,Δy,Δz	node dimensions
ξ_x, ξ_y, ξ_z	mixed coordinates	Φ	magnetic flux
ρ	reflection coefficient	∂	partial derivative

Additional symbols were used to clarify such quantities as link line and stub parameters, voltages and currents. These symbols are more precisely defined in § 2.3.1 and where they are used.

Dummy indices i, j, k are used for compact notation and should be replaced by x, y, z, as explained further in the text.

The symbol $\hat{}$ is used to denote a normalized quantity.

Chapter 1 Introduction

1.1 Numerical modelling with TLM method

The study of electromagnetic problems involving the propagation of electromagnetic waves and their interaction with structures such as antennas, microstrip lines, conductive panels and material discontinuities can be achieved using analytical techniques only in a few very limited and simplified cases. In order to include the study of more complicated practical configurations, it is necessary to resort to computer-based numerical techniques. Such techniques establish numerical models of propagation and coupling which can be easily adapted to deal with very general configurations. The fast development of computer technology in recent decades provided the necessary hardware and software means for the implementation and further enhancement of these modelling techniques.

Several numerical modelling methods for solving electromagnetic problems have been developed, each possessing particular features advantageous to particular types of problems [1, 2]. Methods can be classified in generic groups based on the domain of the variable (time- or frequency-domain) and the domain of the operator (differential or integral). Other approaches, such as the ray methods [3] used at very high frequencies, and hybrid approaches involving more than one method have also been developed.

In dealing with the most general material and conductor configurations at high frequencies, differential time-domain techniques offer the most versatile simulation tool. The foremost methods in this area are the finite-difference time-domain (FDTD) method [4] and the transmission line modelling (TLM) method [5, 6]. There are many similarities between the two methods but the modelling philosophy is different. Whereas in FDTD Maxwell's equations are solved using a differencing scheme, in TLM a scattering approach akin to Huygens principle is implemented by replacing the space domain with a system of interconnected transmission-lines. Such a model is based on the analogy between the voltage variables of the transmission-lines and the field variables of the space.

Since the publication of the pioneering article on the TLM method by P. B. Johns and R. L. Beurle [7] in 1971, the method has been extensively studied and continuously expanded by many researchers, growing up to a recognized, powerful and versatile modelling technique indeed. Confirming its maturity, the First International Workshop on TLM took place in the University of Victoria, Canada, this year (1995), gathering "the protagonist of TLM for a thorough assessment of the state of the art, to explore the capabilities, applications, limitations and future developments of TLM, and to evaluate its strengths and weaknesses with respect to other modelling techniques" [8].

1.2 Objectives of the thesis

Ever since the original paper [7], a series of refinements to the TLM method were proposed and successfully implemented. One of the structures receiving the most attention in recent years is the symmetrical condensed node (SCN), developed by P. B. Johns in 1987 [9], which marked a new phase in three-dimensional (3D) TLM modelling. The TLM method based on symmetrical condensed nodes has been studied, implemented and enhanced widely by academic and non-academic research groups, resulting in a considerable amount of computer code developed by these groups to facilitate electromagnetic simulations. A commercially available 3D TLM simulator 'Micro-Stripes' based exclusively on condensed TLM nodes has been also developed by KCC [10].

Even though the symmetrical condensed node TLM schemes are established in applications covering a wide range of electromagnetic field problems, there have been very few (and only very recent) rigorous investigations about their theoretical foundation, numerical properties and the possibility of deriving new, more efficient, schemes based on the SCN. The availability of fast computer workstations allowed many small and medium-size problems to be solved quickly, overriding the need to derive better, optimal schemes and to implement more efficient algorithms. However, in many areas of practical interest, for example electromagnetic compatibility (EMC), even the most powerful computers are inadequate to the task. This is why more research was considered necessary to give insight into the theoretical foundations of the existing methods, their possible optimization and the development of more advanced formulations.

This thesis aims to fill the gap between the well established application of the TLM condensed node method and its theoretical foundations which have received less attention. This investigation serves not only to theoretically establish the

existing TLM condensed node schemes, but far more importantly, it offers a tool for deriving new schemes with potentially better characteristics.

Another objective of this work is to achieve full characterization of the existing and newly developed nodes. So far, the propagation properties of condensed nodes obtained by solving dispersion relations were studied mainly qualitatively. Only limited practical results are available on the numerical properties of the nodes with stubs and altered link lines which are essential in modelling inhomogeneous media using cells of arbitrary aspect ratio (graded mesh). The thesis aims to describe quantitatively the impact of stub-loading and changing link line impedances on the accuracy, thus offering a better insight into errors due to numerical dispersion when modelling arbitrary configurations.

The combination of these two objectives, namely a) theoretical foundation and b) characterization, opens up the possibility of further advances in the derivation of optimal condensed nodes. Given the theoretical instrument to describe new nodes and a systematic procedure to 'measure' their accuracy and performance, the development of advanced nodes can be directed to achieve the most suitable solution for a given problem. Some of the possible solutions are addressed in this thesis, many others hitherto unexplored are limited only by a researchers imagination.

1.3 Outline of the thesis

This thesis is divided into four parts.

Part One introduces a unified formulation for the calculation of TLM parameters and the theoretical foundation of a general symmetrical condensed node (GSCN). The first chapter of this part (**Chapter 2**) introduces general TLM constitutive relations, which together with a time synchronism condition represent a basic system of equations for deriving the parameters of TLM schemes. The six degrees of freedom found in the definition of a time-domain TLM condensed node scheme are used in the later chapters to derive novel nodes. **Chapter 3** treats scattering in symmetrical condensed nodes. A detailed derivation of the scattering equations for very general nodes is presented, based on established physical principles. In **Chapter 4** a bijective one-to-one mapping between voltage pulses and field components is introduced to enable the derivation of the scattering equations directly from Maxwell's equations by using central differencing and averaging – thus offering a rigorous theoretical foundation for any TLM node derivable from the general symmetrical condensed node (GSCN).

Part Two concentrates on the derivation of a stubless condensed node, referred to as the symmetrical super-condensed node (SSCN). The first chapter of this part (**Chapter 5**) describes the derivation and implementation of the SSCN for modelling arbitrary materials on a variable (graded) mesh. **Chapter 6** shows efficient algorithms for implementation of the scattering procedure in the TLM schemes based on the GSCN, with particular emphasis on the symmetrical super-condensed node.

Part Three treats numerical dispersion in TLM symmetrical condensed node schemes. The first chapter of this part (**Chapter 7**) gives the basic concepts in deriving dispersion relations in algebraic form from the general dispersion relation of eigenvalue form. Analytical expansion of this relation for the SSCN and other available nodes for modelling arbitrary media with variable grading and arbitrary time steps is presented. The following chapter (**Chapter 8**) presents a quantitative analysis and comparison of the propagation error due to numerical dispersion in different TLM schemes and shows possible ways of extracting the information available from the dispersion relations.

In **Part Four**, the features of the GSCN and results of dispersion analysis are combined in order to develop more advanced nodes. **Chapter 9** introduces possible node configurations with improved dispersion characteristics, namely a matched impedance SCN (MSCN) and an adaptable SCN (ASCN) and compares their performance to those of other more traditional nodes. **Chapter 10** offers general remarks on the results achieved in the development and characterization of novel nodes, directions for further investigations and conclusions.

Part I

Theoretical Foundation

Chapter 2 Unified formulation of TLM parameters

2.1 Introduction

The TLM method was originally developed as a two-dimensional (2D) method based on transmission lines interconnected at *shunt nodes* [7]. Generalization of the shunt node to allow modelling of inhomogeneous and lossy materials and the development of another complementary 2D structure known as the *series node* were described in [11, 12]. The combination of the 2D shunt and series nodes into a three-dimensional (3D) structure led to the development of a 3D *expanded node* [13]. The theory and applications of these schemes were reviewed in [14].

The topology of the TLM scheme with the expanded node is similar to that of the finite difference time-domain (FDTD) scheme of Yee [15]. The advantage of the TLM expanded node scheme over the FDTD method is that in TLM three of the six field components are available at each scattering point, rather than one which is case in FDTD modelling. However, this is offset by the use of twice as many variables in TLM than in FDTD.

The main disadvantage of the TLM expanded node and the FDTD method is the complicated topology of the computational cell [9]. The scattering points where different field components are conveniently calculated are spatially separated and they are not updated at the same time. This makes it difficult and liable to error to model arbitrary mixed boundaries and interfaces between different materials [5]. The implementation of variable mesh grading is also not easy.

These difficulties with the TLM expanded node led to the development of a condensed node structure [16, 17], referred to as the asymmetrical condensed node (ACN), having the advantage of performing the scattering operation at one point of space. All of the field components can be also evaluated at one point in space and at the same time. The boundary conditions can be applied at the node or more elegantly halfway between nodes. As in the expanded node, however, an asymmetry remains — depending upon the direction of approach, the first con-

nection in the node is either shunt or series. It means that boundaries viewed in one direction have slightly different properties when viewed in another, especially at high frequencies.

To overcome these difficulties, P. B. Johns developed a symmetrical condensed node [9]. It retains the advantages of condensed scattering and of calculating all field components at one point in space, making it easy to describe boundaries and inhomogeneous media, but it eliminates the asymmetry and cumbersome arithmetics experienced in the asymmetrical node. The detailed theory and applications of the SCN TLM can be found in [6] and it is also the topic of this thesis.

Developments in both 2D and 3D TLM schemes, based on varying the characteristic impedance of link lines and introducing hybrid nodes [18, 19, 20], have resulted in a more efficient implementation of the variable graded mesh and a better modelling of general materials, compared to the original nodes. Recently, frequency-domain (FD) TLM schemes for efficiently solving steady-state field problems [21, 22] have been developed from similar principles.

This chapter presents a unified approach to the derivation of TLM node parameters which can be used for all existing schemes. The rationale behind it is to unify all these developments into a general formulation of TLM, in a manner which does not only link existing methods, but also gives directions for further developments. Using this unified approach, detailed derivation of the parameters for the 3D time-domain schemes is performed, followed by the derivation of the parameters for the 2D TLM and the frequency-domain TLM schemes.

2.2 Configuration of three-dimensional TLM nodes

Figure 2.1 depicts a block of medium (cell) modelled by (a) expanded node, (b) asymmetrical condensed node and (c) symmetrical condensed node. It can be seen that three series circuits of transmission lines, residing on the cell's boundaries in the expanded node (Figure 2.1a) are moved towards the centre of the cell in the condensed nodes (Figure 2.1b,c). The placement of the transmission lines in the ACN can be considered to be at an infinitesimally close distance to the cell's centre, but not exactly at the centre. As a consequence of this, the shunt and series connections are still separated in the ACN, allowing for an equivalent electric circuit to be constructed for the purpose of deriving the scattering matrix [16], but causing asymmetry of the node. By further moving the transmission lines directly into the centre of the cell, the separate shunt and series connections merge into a

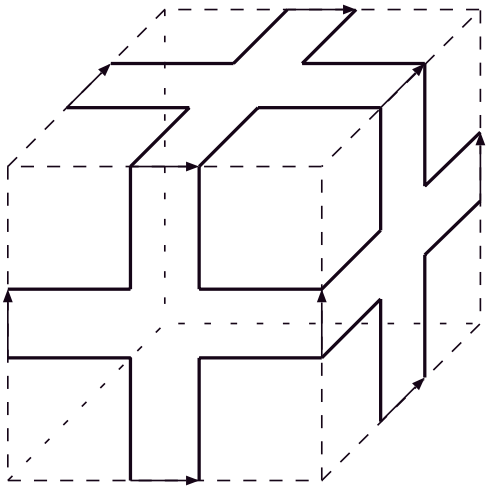

a) Expanded node

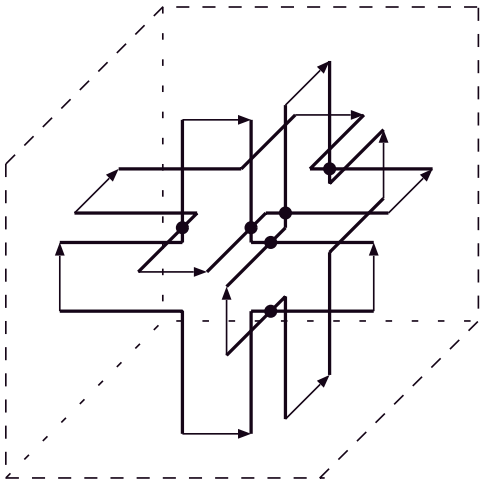

b) Asymmetrical condensed node (ACN)

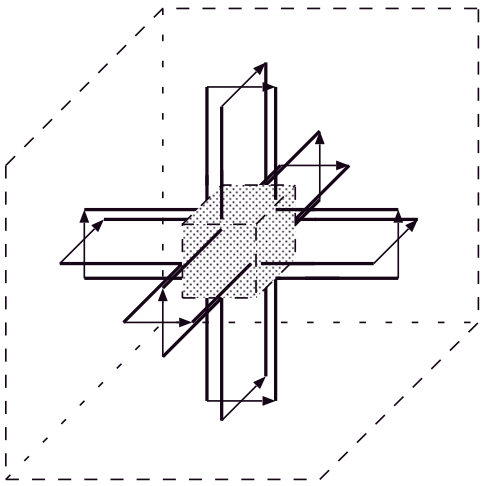

c) Symmetrical condensed node (SCN)

Figure 2.1 *Three-dimensional TLM nodes*

single structure, defined as a 3D symmetrical condensed node, where the physical connection of transmission-lines is undefined (shaded region on Figure 2.1c) and for which a simple equivalent electric circuit no longer exists. In turn, symmetry is established, allowing the identical modelling of the propagation of waves regardless of their direction of incidence.

Another view of the evolution from the expanded to the condensed node is depicted in Figure 2.2. Here, transmission lines are presented by single lines with the polarisation in space determined by the direction of an arrow. The shunt and series connections are represented by the spheres with dark and light shadings, respectively. Six spheres can be noticed in the expanded node and in the ACN from Figures 2.2a,b emphasizing the fact that shunt and series scattering points are still distinguishable. They eventually merge into a single sphere in Figure 2.2c, which can be regarded as a combination of shunt- and series-circuits into a new 'super-network', the symmetrical condensed node.

The advantage in the topology of condensed node modelling can be clearly seen from Figures 2.1 and 2.2 as there exists a full correspondence between a single node and a block of medium modelled by the node. In the expanded node, transmission-lines are placed at the cell's boundaries, therefore the physical parameters of the lines are shared between adjacent cells. This means that it is necessary to introduce an averaging of the parameters of the link lines and stubs at the discontinuities, which is easily avoided in condensed schemes by placing discontinuities halfway between nodes. Note however, that apart from the different topology, on average, the identical number of link lines of the same length is used per cell in all three cases.

In order to accommodate a graded mesh and local increase in electromagnetic parameters, stubs can be loaded into the TLM nodes. In all cases, a maximum of three open-circuit stubs (one for each direction) and three short-circuit stubs are used to account for, respectively, extra capacitance and inductance [9, 13, 16]. The losses can be modelled in a similar manner, by using matched stubs (see § 2.3.5).

A common approach for calculating node parameters in TLM schemes is based on equating total capacitance and inductance contributed by the link and stub lines of a TLM cell to the corresponding parameters of the block of modelled medium [6]. It is clear from the topology of the expanded and condensed nodes depicted in Figures 2.1 and 2.2 that even though these are different geometrical structures, they contain the same number of link lines and stubs per cell. Therefore, their scattering and numerical characteristics, as well as the implementation in a TLM

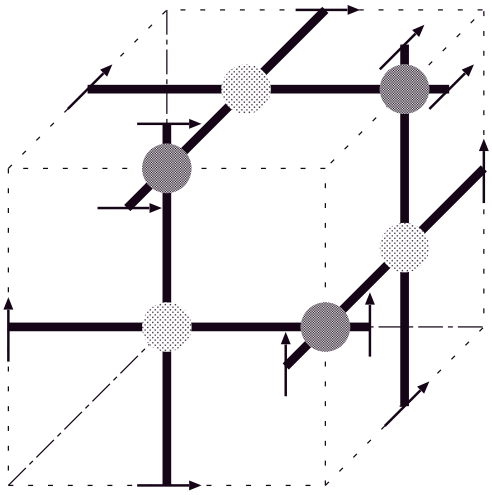

Connections:

shunt

series

a) Expanded node

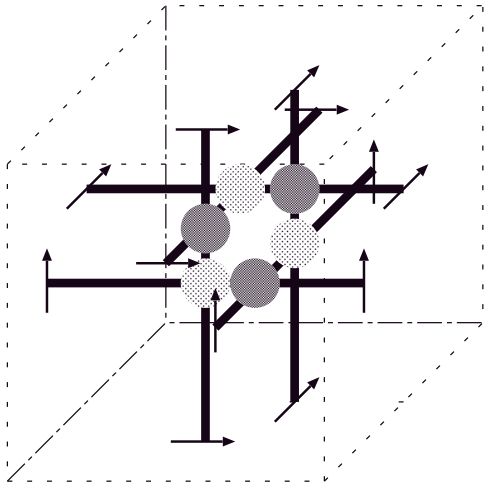

b) Asymmetrical condensed node (ACN)

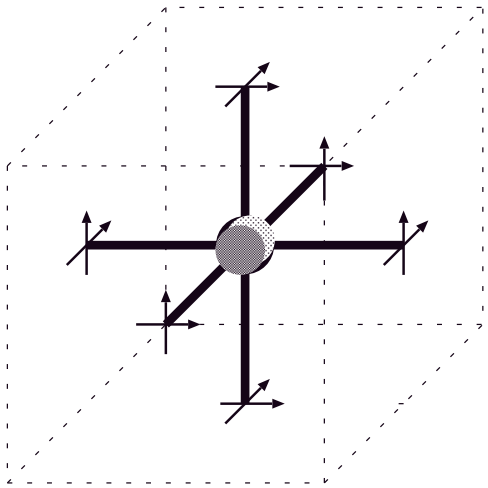

c) Symmetrical condensed node (SCN)

Figure 2.2 *Another view of three-dimensional TLM nodes*

mesh differ, but their link line and stub parameters for a given medium and given node dimensions **must** be identical.

The following derivation of the link and stub parameters of 3D TLM schemes will be performed in respect to the configuration of SCN, but applies also for the schemes based on the other two types of 3D nodes.

2.3 General formulation of TLM parameters

2.3.1 Notation

The basic notation of the voltage pulses and other physical quantities attributed to a TLM node is introduced as follows.

Every voltage pulse attributed to the particular transmission-line can be regarded as an incident (superscript i), reflected (superscript r) or total voltage (no superscript). Total voltage is defined as sum of incident and reflected voltage pulses: $V = V^i + V^r$. Similarly total current on a transmission line is defined as $I = (V^i - V^r)/Z$ where Z is the characteristic impedance of the line.

A voltage pulse on the negative side of the node (assuming the origin of coordinates at the centre of the node) along an i-directed j-polarized transmission line is denoted as V_{inj}, whereas a voltage on the positive side of the same line is given as V_{ipj}. Dummy indices i, j should be replaced by x, y, z, where $i, j \in \{x, y, z\}$ and $i \neq j$. The notation of the twelve link line voltages of the SCN is depicted in Figure 2.3. An identical indexing scheme can be used for the total currents on transmission-lines.

Voltage pulses on the open and short-circuit stubs will be denoted as V_{oi} and V_{si}, respectively, whereas the voltages on 'electric' and 'magnetic' matched stubs are denoted as V_{ei} and V_{mi}, respectively. The first subscript shows the type of the stub. The second subscript i should be replaced by x, y or z depending on which component of the field stubs are contributing to.

Additional notation is introduced for the parameters of each transmission line. The distributed capacitance and inductance of an i-directed, j-polarized link line is denoted by indices according to the direction and the polarization as C_{ij} and L_{ij}. Similarly, the characteristic impedance and admittance of such a line are referred to as Z_{ij} and Y_{ij}, where $i, j \in \{x, y, z\}$ and $i \neq j$.

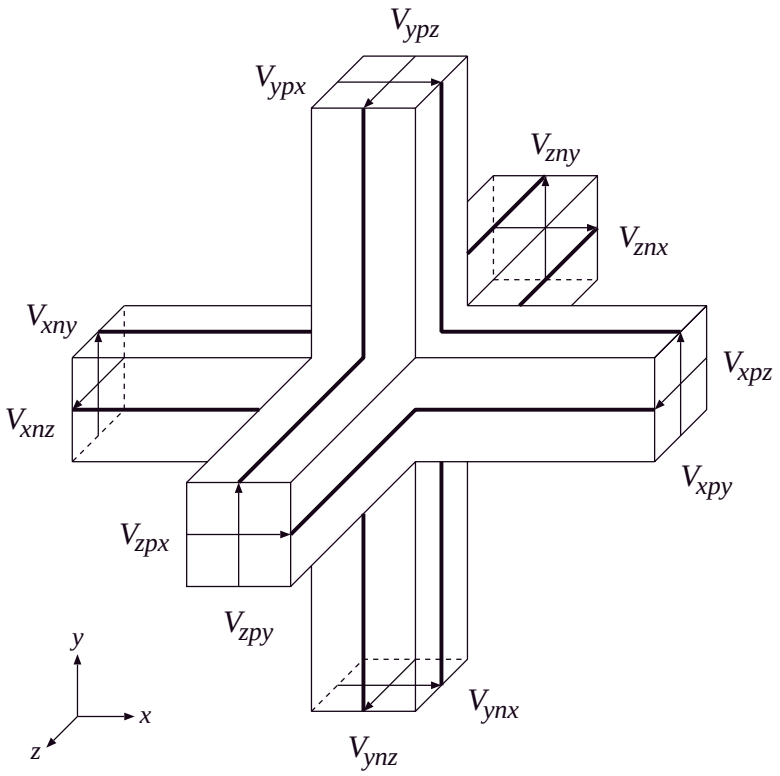

Figure 2.3 *Symmetrical condensed node (SCN)*

The total capacitance of an open-circuit stub and the total inductance of a short-circuit stub, contributing to the cell's capacitance and inductance, respectively, in the i direction, are denoted as C_o^i and L_s^i. The characteristic admittance and impedance of those stubs are given as Y_{oi} and Z_{si}, respectively.

In some special cases, when parameters of link lines differ with respect to the node centre, they will be indexed similarly as voltage pulses, with an extra n or p subscript, depending on the position relative to the centre. For example Z_{xny} is the characteristic impedance of the x-directed y-polarized half link-line positioned on the negative side of the node, and the corresponding total voltage and total current on this line are V_{xny} and I_{xny}, respectively.

2.3.2 Balanced and unbalanced nodes

The link lines connected to a symmetrical condensed node may have up to twelve different values of characteristic impedance — if we allow for the parameters of an i-directed j-polarized link line to be different on different sides of the node. Such a node will be referred to as an *unbalanced node* which, intuitively, is not very physi-

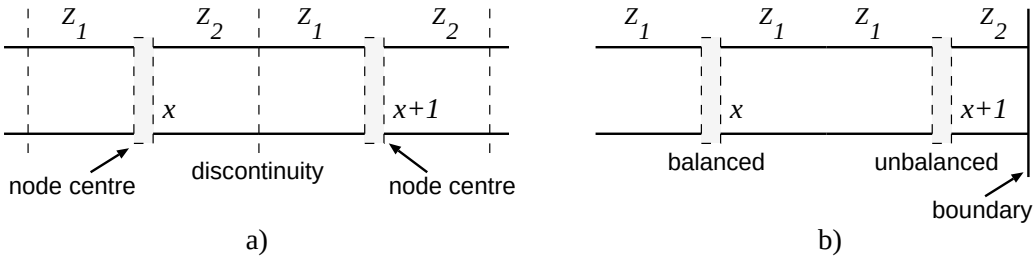

Figure 2.4 *Unbalanced nodes a) in unbounded space b) at the boundary*

cal for modelling wave propagation along continuous unbounded space, since there are unnecessary reflections of voltage pulses on interfaces between the adjacent nodes due to an impedance discontinuity, as shown in Figure 2.4a. Furthermore, it is computationally inefficient to perform scattering at node boundaries as well as at the node centre. Following this intuitive argument, which will be backed further by evidence presented in later chapters, it is assumed that only *balanced nodes*, satisfying the condition $Z_{inj} = Z_{ipj} = Z_{ij}$, are suitable for describing propagation through space.

However, an unbalanced node, with the link lines differing with respect to the node centre, can be implemented at the edge of the modelling space for describing infinitesimally adjustable boundaries [23], as shown in Figure 2.4b. Hence, unbalanced nodes will be included into the study when deriving the scattering properties in Chapter 3, but only balanced nodes, with up to six arbitrary values of link line impedances (one for each direction and polarization), will be considered for the formulation of parameters of a general TLM scheme.

2.3.3 General TLM constitutive relations

A general system of equations used to derive parameters of TLM nodes is described here. The definitions that follow refer to a cuboid cell of space with arbitrary dimensions Δx, Δy, Δz and material properties $\overline{\overline{\varepsilon}}$, $\overline{\overline{\mu}}$ defined as diagonal tensors modelling symmetric anisotropic media:

$$\overline{\overline{\varepsilon}} = \begin{bmatrix} \varepsilon_x & 0 & 0 \\ 0 & \varepsilon_y & 0 \\ 0 & 0 & \varepsilon_z \end{bmatrix} = \varepsilon_0 \begin{bmatrix} \varepsilon_{rx} & 0 & 0 \\ 0 & \varepsilon_{ry} & 0 \\ 0 & 0 & \varepsilon_{rz} \end{bmatrix} \tag{2.1}$$

$$\overline{\overline{\mu}} = \begin{bmatrix} \mu_x & 0 & 0 \\ 0 & \mu_y & 0 \\ 0 & 0 & \mu_z \end{bmatrix} = \mu_0 \begin{bmatrix} \mu_{rx} & 0 & 0 \\ 0 & \mu_{ry} & 0 \\ 0 & 0 & \mu_{rz} \end{bmatrix} \tag{2.2}$$

The total capacitance of the block of space can be calculated from the generalized definition of capacitance:

$$C = \frac{Q}{V} = \frac{\int_S \overline{\overline{\varepsilon}}\, \mathbf{E} \cdot d\mathbf{S}}{\int_+^- \mathbf{E} \cdot d\mathbf{l}} \tag{2.3}$$

giving values for the three principal directions as [18]:

$$C_t^x = \varepsilon_x \frac{\Delta y \Delta z}{\Delta x} \tag{2.4}$$

$$C_t^y = \varepsilon_y \frac{\Delta z \Delta x}{\Delta y} \tag{2.5}$$

$$C_t^z = \varepsilon_z \frac{\Delta x \Delta y}{\Delta z} \tag{2.6}$$

Similarly, the total inductance of the block of space can be calculated from:

$$L = \frac{\Phi}{I} = \frac{\int_S \overline{\overline{\mu}}\, \mathbf{H} \cdot d\mathbf{S}}{\oint \mathbf{H} \cdot d\mathbf{l}} \tag{2.7}$$

giving values for the three principal directions as [18]:

$$L_t^x = \mu_x \frac{\Delta y \Delta z}{\Delta x} \tag{2.8}$$

$$L_t^y = \mu_y \frac{\Delta z \Delta x}{\Delta y} \tag{2.9}$$

$$L_t^z = \mu_z \frac{\Delta x \Delta y}{\Delta z} \tag{2.10}$$

Equations (2.4)–(2.6) and (2.8)–(2.10) can be expressed in a compact form as:

$$\mathbf{C}_t = \overline{\overline{\varepsilon}}\, \boldsymbol{\Delta} \tag{2.11}$$

$$\mathbf{L}_t = \overline{\overline{\mu}}\, \boldsymbol{\Delta} \tag{2.12}$$

where vectors $\mathbf{C}_t$, $\mathbf{L}_t$ and $\boldsymbol{\Delta}$ are defined as:

$$\mathbf{C}_t = \begin{bmatrix} C_t^x \\ C_t^y \\ C_t^z \end{bmatrix} \qquad \mathbf{L}_t = \begin{bmatrix} L_t^x \\ L_t^y \\ L_t^z \end{bmatrix} \qquad \boldsymbol{\Delta} = \begin{bmatrix} \Delta y \Delta z / \Delta x \\ \Delta z \Delta x / \Delta y \\ \Delta x \Delta y / \Delta z \end{bmatrix}$$

Vectors $\vec{\mathbf{C}}_t$, $\vec{\mathbf{L}}_t$ represent total capacitance and inductance of the modelled block of medium which in TLM has to be supplied by the capacitance and inductance

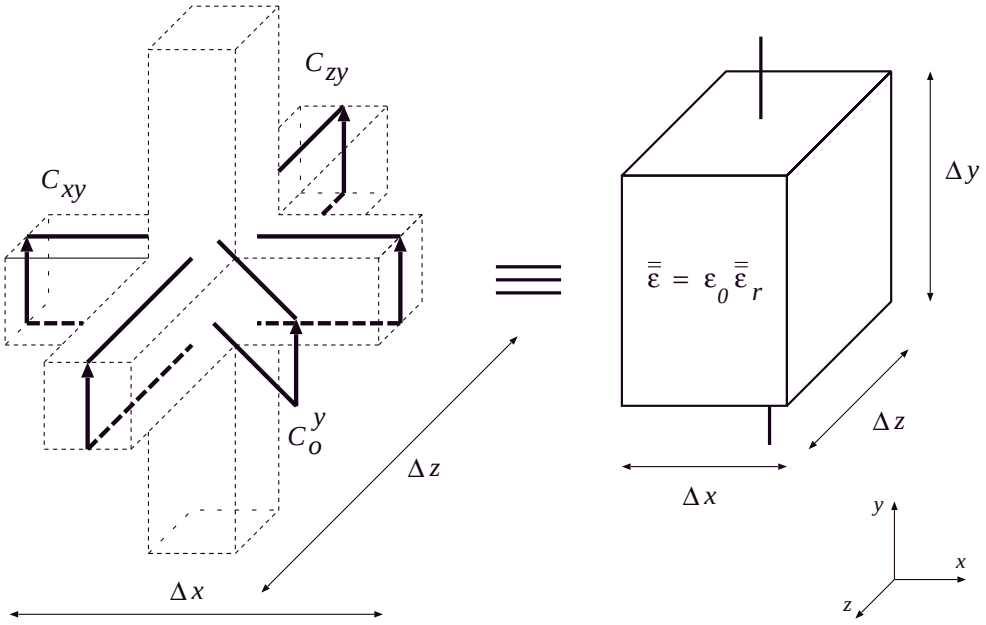

Figure 2.5 *Modelling capacitance in the y-direction*

of the link lines and stubs of a node. Equations (2.11) and (2.12) must hold for any TLM node, constructed by an arbitrary combination of link lines and stubs, and they are therefore referred to as the *general TLM constitutive relations*. Here we examine the derivation of the parameters of 3D TLM nodes described in the previous section, using the notation for the SCN introduced in § 2.3.1.

The total capacitance in, for example, the y-direction, modelled by a symmetrical condensed node is illustrated in Figure 2.5. It can be seen from Figure 2.5 that the cell's total capacitance C_t^y in the y-direction is represented by the distributed capacitance of two y-polarized transmission lines of length Δx and Δz and the capacitance of an open-circuit stub. Thus, it follows that:

$$C_t^y = C_{xy}\Delta x + C_{zy}\Delta z + C_o^y \tag{2.13}$$

The total inductance in, for example, the z-direction, modelled by a symmetrical condensed node is illustrated in Figure 2.6. It can be seen from Figure 2.6 that the cell's total inductance L_t^z in the z-direction is represented by the distributed inductance of two link lines of length Δx and Δy contributing to the z-component of magnetic field, plus the inductance of a short-circuit stub. Thus, it follows that:

$$L_t^z = L_{xy}\Delta x + L_{yx}\Delta y + L_s^z \tag{2.14}$$

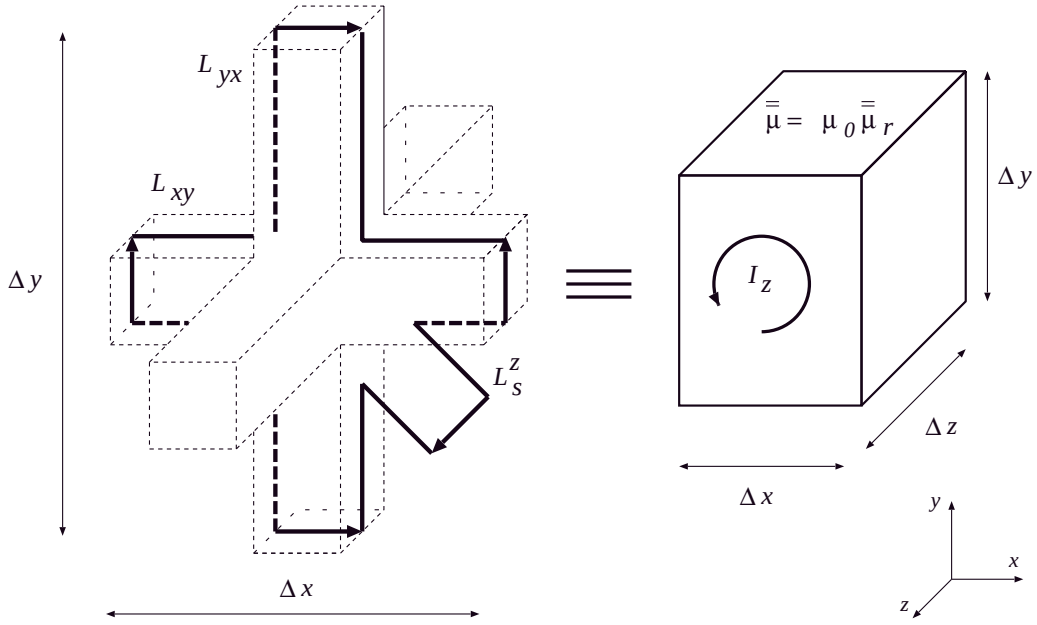

Figure 2.6 *Modelling inductance in the z-direction*

Examining the other possible directions we can also write:

$$C_t^x = C_{zx}\Delta z + C_{yx}\Delta y + C_o^x \tag{2.15}$$

$$C_t^z = C_{yz}\Delta y + C_{xz}\Delta x + C_o^z \tag{2.16}$$

$$L_t^x = L_{yz}\Delta y + L_{zy}\Delta z + L_s^x \tag{2.17}$$

$$L_t^y = L_{zx}\Delta z + L_{xz}\Delta x + L_s^y \tag{2.18}$$

Now, inserting expressions for the total cell's capacitance and inductance contributed by the link and stub lines of a TLM node, given by (2.13)–(2.18), into the general TLM constitutive relations (2.11) and (2.12), it follows that:

$$C_{yx}\,\Delta y \;+\; C_{zx}\,\Delta z \;+\; C_o^x \;=\; \varepsilon_x \frac{\Delta y \Delta z}{\Delta x} \tag{2.19}$$

$$C_{zy}\,\Delta z \;+\; C_{xy}\,\Delta x \;+\; C_o^y \;=\; \varepsilon_y \frac{\Delta z \Delta x}{\Delta y} \tag{2.20}$$

$$C_{xz}\,\Delta x \;+\; C_{yz}\,\Delta y \;+\; C_o^z \;=\; \varepsilon_z \frac{\Delta x \Delta y}{\Delta z} \tag{2.21}$$

$$L_{yz}\,\Delta y \;+\; L_{zy}\,\Delta z \;+\; L_s^x \;=\; \mu_x \frac{\Delta y \Delta z}{\Delta x} \tag{2.22}$$

$$L_{zx}\,\Delta z \;+\; L_{xz}\,\Delta x \;+\; L_s^y \;=\; \mu_y \frac{\Delta z \Delta x}{\Delta y} \tag{2.23}$$

$$L_{xy}\,\Delta x \;+\; L_{yx}\,\Delta y \;+\; L_s^z \;=\; \mu_z \frac{\Delta x \Delta y}{\Delta z} \tag{2.24}$$

The six equations (2.19)–(2.24) represent the basis for the correct modelling of the medium using a generally graded TLM mesh using anyone of the 3D nodes. These equations contain eighteen parameters to be determined: six distributed capacitances and six distributed inductances of link lines, in the form C_{ij} and L_{ij}, three total capacitances of the open-circuit stubs, C_o^i, and three total inductances of the short-circuit stubs L_s^i. Therefore, there are twelve degrees of freedom in the determination of the parameters of link and stub lines in a 3D node.

In time-domain (TD) TLM schemes, time synchronism must be maintained in the mesh, i.e. pulses must arrive at the centre of the nodes simultaneously, after a constant propagation delay, or time step, Δt. The velocity of propagation along, for example an x-directed y-polarized transmission line with the distributed capacitance C_{xy} and inductance L_{xy} is determined by:

$$v_{xy} = \frac{1}{\sqrt{C_{xy}L_{xy}}} \tag{2.25}$$

On the other hand, pulses must travel the node distance Δx in time Δt, i.e.:

$$v_{xy} = \frac{\Delta x}{\Delta t} \tag{2.26}$$

Therefore, combining (2.25) with (2.26), the time synchronism is imposed for the xy line as:

$$\Delta t = \Delta x\sqrt{C_{xy}L_{xy}} \tag{2.27}$$

Similarly we get this condition for other link lines as:

$$\Delta t = \Delta x\sqrt{C_{xz}L_{xz}} \tag{2.28}$$

$$\Delta t = \Delta y\sqrt{C_{yz}L_{yz}} \tag{2.29}$$

$$\Delta t = \Delta y\sqrt{C_{yx}L_{yx}} \tag{2.30}$$

$$\Delta t = \Delta z\sqrt{C_{zx}L_{zx}} \tag{2.31}$$

$$\Delta t = \Delta z\sqrt{C_{zy}L_{zy}} \tag{2.32}$$

With these six extra conditions, six degrees of freedom are still left in solving equations (2.19)–(2.24). Based on this formulation and by applying additional constraints, different versions of stub-loaded and hybrid 3D nodes can be derived.

2.3.4 Compact notation

The six general constitutive relations for the 3D nodes given by (2.19)–(2.24) and the six time synchronism conditions given by (2.27)–(2.32) can be written in a compact form by making use of dummy indices i, j, k.

The six expressions (2.19)–(2.24) can be summarized as:

$$C_{ik}\Delta i + C_{jk}\Delta j + C_o^k = \varepsilon_k \frac{\Delta i \Delta j}{\Delta k} \tag{2.33}$$

$$L_{ij}\Delta i + L_{ji}\Delta j + L_s^k = \mu_k \frac{\Delta i \Delta j}{\Delta k} \tag{2.34}$$

where indices i, j, k can take all possible combinations of x, y, z without repetition, or in strict mathematic notation: $i, j, k \in \{x, y, z\}$ and $i \neq j, k$. The six time synchronism conditions (2.27)–(2.32) can be written as:

$$\Delta t = \Delta i \sqrt{C_{ij} L_{ij}} \tag{2.35}$$

where $i, j \in \{x, y, z\}$ and $i \neq j$.

This compact notation with dummy indices will be used throughout this thesis, and the system of twelve equations determined by the generic formulae (2.33)–(2.35) will be referred to as the general system of equations describing the parameters of a TLM time-domain scheme.

The system of equations (2.33)–(2.35) can be also rewritten in terms of the characteristic impedances and admittances of the link lines and stubs. The characteristic impedance and admittance of an i-directed j-polarized line are defined as:

$$Z_{ij} = \frac{1}{Y_{ij}} = \sqrt{\frac{L_{ij}}{C_{ij}}} \tag{2.36}$$

Combining the time synchronism condition (2.35) with expressions (2.36), the characteristic impedance and admittance of link lines can be written as function of the time step:

$$Z_{ij} = \frac{L_{ij}\Delta i}{\Delta t} \tag{2.37}$$

$$Y_{ij} = \frac{C_{ij}\Delta i}{\Delta t} \tag{2.38}$$

In stubs, pulses have to make a round trip during the time step Δt, thus requiring the effective transit time along the length of a stub to be equal to $\Delta t/2$. Therefore, the characteristic impedance of short-circuit stubs and the characteristic admittance of open-circuit stubs are defined, respectively as [6]:

$$Z_{sk} = \frac{2L_s^k}{\Delta t} \tag{2.39}$$

$$Y_{ok} = \frac{2C_o^k}{\Delta t} \tag{2.40}$$

where $k \in \{x, y, z\}$.

Dividing the system of equations (2.33)–(2.34) by Δt and using formulae (2.37)–(2.40), we obtain:

$$Y_{ik} + Y_{jk} + \frac{Y_{ok}}{2} = \varepsilon_k \frac{\Delta i \Delta j}{\Delta k \Delta t} \tag{2.41}$$

$$Z_{ij} + Z_{ji} + \frac{Z_{sk}}{2} = \mu_k \frac{\Delta i \Delta j}{\Delta k \Delta t} \tag{2.42}$$

The system of equations (2.41)–(2.42) effectively unifies the time synchronism conditions (2.35) and the physical description of the model, based on the capacitances and inductances, given by (2.33)–(2.34). It is expressed directly in terms of the characteristics impedances and admittances of transmission-lines, the quantities which describe scattering and propagation in a TLM mesh. The two systems of equations, one described by (2.33)–(2.35) and another described by (2.41)–(2.42), are equivalent and either can be used in the derivation of the link and stub parameters for time-domain TLM schemes.

2.3.5 Modelling of losses

Losses can be incorporated in a TLM model by introducing lossy stubs into the scattering points [6]. The lossy stubs may be viewed as infinitely long, or equivalently, as terminated (matched) by their own characteristic impedance. Hence, they are often referred to as *matched stubs*. The matched stubs can be used to model both the 'electric' and 'magnetic' losses. Effectively, shunt conductances G can be introduced to the 2D shunt nodes to model electric conductivity σ_e, whereas series resistance R can be introduced to the 2D series nodes to model 'magnetic' conductivity σ_m [24, 25]. In 3D modelling with the expanded node, matched stubs, one per direction, are introduced at the shunt and series connections [13]. A similar procedure can be employed for the ACN, as the shunt and series connections are still distinct. In the SCN, the presence of matched stubs is incorporated directly into the scattering matrix [24, 25]. Matched stubs can be viewed as coupling directly with appropriate field components.

Given the effective electric and 'magnetic' conductivities σ_{ek} and σ_{mk} in the k direction, lossy elements for the 3D time-domain TLM are defined as [24, 25]:

$$G_{ek} = \sigma_{ek} \frac{\Delta i \Delta j}{\Delta k} \tag{2.43}$$

$$R_{mk} = \sigma_{mk} \frac{\Delta i \Delta j}{\Delta k} \tag{2.44}$$

Lossy elements serve merely to model the dissipation of energy; they do not interfere directly with the wave propagation velocity. Hence, the general system of

equations used to determine parameters of link and stub lines, given by (2.33)–(2.34) is not affected by the presence of matched stubs.

In frequency-domain TLM, losses are included directly into the TLM constitutive relations by using complex parameters defined as [26]:

$$\varepsilon_k = \varepsilon'_k - \frac{j\sigma_{ek}}{\omega} \tag{2.45}$$

$$\mu_k = \mu'_k - \frac{j\sigma_{mk}}{\omega} \tag{2.46}$$

where ε'_k, μ'_k represent the real parts of the complex permittivity and permeability, respectively. The losses can be modelled directly by lossy link lines, hence the capacitance and inductance C_{ij} and L_{ij} in equations (2.33)–(2.34) are replaced by terms $C_{ij} - jG_{ij}/\omega$ and $L_{ij} - jR_{ij}/\omega$, respectively, where G_{ij}, R_{ij} are the distributed shunt and series losses of the related link lines.

2.4 Derivation of existing TLM schemes

2.4.1 Stub-loaded nodes

As found in § 2.3.3, to solve the general system of equations for the TLM parameters, six additional constraints have to be imposed. In the case of the traditional stub-loaded nodes [9, 13], these constraints are easily found in the requirement that all six link lines have the same characteristic impedances equal to the intrinsic impedance of the background medium (usually free-space): $Z_0 = \sqrt{\mu_0/\varepsilon_0}$.

Therefore, six extra equations of the form $Z_{ij} = Z_0$ (or equivalently $Y_{ij} = Y_0 = 1/Z_0$) are introduced into the system of equations (2.41)–(2.42), reducing it into:

$$2Y_0 + \frac{Y_{ok}}{2} = \varepsilon_k \frac{\Delta i \Delta j}{\Delta k \Delta t} \tag{2.47}$$

$$2Z_0 + \frac{Z_{sk}}{2} = \mu_k \frac{\Delta i \Delta j}{\Delta k \Delta t} \tag{2.48}$$

Since the impedance of the link lines is set by the background medium, the only parameters to be determined are Y_{ok} and Z_{sk}. These are found from (2.47)–(2.48) as:

$$Y_{ok} = 2Y_0 \left(\frac{\varepsilon_{rk}}{c\Delta t} \frac{\Delta i \Delta j}{\Delta k} - 2 \right) \tag{2.49}$$

$$Z_{sk} = 2Z_0 \left(\frac{\mu_{rk}}{c\Delta t} \frac{\Delta i \Delta j}{\Delta k} - 2 \right) \tag{2.50}$$

where $c = 1/\sqrt{\mu_0\varepsilon_0}$, the wave velocity in the background medium (usually the speed of light in free-space). Replacing dummy indices by x, y and z in equations (2.49)–(2.50) they produce expressions equivalent to those for the expanded node and the SCN obtained in [6, 27, 28].

For stability, it is necessary to ensure that all stubs represent real positive component values [6]. Hence, the maximum time-step for the node can be determined from (2.49)–(2.50) by demanding that Y_{ok} and Z_{sk} are non-negative, giving:

$$\Delta t \leq \frac{\varepsilon_{rk}\Delta i\Delta j}{2c\Delta k} \tag{2.51}$$

$$\Delta t \leq \frac{\mu_{rk}\Delta i\Delta j}{2c\Delta k} \tag{2.52}$$

where $i, j, k \in \{x, y, z\}$ and $i \neq j, k$.

For a uniform mesh ($\Delta i = \Delta j = \Delta k = \Delta l$) and air as the background medium ($\varepsilon_{rk} = \mu_{rk} = 1$), the maximum time step reduces to the well-known relation [9]:

$$\Delta t_{\max} = \frac{\Delta l}{2c} \tag{2.53}$$

When grading is introduced, for example by shrinking one node dimension, say Δx, where $\Delta x < \Delta y$ and $\Delta y = \Delta z$, the maximum time step is determined by:

$$\Delta t_{\max} = \frac{\Delta x}{2c} \tag{2.54}$$

i.e. it is related to the smallest node dimension Δx. However, in another example, by expanding one node dimension, say $\Delta x > \Delta y$ and $\Delta y = \Delta z = \Delta l$, the maximum time step is determined by:

$$\Delta t_{\max} = \frac{\Delta l}{2c} \cdot \frac{\Delta l}{\Delta x} \tag{2.55}$$

In other words, the time step is no longer related to the smallest node dimension, in this case Δl, but has to be further decreased by the factor $\Delta x/\Delta l$ which is in fact the ratio between the largest and the smallest dimension of the node. The implications of this are that, in a large problem where large ratios are used to minimize storage, the resulting time-step may be very small, thus requiring long computational runs. Benefits resulting from reductions in storage using a graded mesh are diminished by the corresponding increases in run time.

It should be pointed out that in a complex mesh consisting of regions with different gradings (*non-uniformly graded mesh*), the maximum time step has to be calculated for each region and the smallest one has to be used as the maximum time step for the entire mesh.

2.4.2 Hybrid nodes

The difficulties caused by the generally small time step in a graded mesh with stub-loaded nodes can be overcome if the condition inherent in the SCN development – that all link lines have the same characteristic impedance – is relaxed. The idea was explored in [29] and implemented for the expanded node in [30]. Its implementation for the SCN, referred to as the *hybrid symmetrical condensed node* (HSCN) was described in [19, 31, 32].

The HSCN consists of link lines that model all required inductance at the node, and hence short-circuit stubs are removed from the node. This is achieved by allowing the link lines which model different components of the magnetic field to have different values. The absence of short-circuit stubs sets three conditions in the form:

$$Z_{sk} = 0 \tag{2.56}$$

where $k \in \{x, y, z\}$. The requirement that the impedances of the link lines modelling the same magnetic field component are equal is given by another three conditions in the form:

$$Z_{ij} = Z_{ji} \tag{2.57}$$

for $i, j \in \{x, y, z\}$ and $i \neq j$. Inserting the conditions (2.56) and (2.57) into the generic equation (2.42), we obtain the characteristic impedances of the link lines as:

$$Z_{ij} = Z_{ji} = \frac{\mu_k \Delta i \Delta j}{2\Delta k \Delta t} = Z_0 \frac{\mu_{rk} \Delta i \Delta j}{2c\Delta t \Delta k} \tag{2.58}$$

Three sets of link lines are described by this equation if i, j are replaced by x, y, z and $i \neq j$. For convenience, the characteristic admittances of link lines are also written as:

$$Y_{ij} = Y_{ji} = Y_0 \frac{2c\Delta t \Delta k}{\mu_{rk} \Delta i \Delta j} \tag{2.59}$$

Inserting this into equation (2.41) by using an appropriate shifting of dummy indices, the characteristic admittances of the open circuit stubs are obtained, after simple algebra, as:

$$Y_{ok} = Y_0 \left[\frac{2\varepsilon_{rk} \Delta i \Delta j}{c\Delta t \Delta k} - \frac{4c\Delta t}{\Delta k} \left(\frac{\Delta i}{\mu_{ri} \Delta j} + \frac{\Delta j}{\mu_{rj} \Delta i} \right) \right] \tag{2.60}$$

Replacing dummy indices by x, y and z in equations (2.59)–(2.60) and taking an isotropic medium ($\varepsilon_{rk} = \varepsilon_r$, $\mu_{rk} = \mu_r$), they produce expressions equivalent to those obtained in [32].

Recently, a complementary HSCN was described [20] in which all the required capacitance is modelled by link lines and short-circuit stubs are used to make up for the deficit in the inductance. The link lines contributing to the same electric field component are set to have the same values of the characteristic impedance. This HSCN is denoted as the Type II HSCN [20], whereas the previously examined HSCN is referred to as the Type I HSCN.

Six additional constraints imposed on the general system of equations (2.41)–(2.42) in this case are given as follows. The absence of open-circuit stubs sets three conditions in the form:

$$Y_{ok} = 0 \tag{2.61}$$

where $k \in \{x, y, z\}$. The requirements for the link line characteristic admittances can be formulated by another three conditions of the form:

$$Y_{ik} = Y_{jk} \tag{2.62}$$

for $i, j, k \in \{x, y, z\}$ and $i \neq j, k$. Inserting the conditions (2.61) and (2.62) into the generic equation (2.41), we obtain the characteristic admittances of the link lines as:

$$Y_{ik} = Y_{jk} = \frac{\varepsilon_k \Delta i \Delta j}{2\Delta k \Delta t} = Y_0 \frac{\varepsilon_{rk} \Delta i \Delta j}{2c\Delta t \Delta k} \tag{2.63}$$

For convenience, the characteristic impedances of link lines are also written as:

$$Z_{ik} = Z_{jk} = Z_0 \frac{2c\Delta t \Delta k}{\varepsilon_{rk} \Delta i \Delta j} \tag{2.64}$$

Inserting this into equation (2.42) by using appropriate shifting of dummy indices, the characteristic impedances of the short circuit stubs are obtained, after simple algebra, as:

$$Z_{sk} = Z_0 \left[\frac{2\mu_{rk} \Delta i \Delta j}{c\Delta t \Delta k} - \frac{4c\Delta t}{\Delta k} \left(\frac{\Delta i}{\varepsilon_{ri} \Delta j} + \frac{\Delta j}{\varepsilon_{rj} \Delta i} \right) \right] \tag{2.65}$$

The definition of the link lines and stubs in the complementary Type II HSCN can be also described by using the definition of the Type I HSCN given by (2.59) and (2.60) and performing the following textual substitutions: $Y_{ij} \rightarrow Z_{ik}$, $Y_{ok} \rightarrow Z_{sk}$, $Y_0 \rightarrow Z_0$, $\mu \rightarrow \varepsilon$ and $\varepsilon \rightarrow \mu$ [20].

The maximum time step for the HSCN can be determined in a similar way as for the stub-loaded nodes, by demanding that parameters of stubs have non-negative

values. For the Type I HSCN, for example, it is demanded from (2.60) that $Y_{ok} \geq 0$, resulting in the definition of the maximum time step given by:

$$\Delta t \leq \frac{1}{2c}\sqrt{\frac{2\varepsilon_{rk}}{1/[\mu_{rj}(\Delta i)^2] + 1/[\mu_{ri}(\Delta j)^2]}} \tag{2.66}$$

where $i, j, k \in \{x, y, z\}$ and $i \neq j, k$.

For the medium with background properties ($\varepsilon_{rk} = \mu_{ri} = \mu_{rj} = 1$) and with grading introduced, for example, by expanding one node dimension, say $\Delta x > \Delta y$ and $\Delta y = \Delta z$, the maximum time step is determined by:

$$\Delta t_{\max} = \frac{\Delta y}{2c} \tag{2.67}$$

i.e. it is related to the smallest node dimension Δy.

In another example, by shrinking one node dimension, say Δx, where $\Delta x < \Delta y$ and $\Delta y = \Delta z$ the maximum time step is determined by:

$$\Delta t_{\max} = \frac{1}{2c}\sqrt{\frac{2}{1/(\Delta x)^2 + 1/(\Delta y)^2}} > \frac{\Delta x}{2c} \tag{2.68}$$

This is always bigger than the time step related to the smallest node dimension, now Δx. In a limiting case when $\Delta x << \Delta y$ we obtain:

$$\Delta t_{\max} \approx \frac{\Delta x\sqrt{2}}{2c} \tag{2.69}$$

After analysing the inequality (2.66) for other possible cases, it is easily found that for any type of grading, the maximum permissible time-step $\Delta t_{\max}$ lies within the limits:

$$\frac{\Delta l}{2c} \leq \Delta t_{\max} < \frac{\Delta l\sqrt{2}}{2c} \tag{2.70}$$

where Δl is the smallest node dimension. If the time step related to the smallest node dimension is defined by $\Delta t_0 = \Delta l/(2c)$, inequality (2.70) can also be expressed as:

$$\Delta t_0 \leq \Delta t_{\max} < \Delta t_0\sqrt{2} \tag{2.71}$$

Practically this means, that in some cases the time step can be chosen to be up to $\sqrt{2}$ times higher than one related to the smallest node dimension.

So, in comparison with the time step in stub-loaded nodes, the value of the time step in hybrid nodes is higher and it is neither strictly dependent on the ratio of the smallest to the biggest node dimension as in the stubbed SCN, nor has it to be always related to the smallest node dimension. The latter fact has been overlooked

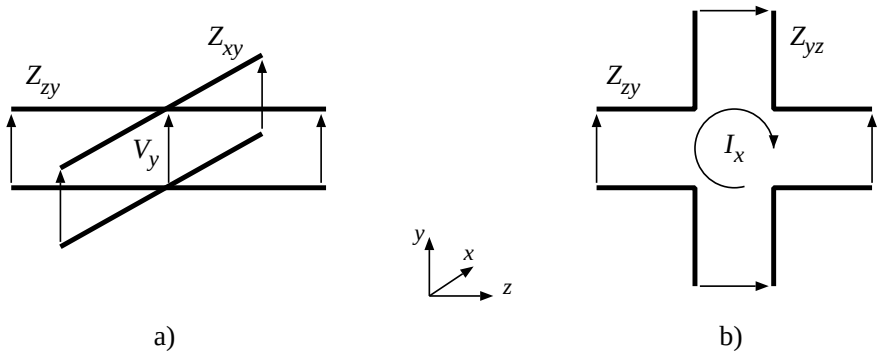

Figure 2.7 *2D TLM nodes. a) Shunt node, b) Series node*

in some recent publications, for example in [20]. Even though stability is always guaranteed when using the time step corresponding to the smallest node dimension in the hybrid node, it is not the optimal solution, either computationally (longer run-time) or from the point of accuracy (see Chapter 8).

2.4.3 Two-dimensional nodes

In many applications, one is only interested in studying propagation on a plane, for which 2D TLM schemes [12] are more efficient than 3D ones. The two basic structures in 2D TLM are shunt and series nodes, shown in Figure 2.7, each consisting of only two link lines. The derivations that follow are for the shunt version of the 2D TLM node. By virtue of the duality between electric and magnetic fields, a similar analysis can be applied to the series node.

Consider the shunt node in Figure 2.7a where only y-polarized link lines exist. On average, a total of three stubs can be added per node: one open-circuit stub modelling capacitance in the y-direction, placed at the node centre, and two short-circuit stubs modelling inductance in the x- and the z-directions, placed at the interface between nodes [18].

The system of equations given by (2.41)–(2.42) reduces in the case of the 2D shunt node depicted in Figure 2.7a to:

$$Y_{xy} + Y_{zy} + \frac{Y_{oy}}{2} = \varepsilon_y \frac{\Delta z \Delta x}{\Delta y \Delta t} \tag{2.72}$$

$$Z_{xy} + \frac{Z_{sz}}{2} = \mu_z \frac{\Delta x \Delta y}{\Delta z \Delta t} \tag{2.73}$$

$$Z_{zy} + \frac{Z_{sx}}{2} = \mu_x \frac{\Delta y \Delta z}{\Delta x \Delta t} \tag{2.74}$$

Since $Y_{xy} = 1/Z_{xy}$ and $Y_{zy} = 1/Z_{zy}$, there are five unknowns, namely Z_{xy}, Z_{zy}, Y_{oy}, Z_{sx} and Z_{sz} in the system of three equations given by (2.72)–(2.74). Hence, extra requirements, similar to those explained already for 3D nodes, can be imposed.

Stub-loaded 2D node

The condition that characteristic impedances of link lines are the same can be imposed on a 2D shunt-node as [7]:

$$Z_{xy} = Z_{zy} = Z_0\sqrt{2} = \sqrt{\frac{2\mu_0}{\varepsilon_0}}$$

which after substituting in (2.72)–(2.74) gives the solution for the parameters of stubs as:

$$Y_{oy} = 2Y_0\left(\frac{\varepsilon_{ry}\Delta z\Delta x}{c\Delta t\Delta y} - \sqrt{2}\right) \tag{2.75}$$

$$Z_{sz} = 2Z_0\left(\frac{\mu_{rz}\Delta x\Delta y}{c\Delta t\Delta z} - \sqrt{2}\right) \tag{2.76}$$

$$Z_{sx} = 2Z_0\left(\frac{\mu_{rx}\Delta y\Delta z}{c\Delta t\Delta x} - \sqrt{2}\right) \tag{2.77}$$

These equations are identical to the expressions given in [18] for an isotropic medium.

The maximum time step in this node can be determined by demanding that the parameters of stubs are positive. Note that the third dimension of the block of space, in this case Δy, appears in the above solutions. It can have any value and should be chosen in such a manner as to allow the highest possible value of the time step. The main disadvantage of this node is that scattering occurs at the interfaces between nodes, because of the presence of short-circuit stubs. Further problems are experienced on the interface between two different media or two different grading schemes, where an averaging of the material and grading parameters has to be performed [18].

Hybrid 2D node

The existence of the short-circuit stubs on interfaces between two nodes in 2D stub-loaded nodes can be avoided by using hybrid nodes [18]. The two extra conditions (no short-circuit stubs) are now given as $Z_{sx} = Z_{sz} = 0$ and equations (2.72)–(2.74) yield the following solutions for the admittance of the link lines and the

open-circuit stub:

$$Y_{xy} = \frac{Y_0}{\Delta y}\frac{c\Delta t\Delta z}{\mu_{rz}\Delta x} \tag{2.78}$$

$$Y_{zy} = \frac{Y_0}{\Delta y}\frac{c\Delta t\Delta x}{\mu_{rx}\Delta z} \tag{2.79}$$

$$Y_{oy} = \frac{2Y_0}{\Delta y}\left[\frac{\varepsilon_{ry}\Delta x\Delta z}{c\Delta t} - c\Delta t\left(\frac{\Delta z}{\mu_{rz}\Delta x} + \frac{\Delta x}{\mu_{rx}\Delta z}\right)\right] \tag{2.80}$$

Note that the third dimension Δy does not play any role in the scattering, since all the admittances in the node can be normalized to $Y_0/\Delta y$.

The maximum time step can be determined from (2.80) by demanding that the admittance of stub is non-negative as:

$$\Delta t_{\max} = \frac{1}{c}\sqrt{\frac{\varepsilon_{ry}}{1/[(\Delta x)^2\mu_{rz}] + 1/[(\Delta z)^2\mu_{rx}]}} \tag{2.81}$$

Distributed 2D node

If the 2D hybrid node operates on the maximum time step defined by (2.81), then the open-circuit stub can be eliminated, as $Y_{oy} = 0$. In this way, a 2D distributed node without stubs is derived [33]. The price of eliminating stubs is paid by having the time step in this node fixed by the material properties and the node dimensions.

Since the TLM mesh in the time domain must operate with an identical time step in all its parts, different grading of the mesh within the same material is not possible with this node. Modelling of inhomogeneous materials can be achieved only if the grading ratio is adjusted within different regions to accommodate the same time step, as shown in [33]. The parameters of the distributed node described by equations (2.78)–(2.79) and (2.81) reduce to those derived in [33] if one assumes isotropic material and defines an equivalent mesh parameter as $\Delta l\sqrt{\epsilon\mu} = \Delta t\sqrt{2}$.

2.4.4 Frequency-domain nodes

Time-domain TLM (TD-TLM) renders Maxwell's equations discrete in both the space and time domains. In frequency-domain TLM (FD-TLM), time-harmonic variations are assumed and hence discretisation in space only is required [34]. As a consequence the impulse synchronism condition imposed in the TD-TLM, given by (2.35), is not applicable in the FD-TLM.

The frequency-domain TLM algorithm can be based on any time-domain TLM node, for example, the HSCN implemented in [22]. However, the less restrictive requirements of FD-TLM (no time synchronism required) permits the modeller to easily avoid the use of stubs. Here, two different FD-TLM schemes based on condensed nodes without stubs are derived from the general system of equations (2.33)–(2.34).

FD-TLM node with matching line impedances

In FD-TLM, voltage phasors are multiplied by a complex exponential factor $\exp(-j\beta_{ij}\Delta i)$, where the phase constant of an i-directed, j-polarized link line, β_{ij} is given by:

$$\beta_{ij} = \omega\sqrt{L_{ij}C_{ij}} \tag{2.82}$$

Originally, the FD-TLM was developed with the condition that the characteristic impedances of the link lines are the same and equal to the intrinsic impedance of an isotropic medium [21], i.e.

$$\sqrt{\frac{L_{ij}}{C_{ij}}} = Z = \sqrt{\frac{\mu}{\varepsilon}}$$

and that the phase constants on each limb are the same for both polarizations, i.e.

$$\beta_{ij} = \beta_{ik}$$

With these conditions, the system of equations (2.33)–(2.34) can be solved in terms of the phase constants as:

$$\beta_{ij} = \beta_{ik} = \frac{\beta_m}{2\Delta i}(S_j + S_k - S_i) \tag{2.83}$$

where the medium phase constant is defined as $\beta_m = \omega\sqrt{\mu\varepsilon}$ and $S_i = \Delta j\Delta k/\Delta i$.

The generalization of this node to include lossy media is given in [26, 34] and the node parameters in this case can be obtained from equations (2.33)–(2.34) after modifying them to include the parameters of a lossy medium, in the manner explained in § 2.3.5.

FD-TLM node with matching phase constants

The condition that the phase constant on each line corresponds to that of the modelled medium can be expressed by:

$$\beta_{ij} = \frac{\omega}{2}\sqrt{\varepsilon_j\mu_k}$$

Substituting this condition in equations (2.33)–(2.34) and using equation (2.82), the characteristic impedances of link lines can be derived as:

$$Z_{ij} = \frac{\Delta j}{\Delta k}\sqrt{\frac{\mu_k}{\epsilon_j}} \tag{2.84}$$

which is equivalent to the solutions given in [35, 36].

The modifications to this node to account for lossy media were shown in [36] and can be derived from equations (2.33)–(2.34) by following the principles explained in § 2.3.5.

2.5 Conclusion

In this chapter, a unified formulation for obtaining the link and stub parameters of TLM nodes was presented and applied in the derivation of all currently available nodes. It was shown that the general system of equations offers six degrees of freedom in formulating time-domain TLM schemes, making it possible to derive nodes with different combinations of stub and link line parameters. The general system of equations defined here will be used later in this thesis as a starting point for deriving new, more efficient nodes.

Chapter 3 Scattering in symmetrical condensed nodes

3.1 Introduction

The scattering procedure represents the core of a TLM algorithm. At each time step, pulses $\mathbf{V}^i$ incident at each node are scattered to produce reflected pulses $\mathbf{V}^r$. The incident and reflected pulses are connected through $\mathbf{V}^r = \mathbf{S}\mathbf{V}^i$ where $\mathbf{S}$ is a scattering matrix dependent on the topology of the node.

A useful feature of the 2D shunt and series nodes is the possibility to represent a node by an equivalent electrical circuit. The scattering matrix for the node can then be easily obtained by replacing transmission-lines and incident pulses by Thevenin equivalent circuits [6]. This is also possible for the 3D nodes where shunt and series circuit are spatially separated, namely in the expanded and the asymmetrical condensed node [13, 16]. A simple equivalent lumped circuit for the symmetrical condensed node cannot be constructed and therefore other methods must be used for the derivation of the scattering properties.

The scattering matrix for the SCN was originally obtained from Maxwell's equations using the concept of charge and energy conservation [9]. This method is unwieldy as it depends on the solution of non-linear simultaneous equations and it is not easy to appreciate the underlying physical conditions which have been imposed. For a general condensed node with arbitrary characteristic impedance of link lines, considered in this work, the original method of determining the scattering properties becomes very complex for practical use.

A simple method for obtaining scattering equations for symmetrical condensed nodes was proposed by Naylor and Ait-Saidi in [37]. Three equivalent voltages (V_x, V_y, V_z) and three equivalent currents (I_x, I_y, I_z) were first obtained from the 'equivalent' shunt and series circuits. Voltage pulses reflected into link lines are then calculated as a suitable combination of these quantities and an incident voltage from the opposite side of the line. The method is extremely simple and it

satisfies scattering equations for the stub-loaded and hybrid nodes [37]. However, the formulation of the method is empirical and the concept of equivalent shunt and series circuits is inconsistent with the topology of the node. Furthermore, it fails when determining the scattering in an unbalanced node proposed for modelling continuously varying boundaries [23] where the characteristic impedances of link lines can vary with respect to the node centre.

Herring and Christopoulos [38, 39] have proposed a method for obtaining the scattering properties of a TLM node, which is based on the following four physical principles: conservation of charge and magnetic flux and continuity of the electric and magnetic fields. A linear system of equations can be constructed from these principles whose solution leads to the empirical formulae introduced in [37], without a need for using inconsistent equivalent circuits. However, in the case when the impedances of link lines vary with respect to the node centre [23], it is not easy to appreciate the conditions imposed for the continuity of electric and magnetic fields.

An improved methodology for obtaining the scattering matrix of symmetrical condensed nodes by applying physical principles on the network of transmission-lines is proposed here. *Equivalent total voltages* and *equivalent total currents* at the centre of the node, corresponding to the appropriate electric and magnetic field components, respectively, are defined by averaging total voltages and currents of link lines using charge and magnetic flux balance conditions. By further exploiting conservation of the charge and magnetic flux, scattering equations for a general node are formulated in an elegant manner. This derivation takes into account the possibility that the impedance of the link lines can be different with respect to the node centre, in order to describe scattering in the unbalanced nodes needed for modelling infinitesimally adjustable boundaries [23]. A complete scattering formulation is presented for the first time in the literature, for a general symmetrical condensed node (GSCN) allowing for the possibility of 12 different link line impedances, 3 open-circuit stubs, 3 short-circuit stubs and 3 electric-loss and 3 magnetic-loss matched stubs.

3.2 Inconsistency in equivalent network representations

In 2D TLM, scattering in a node can be easily determined from an equivalent Thevenin circuit. Take, for example, a shunt connection of transmission lines with different characteristic impedance, including an open-circuit stub with characteristic admittance Y_{oy} and a matched electric-loss stub represented by a shunt

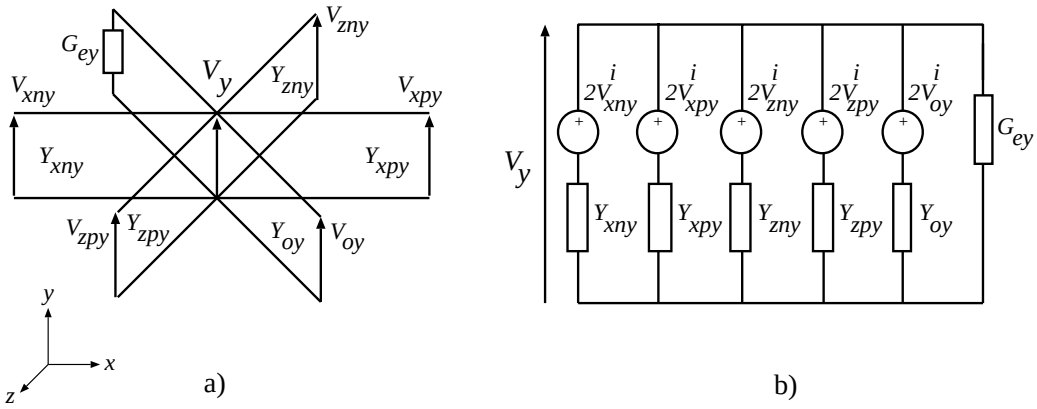

Figure 3.1 *a) 2D TLM shunt node. b) Equivalent Thevenin circuit*

conductance G_{ey}, as depicted in Figure 3.1a.

Because of the physical connection of the transmission-lines, the total voltage V on each transmission line at the centre of the node is the same and equal to V_y. As the total voltage on a line is the sum of an incident and a reflected pulse, $V = V^i + V^r$, the reflected voltage pulse in each line is simply calculated as:

$$V^r = V_y - V^i \tag{3.1}$$

and the only problem to be solved is the calculation of V_y. This can be easily done by replacing the transmission-lines with the equivalent Thevenin circuits, each of which has an admittance equal to the characteristic admittance of the corresponding line and a voltage source equal to $2V^i$ [6]. The equivalent Thevenin circuit for the shunt node is depicted in Figure 3.1b. The total voltage V_y is calculated from there as:

$$V_y = 2\,\frac{Y_{xny}V^i_{xny} + Y_{xpy}V^i_{xpy} + Y_{zny}V^i_{zny} + Y_{zpy}V^i_{zpy} + Y_{oy}V^i_{oy}}{Y_{xny} + Y_{xpy} + Y_{zny} + Y_{zpy} + Y_{oy} + G_{ey}} \tag{3.2}$$

and can be used in (3.1) for the calculation of reflected voltages into link and stub lines. The expression for total voltage V_y given by (3.2) can also be used to calculate electric field component E_y. By using the analogy between electric field components and voltage pulses on transmission-lines [6] it follows that:

$$E_y = -\frac{V_y}{\Delta y} \tag{3.3}$$

In 2D series nodes, transmission-lines with arbitrary characteristic impedances, including a short-circuit stub with characteristic impedance Z_{sz} and a matched magnetic-loss stub represented by a series resistance R_{mz}, are connected as depicted in Figure 3.2a.

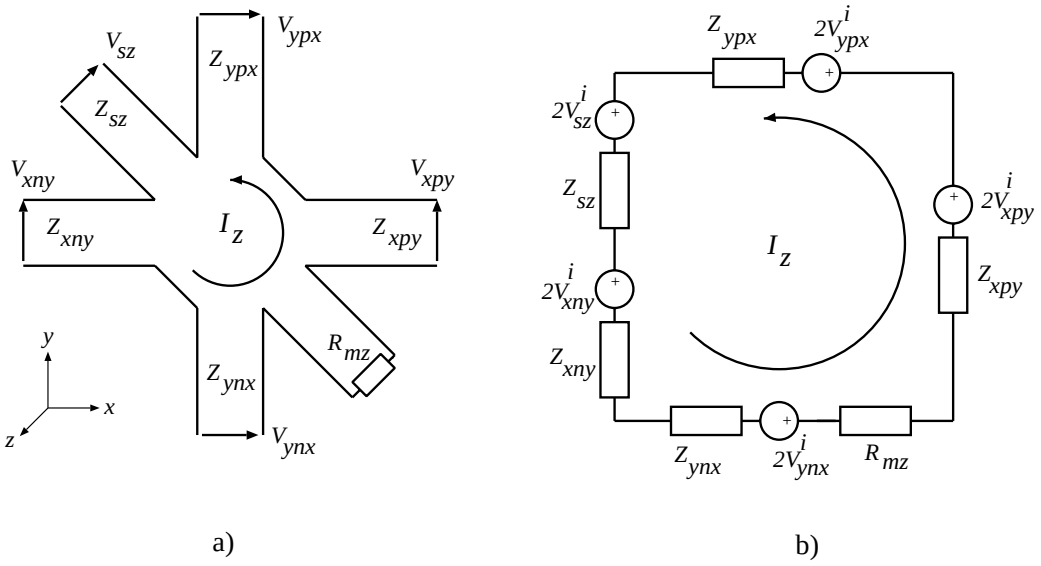

Figure 3.2 *a) 2D TLM series node. b) Equivalent Thevenin circuit*

Because of the physical connection of transmission-lines, the current flowing on each transmission line at the centre of the node is the same, and can be denoted by I_z. As the total current on a transmission line is defined as $I = (V^i - V^r)/Z$, and taking into account the polarities of incident voltage pulses, it follows that $I = \pm I_z$ and the reflected voltage pulse in each line is computed as:

$$V^r = V^i \mp Z I_z \tag{3.4}$$

where Z is the impedance of the appropriate transmission line. The computation of I_z can be easily done by replacing the transmission-lines with equivalent Thevenin circuits, as before. The equivalent Thevenin circuit for a complete series node is depicted in Figure 3.2b. The total current I_z is calculated from there as:

$$I_z = 2\,\frac{V^i_{xpy} - V^i_{xny} - V^i_{ypx} + V^i_{ynx} - V^i_{sz}}{Z_{xny} + Z_{xpy} + Z_{ynx} + Z_{ypx} + Z_{sz} + R_{mz}} \tag{3.5}$$

and can be used in (3.4) for the calculation of reflected voltages into link and stub lines. The definition of I_z given by equation (3.5) can be also used for the computation of the magnetic field component H_z. By exploiting the analogy between magnetic field components and voltage pulses on transmission-lines [6] it follows that:

$$H_z = \frac{I_z}{\Delta z} \tag{3.6}$$

In a 3D symmetrical condensed node, the mapping between field components and total voltages and currents in the centre of the node is identical to that occurring

in the 2D nodes described by equations (3.3) and (3.6). However, as simple shunt or series connections do not exist in the SCN, quantities such as, for example, V_y and I_z, which are related to E_y and H_z, do not physically represent total voltage or total current on transmission-lines. They are merely introduced as convenient average quantities to facilitate computation of the related field components, and will be referred to as *equivalent total voltage* and *equivalent total current*.

Naylor and Ait-Saidi [37] used the shunt network, similar to that depicted in Figure 3.1, to calculate the equivalent total voltage V_y in the stub-loaded symmetrical condensed node. The value of the electric field calculated in this way agrees with that originally obtained by Johns [9] and from this point of view, the decomposition of the condensed node to equivalent shunt and series networks can be justified. However, contrary to the 2D model, the total voltage on an individual link line of the 3D SCN is not identical to the equivalent total voltage, and subsequently, the expression for calculating reflected voltage pulses (3.1) is not valid. It is easily shown, for example, that in the SCN:

$$V_{xny}^r \neq V_y - V_{xny}^i$$

because the calculation of the reflected voltage pulses must take into account other transmission lines forming the series circuit [37].

A similar conclusion can be drawn when using the equivalent series network similar to that shown in Figure 3.2 for computing I_z and subsequently H_z in the SCN. Even though the value of H_z computed in this way is correct, the reflected voltages do not obey equation (3.4).

Therefore, it is clear that the decomposition of the SCN into equivalent shunt and series circuits leads to correct values of the computed field components, but does not give correct values for the reflected voltage pulses. As a result of this inconsistency, in the derivations of the scattering properties of the general SCN which follow, the centre of the node will be treated as an undefined region in which the link lines from adjacent nodes converge. Instead of adhoc equivalent circuits, only established physical principles, i.e. charge and flux conservation and their balance will be used in the derivation.

Note that the derivation of the scattering equations for balanced symmetrical condensed nodes is also performed in Chapter 4 but from different principles — by using central differencing and averaging of Maxwell's equations.

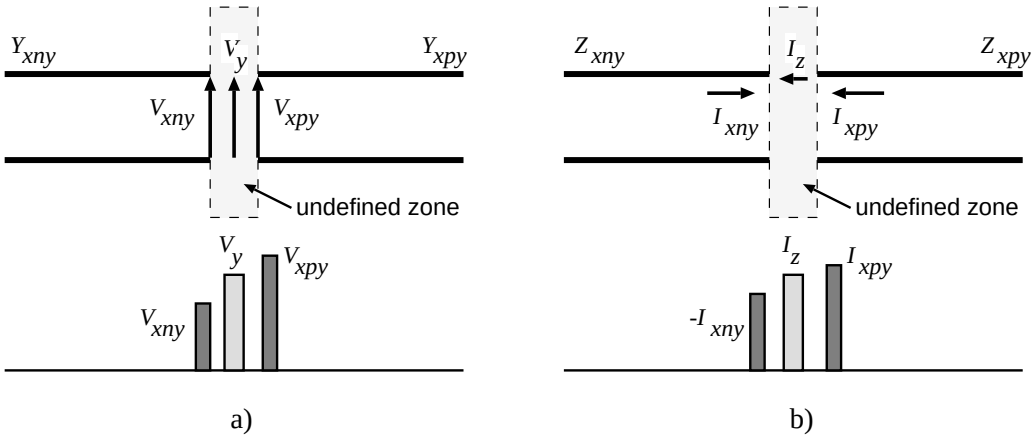

Figure 3.3 *a) Equivalent total voltage b) Equivalent total current*

3.3 Scattering in the general symmetrical condensed node

3.3.1 Scattering into link lines

The total voltage on an individual transmission-line at a scattering point, e.g. the node centre, is equal to the sum of the incident and reflected voltages on this line. In the SCN, it can be easily shown that, for example, for an x-directed, y-polarized line, the total voltages on link lines from different sides of the node centre generally differ, e.g. $V_{xny} \neq V_{xpy}$, as shown in Figure 3.3a. An equivalent total voltage in the centre of the node V_y can be introduced as an average value of V_{xny} and V_{xpy}. The averaging can be done by imposing charge balance on the respective lines, as follows.

The total capacitance associated with one half of a link line may be obtained from (2.38) and is $Y_{line}\Delta t/2$. Using the definition of charge ($Q = CV$) the sum of total charges on the lines in Figure 3.3a lying on the left and right-hand side of the centre is equal to $(V_{xny}Y_{xny} + V_{xpy}Y_{xpy})\Delta t/2$. From the requirement that charge flow across the line must be continuous the total charge at the centre must be $V_y(Y_{xny} + Y_{xpy})\Delta t/2$. By equalizing the sum of charges on individual lines to that in the centre of the node and solving for V_y it follows that:

$$V_y = \frac{Y_{xny}V_{xny} + Y_{xpy}V_{xpy}}{Y_{xny} + Y_{xpy}} \tag{3.7}$$

In the special case when $Y_{xny} = Y_{xpy}$, this equation simplifies to:

$$V_y = \frac{V_{xny} + V_{xpy}}{2} \tag{3.8}$$

which is a simple averaging of the two total voltages on individual link lines.

The total current on an individual transmission-line at a scattering point, e.g. the node centre, can be defined as the difference between the incident and reflected voltages on this line over the impedance Z of the line. Similarly, as for the equivalent total voltage, an equivalent total current, for example I_z, can be introduced by averaging I_{xny} and I_{xpy}, as shown in Figure 3.3b. The averaging can be done by imposing magnetic flux balance on the lines, as follows.

The total inductance associated with one half of a link line may be obtained from (2.37) and is $Z_{line}\Delta t/2$. Using the definition for magnetic flux ($\Phi = LI$) the sum of total flux linkages on the lines shown in Figure 3.3b is equal to $(I_{xpy}Z_{xpy} - I_{xny}Z_{xny})\Delta t/2$. From the requirement that magnetic flux across the line must be continuous the total flux in the centre must be $I_z(Z_{xny}+Z_{xpy})\Delta t/2$. By equalizing the sum of flux linkages on individual lines (taking into account the appropriate orientations of currents) to that in the centre of the node and solving for I_z it follows that:

$$I_z = \frac{Z_{xpy}I_{xpy} - Z_{xny}I_{xny}}{Z_{xny} + Z_{xpy}} \tag{3.9}$$

In the special case when $Z_{xny} = Z_{xpy}$, this equation simplifies to:

$$I_z = \frac{I_{xpy} - I_{xny}}{2} \tag{3.10}$$

which is simple averaging of the two total currents on the individual link lines, taking into account their different orientations.

Expressing the total voltage in terms of the incident and reflected voltages and using the equality

$$\frac{Y_1}{Y_1 + Y_2} = \frac{Z_2}{Z_1 + Z_2}$$

equations (3.7) and (3.9) can be rewritten as

$$V_y = \frac{Z_{xpy}}{Z_{xny} + Z_{xpy}} (V^i_{xny} + V^r_{xny}) + \frac{Z_{xny}}{Z_{xny} + Z_{xpy}} (V^i_{xpy} + V^r_{xpy}) \tag{3.11}$$

$$I_z = \frac{1}{Z_{xny} + Z_{xpy}} (V^i_{xpy} - V^r_{xpy}) - \frac{1}{Z_{xny} + Z_{xpy}} (V^i_{xny} - V^r_{xny}) \tag{3.12}$$

Multiplying equation (3.12) by Z_{xny}, adding it to equation (3.11), and solving for V^r_{xny} we derive:

$$V^r_{xny} = V_y + I_z Z_{xny} + \frac{Z_{xny} - Z_{xpy}}{Z_{xny} + Z_{xpy}} V^i_{xny} - \frac{2Z_{xny}}{Z_{xny} + Z_{xpy}} V^i_{xpy} \tag{3.13}$$

The reflected voltage pulse on the other side of the node centre, V^r_{xpy}, can be derived by multiplying equation (3.12) by Z_{xpy} and subtracting it from equation (3.11). After solving for V^r_{xpy} it follows that:

$$V^r_{xpy} = V_y - I_z Z_{xpy} + \frac{Z_{xpy} - Z_{xny}}{Z_{xny} + Z_{xpy}} V^i_{xpy} - \frac{2Z_{xpy}}{Z_{xny} + Z_{xpy}} V^i_{xny} \tag{3.14}$$

Scattering equations (3.13) and (3.14) can be rewritten as:

$$V^r_{xny} = V_y + I_z Z_{xny} - V^i_{xpy} + h_{xy} \tag{3.15}$$

$$V^r_{xpy} = V_y - I_z Z_{xpy} - V^i_{xny} + h_{xy} \tag{3.16}$$

where h_{xy} is defined as:

$$h_{xy} = \frac{Z_{xny} - Z_{xpy}}{Z_{xny} + Z_{xpy}} \left(V^i_{xny} - V^i_{xpy} \right) \tag{3.17}$$

Note that for a balanced node, with $Z_{xny} = Z_{xpy} = Z_{xy}$, it follows that $h_{xy} = 0$ and equations (3.15)–(3.16) reduce to:

$$V^r_{xny} = V_y + I_z Z_{xy} - V^i_{xpy} \tag{3.18}$$

$$V^r_{xpy} = V_y - I_z Z_{xy} - V^i_{xny} \tag{3.19}$$

The scattering equations (3.18) and (3.19) are in the form which was empirically introduced by Naylor and Ait-Saidi [37].

To completely formulate the scattering equations given by (3.15) and (3.16), the equivalent voltage V_y and equivalent current I_z must be expressed in terms of incident voltages. Before this is done, the scattering into stubs will first be defined.

3.3.2 Scattering into stubs

Stubs are introduced in the condensed node to directly couple with the particular component of the electric or magnetic field. Therefore, the total voltage on the open-circuit and electric-loss stubs is by definition determined by the appropriate electric field component, hence they are identical to the equivalent total voltage in the centre of the node. For the E_y component, $V_{oy} = V_{ey} = V_y$, and reflected voltages are simply determined as:

$$V^r_{oy} = V_y - V^i_{oy} \tag{3.20}$$

$$V^r_{ey} = V_y \tag{3.21}$$

Note that there is no incident pulse from the matched electric-loss stub.

Similarly, the total current flowing through the short-circuit and magnetic-loss stubs is directly determined by the appropriate magnetic field component and is identical to an equivalent total current. For historical reasons, i.e. to maintain consistency with the original scattering matrix derived by Johns [9], the orientation of incident voltages on the short-circuit and magnetic-loss stubs is chosen to be opposite to the orientation of the total current. Therefore, for the H_z component, $I_{sz} = I_{mz} = -I_z$, which expressed in terms of incident and reflected voltages gives:

$$\begin{aligned} \frac{V_{sz}^i - V_{sz}^r}{Z_{sz}} &= -I_z \\ -\frac{V_{mz}^r}{R_{mz}} &= -I_z \end{aligned}$$

Solving for the reflected voltages gives:

$$V_{sz}^r = V_{sz}^i + I_z Z_{sz} \tag{3.22}$$

$$V_{mz}^r = I_z R_{mz} \tag{3.23}$$

Note that there is no incident voltage from the matched magnetic-loss stub.

3.3.3 Derivation of equivalent total voltage

The equivalent total voltage V_y can be derived by combining conditions for charge balance and charge conservation for the transmission-lines coupling with E_y field component, which are depicted in Figure 3.4a. To avoid inconsistencies in decomposing the GSCN into equivalent shunt and series circuits used in [37] the centre of the node is treated as an undefined region.

Charge conservation applied to all lines contributing to E_y can be written as:

$$\Delta Q_y = \sum_n \Delta Q_{n,y} = 0$$

Using the expression $\Delta Q_n = I_n \Delta t$ this condition becomes equivalent to the Kirchhoff's First Law:

$$\sum_n I_{n,y} = 0$$

where $I_{n,y}$ are currents on the y-polarized lines. Current on a transmission line can be represented in terms of incident and reflected voltage as $I = Y(V^i - V^r)$.

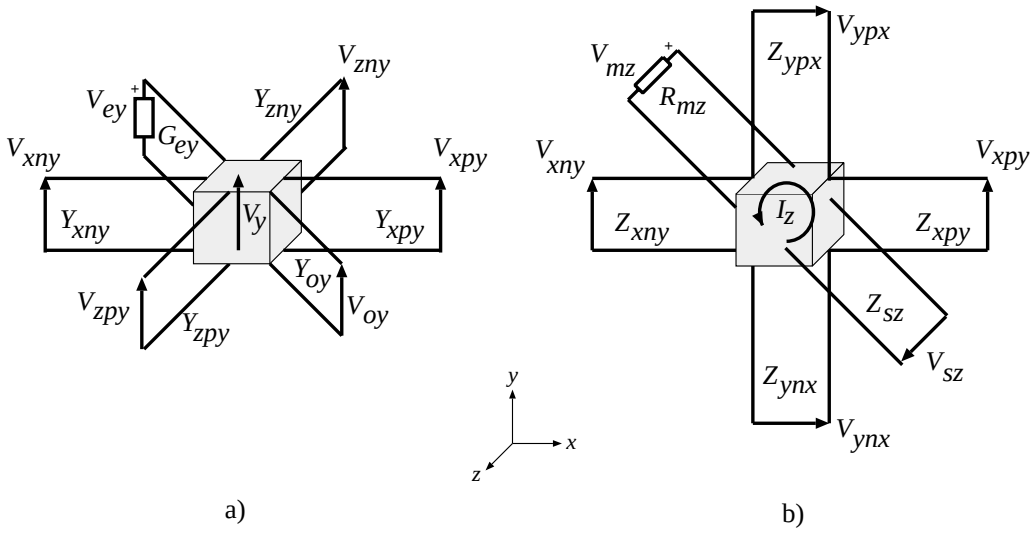

Figure 3.4 *Transmission-lines of the GSCN coupling with a) E_y b) H_z field components*

Therefore, using the notation introduced in § 2.3.1, the charge conservation principle applied to the y-direction can be written as:

$$\begin{aligned} &Y_{xny}(V^i_{xny} - V^r_{xny}) + Y_{xpy}(V^i_{xpy} - V^r_{xpy}) + \\ &Y_{zny}(V^i_{zny} - V^r_{zny}) + Y_{zpy}(V^i_{zpy} - V^r_{zpy}) + \\ &Y_{oy}(V^i_{oy} - V^r_{oy}) - G_{ey}V^r_{ey} = 0 \end{aligned} \tag{3.24}$$

Note that the incident voltage from the matched (conductivity) stub is considered zero. Equations for charge conservation similar to (3.24) can be written for each of the other two coordinate directions.

Using the definition of equivalent total voltage given by (3.7), the voltage pulses reflected to the x-directed y-polarized link lines can be expressed as:

$$Y_{xny}V^r_{xny} + Y_{xpy}V^r_{xpy} = V_y(Y_{xny} + Y_{xpy}) - Y_{xny}V^i_{xny} - Y_{xpy}V^i_{xpy} \tag{3.25}$$

By virtue of symmetry, an equation similar to (3.25) can be written for the z-directed y-polarized lines as:

$$Y_{zny}V^r_{zny} + Y_{zpy}V^r_{zpy} = V_y(Y_{zny} + Y_{zpy}) - Y_{zny}V^i_{zny} - Y_{zpy}V^i_{zpy} \tag{3.26}$$

Inserting equations (3.25) and (3.26) into the charge conservation expression given by (3.24) and making use of the expressions for stubs (3.20) and (3.21), we derive

the equivalent total voltage V_y solely in terms of incident voltages as:

$$V_y = 2\,\frac{Y_{xny}V^i_{xny} + Y_{xpy}V^i_{xpy} + Y_{zny}V^i_{zny} + Y_{zpy}V^i_{zpy} + Y_{oy}V^i_{oy}}{Y_{xny} + Y_{xpy} + Y_{zny} + Y_{zpy} + Y_{oy} + G_{ey}} \tag{3.27}$$

Note that V_y may also be calculated from the Thevenin equivalent circuit obtained from Figure 3.4a when the transmission-lines are connected in parallel. This circuit is misleading, however, since it is inconsistent with the pulses scattered into the link lines, as discussed in § 3.2.

3.3.4 Derivation of equivalent total current

The equivalent total current I_z can be derived by combining conditions for magnetic flux balance and conservation for the transmission-lines coupling with H_z field component, which are depicted in Figure 3.4b.

For n lines crossing a closed surface, magnetic flux conservation in, for example, the z-direction, can be written as:

$$\Delta\Phi_z = \sum_n \Delta\Phi_{n,z} = 0$$

Using the expression $\Delta\Phi_n = V_n\Delta t$ this condition becomes equivalent to the Kirchhoff's Second Law:

$$\sum_n V_{n,z} = 0$$

where $V_{n,z}$ are total voltages on the lines contributing to the magnetic field in the z-direction. Total voltage on a transmission line can be represented in terms of incident and reflected voltage as $V = V^i + V^r$. Therefore, taking into account the orientation of the voltages on lines contributing to H_z (Figure 3.4b), the magnetic flux conservation principle applied to the z-direction can be written as:

$$(V^i_{xpy}+V^r_{xpy})-(V^i_{xny}+V^r_{xny})+(V^i_{ynx}+V^r_{ynx})-(V^i_{ypx}+V^r_{ypx})-(V^i_{sz}+V^r_{sz})-V^r_{mz}=0 \tag{3.28}$$

Note that incident voltage from the matched (resistivity) stub is considered zero. Equations for the flux conservation similar to (3.28) can also be written for the other two coordinate directions.

Using the definition of equivalent total current given by (3.9), the voltage pulses reflected to the x-directed y-polarized link lines can be expressed as:

$$V^r_{xpy} - V^r_{xny} = V^i_{xpy} - V^i_{xny} - I_z(Z_{xny} + Z_{xpy}) \tag{3.29}$$

By virtue of symmetry, an equation similar to (3.29) can be written for the y-directed x-polarized lines as:

$$V^r_{ypx} - V^r_{ynx} = V^i_{ypx} - V^i_{ynx} + I_z(Z_{ynx} + Z_{ypx}) \tag{3.30}$$

Inserting equations (3.29) and (3.30) into the magnetic flux conservation expression given by (3.28) and making use of the expression for stubs (3.22) and (3.23), we derive the equivalent total current I_z solely in terms of incident voltages as:

$$I_z = 2\frac{V^i_{xpy} - V^i_{xny} + V^i_{ynx} - V^i_{ypx} - V^i_{sz}}{Z_{xny} + Z_{xpy} + Z_{ynx} + Z_{ypx} + Z_{sz} + R_{mz}} \tag{3.31}$$

Note that I_z may also be calculated from the Thevenin equivalent circuit obtained when the transmission-lines depicted in Figure 3.4b are connected in series. This circuit is, however, inconsistent with the scattered pulses, as already indicated.

3.3.5 Scattering equations in compact notation

Using similar procedures to those explained in the previous subsection, the scattering equations relating the voltage pulses on other link lines can be derived, giving a complete set of equations as:

$$\begin{aligned}
V^r_{xny} &= V_y + I_z Z_{xny} - V^i_{xpy} + h_{xy} \\
V^r_{xpy} &= V_y - I_z Z_{xpy} - V^i_{xny} + h_{xy} \\
V^r_{ynz} &= V_z + I_x Z_{ynz} - V^i_{ypz} + h_{yz} \\
V^r_{ypz} &= V_z - I_x Z_{ypz} - V^i_{ynz} + h_{yz} \\
V^r_{znx} &= V_x + I_y Z_{znx} - V^i_{zpx} + h_{zx} \\
V^r_{zpx} &= V_x - I_y Z_{zpx} - V^i_{znx} + h_{zx} \\
V^r_{zny} &= V_y - I_x Z_{zny} - V^i_{zpy} + h_{zy} \\
V^r_{zpy} &= V_y + I_x Z_{zpy} - V^i_{zny} + h_{zy} \\
V^r_{xnz} &= V_z - I_y Z_{xnz} - V^i_{xpz} + h_{xz} \\
V^r_{xpz} &= V_z + I_y Z_{xpz} - V^i_{xnz} + h_{xz} \\
V^r_{ynx} &= V_x - I_z Z_{ynx} - V^i_{ypx} + h_{yx} \\
V^r_{ypx} &= V_x + I_z Z_{ypx} - V^i_{ynx} + h_{yx}
\end{aligned}$$

Using dummy indices i, j, k, these can be written in a compact notation as:

$$V^r_{inj} = V_j \pm I_k Z_{inj} - V^i_{ipj} + h_{ij} \tag{3.32}$$

$$V^r_{ipj} = V_j \mp I_k Z_{ipj} - V^i_{inj} + h_{ij} \tag{3.33}$$

where the upper and lower signs apply, respectively, for indices $(i, j, k) \in \{(x, y, z), (y, z, x), (z, x, y)\}$ and $(i, j, k) \in \{(x, z, y), (y, x, z), (z, y, x)\}$.

The equivalent voltage in the i direction, V_i, can be written according to equation (3.27) as:

$$V_i = 2\,\frac{Y_{kni}V^i_{kni} + Y_{kpi}V^i_{kpi} + Y_{jni}V^i_{jni} + Y_{jpi}V^i_{jpi} + Y_{oi}V^i_{oi}}{Y_{kni} + Y_{kpi} + Y_{jni} + Y_{jpi} + Y_{oi} + G_{ei}} \tag{3.34}$$

whereas the equivalent current contributing to the magnetic field in the i direction, I_i, is given according to equation (3.31) by:

$$I_i = 2\,\frac{V^i_{jpk} - V^i_{jnk} + V^i_{knj} - V^i_{kpj} - V^i_{si}}{Z_{jnk} + Z_{jpk} + Z_{knj} + Z_{kpj} + Z_{si} + R_{mi}} \tag{3.35}$$

where $(i, j, k) \in \{(x, y, z), (y, z, x), (z, x, y)\}$. Factor h_{ij} is given according to equation (3.17) as:

$$h_{ij} = \frac{Z_{inj} - Z_{ipj}}{Z_{inj} + Z_{ipj}} \left(V^i_{inj} - V^i_{ipj}\right) \tag{3.36}$$

The voltages reflected to stubs are given, according to equations (3.20)–(3.23) as:

$$V^r_{oi} = V_i - V^i_{oi} \tag{3.37}$$

$$V^r_{si} = I_i Z_{si} + V^i_{si} \tag{3.38}$$

$$V^r_{ei} = V_i \tag{3.39}$$

$$V^r_{mi} = I_i R_{mi} \tag{3.40}$$

where $i \in \{x, y, z\}$.

Therefore, in this way, the scattering properties of the most general condensed node, with 12 different link line impedances and 12 different stubs is described in a rather concise and simple form. This is to be compared with the complexity of the original definition of the node with arbitrary link lines (without stubs) [23].

It should be pointed out that the derivation of the scattering equations was carried out without explicitly enforcing the energy conservation condition — the basic

concept used by Johns [9]. The requirement that energy is conserved in a non-dissipative medium modelled by the GSCN, can be written as:

$$\sum_n Y_n (V_n^r)^2 = \sum_n Y_n (V_n^i)^2 \tag{3.41}$$

where the summation is carried out for all Y_n and V_n, of each transmission line (link and stub) connected into the node. By removing lossy elements from the scattering equations (3.32)–(3.40), setting $G_{ei} = R_{mi} = 0$, it can be proved by direct substitution that reflected and incident voltages indeed satisfy the energy conservation condition (3.41), even for unbalanced nodes with $h_{ij} \neq 0$.

3.3.6 Scattering matrix of the GSCN

As far as computational efficiency is concerned, the scattering procedure could be most efficiently implemented by first computing equivalent total voltages and currents using equations (3.34) and (3.35) and, in case of unbalanced boundary nodes, factors h_{ij} using equation (3.36). Subsequently, voltage reflected to the link lines and stubs can be computed by making use of scattering equations (3.32) and (3.33) for link lines and (3.37) and (3.38) for stubs. The efficient implementation of the scattering procedure for different nodes will be further discussed in Chapter 6.

In order to study the numerical characteristics of different symmetrical condensed node schemes, dispersion relations must be derived. The general dispersion relation for the symmetrical condensed node schemes was formulated in an implicit form of an eigenvalue matrix equation [40] which involves the scattering matrix of the node. Hence, in order to facilitate the dispersion analysis, the scattering matrix for the general symmetrical condensed node needs also to be formulated. Since the unbalanced nodes with 12 possible different link line impedances are not used for modelling of general wave propagation in an unbounded space (apart from boundaries), only balanced nodes, with $Z_{inj} = Z_{ipj} = Z_{ij}$, are considered in the dispersion analysis in Chapter 7. Therefore, only the scattering matrix for balanced GSCN is formulated here.

Using the scattering equations (3.32)–(3.40) applied for the GSCN with $h_{ij} = 0$, we obtain the scattering matrix given in Figure 3.5. The ordering of voltage pulses within the matrix is carried out with respect to the original notation [9]. Because there are no incident voltages from matched (lossy) stubs, the matrix $\mathbf{S}$ is written as a 24×18 matrix rather than a full 24×24 square matrix with zero columns

19 . . . 24. The elements of the scattering matrix $\mathbf{S}$ shown in Figure 3.5 are:

$$\begin{aligned}
a_{ij} &= Q_j - b_{ij} - d_{ij} & b_{ij} &= Q_j \hat{C}_{kj} \\
c_{ij} &= Q_j - b_{ij} + d_{ij} - 1 & d_{ij} &= P_k \hat{L}_{ij} \\
f_k &= 2(1 - P_k - U_k) & e_{ij} &= b_{kj} \\
g_j &= 2(1 - Q_j - W_j) & i_{ij} &= d_{ij} \\
h_j &= g_j - 1 & j_k &= 1 - f_k \\
k_{ij} &= e_{ij} & l_j &= g_j \\
m_k &= 2U_k & n_k &= -m_k
\end{aligned} \tag{3.42}$$

with

$$\hat{C}_{kj} = \frac{Y_{kj}}{Y_{ij} + Y_{kj}} = \frac{Z_{ij}}{Z_{ij} + Z_{kj}} \tag{3.43}$$

$$\hat{L}_{ij} = \frac{Z_{ij}}{Z_{ij} + Z_{ji}} \tag{3.44}$$

$$Q_j = \left(1 + \frac{Y_{oj} + G_{ej}}{2(Y_{ij} + Y_{kj})}\right)^{-1} \tag{3.45}$$

$$P_k = \left(1 + \frac{Z_{sk} + R_{mk}}{2(Z_{ij} + Z_{ji})}\right)^{-1} \tag{3.46}$$

$$W_j = \frac{G_{ej}}{2(Y_{ij} + Y_{kj}) + Y_{oj} + G_{ej}} \tag{3.47}$$

$$U_k = \frac{R_{mk}}{2(Z_{ij} + Z_{ji}) + Z_{sk} + R_{mk}} \tag{3.48}$$

where indices i, j, k take all possible combinations of x, y, z.

The matrix $\mathbf{S}$ can be written in the following partitioned form, where each submatrix represents one of the matrices outlined in Figure 3.5:

$$\mathbf{S} = \begin{bmatrix}
\mathbf{S}_{ln}^{(12\times12)} & \mathbf{S}_{os\to ln}^{(12\times3)} & \mathbf{S}_{ss\to ln}^{(12\times3)} \\
\mathbf{S}_{ln\to os}^{(3\times12)} & \mathbf{S}_{os}^{(3\times3)} & \mathbf{0}^{(3\times3)} \\
\mathbf{S}_{ln\to ss}^{(3\times12)} & \mathbf{0}^{(3\times3)} & \mathbf{S}_{ss}^{(3\times3)} \\
\mathbf{S}_{ln\to el}^{(3\times12)} & \mathbf{S}_{os\to el}^{(3\times3)} & \mathbf{0}^{(3\times3)} \\
\mathbf{S}_{ln\to ml}^{(3\times12)} & \mathbf{0}^{(3\times3)} & \mathbf{S}_{ss\to ml}^{(3\times3)}
\end{bmatrix} \tag{3.49}$$

The indices ln, os, ss, el, ml, indicating the physical purpose of each submatrix, stand for link line, open-circuit stub, short-circuit stub, electric loss and magnetic

$$\mathbf{S} = \left[\begin{array}{c|cccccccccccc|ccc|ccc}
 & 1 & 2 & 3 & 4 & 5 & 6 & 7 & 8 & 9 & 10 & 11 & 12 & 13 & 14 & 15 & 16 & 17 & 18 \\
\hline
1 & a_{yx} & b_{yx} & d_{yx} & 0 & 0 & 0 & 0 & 0 & b_{yx} & 0 & -d_{yx} & c_{yx} & g_x & 0 & 0 & 0 & 0 & i_{yx} \\
2 & b_{zx} & a_{zx} & 0 & 0 & 0 & d_{zx} & 0 & 0 & c_{zx} & -d_{zx} & 0 & b_{zx} & g_x & 0 & 0 & 0 & -i_{zx} & 0 \\
3 & d_{xy} & 0 & a_{xy} & b_{xy} & 0 & 0 & 0 & b_{xy} & 0 & 0 & c_{xy} & -d_{xy} & 0 & g_y & 0 & 0 & 0 & -i_{xy} \\
4 & 0 & 0 & b_{zy} & a_{zy} & d_{zy} & 0 & -d_{zy} & c_{zy} & 0 & 0 & b_{zy} & 0 & 0 & g_y & 0 & i_{zy} & 0 & 0 \\
5 & 0 & 0 & 0 & d_{yz} & a_{yz} & b_{yz} & c_{yz} & -d_{yz} & 0 & b_{yz} & 0 & 0 & 0 & 0 & g_z & -i_{yz} & 0 & 0 \\
6 & 0 & d_{xz} & 0 & 0 & b_{xz} & a_{xz} & b_{xz} & 0 & -d_{xz} & c_{xz} & 0 & 0 & 0 & 0 & g_z & 0 & i_{xz} & 0 \\
7 & 0 & 0 & 0 & -d_{yz} & c_{yz} & b_{yz} & a_{yz} & d_{yz} & 0 & b_{yz} & 0 & 0 & 0 & 0 & g_z & i_{yz} & 0 & 0 \\
8 & 0 & 0 & b_{zy} & c_{zy} & -d_{zy} & 0 & d_{zy} & a_{zy} & 0 & 0 & b_{zy} & 0 & 0 & g_y & 0 & -i_{zy} & 0 & 0 \\
9 & b_{zx} & c_{zx} & 0 & 0 & 0 & -d_{zx} & 0 & 0 & a_{zx} & d_{zx} & 0 & b_{zx} & g_x & 0 & 0 & 0 & i_{zx} & 0 \\
10 & 0 & -d_{xz} & 0 & 0 & b_{xz} & c_{xz} & b_{xz} & 0 & d_{xz} & a_{xz} & 0 & 0 & 0 & 0 & g_z & 0 & -i_{xz} & 0 \\
11 & -d_{xy} & 0 & c_{xy} & b_{xy} & 0 & 0 & 0 & b_{xy} & 0 & 0 & a_{xy} & d_{xy} & 0 & g_y & 0 & 0 & 0 & i_{xy} \\
12 & c_{yx} & b_{yx} & -d_{yx} & 0 & 0 & 0 & 0 & 0 & b_{yx} & 0 & d_{yx} & a_{yx} & g_x & 0 & 0 & 0 & 0 & -i_{yx} \\
\hline
13 & e_{yx} & e_{zx} & 0 & 0 & 0 & 0 & 0 & 0 & e_{zx} & 0 & 0 & e_{yx} & h_x & 0 & 0 & 0 & 0 & 0 \\
14 & 0 & 0 & e_{xy} & e_{zy} & 0 & 0 & 0 & e_{zy} & 0 & 0 & e_{xy} & 0 & 0 & h_y & 0 & 0 & 0 & 0 \\
15 & 0 & 0 & 0 & 0 & e_{yz} & e_{xz} & e_{yz} & 0 & 0 & e_{xz} & 0 & 0 & 0 & 0 & h_z & 0 & 0 & 0 \\
\hline
16 & 0 & 0 & 0 & f_x & -f_x & 0 & f_x & -f_x & 0 & 0 & 0 & 0 & 0 & 0 & 0 & j_x & 0 & 0 \\
17 & 0 & -f_y & 0 & 0 & 0 & f_y & 0 & 0 & f_y & -f_y & 0 & 0 & 0 & 0 & 0 & 0 & j_y & 0 \\
18 & f_z & 0 & -f_z & 0 & 0 & 0 & 0 & 0 & 0 & 0 & f_z & -f_z & 0 & 0 & 0 & 0 & 0 & j_z \\
\hline
19 & k_{yx} & k_{zx} & 0 & 0 & 0 & 0 & 0 & 0 & k_{zx} & 0 & 0 & k_{yx} & l_x & 0 & 0 & 0 & 0 & 0 \\
20 & 0 & 0 & k_{xy} & k_{zy} & 0 & 0 & 0 & k_{zy} & 0 & 0 & k_{xy} & 0 & 0 & l_y & 0 & 0 & 0 & 0 \\
21 & 0 & 0 & 0 & 0 & k_{yz} & k_{xz} & k_{yz} & 0 & 0 & k_{xz} & 0 & 0 & 0 & 0 & l_z & 0 & 0 & 0 \\
\hline
22 & 0 & 0 & 0 & m_x & -m_x & 0 & m_x & -m_x & 0 & 0 & 0 & 0 & 0 & 0 & 0 & n_x & 0 & 0 \\
23 & 0 & -m_y & 0 & 0 & 0 & m_y & 0 & 0 & m_y & -m_y & 0 & 0 & 0 & 0 & 0 & 0 & n_y & 0 \\
24 & m_z & 0 & -m_z & 0 & 0 & 0 & 0 & 0 & 0 & 0 & m_z & -m_z & 0 & 0 & 0 & 0 & 0 & n_z
\end{array}\right]$$

Figure 3.5 *Scattering matrix of the general symmetrical condensed node (GSCN). (The first row and column are not part of the matrix. They give the port numbering for convenience)*

loss voltage ports, respectively. The superscripts of the submatrices define their size. Some partitions can be removed from the matrix if stubs or lossy elements are not used. For example, if short-circuit stubs and lossy elements are not used in the node, all partitions with indices *ss*, *el* and *ml* can be removed from $\mathbf{S}$ giving a 15×15 matrix.

By removing lossy elements from the node, setting $G_{ej} = 0$ and $R_{mk} = 0$ in (3.45)–(3.48) and eliminating rows $19 \ldots 24$ in the scattering matrix $\mathbf{S}$, it can be shown that the lossless GSCN conserves energy by confirming that $\mathbf{S}^T\mathbf{Y}\mathbf{S} = \mathbf{Y}$ [41], where $\mathbf{Y}$ is diagonal matrix with elements corresponding to the characteristic admittances of link lines and stubs.

The matrix $\mathbf{S}$ has identical structure to the scattering matrix for the stub-loaded

SCN [6]. By setting the characteristic impedances of link lines equal to the intrinsic impedance of the background medium, i.e. letting $Z_{ij} = Z_0$, the elements of the GSCN and the SCN scattering matrix become equal, as expected. If an homogeneous lossless medium is modelled on a uniform mesh, then stubs and lossy elements can be eliminated by setting $Y_{oj} = Z_{sk} = G_{ej} = R_{mk} = 0$ in (3.45)–(3.48) and the partition $\mathbf{S}_{ln}$ of the matrix $\mathbf{S}$ becomes equal to the original 12-port SCN matrix [9] with the elements $a_{ij} = c_{ij} = 0$ and $b_{ij} = d_{ij} = 1/2$.

Similarly, by setting $Z_{ij} = Z_{ji}$ and $Z_{sk} = 0$, for all combinations of indices $i, j, k \in \{x, y, z\}, i \neq j, k$ and eliminating partitions of $\mathbf{S}$ related to the short-circuit stubs, the scattering matrix of the HSCN [19, 20] is derived. The scattering matrix for the Type II HSCN [20] can be derived from $\mathbf{S}$ by setting $Y_{ij} = Y_{kj}$, $Y_{oj} = 0$ and eliminating the partitions related to the open-circuit stubs.

Therefore, the scattering matrix of the GSCN unifies all the scattering matrices of the existing stub-loaded and hybrid nodes, described so far in the literature [6, 9, 19, 20, 25]. It should be pointed out again, that although the scattering can be expressed concisely in matrix notation, it is not appropriate, as far as computational efficiency is concerned, to implement the scattering procedure in this form. However, the scattering matrix of the GSCN, presented here, will be used for dispersion analysis in Part Three of this thesis.

Chapter 4 Derivation of the general SCN from Maxwell's equations

4.1 Introduction

In previous chapters, parameters and scattering properties of a most general symmetrical condensed node were described. The derivation was performed taking into account the analogy between field components and voltage pulses, inherent for the TLM modelling, and hence is referred to as the derivation from the *equivalent network model*. Scattering properties of the general node were formulated by using physical principles applied to the propagation of pulses along a network of transmission lines, thus indirectly relating them to the basic field propagation principles described by Maxwell's equations.

In this chapter, TLM method based on the general symmetrical condensed node will be derived directly from Maxwell's equations. The mathematical tool which will be used is based on finite differencing and central averaging, similar to that used in [42]. Based on this derivation, a direct correspondence between the general condensed TLM scheme and the finite difference method will be established. So far in the literature, a similar equivalence has been established for the case of the basic 12-port SCN modelling free space on a uniform mesh [43] and for the stub-loaded and hybrid SCN modelling general anisotropic media on a graded mesh [42]. A field theoretical derivation of TLM from the method of moments for the case of the basic 12-port SCN was also reported in [44].

The derivation presented here is valid for the balanced general symmetrical condensed node (GSCN). It unifies the formulations of previous stub-loaded and hybrid nodes and provides a rigorous theoretical foundation for all new nodes derivable from the GSCN.

4.2 Mapping between voltage pulses and field components

In the TLM method both space and time are discretized. This can be used to express continuous space coordinates (x, y, z) and the time coordinate t by discrete ones, $\hat{x}$, $\hat{y}$, $\hat{z}$ and $\hat{t}$, using the following transformations:

$$x = \hat{x}\Delta x; \qquad y = \hat{y}\Delta y; \qquad y = \hat{z}\Delta z; \tag{4.1}$$

$$t = \hat{t}\Delta t \tag{4.2}$$

where Δx, Δy and Δz are the node dimensions in three directions and Δt is the time step. For a node located at the point (p, q, r), the discrete coordinates of its boundaries can be viewed as shifted from the node centre by half of the appropriate discrete coordinate unit, i.e. : $(p \pm \frac{1}{2}, q, r)$ for the x-direction, $(p, q \pm \frac{1}{2}, r)$ for the y-direction and $(p, q, r \pm \frac{1}{2})$ for the z-direction. The coordinates of the boundaries and the centre of the node located at (p, q, r) can be denoted in shorthand notation as:

$$(p \pm \tfrac{1}{2}, q, r) = (x^{\pm}) \qquad (p, q \pm \tfrac{1}{2}, r) = (y^{\pm})$$

$$(p, q, r \pm \tfrac{1}{2}) = (z^{\pm}) \qquad (p, q, r) = (c)$$

The voltage pulses are considered as being incident to and scattered from the node centre at the discrete time moments $n-1$, n, $n+1$ ... whereas they arrive at the node boundaries at the time moments $n - \frac{1}{2}$, $n + \frac{1}{2}$ ....

Another fundamental property of TLM is that there exists a direct correspondence between field components and equivalent voltages and currents on transmission lines, which can be expressed through the following transformations [6]:

$$E_i = \frac{-V_i}{\Delta i} \qquad H_i = \frac{I_i}{\Delta i} \tag{4.3}$$

where $i \in \{x, y, z\}$. Taking into account this mapping, it will be assumed in the following derivations that V_i and I_i effectively represent electric and magnetic field components in the i-direction, respectively.

In a general symmetrical condensed node, a total of eighteen voltage pulses travelling along link lines and stubs is used to describe the wave propagating in general media. Looking at the centre of a node, this means that the six field components (E_x, E_y, E_z, H_x, H_y, H_z) available at a single point are described by eighteen voltage pulses. As the number of variables is different, a bijective one-to-one mapping between voltage pulses and field components is not possible in the node centre, as detailed in [44]. However, a bijective mapping is possible between the voltage

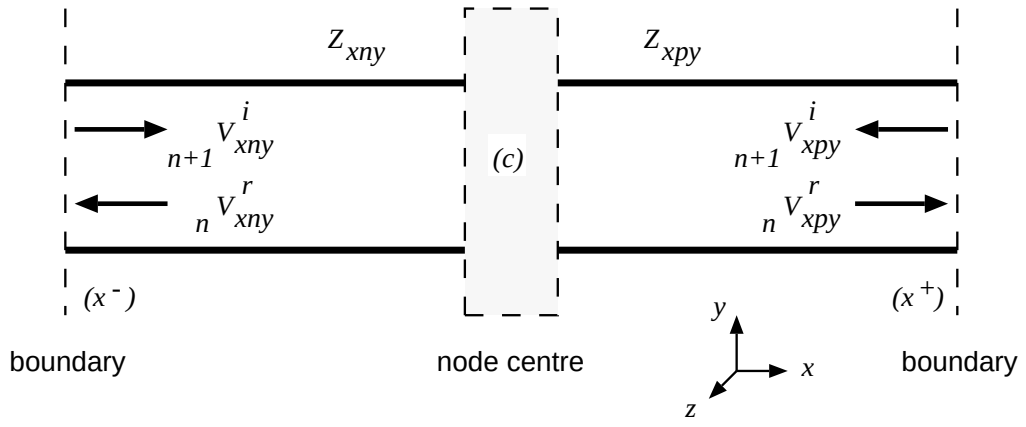

Figure 4.1 *Voltage pulses at the boundaries*

pulses and field components sampled at the cell's boundaries. This mapping was referred to in [44] as *cell boundary mapping* and will be discussed here applied to a more general case and with the sampling of field components at time moments $n \pm \frac{1}{2}$, as in [42].

Take, for example, an x-directed y-polarized link line in a general case with different impedances with respect to the node centre, Z_{xny} and Z_{xpy}, as depicted in Figure 4.1. At a discrete time moment $n + \frac{1}{2}$ at the boundary (x^-) we have a voltage pulse reflected from the node at the time moment n, described as ${}_nV^r_{xny}$ and a voltage pulse which will be incident on the node at the time moment $n+1$, denoted as ${}_{n+1}V^i_{xny}$.

The total voltage and total current on the boundary (x^-) of the xy link line at the time moment $n + \frac{1}{2}$, which are equivalent to the field components E_y and H_z, respectively, can be written as:

$$ {}_{n+\frac{1}{2}}V_y(x^-) = {}_nV^r_{xny} + {}_{n+1}V^i_{xny} \tag{4.4} $$

$$ {}_{n+\frac{1}{2}}I_z(x^-) = \frac{{}_nV^r_{xny} - {}_{n+1}V^i_{xny}}{Z_{xny}} \tag{4.5} $$

Taking into account (4.3), it becomes obvious that a mapping is established between voltage pulses ${}_nV^r_{xny}$ and ${}_{n+1}V^i_{xny}$ on the one side and the field components E_y and H_z on the other. This mapping involves the voltage pulses and characteristic impedance belonging only to the one node, so it is clearly localized in space as it does not depend on the physical parameters of the adjacent nodes. The mapping is *bijective* since the reflected and incident voltage pulses can also be expressed as combinations of the field components. It follows from (4.4)–(4.5),

after simple algebraic manipulations, that:

$$2 \cdot {}_{n}V_{xny}{}^{r} = {}_{n+\frac{1}{2}}V_y(x^-) + {}_{n+\frac{1}{2}}I_z(x^-)\, Z_{xny} \tag{4.6}$$

$$2 \cdot {}_{n+1}V^i_{xny} = {}_{n+\frac{1}{2}}V_y(x^-) - {}_{n+\frac{1}{2}}I_z(x^-)\, Z_{xny} \tag{4.7}$$

Similarly, by analysing voltage pulses at the boundary (x^+), depicted in Figure 4.1, it follows that:

$${}_{n+\frac{1}{2}}V_y(x^+) = {}_{n}V^r_{xpy} + {}_{n+1}V^i_{xpy} \tag{4.8}$$

$${}_{n+\frac{1}{2}}I_z(x^+) = \frac{-({}_{n}V^r_{xpy} - {}_{n+1}V^i_{xpy})}{Z_{xpy}} \tag{4.9}$$

The voltage pulses can be expressed from (4.8)–(4.9) as combinations of the field components:

$$2 \cdot {}_{n}V^r_{xpy} = {}_{n+\frac{1}{2}}V_y(x^+) - {}_{n+\frac{1}{2}}I_z(x^+)Z_{xpy} \tag{4.10}$$

$$2 \cdot {}_{n+1}V^i_{xpy} = {}_{n+\frac{1}{2}}V_y(x^+) + {}_{n+\frac{1}{2}}I_z(x^+)Z_{xpy} \tag{4.11}$$

Applying the same procedure to the other link lines a set of 24 equations, describing relationships between voltage pulses reflected and incident at a node and wave field components at the boundaries, can be constructed. By introducing mapping of dummy indices as $(i, j, k) \in \{(x, y, z), (y, z, x), (z, x, y)\}$, the full set of equations, similar to (4.4)–(4.5) and (4.8)–(4.9), can be written in a compact form as:

$$\begin{aligned}
{}_{n+\frac{1}{2}}V_i(k^-) &= {}_{n}V^r_{kni} + {}_{n+1}V^i_{kni} \\
{}_{n+\frac{1}{2}}V_i(k^+) &= {}_{n}V^r_{kpi} + {}_{n+1}V^i_{kpi} \\
{}_{n+\frac{1}{2}}V_i(j^-) &= {}_{n}V^r_{jni} + {}_{n+1}V^i_{jni} \\
{}_{n+\frac{1}{2}}V_i(j^+) &= {}_{n}V^r_{jpi} + {}_{n+1}V^i_{jpi} \\
{}_{n+\frac{1}{2}}I_j(k^-)Z_{kni} &= {}_{n}V^r_{kni} - {}_{n+1}V^i_{kni} \\
{}_{n+\frac{1}{2}}I_j(k^+)Z_{kpi} &= -({}_{n}V^r_{kpi} - {}_{n+1}V^i_{kpi}) \\
{}_{n+\frac{1}{2}}I_k(j^-)Z_{jni} &= -({}_{n}V^r_{jni} - {}_{n+1}V^i_{jni}) \\
{}_{n+\frac{1}{2}}I_k(j^+)Z_{jpi} &= {}_{n}V^r_{jpi} - {}_{n+1}V^i_{jpi}
\end{aligned} \tag{4.12}$$

Combining equations (4.12) in a similar manner to that used before, and shifting time index of incident voltage pulses one step back in time ($n + 1 \rightarrow n$), the

voltages pulses incident to and reflected from the node at the time step n can be expressed through the combination of the field components at the boundaries by:

$$\begin{aligned}
2 \cdot {}_nV^i_{kni} &= {}_{n-\frac{1}{2}}V_i(k^-) - {}_{n-\frac{1}{2}}I_j(k^-)\, Z_{kni} \\
2 \cdot {}_nV^r_{kni} &= {}_{n+\frac{1}{2}}V_i(k^-) + {}_{n+\frac{1}{2}}I_j(k^-)\, Z_{kni} \\
2 \cdot {}_nV^i_{kpi} &= {}_{n-\frac{1}{2}}V_i(k^+) + {}_{n-\frac{1}{2}}I_j(k^+)\, Z_{kpi} \\
2 \cdot {}_nV^r_{kpi} &= {}_{n+\frac{1}{2}}V_i(k^+) - {}_{n+\frac{1}{2}}I_j(k^+)\, Z_{kpi} \\
2 \cdot {}_nV^i_{jni} &= {}_{n-\frac{1}{2}}V_i(j^-) + {}_{n-\frac{1}{2}}I_k(j^-)\, Z_{jni} \\
2 \cdot {}_nV^r_{jni} &= {}_{n+\frac{1}{2}}V_i(j^-) - {}_{n+\frac{1}{2}}I_k(j^-)\, Z_{jni} \\
2 \cdot {}_nV^i_{jpi} &= {}_{n-\frac{1}{2}}V_i(j^+) - {}_{n-\frac{1}{2}}I_k(j^+)\, Z_{jpi} \\
2 \cdot {}_nV^r_{jpi} &= {}_{n+\frac{1}{2}}V_i(j^+) + {}_{n+\frac{1}{2}}I_k(j^+)\, Z_{jpi}
\end{aligned} \tag{4.13}$$

In this way, a full bijective mapping is established between the link line voltage pulses, incident and reflected at the node at the time moment n, and field components at the boundaries, sampled at the time moments $n \pm \frac{1}{2}$. In order to facilitate the derivation of the GSCN TLM from Maxwell's equations by using central differencing and averaging in a manner similar to that performed in [42], we also need to express voltage pulses incident to and reflected from the stubs in terms of field components taken at the time moments $n + \frac{1}{2}$ and $n - \frac{1}{2}$. As the directions of the stub transmission-lines are not defined in space (apart from their polarization), we assume that all field components related to stubs, sampled at $n \pm \frac{1}{2}$, are taken at unknown positions denoted as (u).

For open-circuit stubs, the total current at the end of the stub, taken at the time moment $n + \frac{1}{2}$ must be zero, therefore

$${}_nV^r_{oi} = {}_{n+1}V^i_{oi} \tag{4.14}$$

where $i \in \{x, y, z\}$. At the same moment, the total voltage at the open-circuit stub, equivalent to the electric field in the i-direction, is given by

$${}_{n+\frac{1}{2}}V_i(u) = {}_nV^r_{oi} + {}_{n+1}V^i_{oi} \tag{4.15}$$

Combining (4.14) and (4.15) voltage pulses can be expressed in terms of the electric field components taken at time moment $n \pm \frac{1}{2}$ as:

$$\begin{aligned}
2 \cdot {}_nV^r_{oi} &= {}_{n+\frac{1}{2}}V_i(u) \\
2 \cdot {}_nV^i_{oi} &= {}_{n-\frac{1}{2}}V_i(u)
\end{aligned} \tag{4.16}$$

For short-circuit stubs, the total voltage at the end of the stub, taken at the time moment $n + \frac{1}{2}$ must be zero, therefore

$$ {}_nV^r_{si} = -\,{}_{n+1}V^i_{si} \tag{4.17} $$

where $i \in \{x, y, z\}$. At the same moment, the total current at the short-circuit stub, equivalent to the magnetic field in the i-direction, is given by

$$ {}_{n+\frac{1}{2}}I_i(u) = \frac{{}_nV^r_{si} - {}_{n+1}V^i_{si}}{Z_{si}} \tag{4.18} $$

Combining (4.17) and (4.18) voltage pulses can be expressed in terms of the magnetic field components taken at $n \pm \frac{1}{2}$ as:

$$ \begin{aligned} 2 \cdot {}_nV^r_{si} &= {}_{n+\frac{1}{2}}I_i(u)\, Z_{si} \\ 2 \cdot {}_nV^i_{si} &= -\,{}_{n-\frac{1}{2}}I_i(u)\, Z_{si} \end{aligned} \tag{4.19} $$

Through equations (4.13), (4.16) and (4.19), all voltage pulses, incident to and reflected from the node centre, at the time moment n, have been expressed in terms of field components taken at boundaries at the time moments $n \pm \frac{1}{2}$.

4.3 Derivation of scattering equations by averaging of fields

The scattering equations for the GSCN are derived in § 3.3.1 by averaging total voltages and currents on individual link lines, in the distance infinitesimally close to the node centre at a single moment in time coinciding with the scattering in the node. Here, as we have established a mapping between the voltage pulses at the node and field components at the boundaries, the scattering equations will be derived after averaging the boundary field components to obtain field components in the centre of the node. Since Maxwell's equations describe wave propagation in space and time, averaging must be done by using a mixed space-time coordinate system [42] defined by:

$$ \xi_k = \hat{k} + \hat{t}; \qquad \eta_k = \hat{k} - \hat{t} $$

for $k \in \{x, y, z\}$.

Take for example an x-directed y-polarized link line, which models E_y and H_z field components, depicted in Figure 4.2. In order to derive the voltage pulse reflected to the half of the link line denoted by xny, one should average field components E_y and H_z taken from the boundaries (x^+) and (x^-). From equation (4.6), it can be seen that ${}_nV^r_{xny}$ is described by the sum of ${}_{n+\frac{1}{2}}V_y(x^-)$ and ${}_{n+\frac{1}{2}}I_z(x^-)\, Z_{xny}$.

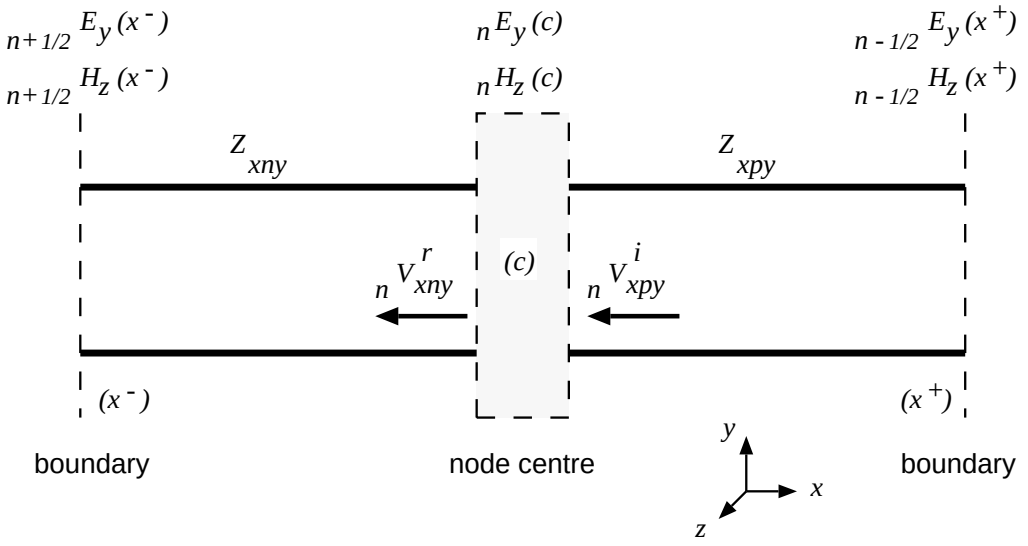

Figure 4.2 *Voltage pulses and fields involved in the derivation of* V^r_{xny}

As the offsets in the space and time coordinates have different signs, i.e. (x^-) corresponds to time moment $n+\frac{1}{2}$, the averaging needed to calculate V^r_{xny} must be done with respect to the mixed coordinate $\eta_x = \hat{x} - \hat{t}$.

When modelling propagation through a continuous homogeneous block of space (cell), represented by a TLM node with its centre corresponding to the geometrical centre of the modelled cuboid cell, the only averaging of the fields, which has a clear physical interpretation, is a simple centred averaging. If this averaging is carried out with respect to the mixed space-time coordinate η_x then it follows that:

$$ {}_nV_y(c) = \frac{{}_{n-\frac{1}{2}}V_y(x^+) + {}_{n+\frac{1}{2}}V_y(x^-)}{2} \tag{4.20} $$

$$ {}_nI_z(c) = \frac{{}_{n-\frac{1}{2}}I_z(x^+) + {}_{n+\frac{1}{2}}I_z(x^-)}{2} \tag{4.21} $$

Equations (4.20) and (4.21) have a physical interpretation that field components in the centre of the node are calculated as an arithmetic mean of the field components on the one side of the link line sampled before the scattering (time moment $n-\frac{1}{2}$, position x^+), and the field components on the other side of link line sampled after the scattering (time moment $n+\frac{1}{2}$, position x^-). The characteristic impedance of the link lines are not taken into account here, as they are not directly related to the field values.

Multiplying (4.21) by Z_{xny} and adding it to (4.20), then expressing the field com-

ponents at the boundaries by making use of the mappings (4.12), and finally solving for V^r_{xny} we obtain:

$$ {}_nV^r_{xny} = {}_nV_y(c) + {}_nI_z(c)\, Z_{xny} - {}_nV^i_{xpy} \frac{Z_{xny} + Z_{xpy}}{2Z_{xpy}} + {}_{n-1}V^r_{xpy} \frac{Z_{xny} - Z_{xpy}}{2Z_{xpy}} \quad (4.22) $$

Because of the appearance of ${}_{n-1}V^r_{xpy}$, this result suggests that the TLM method is not an one-step finite difference method. However, when imposing the condition for balanced nodes, $Z_{xny} = Z_{xpy} = Z_{xy}$, the expression (4.22) simplifies to:

$$ {}_nV^r_{xny} = {}_nV_y(c) + {}_nI_z(c)\, Z_{xy} - {}_nV^i_{xpy} \quad (4.23) $$

which is equivalent to (3.18) derived in Chapter 3.

The conclusion which can be drawn here is that only the scattering equations for balanced nodes are derived properly in this way and that unbalanced nodes may not model wave propagation correctly. This is in agreement with the intuitive assumptions made in § 2.3.2 that only balanced nodes should be used for modelling of waves in general unbounded media[1]. However, this does not diminish the validity of unbalanced nodes for modelling adjustable boundaries [23], since in this case, the node boundaries are placed at different distances from the node centre, i.e. the node centre does not correspond to the geometrical cell's centre — therefore, the simple centred averaging given by (4.20) and (4.21) is not applicable to the derivation of the scattering equations for such nodes.

In order to derive scattering equation for calculating V^r_{xpy}, a similar procedure to that used for the derivation of V^r_{xny} can be applied. From equation (4.10), it can be seen that ${}_nV^r_{xpy}$ is described by the difference of ${}_{n+\frac{1}{2}}V_y(x^+)$ and ${}_{n+\frac{1}{2}}I_z(x^+)\, Z_{xpy}$. As the offsets in the space and time coordinates have equal signs, i.e. (x^+) corresponds to $n + \frac{1}{2}$, the averaging needed to calculate V^r_{xpy} must be done with respect to the mixed coordinate $\xi_x = \hat{x} + \hat{t}$. Hence, the averaging of the appropriate field component can be written as:

$$ {}_nV_y(c) = \frac{{}_{n-\frac{1}{2}}V_y(x^-) + {}_{n+\frac{1}{2}}V_y(x^+)}{2} \quad (4.24) $$

$$ {}_nI_z(c) = \frac{{}_{n-\frac{1}{2}}I_z(x^-) + {}_{n+\frac{1}{2}}I_z(x^+)}{2} \quad (4.25) $$

[1] Several numerical experiments were undertaken to test these findings, and the results have confirmed the assumptions. TLM simulations performed on the mesh of unbalanced nodes whose parameters were chosen to satisfy general TLM constitutive relations (2.11) and (2.12), failed to provide proper solution for the wave propagation in a 3D homogeneous resonator.

By applying a similar procedure to that used before, and using the condition for balanced nodes, $Z_{xny} = Z_{xpy} = Z_{xy}$, we obtain:

$$ {}_nV^r_{xpy} = {}_nV_y(c) - {}_nI_z(c)\, Z_{xy} - {}_nV^i_{xny} \tag{4.26} $$

which is equivalent to (3.19) derived in Chapter 3.

By using similar methodology, the pulses reflected to other link lines can be also derived. Complete scattering equations for the link lines, can be written in the compact form, by introducing indices $(i, j, k) \in \{(x, y, z), (y, z, x), (z, x, y)\}$, as:

$$ \begin{aligned} V^r_{inj} &= V_j + I_k Z_{ij} - V^i_{ipj} \\ V^r_{ipj} &= V_j - I_k Z_{ij} - V^i_{inj} \\ V^r_{knj} &= V_j - I_i Z_{kj} - V^i_{kpj} \\ V^r_{kpj} &= V_j + I_i Z_{kj} - V^i_{knj} \end{aligned} \tag{4.27} $$

where the time index n and space coordinate (c) are omitted.

It remains to derive scattering equations for stubs. As the voltage pulses in stubs do not propagate in space, only averaging with respect to the time coordinate needs to be performed. For the electric field associated with open-circuit stubs and the magnetic field associated with short-circuit stubs, it follows, respectively, that:

$$ {}_nV_i(c) = \frac{{}_{n-\frac{1}{2}}V_i(u) + {}_{n+\frac{1}{2}}V_i(u)}{2} \tag{4.28} $$

$$ {}_nI_i(c) = \frac{{}_{n-\frac{1}{2}}I_i(u) + {}_{n+\frac{1}{2}}I_i(u)}{2} \tag{4.29} $$

Combining the definitions of voltage pulses reflected and incident to stubs given by (4.16) and (4.19), with (4.28) and (4.29), respectively, we obtain:

$$ {}_nV^r_{oi} = {}_nV_i(c) - {}_nV^i_{oi} \tag{4.30} $$

$$ {}_nV^r_{si} = {}_nI_i(c)\, Z_{si} + {}_nV^i_{si} \tag{4.31} $$

which are equivalent to (3.37) and (3.38) derived in Chapter 3.

The next step in order to fully describe scattering in the GSCN will be the formulation of $V_k(c)$ and $I_k(c)$ in terms of incident voltages. This will be presented in the following section, by performing the central differencing of Maxwell's equations.

4.4 Central differencing of Maxwell's equations

Maxwell's equations, written in the Cartesian coordinate system, are given as:

$$\begin{aligned}
\varepsilon_0\varepsilon_{rx}\frac{\partial E_x}{\partial t} &= \frac{\partial H_z}{\partial y} - \frac{\partial H_y}{\partial z} - \sigma_{ex}E_x \\
\varepsilon_0\varepsilon_{ry}\frac{\partial E_y}{\partial t} &= \frac{\partial H_x}{\partial z} - \frac{\partial H_z}{\partial x} - \sigma_{ey}E_y \\
\varepsilon_0\varepsilon_{rz}\frac{\partial E_z}{\partial t} &= \frac{\partial H_y}{\partial x} - \frac{\partial H_x}{\partial y} - \sigma_{ez}E_z \\
\mu_0\mu_{rx}\frac{\partial H_x}{\partial t} &= \frac{\partial E_y}{\partial z} - \frac{\partial E_z}{\partial y} - \sigma_{mx}H_x \\
\mu_0\mu_{ry}\frac{\partial H_y}{\partial t} &= \frac{\partial E_z}{\partial x} - \frac{\partial E_x}{\partial z} - \sigma_{my}H_y \\
\mu_0\mu_{rz}\frac{\partial H_z}{\partial t} &= \frac{\partial E_x}{\partial y} - \frac{\partial E_y}{\partial x} - \sigma_{mz}H_z
\end{aligned} \tag{4.32}$$

where ε_{ri} and μ_{ri} are, respectively, the relative permittivity and permeability, and σ_{ei} and σ_{mi} are, respectively, the equivalent electric and magnetic conductivities in the i-direction.

By introducing a mapping of indices given by:

$$(i,j,k) \in \{(x,y,z),(y,z,x),(z,x,y)\} \tag{4.33}$$

the six equations contained in (4.32) can be rewritten in a compact form as:

$$\begin{aligned}
\varepsilon_0\varepsilon_{ri}\frac{\partial E_i}{\partial t} &= \frac{\partial H_k}{\partial j} - \frac{\partial H_j}{\partial k} - \sigma_{ei}E_i \\
\mu_0\mu_{ri}\frac{\partial H_i}{\partial t} &= \frac{\partial E_j}{\partial k} - \frac{\partial E_k}{\partial j} - \sigma_{mi}H_i
\end{aligned} \tag{4.34}$$

The mapping given by (4.33) will be used throughout this section. It allows the rotation of dummy indices i,j,k in an arbitrary expression F, making the expressions $F(i,j,k)$, $F(j,k,i)$ and $F(k,i,j)$ equivalent.

After performing the coordinate transformations (4.1) and (4.2) which discretize space and time, and field transformations (4.3) which establish the analogy of the field components E_i and H_i with the equivalent total voltages V_i and currents I_i, Maxwell's equations (4.34) can be rewritten as:

$$\begin{aligned}
\varepsilon_0\varepsilon_{ri}\frac{\Delta j\Delta k}{\Delta i\Delta t}\frac{\partial V_i}{\partial \hat{t}} &= \frac{\partial I_j}{\partial \hat{k}} - \frac{\partial I_k}{\partial \hat{j}} - \sigma_{ei}\frac{\Delta j\Delta k}{\Delta i}V_i \\
\mu_0\mu_{ri}\frac{\Delta j\Delta k}{\Delta i\Delta t}\frac{\partial I_i}{\partial \hat{t}} &= \frac{\partial V_k}{\partial \hat{j}} - \frac{\partial V_j}{\partial \hat{k}} - \sigma_{mi}\frac{\Delta j\Delta k}{\Delta i}I_i
\end{aligned} \tag{4.35}$$

By making further use of the TLM general constitutive relations (2.41)–(2.42) and the definitions of lossy elements (2.43)–(2.44), Maxwell's equations (4.35) can be rewritten as:

$$\begin{aligned}\left(Y_{ki}+Y_{ji}+\frac{Y_{oi}}{2}\right)\frac{\partial V_i}{\partial \hat{t}} &= \frac{\partial I_j}{\partial \hat{k}}-\frac{\partial I_k}{\partial \hat{j}}-G_{ei}V_i \\ \left(Z_{jk}+Z_{kj}+\frac{Z_{si}}{2}\right)\frac{\partial I_i}{\partial \hat{t}} &= \frac{\partial V_k}{\partial \hat{j}}-\frac{\partial V_j}{\partial \hat{k}}-R_{mi}I_i \end{aligned} \tag{4.36}$$

In this formulation Maxwell's equations are written in terms of the parameters of the transmission-lines (Z, Y, R, G) and equivalent voltages V and currents I, corresponding to the electric and magnetic field components E and H, respectively. The electromagnetic properties of the medium (μ, ε, σ_e, σ_m), the node dimensions (Δx, Δy and Δz) and the time step Δt are not directly involved in equations (4.36). This formulation therefore offers a great degree of generality: as long as the constitutive relations (2.41) and (2.42) are satisfied, equations (4.36) are valid for a general condensed node with an arbitrary number of stubs and arbitrary link line impedances, modelling an arbitrary medium on an arbitrarily graded mesh with an arbitrary time step. Both the traditional stub-loaded SCN [9] and hybrid nodes [19, 20] are therefore included in this formulation.

Maxwell's equations (4.36) can be further manipulated by making use of the mixed space-time coordinates defined, as before, by:

$$\xi_k = \hat{k}+\hat{t}; \qquad \eta_k = \hat{k}-\hat{t} \tag{4.37}$$

for $k \in \{x, y, z\}$. Using the rules for differential calculus, it can be shown that:

$$\frac{\partial a}{\partial x}+\frac{\partial b}{\partial y}=\frac{1}{2}\frac{\partial(a+b)}{\partial(x+y)}+\frac{1}{2}\frac{\partial(a-b)}{\partial(x-y)}$$

Applying this rule and introducing mixed coordinates (4.37), Maxwell's equations (4.36) can be rewritten as:

$$\begin{aligned}&\frac{Y_{ki}}{2}\left(\frac{\partial(V_i-I_jZ_{ki})}{\partial\xi_k}-\frac{\partial(V_i+I_jZ_{ki})}{\partial\eta_k}\right)+\frac{Y_{ji}}{2}\left(\frac{\partial(V_i+I_kZ_{ji})}{\partial\xi_j}-\frac{\partial(V_i-I_kZ_{ji})}{\partial\eta_j}\right)\\ &\qquad+\frac{Y_{oi}}{2}\frac{\partial V_i}{\partial\hat{t}}+G_{ei}V_i=0\\ &-\frac{1}{2}\left(\frac{\partial(V_k-I_iZ_{jk})}{\partial\xi_j}+\frac{\partial(V_k+I_iZ_{jk})}{\partial\eta_j}\right)+\frac{1}{2}\left(\frac{\partial(V_j+I_iZ_{kj})}{\partial\xi_k}+\frac{\partial(V_j-I_iZ_{kj})}{\partial\eta_k}\right)\\ &\qquad+\frac{Z_{si}}{2}\frac{\partial I_i}{\partial\hat{t}}+R_{mi}I_i=0\end{aligned} \tag{4.38}$$

A set of finite difference equations can be obtained from the differential Maxwell's equations (4.38) by applying central-differencing at the point (n, p, q, r) [42], where n is a time and p, q, r are space coordinates The space coordinates of the cell's boundaries and the cell's centre are referred to, as before, by:

$$(p \pm \tfrac{1}{2}, q, r) = (x^{\pm}) \qquad (p, q \pm \tfrac{1}{2}, r) = (y^{\pm})$$

$$(p, q, r \pm \tfrac{1}{2}) = (z^{\pm}) \qquad (p, q, r) = (c)$$

The terms associated with the mixed coordinates ξ_k are differenced as, for example:

$$\frac{\partial(V_i - I_j Z_{ki})}{\partial \xi_k} = [{}_{n+\frac{1}{2}}V_i(k^+) - {}_{n+\frac{1}{2}}I_j(k^+)Z_{ki}] - [{}_{n-\frac{1}{2}}V_i(k^-) - {}_{n-\frac{1}{2}}I_j(k^-)Z_{ki}]$$

whereas terms associated with η_k are differenced as, for example:

$$\frac{\partial(V_i + I_j Z_{ki})}{\partial \eta_k} = [{}_{n-\frac{1}{2}}V_i(k^+) + {}_{n-\frac{1}{2}}I_j(k^+)Z_{ki}] - [{}_{n+\frac{1}{2}}V_i(k^-) + {}_{n+\frac{1}{2}}I_j(k^-)Z_{ki}]$$

The terms associated with the time coordinate $\hat{t}$ are differenced as, for example:

$$\frac{\partial V_i}{\partial \hat{t}} = {}_{n+\frac{1}{2}}V_i(u) - {}_{n-\frac{1}{2}}V_i(u)$$

where (u) denotes unknown space locations.

The set of difference equations obtained in this way from (4.38) contains electric and magnetic field terms, V_i and I_i, sampled at time moments $n \pm \frac{1}{2}$. It is possible now to substitute variable transformations defined by generic equations (4.13), (4.16) and (4.19) into the difference equations obtained from (4.38), to derive:

$$Y_{ki} \cdot ({}_nV^i_{kni} + {}_nV^i_{kpi}) + Y_{ji} \cdot ({}_nV^i_{jni} + {}_nV^i_{jpi}) + Y_{oi} \cdot {}_nV^i_{oi} = Y_{ki} \cdot ({}_nV^r_{kni} + {}_nV^r_{kpi}) + Y_{ji} \cdot ({}_nV^r_{jni} + {}_nV^r_{jpi}) + Y_{oi} \cdot {}_nV^r_{oi} + G_{ei} \cdot {}_nV_i(c) \tag{4.39}$$

$$-({}_nV^i_{jnk} - {}_nV^i_{jpk} - {}_nV^i_{knj} + {}_nV^i_{kpj} + {}_nV^i_{si}) = {}_nV^r_{jnk} - {}_nV^r_{jpk} - {}_nV^r_{knj} + {}_nV^r_{kpj} + {}_nV^r_{si} + R_{mi} \cdot {}_nI_i(c) \tag{4.40}$$

Comparing these two equations with the equations for charge and flux conservation described in Chapter 3 by (3.24) and (3.28), by replacing (i, j, k) with (y, z, x) and (z, x, y) respectively, it can be seen that they are fully equivalent in the case of

balanced nodes. Therefore, by differencing Maxwell's equations and applying appropriate variable transformation, we arrived at the same fundamental laws which were used for the derivation of scattering equations based on the transmission-line theory and equivalent network model in Chapter 3.

Another set of finite difference equations can be obtained from Maxwell's equations (4.36) by using central differencing at the point $(n+1/2, p, q, r)$:

$$\begin{aligned}
&\left(Y_{ki}+Y_{ji}+\frac{Y_{oi}}{2}\right)\left[{}_{n+1}V_i(c)-{}_{n}V_i(c)\right]= \\
&\quad\left[{}_{n+\frac{1}{2}}I_j(k^+)-{}_{n+\frac{1}{2}}I_j(k^-)\right]-\left[{}_{n+\frac{1}{2}}I_k(j^+)-{}_{n+\frac{1}{2}}I_k(j^-)\right]-G_{ei}\cdot{}_{n+\frac{1}{2}}V_i(c) \\
&\left(Z_{jk}+Z_{kj}+\frac{Z_{si}}{2}\right)\left[{}_{n+1}I_i(c)-{}_{n}I_i(c)\right]= \\
&\quad\left[{}_{n+\frac{1}{2}}V_k(j^+)-{}_{n+\frac{1}{2}}V_k(j^-)\right]-\left[{}_{n+\frac{1}{2}}V_j(k^+)-{}_{n+\frac{1}{2}}V_j(k^-)\right]-R_{mi}\cdot{}_{n+\frac{1}{2}}I_i(c)
\end{aligned} \tag{4.41}$$

The field terms ${}_{n+\frac{1}{2}}V_i(c)$ and ${}_{n+\frac{1}{2}}I_i(c)$ can be approximated using central averaging with respect to $\hat{t}$:

$$2\cdot{}_{n+\frac{1}{2}}A_i(c)\approx{}_{n}A_i(c)+{}_{n+1}A_i(c)\qquad A\in\{V,I\} \tag{4.42}$$

The remaining field terms sampled at the time moment $n+\frac{1}{2}$ can be substituted using variable transformations (4.12). Applying these two steps to equations (4.41) and taking into account equalities (4.14) and (4.17), the following expressions are derived:

$$\begin{aligned}
&\left(Y_{ki}+Y_{ji}+\frac{Y_{oi}+G_{ei}}{2}\right)\left[{}_{n+1}V_i(c)-{}_{n}V_i(c)\right]= \\
&\quad Y_{ki}\cdot({}_{n+1}V^i_{kni}+{}_{n+1}V^i_{kpi})+Y_{ji}\cdot({}_{n+1}V^i_{jni}+{}_{n+1}V^i_{jpi})+Y_{oi}\cdot{}_{n+1}V^i_{oi} \\
&\quad-\left[Y_{ki}\cdot({}_{n}V^r_{kni}+{}_{n}V^r_{kpi})+Y_{ji}\cdot({}_{n}V^r_{jni}+{}_{n}V^r_{jpi})+Y_{oi}\cdot{}_{n}V^r_{oi}+G_{ei}\cdot{}_{n}V_i(c)\right]
\end{aligned} \tag{4.43}$$

$$\begin{aligned}
&\left(Z_{jk}+Z_{kj}+\frac{Z_{si}+R_{mi}}{2}\right)\left[{}_{n+1}I_i(c)-{}_{n}I_i(c)\right]= \\
&\quad-\left[{}_{n}V^r_{jnk}-{}_{n}V^r_{jpk}-{}_{n}V^r_{knj}+{}_{n}V^r_{kpj}+{}_{n}V^r_{si}+R_{mi}\cdot{}_{n}I_i(c)\right] \\
&\quad-\left[{}_{n+1}V^i_{jnk}-{}_{n+1}V^i_{jpk}-{}_{n+1}V^i_{knj}+{}_{n+1}V^i_{kpj}+{}_{n+1}V^i_{si}\right]
\end{aligned} \tag{4.44}$$

Finally, substituting (4.39)–(4.40) into (4.43)–(4.44) we obtain:

$$ {}_nV_i(c) = 2\,\frac{Y_{ki}\cdot({}_nV^i_{kni}+{}_nV^i_{kpi})+Y_{ji}\cdot({}_nV^i_{jni}+{}_nV^i_{jpi})+Y_{oi}\cdot{}_nV^i_{oi}}{2\,(Y_{ki}+Y_{ji})+Y_{oi}+G_{ei}} \tag{4.45} $$

$$ {}_nI_i(c) = \frac{2({}_nV^i_{jpk}-{}_nV^i_{jnk}+{}_nV^i_{knj}-{}_nV^i_{kpj}-{}_nV^i_{si})}{2(Z_{jk}+Z_{kj})+Z_{si}+R_{mi}} \tag{4.46} $$

which are, for the case of a balanced node, equivalent to the expressions (3.34) and (3.35) derived in Chapter 3 using the network model.

4.5 Discussion

A full equivalence between the TLM method with general symmetrical condensed nodes and a finite-difference model of Maxwell's equations was established through the derivation performed in this chapter. By comparing this derivation with the one performed in Chapter 3, it becomes obvious that the GSCN TLM method can be considered as either a physical model of the transmission line network (based on Huygen's principle) or a mathematical model of the finite difference method (based on Maxwell's equations), depending on which concept one feels more comfortable with [42].

It must be noted that this equivalence is valid only for balanced nodes, since the scattering equations derived by using the two different approaches are identical in this case. On the other hand, the central averaging applied to unbalanced nodes do not yield the solution of the scattering equations derived from the equivalent network model in Chapter 3. This means that, even though the scattering equations obtained there satisfy the energy conservation, they may not model properly propagation of waves in general media, as it was intuitively predicted in Chapter 2. Results from several numerical experiments (not included here) confirmed these conclusions.

However, the results obtained in [23] where unbalanced nodes were used to allow placement of infinitesimally adjustable boundaries, suggest that these nodes can be used for such applications. It is important to note, that when unbalanced nodes are used for modelling varying boundaries, the physical length of their arms differs with respect to the node centre, and therefore a simple centred averaging, as used in this chapter, is inappropriate. Further investigation is needed to find if an appropriate averaging can be applied for unbalanced nodes placed out of the boundaries, such that correct modelling of fields can be obtained. Physical

intuition and failure to implement successfully such a model as a general simulation tool so far, suggest that unbalanced nodes should only be applied in modelling special features such as boundaries, discontinuities in medium parameters, thin conductors, etc.

Another important issue examined in this chapter was the mapping between field components and voltage pulses. Following the derivation performed here, it is shown that in the GSCN TLM, all field components can be obtained from the centre of a cell at the time moments $n-1$, n, $n+1$, ..., using equations (4.45)–(4.46) and the transformation (4.3). In addition, fields can be obtained at the cell's boundaries at the time moments $n-\frac{1}{2}$, $n+\frac{1}{2}$, ..., by exploiting equations (4.12). Therefore, output and the excitation in the GSCN can be taken/applied both at the cell's centre and at the cell's boundaries.

The accuracy of the general condensed node TLM scheme can be also assessed from the derivations performed in this chapter. The errors introduced during the derivation of the scattering equations (4.27) and field expressions (4.45)–(4.46) are only associated with the central differencing and central averaging. Both of them have 2nd order accuracy. Since the derivations were carried out for a generally graded mesh, it can be concluded that the GSCN TLM method always has 2nd order accuracy regardless of the grading of the mesh. This property gives the TLM method certain advantages in applications where graded meshes are required [42].

The full equivalence established between the GSCN TLM and Maxwell's equations offers a rigorous theoretical foundation to all nodes contained in the formulation of the GSCN. Furthermore, it opens up the prospect of developing new nodes with hitherto unexplored combinations of link and stub parameters which can potentially offer more efficient use of computational resources (memory and run-time) or/and improve the dispersion characteristics of the method. This will be further explored in the rest of the thesis.

Part II

Symmetrical Super-Condensed Node

Chapter 5 Development of the TLM symmetrical super-condensed node

5.1 Introduction

The general system of equations describing the parameters of a TLM time-domain scheme, introduced in Chapter 2, suggested the existence of six degrees of freedom in the formulation of link and stub parameters of a particular three-dimensional TLM node. For convenience, this system of equations is written again using the compact notation with dummy indices $i, j, k \in \{x, y, z\}$, $i \neq j, k$:

$$C_{ik}\Delta i + C_{jk}\Delta j + C_o^k = \varepsilon_k \frac{\Delta i \Delta j}{\Delta k} \tag{5.1}$$

$$L_{ij}\Delta i + L_{ji}\Delta j + L_s^k = \mu_k \frac{\Delta i \Delta j}{\Delta k} \tag{5.2}$$

$$\Delta t = \Delta i \sqrt{C_{ij} L_{ij}} \tag{5.3}$$

The three equations contained in (5.1), the three equations contained in (5.2) and the six equations contained in (5.3), describe basic relationships between the material properties ε, μ, node dimensions Δx, Δy, Δz and time step Δt on the one side, and parameters of transmission-lines expressed through the link line distributed capacitances and inductances, C_{ij} and L_{ij}, and stub total capacitances and inductances C_o^k and L_s^k, on the other. In total, eighteen transmission-line variables are defined by twelve equations given by (5.1)–(5.3), thus leaving six degrees of freedom in determining parameters of a particular TLM node.

Traditionally, in the original TLM schemes [9, 13], the characteristic impedance of link lines is kept constant and equal to Z_0, the intrinsic impedance of the background medium. This was imposed intuitively, in order to follow the analogy between the waves propagating in space and voltage pulses propagating along transmission-lines. Six additional conditions in the form $\sqrt{L_{ij}/C_{ij}} = Z_0$ are therefore imposed on the general system of equations (5.1)–(5.3). As a result of this,

stubs must be added in the node in order to model non-uniform media with local increase in dielectric permittivity ε or magnetic permeability μ and to allow for a graded mesh with nodes of arbitrary aspect ratio ($\Delta x \neq \Delta y \neq \Delta z$). The calculation of the parameters of the stub-loaded node was shown in § 2.4.1.

The disadvantage of the traditional stub-loaded node is that the memory requirements are increased by up to 50% compared to the basic 12-port node, to store voltage pulses from six stubs. The scattering algorithm is also more complicated, thus increasing the computer processor (CPU) run-time. Also, a severe limitation is imposed on the maximum time step used on a graded mesh. It was shown in § 2.4.1 that the time step in the stub-loaded nodes is in some cases dependent on the ratio of the smallest to the largest node dimension, requiring the whole simulation process to run for a prohibitively large number of iterations in order to make up for the small time step.

The severe restrictions in time step imposed in the stub-loaded nodes were overcome in the hybrid symmetrical condensed nodes (HSCN) [19], by allowing for different link line characteristic impedances in a node. The six conditions imposed on the general system of equations and the derivation of the stub and link line parameters were discussed in § 2.4.2. Since the HSCN uses either open-circuit (Type I [19]) or short-circuit stubs (Type II [20]), the memory requirement is reduced by three stub locations, making the method more computationally efficient.

By studying the general system of equations (5.1)–(5.3), it appears that stubs might be removed all together. Indeed, six additional constraints in the form

$$C_o^k = 0 \qquad k \in \{x, y, z\} \tag{5.4}$$

$$L_s^k = 0 \qquad k \in \{x, y, z\} \tag{5.5}$$

imposed on equations (5.1)–(5.2) will eliminate stub parameters from the general system of equations, thus leaving only 12 distributed capacitances and inductances of link lines to be solved from the system of 12 non-linear equations (5.1)–(5.3).

If such a system can provide physical solutions, it would mean that general non-uniform media can be modelled on a graded mesh with nodes without stubs. The savings in memory storage for such a method would be substantial compared to the nodes with stubs, and the scattering algorithm might be simplified due to reduced number of voltage pulses involved. In the following sections, it will be shown that a solution of (5.1)–(5.3) for the node without stubs does indeed exist. The new stubless node will be referred to as the symmetrical super-condensed node (SSCN) to reflect the fact that stubs are totally removed from the node.

For methodological reasons, due to the complexity involved with anisotropic materials, the derivation of the SSCN parameters that follows will be performed separately for isotropic and anisotropic media. Both derivations will assume TLM nodes with arbitrary aspect ratio (graded mesh).

5.2 Derivation of the SSCN for isotropic media

5.2.1 Link line parameters

Imposing the six additional constraints to remove stubs, given by (5.4)–(5.5), on the system of equations (5.1)–(5.2), and assuming an isotropic medium ($\varepsilon_k = \varepsilon$, $\mu_k = \mu$), the TLM constitutive relations for the SSCN can be written as:

$$C_{ik}\Delta i + C_{jk}\Delta j = \varepsilon\frac{\Delta i\Delta j}{\Delta k} \tag{5.6}$$

$$L_{ij}\Delta i + L_{ji}\Delta j = \mu\frac{\Delta i\Delta j}{\Delta k} \tag{5.7}$$

The time synchronism condition given by (5.3) remains unchanged. Since the system of equations formed by (5.6)–(5.7) and (5.3) is non-linear, certain algebraic manipulations are needed to facilitate its solution. In order to express (5.6) and (5.7) in a more elegant form, normalized parameters for the link lines are introduced as follows.

For a plane electromagnetic wave propagating in the i-direction with tangential field components E_j and H_k, the total capacitance of the block of medium, C_j^t, and its total inductance L_k^t are given from (2.3) and (2.7) as:

$$C_j^t = \varepsilon\,\frac{\Delta i\Delta k}{\Delta j} \qquad\qquad L_k^t = \mu\,\frac{\Delta i\Delta j}{\Delta k}$$

It is convenient to normalize the parameters of the link line to those of the block of medium, so the normalized distributed capacitance $\hat{C}_{ij}$ and the normalized distributed inductance $\hat{L}_{ij}$ of the i-directed j-polarized link line are defined, respectively, as:

$$\hat{C}_{ij} = \frac{C_{ij}\Delta i}{C_j^t} = \frac{C_{ij}}{\varepsilon}\frac{\Delta j}{\Delta k} \tag{5.8}$$

$$\hat{L}_{ij} = \frac{L_{ij}\Delta i}{L_k^t} = \frac{L_{ij}}{\mu}\frac{\Delta k}{\Delta j} \tag{5.9}$$

An *equivalent cubic cell parameter*, Δl, is also introduced, which actually represents the dimension of a cubic cell having the same propagation delay Δt as an

arbitrarily graded TLM cell [33]. The velocity v of a pulse propagating along a transmission line in the basic 12-port SCN is twice the plane wave velocity in the medium with properties ε, μ [9] and is given by:

$$v = \frac{\Delta l}{\Delta t} = \frac{2}{\sqrt{\varepsilon\mu}}$$

Thus, Δl is given by:

$$\Delta l = \frac{2\Delta t}{\sqrt{\varepsilon\mu}} \tag{5.10}$$

Multiplying (5.6) by $\Delta k/(\varepsilon \Delta i \Delta j)$ and using (5.8) we obtain:

$$\hat{C}_{ik} + \hat{C}_{jk} = 1 \tag{5.11}$$

Multiplying (5.7) by $\Delta k/(\mu \Delta i \Delta j)$ and using (5.9) we obtain:

$$\hat{L}_{ij} + \hat{L}_{ji} = 1 \tag{5.12}$$

Using (5.8), (5.9) and (5.10), the time synchronism condition (5.3) can also be rewritten in terms of the equivalent cubic cell and normalized link line parameters as:

$$\Delta l = 2\Delta i\sqrt{\hat{C}_{ij}\hat{L}_{ij}} \tag{5.13}$$

A system of 12 equations (5.11)–(5.13) for 12 unknown variables $\hat{C}_{ij}$ and $\hat{L}_{ij}$ can now be solved. Taking $\hat{L}_{ij}$ from (5.13) for all possible combinations of $i, j \in \{x, y, z\}$ and substituting in (5.12) three equations in the generic form are obtained:

$$\frac{(\Delta l)^2}{4\hat{C}_{ij}(\Delta i)^2} + \frac{(\Delta l)^2}{4\hat{C}_{ji}(\Delta j)^2} = 1 \tag{5.14}$$

Substituting $\hat{C}_{ji}$ in (5.14) using an instance of (5.11) and dividing (5.14) by $(\Delta l)^2/4$ we obtain:

$$\frac{1}{\hat{C}_{ij}(\Delta i)^2} + \frac{1}{(1-\hat{C}_{ki})(\Delta j)^2} = \frac{4}{(\Delta l)^2} \tag{5.15}$$

Substituting triplets (i, j, k) in (5.15) with (x, y, z), (y, z, x) and (z, x, y) respectively, a system of three equations with three unknowns $\hat{C}_{xy}$, $\hat{C}_{yz}$, $\hat{C}_{zx}$ is obtained:

$$\frac{1}{\hat{C}_{xy}(\Delta x)^2} + \frac{1}{(1-\hat{C}_{zx})(\Delta y)^2} = \frac{4}{(\Delta l)^2} \tag{5.16}$$

$$\frac{1}{\hat{C}_{yz}(\Delta y)^2} + \frac{1}{(1-\hat{C}_{xy})(\Delta z)^2} = \frac{4}{(\Delta l)^2} \tag{5.17}$$

$$\frac{1}{\hat{C}_{zx}(\Delta z)^2} + \frac{1}{(1-\hat{C}_{yz})(\Delta x)^2} = \frac{4}{(\Delta l)^2} \tag{5.18}$$

This system gives a solution for $\hat{C}_{xy}$, $\hat{C}_{yz}$, $\hat{C}_{zx}$ in the form:

$$\hat{C}_{ij} = \frac{2(\Delta j)^2(\Delta k)^2 + B}{2(\Delta i)^2(\Delta k)^2[(2\Delta j/\Delta l)^2 - 1]} \tag{5.19}$$

where

$$B = A \pm \sqrt{A^2 - (\Delta x \Delta y \Delta z \Delta l)^2} \tag{5.20}$$

with

$$A = (\Delta x \Delta y \Delta z)^2 \left(\frac{4}{(\Delta l)^2} - \frac{1}{(\Delta x)^2} - \frac{1}{(\Delta y)^2} - \frac{1}{(\Delta z)^2} \right) \tag{5.21}$$

The other three normalized capacitances, namely $\hat{C}_{xz}$, $\hat{C}_{yx}$ and $\hat{C}_{zy}$, can be found using (5.11). Note from (5.20) that there are two sets of solutions for the link line parameters of the SSCN. Both solutions are physical and either can be used in the definition of the SSCN within the frequency band of interest. This will be confirmed in Chapter 8 after performing dispersion analysis of the SSCN.

Finally, the characteristic impedance Z_{ij} can be expressed in terms of $\hat{C}_{ij}$ by making use of (5.8), (5.9) and (5.13):

$$Z_{ij} = \frac{1}{Y_{ij}} = \sqrt{\frac{L_{ij}}{C_{ij}}} = \frac{\Delta j}{\Delta i \Delta k} \cdot \frac{\Delta l}{2\hat{C}_{ij}} \sqrt{\frac{\mu}{\varepsilon}} \tag{5.22}$$

In this way, the characteristic impedances of six link lines, Z_{ij}, are found for the SSCN modelling an isotropic medium in a mesh containing nodes with arbitrary aspect ratio.

For the benefit of later derivations the system of equations (5.11)–(5.13) is also solved directly in terms of $\hat{L}_{ij}$. Taking $\hat{C}_{ij}$ from (5.13) for all possible combinations of $i, j \in \{x, y, z\}$ and substituting in (5.11) three equations are obtained in the generic form:

$$\frac{(\Delta l)^2}{4\hat{L}_{ik}(\Delta i)^2} + \frac{(\Delta l)^2}{4\hat{L}_{jk}(\Delta j)^2} = 1 \tag{5.23}$$

Substituting $\hat{L}_{jk}$ in (5.23) using an instance of (5.12) and dividing (5.23) by $(\Delta l)^2/4$ we obtain:

$$\frac{1}{\hat{L}_{ik}(\Delta i)^2} + \frac{1}{(1 - \hat{L}_{kj})(\Delta j)^2} = \frac{4}{(\Delta l)^2} \tag{5.24}$$

The system of equations (5.24) has a similar form to (5.15). Moreover, if we introduce the mapping $\hat{C}_{ij} \leftrightarrow \hat{L}_{ik}$ for all possible combinations of $i, j, k \in \{x, y, z\}$

the two systems of equations become equivalent, which leads to an interesting relation for the SSCN modelling an isotropic medium:

$$\hat{C}_{ij} = \hat{L}_{ik} \tag{5.25}$$

The characteristic impedance Z_{ij} can be also expressed in terms of $\hat{L}_{ij}$ by making use of (5.8), (5.9) and (5.13) as:

$$Z_{ij} = \sqrt{\frac{L_{ij}}{C_{ij}}} = \frac{\Delta i \Delta j}{\Delta k} \cdot \frac{2\hat{L}_{ij}}{\Delta l}\sqrt{\frac{\mu}{\varepsilon}} \tag{5.26}$$

The following interesting relationships can be derived by making use of (5.22) and (5.11):

$$\frac{Y_{ij}}{Y_{ij} + Y_{kj}} = \frac{\hat{C}_{ij}}{\hat{C}_{ij} + \hat{C}_{kj}} = \hat{C}_{ij} \tag{5.27}$$

or using (5.26) and (5.12):

$$\frac{Z_{ij}}{Z_{ij} + Z_{ji}} = \frac{\hat{L}_{ij}}{\hat{L}_{ij} + \hat{L}_{ji}} = \hat{L}_{ij} \tag{5.28}$$

These expressions can be used for the optimization of scattering procedure in the lossless SSCN, as will be shown in Chapter 6.

5.2.2 Maximum time step

So far, the parameters of the link lines have been obtained in terms of the linear dimensions of a node and the properties of the medium, but the time step, or propagation delay, Δt, and accordingly the equivalent cubic cell parameter Δl, which was used in (5.19), have not been determined yet.

Examining the solution for $\hat{C}_{ij}$ described by (5.19)–(5.21) and demanding that it is a real and positive number, (because the characteristic impedance of a link line must be real and positive when modelling passive media [6]), the following condition is imposed:

$$A \geq \Delta x \Delta y \Delta z \Delta l$$

After substituting A using (5.21) and some algebraic manipulations, a cubic inequality in terms of Δl can be constructed as:

$$\Delta x \Delta y \Delta z \left(\frac{4}{(\Delta l)^2} - \frac{1}{(\Delta x)^2} - \frac{1}{(\Delta y)^2} - \frac{1}{(\Delta z)^2} \right) - \Delta l \geq 0 \tag{5.29}$$

After performing substitutions given by:

$$a = \frac{1}{\Delta x} \qquad b = \frac{1}{\Delta y} \qquad c = \frac{1}{\Delta z} \qquad h = \frac{2}{\Delta l}$$

into (5.29) and simple algebraic manipulations, a cubic inequality in terms of h is obtained as:

$$h^3 - (a^2 + b^2 + c^2)\, h - 2abc \geq 0$$

Since the quadratic term h^2 is missing, this inequality can be solved using the procedure for finding roots of a *reduced cubic equation* [45], described in a general form:

$$h^3 + Ch + D = 0$$

where in our case $C = -(a^2 + b^2 + c^2)$ and $D = -2abc$. The solution of a reduced cubic equation can be expressed in a trigonometric form if all of its roots are real. This property is satisfied if [45]:

$$D^2 + 4\frac{C^3}{27} \leq 0$$

which in our case, after replacing C and D, gives after some manipulation:

$$\sqrt[3]{a^2b^2c^2} \leq \frac{a^2 + b^2 + c^2}{3}$$

This inequality is always satisfied because of the fact that the geometric mean is never bigger than the arithmetic mean.

Following the procedure for solving a reduced cubic equation with real roots [45] and using previous substitutions, the physical solution of (5.29) for Δl is obtained as:

$$\Delta l \leq \Delta l_{\max} = \frac{2}{E \cos\left[\frac{1}{3}\arccos\left(\frac{F}{E^3}\right)\right]} \tag{5.30}$$

where

$$E = \sqrt{\frac{4}{3}\left(\frac{1}{(\Delta x)^2} + \frac{1}{(\Delta y)^2} + \frac{1}{(\Delta z)^2}\right)} \qquad F = \frac{8}{\Delta x \Delta y \Delta z}$$

The maximum time step is then calculated using (5.10) as:

$$\Delta t_{\max} = \frac{\Delta l_{\max}\sqrt{\varepsilon\mu}}{2} \tag{5.31}$$

Using similar expressions for the maximum time steps for the stub-loaded and hybrid nodes, derived earlier in § 2.4.1 and § 2.4.2, a comparison of the maximum

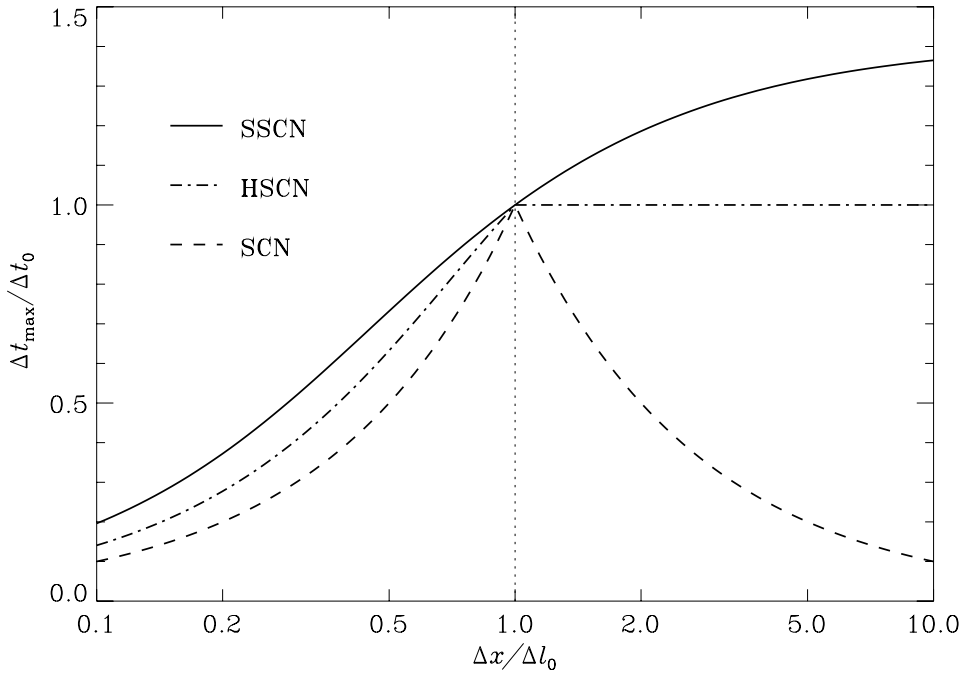

Figure 5.1 *Maximum time step for different nodes*

permissible time step in graded meshes for three different nodes, namely the stub-loaded SCN [9], the HSCN [19] and the SSCN, is made in Figure 5.1. The node spacing in the y- and z-directions is fixed at $\Delta y = \Delta z = \Delta l_0$, while Δx varies from $0.1\Delta l_0$ to $10\Delta l_0$. The maximum time step $\Delta t_{\max}$ is given relative to the time step Δt_0 used in a uniform mesh with node spacing Δl_0, i.e. $\Delta t_0 = \Delta l_0/(2c)$. The horizontal axis is plotted of a logarithmic scale.

It is clear from Figure 5.1 that the time step allowed in the SSCN, when either shrinking ($\Delta x/\Delta l_0 < 1$) or expanding ($\Delta x/\Delta l_0 > 1$) the node along one dimension, is consistently higher than for the HSCN and the stub-loaded SCN. This means that in addition to the reduced memory storage of the TLM SSCN due to the absence of stubs, simulations can be also completed faster due to the larger allowed time step in a graded TLM mesh.

It should be pointed out that in an actual implementation of the SSCN on a TLM mesh containing layers with different material properties and variable gradings, the time step in the mesh must be chosen as the smallest of all maximum permissible time steps calculated for each separate unique node region using formulae (5.30) and (5.31). The term *unique node region* is defined as the region of TLM nodes describing the same material properties (ε, μ, σ) on a part of the mesh where the cells are of the same linear dimensions ($\Delta x, \Delta y, \Delta z$).

5.2.3 SSCN for a uniform mesh

The expressions for the parameters of link lines, derived in § 5.2.1 for the case of a TLM mesh with nodes of arbitrary aspect ratio, are considerably simplified if a regular uniform mesh is assumed with:

$$\Delta x = \Delta y = \Delta z = \Delta l_0 \tag{5.32}$$

The time step Δt is related to the node dimension Δl_0 through the parameters of the background medium (ε_0, μ_0) as [9]:

$$\Delta l_0 = \frac{2\Delta t}{\sqrt{\varepsilon_0 \mu_0}}$$

The ratio of Δl_0 over the equivalent cubic cell parameter Δl is obtained by making use of (5.10) as:

$$\frac{\Delta l_0}{\Delta l} = \sqrt{\varepsilon_r \mu_r} \tag{5.33}$$

Substituting (5.32) into the solution (5.19) and making use of (5.33) the normalized capacitances $\hat{C}_{xy}$, $\hat{C}_{yz}$ and $\hat{C}_{zx}$ are derived after some algebraic manipulations as:

$$\hat{C}_{xy} = \hat{C}_{yz} = \hat{C}_{zx} = \hat{C}_p = \frac{1 \pm \sqrt{1 - \dfrac{1}{\varepsilon_r \mu_r}}}{2} \tag{5.34}$$

Another three normalized capacitances, $\hat{C}_{zy}$, $\hat{C}_{xz}$ and $\hat{C}_{yx}$, are derived by combining (5.34) with (5.11) as:

$$\hat{C}_{zy} = \hat{C}_{xz} = \hat{C}_{yx} = \hat{C}_n = 1 - \hat{C}_p = \frac{1 \mp \sqrt{1 - \dfrac{1}{\varepsilon_r \mu_r}}}{2} \tag{5.35}$$

Subsequently, the characteristic impedances of the link lines are derived by substituting (5.32)–(5.35) into (5.22) as:

$$Z_{xy} = Z_{yz} = Z_{zx} = Z_p = \left(\sqrt{\varepsilon_r \mu_r} \mp \sqrt{\varepsilon_r \mu_r - 1}\right) \sqrt{\frac{\mu}{\varepsilon}} \tag{5.36}$$

$$Z_{zy} = Z_{xz} = Z_{yx} = Z_n = \left(\sqrt{\varepsilon_r \mu_r} \pm \sqrt{\varepsilon_r \mu_r - 1}\right) \sqrt{\frac{\mu}{\varepsilon}} \tag{5.37}$$

The characteristic impedances Z_p and Z_n can be rewritten in a more elegant form as:

$$Z_p = \frac{Z}{A_1} \qquad\qquad Z_n = Z\, A_1 \tag{5.38}$$

by introducing

$$A_1 = \sqrt{\varepsilon_r \mu_r} \pm \sqrt{\varepsilon_r \mu_r - 1}$$

and the intrinsic impedance of the modelled medium (μ, ε) as

$$Z = \sqrt{\frac{\mu}{\varepsilon}}$$

The derivation performed here shows that only two different impedances of link lines, Z_p and Z_n, are necessary for modelling materials with non-background properties using the SSCN on a uniform TLM mesh. It is easily confirmed that in the case of a background medium ($\varepsilon_r = \mu_r = 1$) it follows that $A_1 = 1$ and $Z = Z_0 = \sqrt{\mu_0/\varepsilon_0}$ and therefore $Z_n = Z_p = Z_0$, or in other words, the SSCN simplifies to the basic 12-port node.

5.3 Derivation of the SSCN for anisotropic media

5.3.1 Link line parameters

The derivation of the SSCN for anisotropic materials requires more effort because a more complicated system of equations needs to be solved. The procedure is, however, similar to that used for the SSCN in isotropic media.

Imposing the six additional constraints for removing stubs, given by (5.4)–(5.5), to the general system of equations (5.1)–(5.2), the TLM constitutive relations for the SSCN in an anisotropic medium can be written as:

$$C_{ik}\Delta i + C_{jk}\Delta j = \varepsilon_k \frac{\Delta i \Delta j}{\Delta k} \tag{5.39}$$

$$L_{ij}\Delta i + L_{ji}\Delta j = \mu_k \frac{\Delta i \Delta j}{\Delta k} \tag{5.40}$$

By introducing normalized quantities as:

$$\hat{C}_{ij} = \frac{C_{ij}}{\varepsilon_j}\frac{\Delta j}{\Delta k} \tag{5.41}$$

$$\hat{L}_{ij} = \frac{L_{ij}}{\mu_k}\frac{\Delta k}{\Delta j} \tag{5.42}$$

equations (5.39) and (5.40) are rewritten as:

$$\hat{C}_{ik} + \hat{C}_{jk} = 1 \tag{5.43}$$

$$\hat{L}_{ij} + \hat{L}_{ji} = 1 \tag{5.44}$$

Using the definitions (5.41)–(5.42) and the time synchronism condition (5.3), the product of $\hat{L}_{ij}$ and $\hat{C}_{ij}$, denoted by r_{ij}, can be expressed in terms of the time step, node dimensions and material properties as:

$$r_{ij} = \hat{C}_{ij}\hat{L}_{ij} = \frac{C_{ij}L_{ij}}{\varepsilon_j \mu_k} = \left(\frac{\Delta t}{\Delta i}\right)^2 \frac{1}{\varepsilon_j \mu_k} \tag{5.45}$$

By inserting

$$\hat{L}_{ij} = \frac{r_{ij}}{\hat{C}_{ij}} \qquad\qquad \hat{L}_{ji} = \frac{r_{ji}}{\hat{C}_{ji}}$$

into equation (5.44) and using an instance of the generic equation (5.43), we obtain:

$$\frac{r_{ij}}{\hat{C}_{ij}} + \frac{r_{ji}}{1 - \hat{C}_{ki}} = 1 \tag{5.46}$$

Substituting triplets (i, j, k) in (5.46) with (x, y, z), (y, z, x) and (z, x, y), a system of three equations with three unknowns $\hat{C}_{xy}$, $\hat{C}_{yz}$ and $\hat{C}_{zx}$ is obtained as:

$$\frac{r_{xy}}{\hat{C}_{xy}} + \frac{r_{yx}}{1 - \hat{C}_{zx}} = 1 \tag{5.47}$$

$$\frac{r_{yz}}{\hat{C}_{yz}} + \frac{r_{zy}}{1 - \hat{C}_{xy}} = 1 \tag{5.48}$$

$$\frac{r_{zx}}{\hat{C}_{zx}} + \frac{r_{xz}}{1 - \hat{C}_{yz}} = 1 \tag{5.49}$$

This system gives a solution for $\hat{C}_{xy}$, $\hat{C}_{yz}$, $\hat{C}_{zx}$ in the form:

$$\hat{C}_{ij} = \frac{2\, r_{ij}(1 - r_{jk} - r_{ki} - r_{ik}) + B}{2\,(1 - r_{jk} - r_{ki} - r_{ji} - r_{ik} + r_{jk}r_{ki} + r_{ji}r_{ik} + r_{ji}r_{jk})} \tag{5.50}$$

where

$$B = A \pm \sqrt{A\,[A - (\sqrt{r_{xy}r_{yz}r_{zx}} + \sqrt{r_{xz}r_{yx}r_{zy}})^2]} \tag{5.51}$$

with

$$A = 1 - \sum_{p,q} r_{pq} + \sum_{p,q,s} r_{pq}r_{ps} + \sum_{p,q,s} r_{pq}r_{qs} \qquad p, q, s \in \{x, y, z\} \quad \wedge \quad p \neq q \neq s \tag{5.52}$$

The remaining three normalized capacitances, namely $\hat{C}_{xz}$, $\hat{C}_{yx}$ and $\hat{C}_{zy}$, can be found using (5.43). Note from (5.50) that, as before, there are two sets of solutions and either can be used in the definition of the SSCN.

Finally, the characteristic impedance Z_{ij} can be expressed in terms of $\hat{C}_{ij}$ by making use of (5.41), (5.42) and (5.45) as:

$$Z_{ij} = \sqrt{\frac{L_{ij}}{C_{ij}}} = \frac{\Delta j \Delta t}{\Delta i \Delta k\, \varepsilon_j \hat{C}_{ij}} \tag{5.53}$$

Note that, as with the isotropic case, the derivation can be also done by solving the general system of equations in terms of $\hat{L}_{ij}$. The relationships between the normalized distributed parameters and ratios of characteristic impedances and admittances given for the isotropic SSCN by expressions (5.27) and (5.28) are valid for the anisotropic case, too.

However, it can be easily confirmed that in the anisotropic case the identity (5.25), i.e. $\hat{C}_{ij} = \hat{L}_{ik}$, does not hold. Also, contrary to the isotropic SSCN, the solution given by (5.50)–(5.52) do not simplify for the case of a uniform TLM mesh.

5.3.2 Maximum time step

Examining the solution for $\hat{C}_{ij}$ described by (5.50)–(5.52) and demanding, as before, that it is a real and positive number, the following condition is imposed

$$A - (\sqrt{r_{xy}r_{yz}r_{zx}} + \sqrt{r_{xz}r_{yx}r_{zy}})^2 \geq 0 \tag{5.54}$$

After substituting A and r_{ij}, using (5.52) and (5.45), into (5.54), this becomes a cubic inequality in $(\Delta t)^2$. By further introducing:

$$p_{ij} = \frac{1}{(\Delta i)^2 \varepsilon_j \mu_k} \qquad h = \frac{1}{(\Delta t)^2} \qquad r_{ij} = \frac{p_{ij}}{h}$$

the solutions of (5.54) can be sought as roots of a cubic equation in terms of h, given by:

$$h^3 + bh^2 + ch + d = 0 \tag{5.55}$$

where

$$\begin{aligned} b &= -\sum_{q,r} p_{qr} && q, r \in \{x, y, z\} \quad \wedge \quad q \neq r \\ c &= \sum_{q,r,s} p_{qr}p_{qs} + \sum_{q,r,s} p_{qr}p_{rs} && q, r, s \in \{x, y, z\} \quad \wedge \quad q \neq r, s \\ d &= -(\sqrt{p_{xy}p_{yz}p_{zx}} + \sqrt{p_{xz}p_{yx}p_{zy}})^2 \end{aligned} \tag{5.56}$$

After introducing the following substitutions [45]:

$$h = g - \frac{b}{3} \qquad C = c - \frac{b^2}{3} \qquad D = d - \frac{bc}{3} + \frac{2b^3}{27} \tag{5.57}$$

equation (5.55) simplifies to a reduced cubic equation in terms of g:

$$g^3 + Cg + D = 0 \tag{5.58}$$

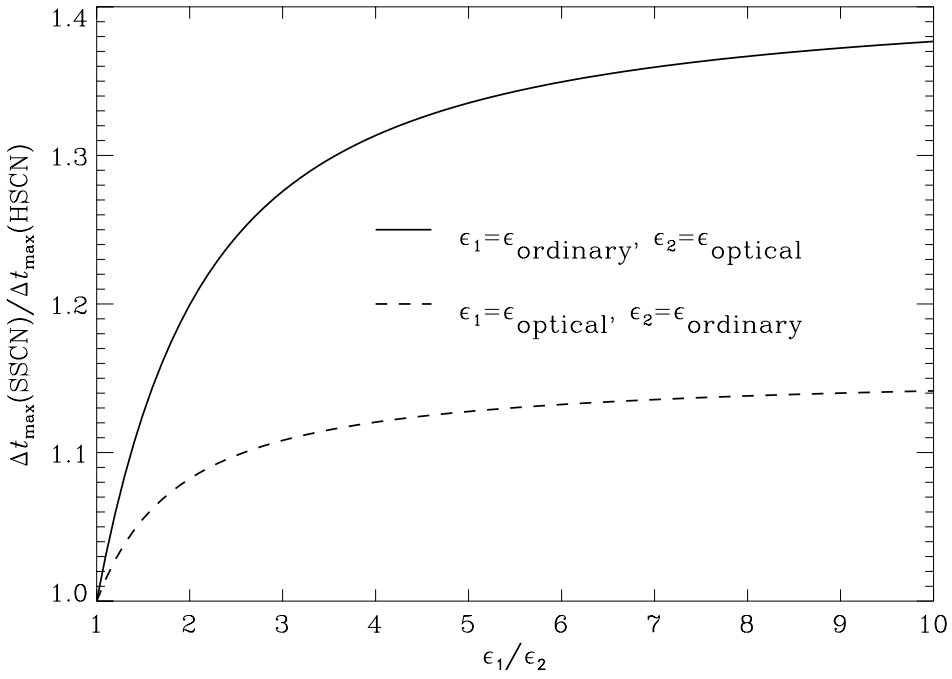

Figure 5.2 *Ratio of maximum time steps in the SSCN and HSCN when modelling uniaxial anisotropic dielectric media*

As in case of the isotropic SSCN, by following the procedure for solving reduced cubic equation with real roots [45] and using previous substitutions, the physical solution of (5.54) for Δt is obtained as:

$$\Delta t \leq \Delta t_{\max} = \sqrt{\frac{1}{E\cos\left[\frac{1}{3}\arccos\left(\frac{F}{E^3}\right)\right] - \frac{b}{3}}} \tag{5.59}$$

where

$$E = \sqrt{-4C/3} \qquad F = -4D$$

and b, C and D are defined by (5.56) and (5.57).

In order to compare the values of maximum time step in the SSCN to that of the HSCN [32], an example of modelling uniaxial anisotropic dielectrics on a uniform mesh is presented. Uniaxial dielectric materials have their electric properties described by a diagonal tensor, with equal dielectric constants along the two of the principal axis, for example, $\varepsilon_x = \varepsilon_y \neq \varepsilon_z$ [46]. In this case, the x- and y-axes are called *ordinary* axes and the z-axis is the *extraordinary* or *optic* axis. Using the expressions (5.59) and (2.66), the ratio of $\Delta t_{\max}$ for the SSCN over $\Delta t_{\max}$ for the HSCN is calculated and plotted in Figure 5.2.

Two cases are considered, for a dielectric permittivity along the optical axis being: a) smaller (plotted by solid line) and b) bigger (plotted by broken line) in comparison to that along ordinary axes. It can be seen from Figure 5.2 that in both cases, the time step allowed in the SSCN is higher than for the HSCN.

5.4 Implementation of the SSCN in a TLM mesh

5.4.1 Scattering properties

The scattering properties for the symmetrical super-condensed node can be easily derived from the scattering equations of a general node described in Chapter 3. By substituting conditions for balanced nodes, $Z_{inj} = Z_{ipj} = Z_{ij}$ and $h_{ij} = 0$, into the general equations (3.32)–(3.33), we obtain:

$$V^r_{inj} = V_j \pm I_k Z_{ij} - V^i_{ipj} \tag{5.60}$$

$$V^r_{ipj} = V_j \mp I_k Z_{ij} - V^i_{inj} \tag{5.61}$$

where the upper and lower signs apply, respectively, for indices $(i,j,k) \in \{(x,y,z),\ (y,z,x),\ (z,x,y)\}$ and $(i,j,k) \in \{(x,z,y),\ (y,x,z),\ (z,y,x)\}$. By removing stub values from equations (3.34) and (3.35) and shifting dummy indices, the equivalent total voltage V_j and the equivalent total current I_k are derived as:

$$V_j = 2\,\frac{Y_{ij}(V^i_{inj} + V^i_{ipj}) + Y_{kj}(V^i_{knj} + V^i_{kpj})}{2Y_{ij} + 2Y_{kj} + G_{ej}} \tag{5.62}$$

$$I_k = 2\,\frac{V^i_{ipj} - V^i_{inj} + V^i_{jni} - V^i_{jpi}}{2Z_{ij} + 2Z_{ji} + R_{mk}} \tag{5.63}$$

The scattering procedure for the SSCN is therefore completely described by 12 equations obtainable from (5.60)–(5.61) and the definitions of equivalent voltages and currents given by (5.62)–(5.63). Efficient implementations of the scattering procedure for the SSCN and other nodes derivable from the GSCN will be further discussed in Chapter 6.

5.4.2 Connection

Inside a unique node region, the transfer of voltage pulses, called 'connection', proceeds as in a traditional TLM mesh [6] constructed using nodes of constant link line characteristic impedance. It is accomplished by simply swapping the pulses between adjacent ports of two neighbouring nodes. This is valid for the

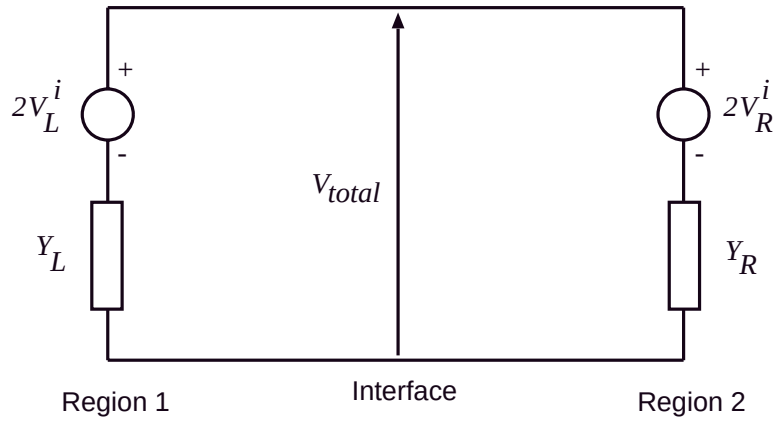

Figure 5.3 *Connection at the interface between two unique node regions*

SSCN since the characteristic impedance of a link line is the same on either side of the node centre, i.e. the SSCN is a balanced node.

Care must be taken at the interface between two different node regions where the characteristic impedance changes. A simple two-port junction, depicted in Figure 5.3 by an equivalent Thevenin circuit, must be modelled to calculate appropriate reflected and transmitted voltage pulses. The superscript i for voltage pulses means that they are incident to the interface (not to the node centre).

A common approach for implementing this algorithm is to first calculate the total voltage at the interface, V_{total}, as:

$$V_{total} = \frac{2Y_L V_L^i + 2Y_R V_R^i}{Y_L + Y_R} \tag{5.64}$$

Subsequently, the reflected voltages on the left and right-hand side, V_L^r and V_R^r respectively, can be calculated by:

$$V_L^r = V_{total} - V_L^i \tag{5.65}$$

$$V_R^r = V_{total} - V_R^i \tag{5.66}$$

Note that this procedure requires storage of at least two coefficients per interface per polarization, namely $2Y_L/(Y_L + Y_R)$ and $2Y_R/(Y_L + Y_R)$. A computation of V_{total} requires at least two multiplicative (MUL) operations.

A more efficient implementation becomes evident after some algebraic manipulations with equations (5.64)–(5.66) which result in the following expressions:

$$V_L^r = \frac{Y_L - Y_R}{Y_L + Y_R}(V_L^i - V_R^i) + V_R^i \tag{5.67}$$

$$V_R^r = \frac{Y_L - Y_R}{Y_L + Y_R}(V_L^i - V_R^i) + V_L^i \tag{5.68}$$

In this new form only one MUL operation is required and only one coefficient $(Y_L - Y_R)/(Y_L + Y_R)$ needs to be stored per polarization per interface to calculate both reflected voltages.

5.4.3 External boundaries

External boundaries of arbitrary reflection coefficient ρ_w are modelled in TLM by terminating the link lines at the edge of the problem space with an appropriate load [39]. If the characteristic impedance of a link line differs from the intrinsic impedance of medium, the equivalent link line reflection coefficient, ρ_{ij}, generally differs from ρ_w.

For a plane electromagnetic wave propagating in the i-direction with tangential field components E_j and H_k, the total capacitance of the block of medium, C_j^t, and the total inductance L_k^t are given from (2.3) and (2.7) as:

$$C_j^t = \varepsilon_j \frac{\Delta i \Delta k}{\Delta j} \qquad\qquad L_k^t = \mu_k \frac{\Delta i \Delta j}{\Delta k}$$

The intrinsic impedance of the medium seen by such a wave is defined by:

$$Z_{ij}^m = \sqrt{\frac{L_k^t}{C_j^t}} = \sqrt{\frac{\mu_k}{\varepsilon_j}} \frac{\Delta j}{\Delta k}$$

and the resistance needed to terminate it in order to give reflection coefficient ρ_w can be calculated from

$$R = Z_{ij}^m \frac{1 + \rho_w}{1 - \rho_w}$$

since:

$$\rho_w = \frac{R - Z_{ij}^m}{R + Z_{ij}^m}$$

The link line reflection coefficient, ρ_{ij} , is then found by terminating the link line, of characteristic impedance Z_{ij}, with this same resistance:

$$\rho_{ij} = \frac{R - Z_{ij}}{R + Z_{ij}} = \frac{(1 + \rho_w) - \hat{Z}_{ij}(1 - \rho_w)}{(1 + \rho_w) + \hat{Z}_{ij}(1 - \rho_w)} \tag{5.69}$$

where a normalized characteristic impedance is introduced as $\hat{Z}_{ij} = Z_{ij}/Z_{ij}^m$.

If the external boundary represents an electric wall, $\rho_w = -1$, than it follows from (5.69) that $\rho_{ij} = -1$. Similarly, for a magnetic wall, $\rho_w = 1$, and from (5.69) it follows that $\rho_{ij} = 1$. Therefore, when modelling electric or magnetic walls, we have $\rho_w = \rho_{ij}$.

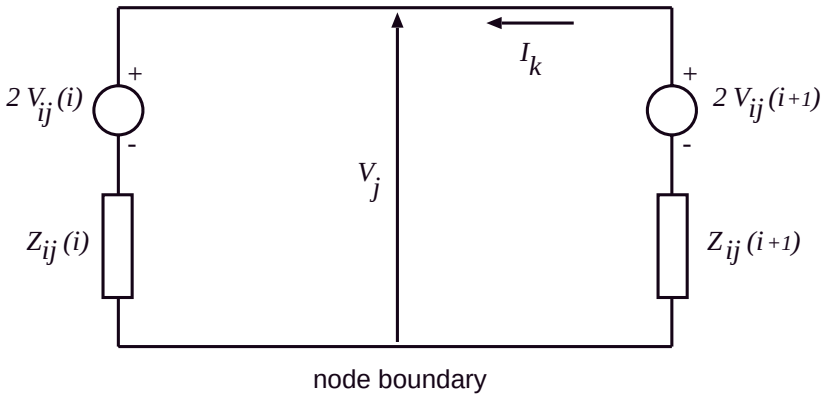

Figure 5.4 *Thevenin circuit for computing output values on link lines*

If an absorbing boundary is modelled, with $\rho_w = 0$, then it follows from (5.69) that:

$$\rho_{ij} = \frac{1 - \hat{Z}_{ij}}{1 + \hat{Z}_{ij}} \neq 0$$

5.4.4 Output

Information on electric and magnetic field components can be extracted from an SSCN TLM mesh through appropriate values of equivalent voltages and currents using the formulae:

$$E_j = -\frac{V_j}{\Delta j} \qquad H_k = \frac{I_k}{\Delta k}$$

Field values at a node can be readily obtained using formulae which define equivalent voltages (5.62) and equivalent currents (5.63) already used in the scattering procedure.

In obtaining the output on link lines, the different characteristic impedances on interfaces between two node regions must be taken into account. Equivalent voltages and currents are found by solving the equivalent Thevenin circuit shown in Figure 5.4 as:

$$V_j = \frac{2\left[V_{ij}(i)Y_{ij}(i) + V_{ij}(i+1)Y_{ij}(i+1)\right]}{Y_{ij}(i) + Y_{ij}(i+1)} \tag{5.70}$$

$$I_k = \frac{2\left[V_{ij}(i+1) - V_{ij}(i)\right]}{Z_{ij}(i) + Z_{ij}(i+1)} \tag{5.71}$$

If the output is required on a link line completely inside the unique node region, i.e. $Z_{ij}(i) = Z_{ij}(i+1)$, formulae (5.70) and (5.71) are simplified to:

$$V_j = V_{ij}(i) + V_{ij}(i+1) \tag{5.72}$$

$$I_k = \frac{V_{ij}(i+1) - V_{ij}(i)}{Z_{ij}} \tag{5.73}$$

which can be also derived from the cell boundary mapping introduced in Chapter 4 by equations (4.12).

5.4.5 Excitation

If the excitation of a TLM mesh is specified in terms of field components, then the appropriate incident voltage pulses required to start the simulation must be injected into the mesh. When exciting a particular field component, care must be taken not to excite others. This can be accomplished if the electric charge and the magnetic flux are applied symmetrically with respect to the node centre.

In exciting the electric field component E_j, pulses must be injected into the mesh to give an equivalent voltage $V_j = -E_j \Delta j$. From equation (5.62) and the charge symmetry conditions, the following ports need to be excited:

$$V^i_{inj} = V^i_{ipj} = \frac{V_j}{8} \cdot \frac{2Y_{ij} + 2Y_{kj} + G_{ej}}{Y_{ij}} \tag{5.74}$$

$$V^i_{knj} = V^i_{kpj} = \frac{V_j}{8} \cdot \frac{2Y_{ij} + 2Y_{kj} + G_{ej}}{Y_{kj}} \tag{5.75}$$

From (5.62) and (5.63) it can be confirmed that all other equivalent voltages and currents are zero, therefore only the desired field component is excited. For the SSCN modelling a lossless medium ($G_{ej} = 0$), after using (5.27), the expressions (5.74)–(5.75) simplify to:

$$V^i_{inj} = V^i_{ipj} = \frac{V_j}{4\hat{C}_{ij}} \qquad V^i_{knj} = V^i_{kpj} = \frac{V_j}{4\hat{C}_{kj}}$$

Similarly, for exciting the magnetic field component H_k, pulses must be injected into the mesh to give an equivalent current $I_k = H_k \Delta k$. Applying symmetry conditions for the magnetic flux and using (5.63), it can be easily shown that the following voltage pulses need to be injected:

$$V_{ipj} = -V_{inj} = V_{jni} = -V_{jpi} = \frac{I_k}{8} \cdot (2Z_{ij} + 2Z_{ji} + R_{mk}) \tag{5.76}$$

For the SSCN modelling lossless medium ($R_{mk} = 0$), after using (5.28), the expression (5.76) simplifies to:

$$V_{ipj} = -V_{inj} = V_{jni} = -V_{jpi} = \frac{I_k Z_{ij}}{4\hat{L}_{ij}} = \frac{I_k Z_{ji}}{4\hat{L}_{ji}}$$

For exciting field components on a link line, formulae (5.70) and (5.71) with conditions $I_k = 0$ and $V_j = 0$ respectively, can be used to obtain the values of voltages for the electric field E_j excitation as:

$$V_{ij}(i) = V_{ij}(i+1) = \frac{V_j}{2} \tag{5.77}$$

and the magnetic field H_k excitation as:

$$V_{ij}(i) = -\frac{I_k Z_{ij}(i)}{2} \tag{5.78}$$

$$V_{ij}(i+1) = \frac{I_k Z_{ij}(i+1)}{2} \tag{5.79}$$

5.4.6 Other features

A number of other features, e.g. internal boundaries, thin features (wires, films, apertures), voltage and current sources, etc., can be implemented in a TLM mesh based on the SSCN. Procedures similar to the ones normally used in the TLM mesh with traditional SCN [6] can also be used in the mesh based on the SSCN. Attention must be paid to the fact that the characteristic impedances of link lines in SSCN TLM are different in different node regions. This should be dealt with in the implementation in a manner similar to the one used in the definition of outputs and excitation in the SSCN TLM mesh, described earlier in this section.

5.5 Numerical examples

To validate the proposed TLM SSCN algorithm, a series of numerical simulations was performed. The examples presented here are classified into three groups:

- modelling isotropic materials on a uniform mesh
- modelling isotropic materials on a graded mesh
- modelling anisotropic materials on a graded mesh

5.5.1 Isotropic materials on a uniform mesh

To test the new SSCN, a homogeneous problem is first modelled, an $1m^3$ air-filled cavity with perfect electric walls. The modelling of this problem normally can be accomplished using the basic 12-port symmetrical condensed node. However, to test the nodes capable of modelling materials different from the background, such as the SSCN, we can, for example, introduce a hypothetical background medium $\varepsilon_{r0} = 0.5$ and model the air as a medium with non-background electromagnetic

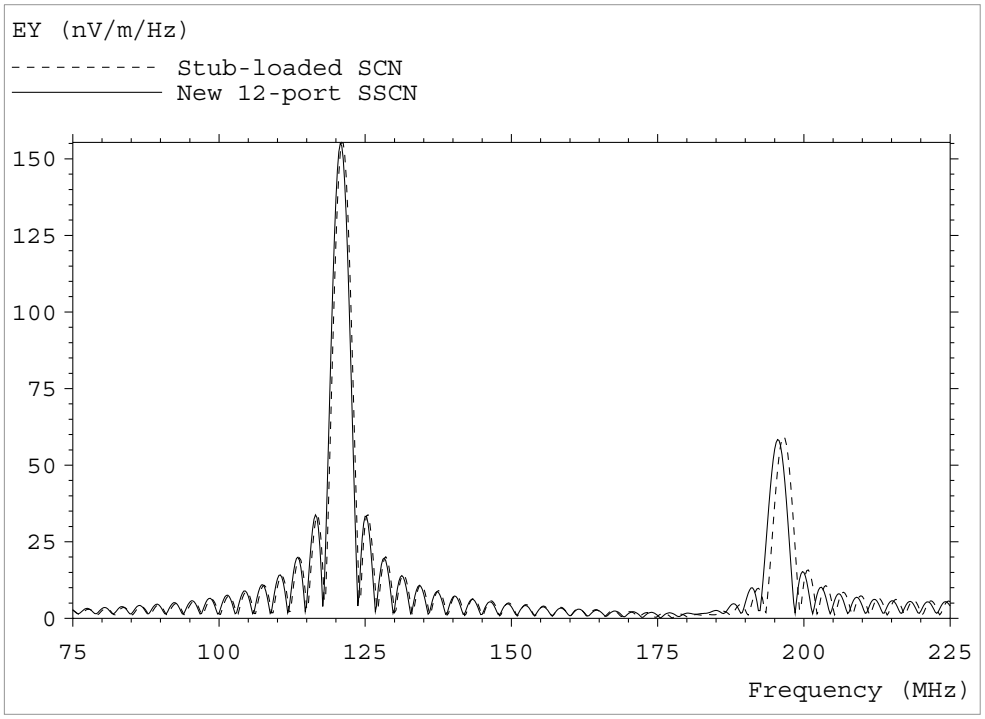

Figure 5.5 *Frequency response in inhomogeneous cavity*

properties. Separate simulations with both the 12-port SCN and the SSCN were performed using the node spacing of $\Delta l = 5$cm and first two cavity resonances were computed. The results obtained using the two methods are reported in Table 5.1.

	Analytical	12-port SCN	New SSCN
TE_{110} [MHz]	212.0	211.9	211.7
TE_{210} [MHz]	335.2	334.9	334.0

Table 5.1 *Cavity resonances using different methods*

It can be seen from Table 5.1 that results obtained using the SSCN agree well with those obtained analytically and with the 12-port SCN, thus confirming that propagation of electromagnetic waves through a homogeneous medium can be modelled accurately without introducing stubs.

The next step is to model an inhomogeneous problem, to test the implementation of the connection procedure on the interface between two different materials. An air cavity, half filled with a medium of properties $\varepsilon_r = \mu_r = 2$, was chosen. Figure 5.5 shows the first two resonances calculated for such a cavity, comparing the results for the stub-loaded SCN and the SSCN. It can be seen from Figure 5.5

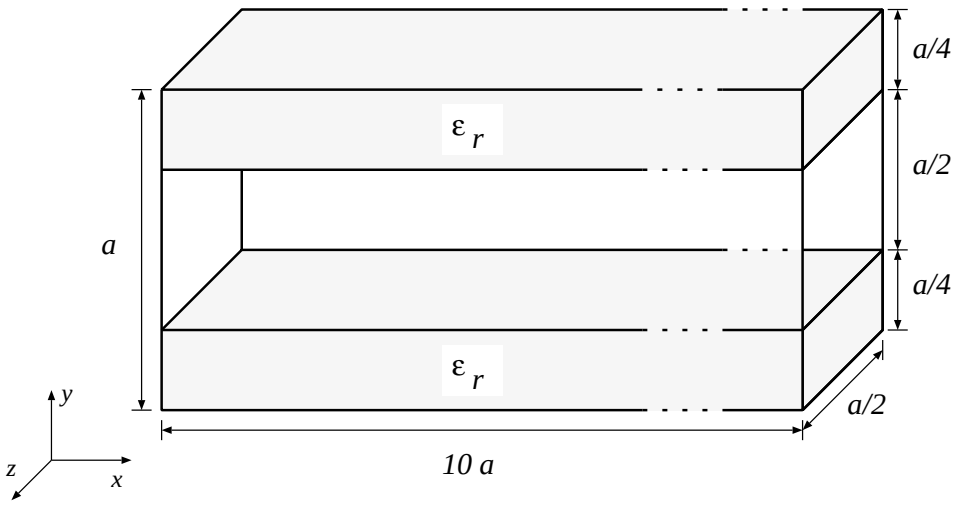

Figure 5.6 *Resonator loaded with dielectric layers of ε_r=4 (a=7.112mm)*

that the results agree well, therefore, the SSCN was successfully implemented for modelling inhomogeneous problems on a uniform mesh.

5.5.2 Isotropic materials on a graded mesh

To validate the proposed TLM SSCN algorithm for the case of a graded mesh, a canonical resonator loaded with dielectric was modelled, as illustrated in Figure 5.6. Dielectric layers with relative permittivity $\varepsilon_r = 4$ were placed at the top and bottom of the cavity which was otherwise filled with air ($\varepsilon_{r0} = 1$). The dimension a of the resonator was $a = 7.112$mm.

The benchmark resonant frequency for the TE_{110} mode, obtained by using two different TLM methods on a very fine uniform mesh, namely the stub-loaded SCN and the SSCN, is $f_0 = 16.595$GHz. Using the SSCN TLM method on a fine uniform mesh of $400 \times 40 \times 1$ cells a resonant frequency $f = 16.584$GHz was obtained, which is 0.07% lower value than f_0. Note that appropriate excitation and short-circuit boundary conditions were used to reduce the number of cells in the z-direction, since for this particular mode there is no propagation in the z-direction.

A coarse uniform mesh with $40 \times 4 \times 1$ cells was then used, part of which is illustrated in Figure 5.7a. A resonant frequency of 15.480GHz was obtained, underestimating f_0 by 6.72%. This inaccuracy occurred mainly because only one node per dielectric layer was used in the y-direction. The time step used in this simulation was $\Delta t_0 = 2.965$ps.

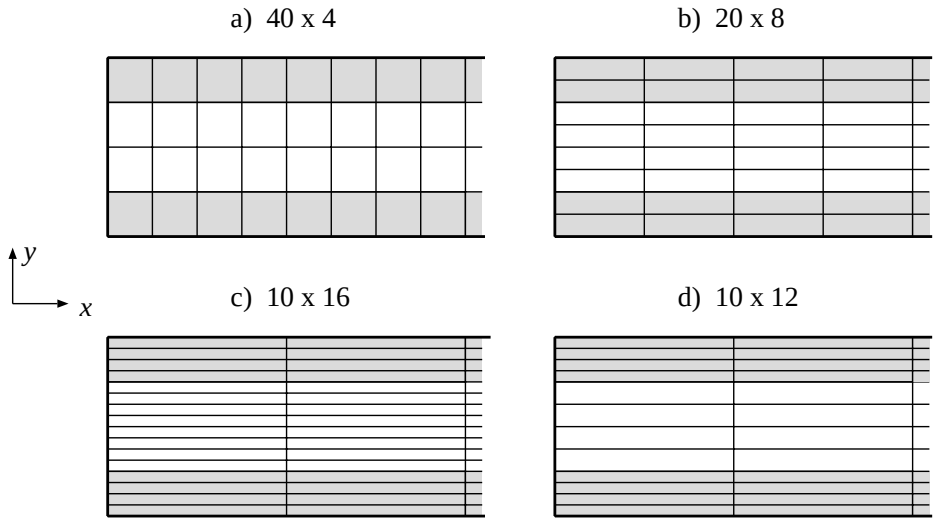

Figure 5.7 *Schematic of different gradings of the TLM mesh*

Retaining the same number of cells, by increasing the node dimension in the x-direction by a factor of 2 and decreasing it by the same factor in the y-direction, as illustrated in Figure 5.7b, a uniformly graded mesh of $20 \times 8 \times 1$ cells was used and the resonant frequency obtained was 16.322 GHz, i.e. 1.65% below the correct one. The time step was slightly decreased ($0.899\Delta t_0$), but the number of cells and memory requirements remained the same and a more accurate result was achieved than in the case of the cubic cell mesh.

A further increase in aspect ratio, illustrated in Figure 5.7c, produced a mesh of $10 \times 16 \times 1$ cells and the simulated resonant frequency of 16.530GHz was just 0.39% below the correct one. However, even though the same number of cells was used, the time step was decreased to $0.491\Delta t_0$.

So far, only uniformly graded meshes were used to achieve the improvement in the modelled resonant frequency. Consider now a grading case when the grading in the y-direction within the dielectric is higher than in the region of free space. Since the propagation velocity in the dielectric is $\sqrt{\varepsilon_r} = 2$ times lower than in free space, that part of the mesh was graded with twice as many cells. However, to maintain a reasonable number of cells, node spacing was increased in the free-space region, thus forming a mesh of $10 \times 12 \times 1$ cells, part of which is shown in Figure 5.7d. The number of cells for this mesh was 25% lower then in the previous case, the allowable time step was almost twice as high, namely $0.938\Delta t_0$, and the modelled frequency obtained was $f = 16.584$GHz. Accuracy in this case was the same as that achieved with a fine uniform mesh ($400 \times 40 \times 1$ cells). However the number of TLM cells used in the non-uniformly graded SSCN mesh was over hundred

times smaller and the time step was almost 10 times higher than in the uniform case. By increasing the resolution of the non-uniformly graded SSCN mesh, by a factor of 2, i.e. using $20 \times 24 \times 1$ cells, a resonant frequency of $f = 16.594$GHz was obtained, which is an accuracy of better than 10^{-4}.

The results obtained for the different mesh configurations are summarized in Table 5.2.

Mesh	Freq.[GHz]	Error [%]	Time-step per Δt_0
U: 400×40	16.584	0.07	0.100
U: 40×4	15.480	6.72	1.000
G: 20×8	16.322	1.65	0.899
G: 12×12	16.476	0.72	0.645
G: 10×16	16.530	0.39	0.491
N: 10×12	16.584	0.07	0.938
N: 20×24	16.594	0.01	0.469

U – uniform mesh, G – uniformly graded mesh, N – nonuniformly graded mesh

Table 5.2 *Calculation of TE_{110} frequency for different grading cases*

It is clear from Table 5.2 that a uniformly graded mesh offers better results with less memory requirements than a uniform mesh, but that a non-uniformly graded mesh chosen in an appropriate manner shows even better characteristics.

5.5.3 Anisotropic materials on a graded mesh

To validate the formulation of the 12-port super-condensed node for anisotropic media, edge coupled microstrip lines on an anisotropic sapphire substrate were modelled. The geometry of the modelled structure and axial components of the dielectric constant of sapphire are shown in Figure 5.8a.

In order to facilitate an efficient computation, non-uniform grading of the mesh in the transverse plane was used, as depicted in Figure 5.8b. Symmetry was exploited by introducing a magnetic wall in the centre of the structure, as shown in Figure 5.8b.

Odd and even mode dispersion characteristics obtained from TLM simulations using the SSCN are plotted in Figure 5.8c. They are found to be in excellent agreement with the results obtained using other analytical and numerical techniques, presented in [47, 48].

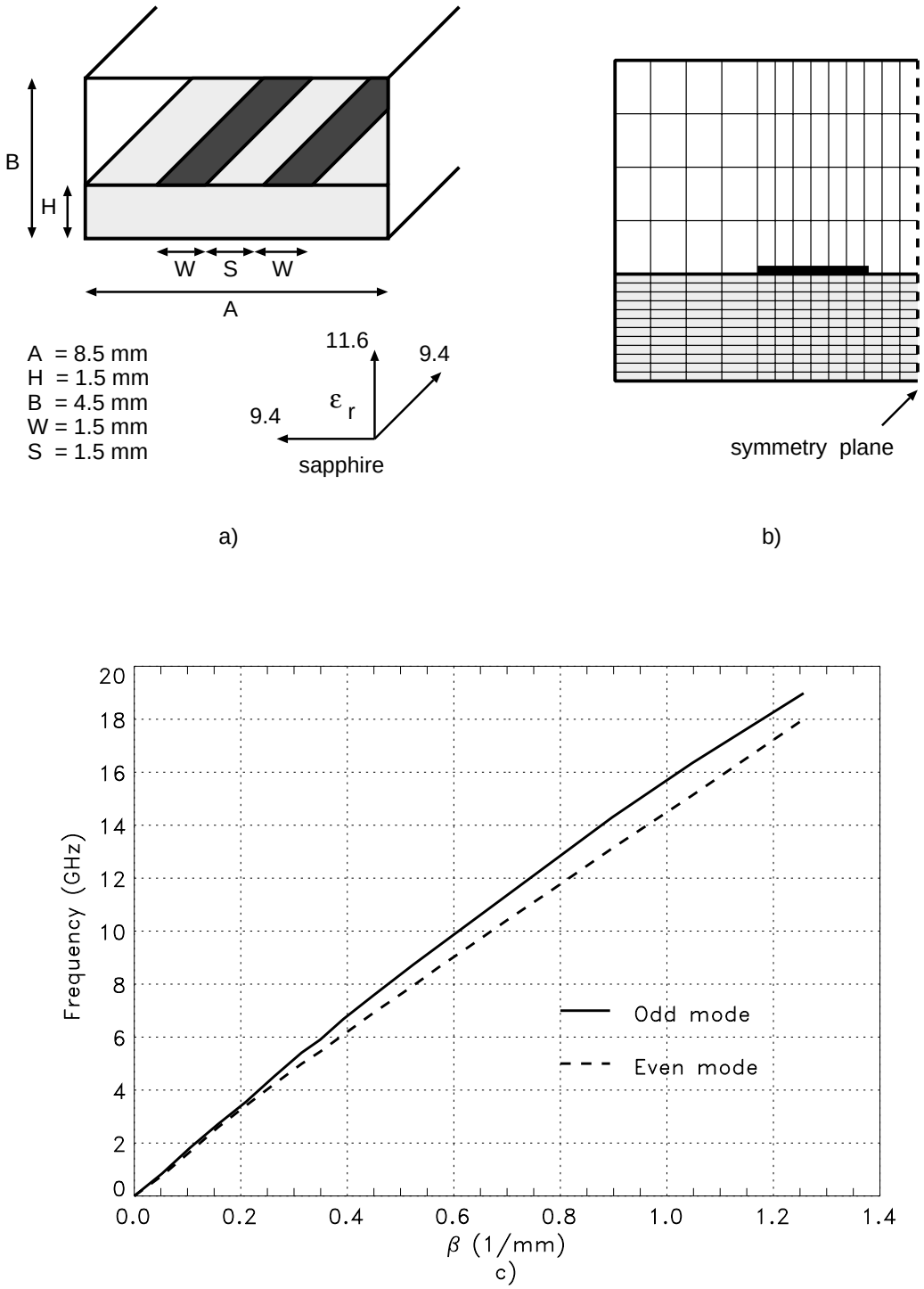

Figure 5.8 *Edge coupled microstrip lines on sapphire: a) Geometry b) Schematic of grading c) Dispersion characteristics*

5.6 Discussion

A substantial development to the TLM method was described in this chapter. Using the general system of equations for calculating the parameters of TLM schemes, established in Chapter 2, and the scattering formulation of the general symmetrical condensed node, derived in Chapters 3 and 4, a node without stubs, referred to as the symmetrical super-condensed node (SSCN), capable of modelling general non-uniform problems, was developed. The parameters and scattering properties of this node, its implementation including the maximum permissible time step, connection, boundaries, excitation and output, were described. The use of normalized quantities introduced in this chapter enhanced physical understanding and simplified the derivation of the SSCN.

Because stubs are removed from the node, the SSCN requires fewer memory locations than the stub-loaded or the hybrid nodes. It was also shown that the maximum permissible time step in the SSCN is generally higher from that found in the previous nodes. The numerical results presented for modelling different isotropic and anisotropic problems confirmed the proposed implementation procedures for the SSCN TLM method and showed its high versatility.

From the discussion in Chapter 2 on the topology of the three basic nodal structures used in 3D TLM, namely the expanded node, the asymmetrical condensed node and the symmetrical condensed node, it follows that the formulation of parameters of the link lines and the maximum time step derived here is valid also for equivalent stubless nodes based on the other two types of 3D nodes. For example, it can be shown that the link line parameters of a distributed expanded node described in [49] are equivalent to those of the SSCN derived here, if a homogeneous medium with background properties and an appropriate time step is assumed.

Following the equivalency between the parameters of the three basic nodal structures, it appears that a stubless expanded node can be developed to accommodate inhomogeneous problems and arbitrary non-uniform grading of the mesh, as well. However, difficulties in implementing such a node may be experienced because of the node's non-condensed topology, i.e. because the parameters of link lines are shared between adjacent cells (see Figure 2.1) and, hence, an averaging of cell's parameters at interfaces will have to be performed [18].

Chapter 6 Efficient computational algorithms

6.1 Introduction

In the efficient computer implementation of a numerical method, the main objectives are to achieve minimization of memory storage and computer (CPU) runtime, so that problems can be modelled in fine detail and with a reasonable speed. In time-domain methods it is also of great importance that the time step can be chosen sufficiently high as to allow a faster completion of the simulation process.

The total memory requirement is dependent on the number of variables stored per a discretized space cell. In the TLM method, this discretized cell is represented by a TLM node. The number of variables that is required to store per TLM node in order to run a TLM simulation is dependent on the number of voltage pulses incident on the node. The number of incident voltage pulses is further dependent on the number of transmission lines connected at the node centre.

In 3D TLM, the nodes are constructed by 12 link lines and up to 6 open- and short-circuit stubs, as detailed in previous chapters. The link lines must be present in all nodal configurations in order to facilitate connections between adjacent nodes. Stubs are introduced into the node to allow modelling of non-uniform materials and the use of a graded mesh with cells of arbitrary aspect ratio.

It has been demonstrated in Chapter 5 that a symmetrical super-condensed node can be constructed which allows modelling of inhomogeneous media on a graded mesh exclusively using link lines. Thus, due to the absence of stubs, the memory storage requirements can be greatly reduced compared to the traditional stub-loaded and hybrid nodes. The number of voltage pulses incident on the node centre in three different nodal configurations capable of modelling general problems are summarized in Table 6.1.

Having reduced the memory requirements in the TLM by introducing an all-link line symmetrical super-condensed node, the possibility of optimizing CPU run-

	Stub-loaded SCN	Hybrid SCN	12-port SSCN
Number of pulses	18	15	12
Relative storage	1.00	0.83	0.66

Table 6.1 *Number of incident voltage pulses per node and the memory requirements relative to the stub-loaded node*

time of TLM calculations will now be investigated. The maximum permissible time step in available nodes has been already determined and compared in Chapter 5 where it was found that the SSCN generally offers a higher time step with graded meshes and anisotropic problems than the stub-loaded and hybrid nodes.

In optimizing the TLM calculations, special attention must be paid in coding the procedures which are related to all nodes in the mesh. These are the scattering and connection procedures.

The connection process in TLM is fairly inexpensive in terms of run-time: it is, in the majority of cases, just a simple swapping of pulses between adjacent nodes. In cases where link line impedances vary (HSCN, SSCN, GSCN), a reflection/transmission process needs to be modelled at interfaces between distinct node regions. An efficient implementation of this algorithm was shown in § 5.4.2. However, this process occurs only in a limited number of node interfaces and therefore does not represent a big factor to the overall efficiency.

A far more computationally demanding operation is the scattering procedure and it is of a great importance to optimize it as far as possible. The rest of this chapter will be completely devoted to discussion of efficient implementations of the scattering procedure in the nodes derivable from the general symmetrical condensed node (GSCN).

6.2 Storage of the scattering coefficients

In every condensed node, apart from the 12-port SCN, the scattering coefficients are dependent on the characteristic impedances of link lines and stubs, and through them on the material properties and node aspect ratios. If a lossy medium is modelled, they are also dependent on the values of lossy elements expressed through shunt conductances and series resistances. Therefore, it is necessary to store appropriate node parameters in order to describe scattering in different parts of a TLM mesh.

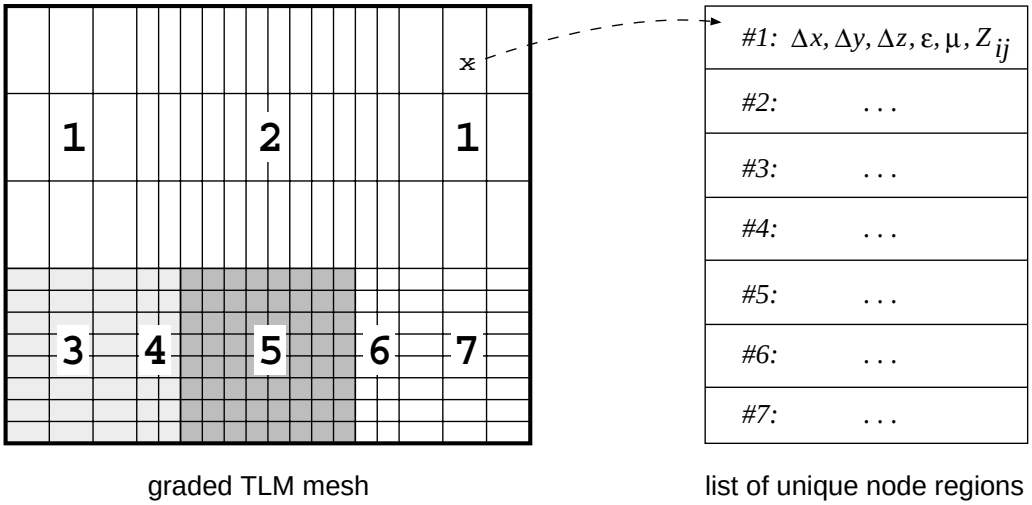

Figure 6.1 *Storage of parameters of the TLM nodes*

The storage of the scattering parameters on a *per node* basis would be computationally unacceptable, since the memory requirements would dramatically increase. Thus, a possible solution is to store scattering coefficients on a *per unique node region* basis and to assign an identifier to every node in the mesh pointing to the related node region [39]. A separate list of the node regions can than be maintained, as for example depicted in Figure 6.1. Note that the *unique node region* is defined as the region of TLM nodes describing the same material properties (ε, μ, σ) on a part of the mesh where the cells are of the same linear dimensions ($\Delta x, \Delta y, \Delta z$).

The example presented in Figure 6.1 shows a possible grading of an inhomogeneous problem with three different media and a number of different aspect ratios of the nodes. A total of seven unique node regions can be identified in the figure. The parameters of these node regions are stored in a separate list and every node has a pointer to the list. The organization of the node parameters in this way means that only storage for incident/reflected voltages and a (byte) identifier is required on a *per node* basis, thus making significant savings in memory since the number of distinct node regions is usually much smaller than the number of nodes — in this example there are 198 nodes and 7 node regions. In the following derivations of the most efficient scattering algorithms it is assumed that the scattering coefficients are stored on a *per unique node region* basis.

Even though a node region can be completely described by the characteristic impedances of link lines and stubs, it makes sense from the computational viewpoint to calculate and store the appropriate scattering coefficients. The calculation

of the coefficients should be done in the preprocessing stage in order to avoid the recalculation at every time step. It is important to store the coefficients in the form which will require the least computational effort in the main time stepping process.

In most modern computers performing floating point arithmetic, additive (ADD) and subtractive (SUB) operations are executed faster than multiplications (MUL) and especially divisions (DIV). For this reason it is appropriate to reduce MUL operations as far as possible and not to use divisions at all. By appropriate storing of scattering coefficients, divisions can be completely avoided, while multiplications can be reduced, as will be shown in the following sections.

Initially, the scattering procedure for the SCN was described by the scattering matrix [9]. The implementation of scattering by using directly the elements of the matrix would be inefficient due to a large number of zeros in the matrix. Improvements to the scattering algorithm were first proposed by Tong and Fujino [50], however, the most efficient approach appears to be one based on the scattering equations introduced by Naylor and Ait-Saidi [37]. Efficient scattering algorithms, based on the similar equations but generalized for the treatment of arbitrary unbalanced and balanced nodes as described in Part One of this thesis, will be examined here.

6.3 Scattering in nodes with stubs

In this section, scattering algorithms for general nodes, as well as for the available stub-loaded and hybrid nodes are described.

6.3.1 Unbalanced nodes

The scattering process for a most general unbalanced node, with 12 different link line characteristic impedances and up to 6 stubs and 6 lossy elements was described in Chapter 3 by:

Scattering into link lines:

$$V^r_{inj} = V_j \pm I_k Z_{inj} - V^i_{ipj} + h_{ij} \tag{6.1}$$

$$V^r_{ipj} = V_j \mp I_k Z_{ipj} - V^i_{inj} + h_{ij} \tag{6.2}$$

where the upper and lower signs apply, respectively, for indices $(i,j,k) \in \{(x,y,z),$ $(y,z,x),$ $(z,x,y)\}$ and $(i,j,k) \in \{(x,z,y),$ $(y,x,z),$ $(z,y,x)\}$.

Scattering into stubs:

$$V_{oi}^r = V_i - V_{oi}^i \tag{6.3}$$

$$V_{si}^r = I_i Z_{si} + V_{si}^i \tag{6.4}$$

where $i \in \{x, y, z\}$.

Definitions for V_j, I_k and h_{ij}:

$$V_j = 2\,\frac{Y_{inj}V_{inj}^i + Y_{ipj}V_{ipj}^i + Y_{knj}V_{knj}^i + Y_{kpj}V_{kpj}^i + Y_{oj}V_{oj}^i}{Y_{inj} + Y_{ipj} + Y_{knj} + Y_{kpj} + Y_{oj} + G_{ej}} \tag{6.5}$$

$$I_k = 2\,\frac{V_{ipj}^i - V_{inj}^i + V_{jni}^i - V_{jpi}^i - V_{sk}^i}{Z_{inj} + Z_{ipj} + Z_{jni} + Z_{jpi} + Z_{sk} + R_{mk}} \tag{6.6}$$

$$h_{ij} = \frac{Z_{inj} - Z_{ipj}}{Z_{inj} + Z_{ipj}} \left(V_{inj}^i - V_{ipj}^i\right) \tag{6.7}$$

where $(i, j, k) \in \{(x, y, z),\ (y, z, x),\ (z, x, y)\}$.

In the implementation of the scattering procedure described by the above relations, it is most efficient to calculate first terms related to the equivalent voltages and currents, e.g. V_j, $I_k Z_{inj}$ and the coefficients h_{ij}.

To compute three equivalent voltages V_x, V_y and V_z using (6.5), 15 MUL and 12 ADD operations are required, provided that 15 coefficients of the form

$$\frac{2Y_{inj}}{Y_{inj} + Y_{ipj} + Y_{knj} + Y_{kpj} + Y_{oj} + G_{ej}}$$

are stored per unique node region.

For calculating 12 possible terms $I_k Z_{inj}$ and $I_k Z_{ipj}$ and three terms $I_i Z_{si}$, by making use of equation (6.6), 15 MUL and 12 ADD/SUB operations are required, with another 15 coefficients stored in the form:

$$\frac{2Z_{inj}}{Z_{inj} + Z_{ipj} + Z_{jni} + Z_{jpi} + Z_{sk} + R_{mk}}$$

To compute six possible terms h_{ij} using (6.7), 6 MUL are needed and 6 coefficients in form $(Z_{inj} - Z_{ipj})/(Z_{inj} + Z_{ipj})$ must be stored. This step assumes that differences $V_{inj}^i - V_{ipj}^i$ have already been computed while calculating the equivalent currents.

The scattering procedure is accomplished by performing an additional 6 ADD for the summation of V_j and h_{ij}, followed by the remaining 24 ADD/SUB operations

required in equations (6.1)–(6.2) and 6 ADD/SUB in equations (6.3)–(6.4). This gives a total of 60 ADD/SUB and 36 MUL operations per node per time step for the scattering in the unbalanced general node, provided that 36 scattering coefficients are stored per node region.

This algorithm applies for a very general case when twelve different link line impedances, six stubs and six lossy elements are present in a node. Since this node is unbalanced, it should be used only for modelling boundaries [23] and not throughout the mesh. Thus, the complexity of the scattering procedure of such a node will not have a significant effect on the overall efficiency.

6.3.2 Balanced nodes

By applying conditions for balanced nodes, $Z_{inj} = Z_{ipj} = Z_{ij}$ and $h_{ij} = 0$, the implementation of the scattering procedure described by equations (6.1)–(6.7) becomes more efficient.

To compute three node voltages V_x, V_y and V_z using (6.5), 9 MUL and 12 ADD operations are required, provided that nine coefficients of the form

$$\frac{2Y_{ij}}{2(Y_{ij} + Y_{kj}) + Y_{oj} + G_{ej}}$$

are stored per unique node region.

For calculating six possible terms $I_k Z_{ij}$ and three terms $I_i Z_{si}$, 9 MUL and 12 ADD/SUB operations are required, with another nine coefficients stored in the form:

$$\frac{2Z_{ij}}{2(Z_{ij} + Z_{ji}) + Z_{sk} + R_{mk}}$$

The scattering procedure is accomplished by performing additional 24 ADD and SUB operations in equations (6.1)–(6.2), assuming that $h_{ij} = 0$, and 6 ADD/SUB in equations (6.3)–(6.4). This gives a total of 54 ADD/SUB and 18 MUL operations per node per time step for the scattering in the balanced GSCN, provided that 18 scattering coefficients are stored per node region.

This algorithm applies for a general case when six different link line impedances, six stubs and six lossy elements are present in a variable graded mesh modelling inhomogeneous, anisotropic problems. In the TLM nodes derivable from the GSCN, extra restrictions related to link and stub parameters are applied, as discussed in Chapter 2, so that the scattering can be simplified to some extent.

In the stub-loaded SCN, the characteristic impedance of link lines is constant and equal to that of the background medium, Z_0. Equations (6.1)–(6.6) simplify and the complete procedure can be implemented with 54 ADD/SUB and 12 MUL operations [39], with the storage of up to 12 scattering coefficients. When using a uniform mesh to model dielectric or magnetic materials, with only one type of stub, the requirements are reduced to 48 ADD/SUB and 9 MUL operations. Similar analysis can be applied to the hybrid node (HSCN) to find that 48 ADD/SUB and 12 MUL operations are required with 12 coefficients stored per node region.

6.4 Scattering in the SSCN

The scattering for the super-condensed node (SSCN) was described in Chapter 5 by equations (5.60)–(5.63). From there, it can be easily found that in the SSCN with both electric and magnetic losses, 42 ADD/SUB and 12 MUL operations are required for the scattering procedure, provided that 12 scattering coefficients are stored. However, in the case with no losses, a significantly more efficient algorithm can be implemented, requiring only 6 MUL and 48 ADD/SUB operations. A description of this algorithm follows.

Following equations (5.60)–(5.63), the scattering procedure in the lossless TLM symmetrical super-condensed node (SSCN) can be written as:

$$V^r_{inj} = V_j + I^{(ij)}_k Z_{ij} - V^i_{ipj} \tag{6.8}$$

$$V^r_{ipj} = V_j - I^{(ij)}_k Z_{ij} - V^i_{inj} \tag{6.9}$$

where the equivalent voltage V_j is:

$$V_j = \frac{Y_{ij}}{Y_{ij}+Y_{kj}}(V^i_{inj} + V^i_{ipj}) + \frac{Y_{kj}}{Y_{ij}+Y_{kj}}(V^i_{knj} + V^i_{kpj}) \tag{6.10}$$

and the equivalent loop current $I^{(ij)}_k$ is:

$$I^{(ij)}_k = \frac{V^i_{ipj} - V^i_{inj} + V^i_{jni} - V^i_{jpi}}{Z_{ij} + Z_{ji}} \tag{6.11}$$

Indices i, j, k take all possible combinations of x, y, z, i.e. $(i, j, k) \in \{(x, y, z), (y, z, x), (z, x, y), (y, x, z), (z, y, x), (x, z, y)\}$, giving a set of 12 scattering equations which completely describe the scattering in the SSCN.

Note that mapping of indices allowed here is slightly different to that used in equations (5.60)–(5.63), as an equivalent loop current $I^{(ij)}_k$ is introduced in order

to allow for an optimized scattering algorithm. Generally $I_k^{(ij)} = \pm I_k$, which is dependent on the order of indices i, j, i.e. $I_k^{(ij)} = -I_k^{(ji)}$.

In the implementation of the scattering procedure described by equations (6.8)–(6.11), it is useful first to calculate terms of equations (6.8)–(6.9) related to the equivalent voltages and currents, V_j and $I_k^{(ij)} Z_{ij}$

Three voltages V_x, V_y and V_z can be calculated from (6.10). Let us recall from equation (5.27) that normalized capacitances can be expressed in a generic form as:

$$\hat{C}_{ij} = \frac{Y_{ij}}{Y_{ij} + Y_{kj}} \tag{6.12}$$

for $i, j \in \{x, y, z\}$. Note from (6.12) that:

$$\hat{C}_{kj} = 1 - \hat{C}_{ij} \tag{6.13}$$

Let us also introduce sums of incident voltages on the link lines with identical directions and polarizations as:

$$V_{isj} = V_{ipj}^i + V_{inj}^i \tag{6.14}$$

Substituting equations (6.12)–(6.14) into (6.10) gives:

$$\begin{aligned} V_j &= \hat{C}_{ij} V_{isj} + \hat{C}_{kj} V_{ksj} \\ &= \hat{C}_{ij} V_{isj} + (1 - \hat{C}_{ij}) V_{ksj} \end{aligned}$$

and finally:

$$V_j = \hat{C}_{ij}(V_{isj} - V_{ksj}) + V_{ksj} \tag{6.15}$$

It is enough to map indices (i, j, k) to $\{(x, y, z), (y, z, x), (z, x, y)\}$ and to obtain all three nodal voltages V_x, V_y and V_z from (6.15). The most efficient procedure is first to calculate the sums of voltages on the same link line using (6.14), for which a total of six ADD operations are performed. Then, three SUB operations are needed to calculate $V_{isj} - V_{ksj}$, three MUL operations are needed for $\hat{C}_{ij}(V_{isj} - V_{ksj})$ and finally three ADD operations are needed for adding V_{ksj} to the partial results obtained. Therefore, a total of 12 ADD/SUB and 3 MUL operations are needed to obtain the three nodal voltages V_x, V_y and V_z. For this case, the storage of three scattering coefficients, $\hat{C}_{xy}$, $\hat{C}_{yz}$ and $\hat{C}_{zx}$ is required.

For the calculations of terms $I_k^{(ij)} Z_{ij}$ we recall from equation (5.28) that the normalized inductances can be expressed in a generic form as:

$$\hat{L}_{ij} = \frac{Z_{ij}}{Z_{ij} + Z_{ji}} \tag{6.16}$$

for $i, j \in \{x, y, z\}$. Note from (6.16) that:

$$\hat{L}_{ji} = 1 - \hat{L}_{ij} \tag{6.17}$$

Let us also introduce a combination of voltages contributing to the magnetic field in the k direction as:

$$V_k^{(ij)} = V_{ipj}^i - V_{inj}^i + V_{jni}^i - V_{jpi}^i \tag{6.18}$$

Note from (6.18) that:

$$V_k^{(ji)} = -V_k^{(ij)} \tag{6.19}$$

Substituting equations (6.16)–(6.18) into (6.11) gives:

$$I_k^{(ij)} Z_{ij} = \hat{L}_{ij} V_k^{(ij)} \tag{6.20}$$

By swapping indices i, j in (6.20), and taking into account (6.17) and (6.19) it is found that:

$$\begin{aligned} I_k^{(ji)} Z_{ji} &= \hat{L}_{ji} V_k^{(ji)} \\ &= (1 - \hat{L}_{ij})(-V_k^{(ij)}) \end{aligned}$$

and finally:

$$I_k^{(ji)} Z_{ji} = I_k^{(ij)} Z_{ij} - V_k^{(ij)} \tag{6.21}$$

By introducing mappings for indices (i, j, k) to $\{(x, y, z),\ (y, z, x),\ (z, x, y)\}$ all terms $I_k^{(ij)} Z_{ij}$ and $I_k^{(ji)} Z_{ji}$ can be calculated by making use of equations (6.20) and (6.21). The most efficient procedure is first to calculate terms $V_k^{(ij)}$ using (6.18), for which a total of nine ADD/SUB operations are performed. Then, three MUL operations are needed for $\hat{L}_{ij} V_k^{(ij)}$ in (6.20) and finally three SUB operations are needed for obtaining terms $I_k^{(ji)} Z_{ji}$ using equation (6.21). Therefore, a total of 12 ADD/SUB and 3 MUL operations are needed to obtain terms $I_x^{(yz)} Z_{yz}$, $I_x^{(zy)} Z_{zy}$, $I_y^{(zx)} Z_{zx}$, $I_y^{(xz)} Z_{xz}$, $I_z^{(xy)} Z_{xy}$ and $I_z^{(yx)} Z_{yx}$. The three scattering coefficients, namely $\hat{L}_{xy}$, $\hat{L}_{yz}$ and $\hat{L}_{zx}$ need to be stored.

Finally, to accomplish the scattering procedure the 24 additional ADD/SUB operations required in equations (6.8)–(6.9) need to be performed. This gives a total of 48 ADD/SUB and 6 MUL operations per node per time step for the scattering in the SSCN, provided that six scattering coefficients are stored.

It is interesting to note that in case of modelling isotropic media, the relationship (5.25) applies:

$$\hat{L}_{ij} = \hat{C}_{ik}$$

which can be used to further optimize the number of stored scattering coefficients. By using this identity, equation (6.20) can be rewritten as:

$$I_k^{(ij)} Z_{ij} = \hat{C}_{ik} V_k^{(ij)} \tag{6.22}$$

By introducing mappings for indices (i, j, k) to $\{(x, z, y),\ (y, x, z),\ (z, y, x)\}$ all terms $I_k^{(ij)} Z_{ij}$ and $I_k^{(ji)} Z_{ji}$ can be calculated by making use of equations (6.22) and (6.21). Note that the three scattering coefficients appearing in (6.22), namely $\hat{C}_{xy}$, $\hat{C}_{yz}$ and $\hat{C}_{zx}$, have already been used for the computation of equivalent voltages. Therefore, in an isotropic case, only three scattering coefficients need to be stored. Furthermore, when modelling isotropic media on a uniform mesh it follows from (5.34) that:

$$\hat{C}_{xy} = \hat{C}_{yz} = \hat{C}_{zx}$$

Hence, in the case of a uniform mesh, only one scattering coefficient is sufficient to efficiently perform the complete scattering process in the SSCN.

6.5 Scattering in the 12-port SCN

When modelling regions with background parameters on a uniform mesh, all condensed nodes simplify to the basic 12-port SCN and for this part of the mesh further gains in the computational efficiency can be made by implementing a separate procedure. By substituting, for example, $Z_{ij} = 1/Y_{ij} = Z_0$ in equations (6.8)–(6.11) for all possible combinations of $i, j \in \{x, y, z\}$ the scattering equations in the case of basic 12-port SCN can be rewritten as:

$$V_{inj}^r = \frac{1}{2}(V_{knj}^i + V_{kpj}^i + V_{jni}^i - V_{jpi}^i) \tag{6.23}$$

$$V_{ipj}^r = \frac{1}{2}(V_{knj}^i + V_{kpj}^i + V_{jpi}^i - V_{jni}^i) \tag{6.24}$$

The implementation of the complete scattering procedure in this form will require at least 12 multiplications by 1/2. This can be however improved, as follows. Introducing partial sums and differences as

$$V_{isj} = V_{inj}^i + V_{ipj}^i$$

$$V_{idj} = V_{inj}^i - V_{ipj}^i$$

and using the identity

$$\frac{1}{2}(a - b) = \frac{1}{2}(a + b) - b$$

equations (6.23)–(6.24) can be rewritten as:

$$V^r_{inj} = \frac{1}{2}(V_{ksj} + V_{jdi}) \tag{6.25}$$

$$V^r_{ipj} = \frac{1}{2}(V_{ksj} - V_{jdi}) = V^r_{inj} - V_{jdi} \tag{6.26}$$

Therefore, after calculating partial sums V_{isj} and partial differences V_{idj}, which takes 6 ADD and 6 SUB operations, reflected voltages V^r_{inj} can be computed from (6.25) by performing additional 6 ADD and 6 MUL by 0.5. These reflected voltages can be subsequently used in the computation of V^r_{ipj} through (6.26) requiring only additional 6 SUB operations.

Therefore, in this way, the scattering procedure for the 12-port node is accomplished with only 24 ADD/SUB operations and 6 MUL by a constant (1/2), with no need to store coefficients.

6.6 Discussion

A comparison of computational requirements of different TLM nodes is made in Tables 6.2–6.4.

	unbalanced GSCN	balanced GSCN
ADD/SUB oper.	60	54
MUL operations	36	18
stored coefficients	36	18
incident voltages	18	18

Table 6.2 *Comparison in the computational efficiency of balanced and unbalanced general symmetrical condensed nodes*

	GSCN	stub.SCN	HSCN	SSCN
ADD/SUB oper.	54	54	48	42
MUL operations	18	12	12	12
stored coefficients	18	12	12	12
incident voltages	18	18	15	12

Table 6.3 *Comparison in the computational efficiency of various balanced nodes modelling lossy general anisotropic media*

	stub.SCN	HSCN	SSCN	12-port SCN
Operations per node per time step				
ADD/SUB	54	48	48	24
MUL	12	12	6	6
Number of scattering coefficients to store				
anisotropic media – any mesh	12	9	6	N/A
isotropic media – graded mesh	12	9	3	N/A
isotropic media – uniform mesh	4	2	1	0

Table 6.4 *Comparison in the computational efficiency of various balanced nodes modelling lossless media*

It can be seen from Table 6.2 that balanced nodes are significantly more efficient than the unbalanced ones. The number of multiplicative operations (MUL), which are the most computationally demanding, is twice as higher in the unbalanced nodes. However, following the discussion given in Chapter 4 that the unbalanced nodes should not be used for the general modelling of the wave propagation in unbounded space, the complexity of their scattering algorithm does not pose a particular problem. Their possible use in modelling adjustable boundaries does not significantly decrease overall efficiency since the number of boundary nodes is much smaller than the total number of nodes.

It can be seen from Table 6.3 that the nodes derivable from the balanced GSCN, namely the stub-loaded SCN, the HSCN and the SSCN can be implemented more efficiently than the GSCN. For modelling general lossy anisotropic media on a variable graded mesh, the number of MUL operations is the same in all three practical nodal structures (12), while the number of ADD/SUB operations decreases with the number of incident voltages.

However, a real improvement in efficiency when modelling the lossless media with the SSCN can be noticed from Table 6.4. Here, the number of MUL operations for modelling any anisotropic lossless medium on a graded mesh is decreased to only 6. In fact, this number of MUL operations is the best that one can achieve, even when using the basic 12-port SCN which is only capable of modelling a homogeneous medium with background properties. It can be also seen from Table 6.4, that the number of scattering coefficients required to be stored per node region is significantly reduced for the case of the SSCN.

After carefully examining the computational aspects of the available symmetrical condensed nodes some conclusions can be drawn. It is obvious from the above discussions that the removal of stubs from the general node, through the SSCN, resulted in the development of a computationally efficient method with significant savings in memory storage, improvements in the CPU run-time performance and the possibility of using a higher time-step.

One more aspect remains to be examined – the numerical dispersion of the available methods, or in other words, their accuracy. The impact of introducing stubs and altering link lines on the accuracy of the TLM method when modelling general media and using a graded mesh must now be investigated. This will give a better insight into the dispersion behaviour of different nodes and point to potential developments of more improved nodal structures.

The dispersion characteristics of the traditional and the newly developed symmetrical condensed nodes will be the topic of the following, Part Three of the thesis.

Part III

Dispersion Analysis

Chapter 7 Dispersion relations of symmetrical condensed nodes

7.1 Introduction

As a result of the process of space discretization in modelling electromagnetic problems, variation in the wave propagation velocity with frequency occurs in all numerical schemes, even in cases where the numerical method is intended to simulate non-dispersive media. This phenomenon is usually described as *numerical dispersion*. Although errors introduced due to the numerical dispersion are generally small they nevertheless become unacceptable in certain applications such as, for example, narrow-band microwave circuits where small numerical frequency shifts can make the interpretation of results difficult. Similarly, if propagation over several wavelengths is simulated, unacceptable numerical phase shifts may occur.

To allow the study of the numerical dispersion in different modelling methods, the *dispersion relation* for a particular scheme must be obtained. In general, this dispersion relation describes the functional relationship between the angular frequency ω and the wave, or propagation vector, $\vec{k}$. The dispersion relation of Maxwell's equations in an isotropic non-dispersive medium with electromagnetic parameters ε, μ is [46]:

$$k^2 = \varepsilon\mu\,\omega^2 \tag{7.1}$$

where the amplitude of the propagation vector, denoted by k and also referred to as the propagation constant or wave number, is defined by

$$k = \sqrt{k_x^2 + k_y^2 + k_z^2} \tag{7.2}$$

where k_x, k_y and k_z are Cartesian components of the vector $\vec{k}$.

The phase velocity v_p and the group velocity v_g are defined as [46]:

$$v_p = \frac{\omega}{k} \qquad\qquad v_g = \left(\frac{\partial k}{\partial \omega}\right)^{-1} \tag{7.3}$$

It follows from the dispersion relation (7.1) that the group and phase velocities in non-dispersive media are equal. They are independent of frequency and determined only by the properties of the medium:

$$v_p = v_g = v = \frac{1}{\sqrt{\varepsilon\mu}}$$

The dispersion characteristics $k = F(\omega)$ for such media are straight lines with a slope of $1/v = \sqrt{\varepsilon\mu}$ and they will be referred further in the text as linear dispersion characteristics.

It is shown in this chapter that in TLM, as in other discrete numerical schemes, the modelled group and phase velocities follow the physical velocities closely only within a low-frequency band or, equivalently, for sufficiently fine spatial discretization. At higher frequencies the numerical dispersion increases, thus causing a deviation in the modelled wave velocities. In general, for numerical schemes modelling non-dispersive media, one can write:

$$\frac{\partial k}{\partial \omega} \neq const$$

but

$$\lim_{\omega \to 0} \frac{\partial k}{\partial \omega} = \frac{k}{\omega} = const = \sqrt{\varepsilon\mu}$$

The original analysis of the dispersion characteristics of the TLM mesh can be found in [51]. A limitation of this analysis procedure is that an equivalent circuit model of TLM node is required. As a practical equivalent circuit model for the 3D symmetrical condensed node does not exist, its dispersion relation cannot be derived by this procedure, except for special cases such as propagation along the axis and diagonal directions [5].

An extensive study in formulating a general dispersion relation for the SCN TLM mesh was pursued by Nielsen and Hoefer, which was reported in a series of publications [40, 52, 53, 54, 55]. In these references, the general dispersion relation, based on the application of Floquet's theorem, was formulated for the basic 12-port SCN. It was given in an implicit matrix form which can be solved numerically to study the dispersion characteristics of the SCN. An investigation of the spurious modes supported by the condensed node meshes was also carried out.

This work was followed up by other authors who extended the definition of the general dispersion relation to include nodes with stubs, different link line impedances and arbitrary aspect ratios [56, 57, 58, 59]. Dispersion in lossy media was also

investigated [60]. Most of these results were computed numerically due to the complexity of obtaining closed-form solutions for the general dispersion relation. They were computed either for propagation on a coordinate plane, or along particular directions. The closed algebraic solution describing completely the propagation in all directions was recently obtained for the 12-port SCN [61, 62]. An analytical study of the dispersion in anisotropic media modelled by TLM condensed nodes was also performed for propagation along axes and diagonal directions [63].

In this chapter, dispersion relations in algebraic forms for propagation in arbitrary directions will be derived for the stub-loaded SCN, the HSCN and the SSCN and their solutions will be explored. The analytical expansion of the general TLM dispersion relation is important as it enables, for the first time, a comprehensive mathematical analysis and comparisons of the dispersion behaviour of different nodes. This facilitates a thorough assessment of their accuracy in modelling EM problems, pursued in Chapter 8. It also offers an insight into the dispersion error trends for different nodal structures, which can be used in the development of new, more accurate TLM nodes, pursued in Chapter 9.

7.2 General dispersion relation for TLM

The general TLM dispersion relation for time-domain schemes can be written in matrix form as [62]:

$$\det(\mathbf{PS} - e^{j\theta}\mathbf{I}) = 0 \tag{7.4}$$

where θ is the phase shift along the constituent transmission lines, defined by $\theta = \omega\Delta t$, $\mathbf{I}$ is the identity matrix, $\mathbf{S}$ is the scattering matrix of the node, while $\mathbf{P}$ is a connection matrix. These parameters will be described in detail for time-domain TLM nodes modelling lossless media with arbitrary ε and μ on a graded mesh.

The phase shift θ can, in the case of a uniform mesh, be written in terms of the propagation constant along the constituent transmission lines, $k_l = \omega/v_l$, where v_l is a voltage pulse velocity on the line, and the node spacing $\Delta l = v_l\Delta t$ as:

$$\theta = \omega\Delta t = k_l v_l \Delta t = k_l \Delta l$$

This last definition was used in the original work by Nielsen and Hoefer [52]. In the graded mesh, the node spacing and the velocity of propagation on the individual link lines differ, and in this case k_l and Δl can be regarded, respectively, as an equivalent propagation constant and an equivalent cubic cell parameter [49].

The scattering matrix **S**, valid for a balanced general symmetrical condensed node, was derived in Chapter 3 and was shown in Figure 3.5. For the dispersion analysis of various nodes derivable from the GSCN, the scattering matrix with no losses is used, therefore rows 19–24 are removed from the matrix.

The connection matrix **P** represent Floquet's theorem, relating the voltage pulses at one node to the voltage pulses at neighbouring nodes along the periodic network of transmission lines. It contains the Cartesian components of the propagation vector $\vec{k} = (k_x, k_y, k_z)$ describing phase shifts along the three coordinate directions. The elements of **P** are zero, except [57]:

$$\begin{aligned}
\mathbf{P}_{3,11} &= \mathbf{P}_{6,10} = e^{jk_x\Delta x} \\
\mathbf{P}_{1,12} &= \mathbf{P}_{5,7} = e^{jk_y\Delta y} \\
\mathbf{P}_{2,9} &= \mathbf{P}_{4,8} = e^{jk_z\Delta z} \\
\mathbf{P}_{10,6} &= \mathbf{P}_{11,3} = e^{-jk_x\Delta x} \\
\mathbf{P}_{7,5} &= \mathbf{P}_{12,1} = e^{-jk_y\Delta y} \\
\mathbf{P}_{8,4} &= \mathbf{P}_{9,2} = e^{-jk_z\Delta z} \\
\mathbf{P}_{13,13} &= \mathbf{P}_{14,14} = \mathbf{P}_{15,15} = 1 \\
\mathbf{P}_{16,16} &= \mathbf{P}_{17,17} = \mathbf{P}_{18,18} = -1
\end{aligned} \tag{7.5}$$

Note that in the node without open-circuit stubs and/or without short-circuit stubs, rows and columns 13–15 and/or 16–18, respectively, are removed from the matrix **P**.

The general dispersion relation (7.4) is therefore defined as an implicit function of the angular frequency ω (through θ) and the propagation vector $\vec{k}$ (through **P**). In addition, the relation (7.4) is function of the time step, mesh grading and material properties (through the definition of the parameters of **S**). Therefore, nodes with different scattering matrices will have different dispersion relations and hence different numerical properties.

Relation (7.4) can be solved as an eigenvalue problem, because the left-hand side of (7.4) represents the characteristic polynomial of the matrix **PS** in terms of $e^{j\theta}$. Finding the analytical solutions to the general relation (7.4) is a complex algebraic process and will be described in the following sections. Before this is done, it will be proved that the dispersion analysis performed using the scattering matrix for balanced nodes, shown in Figure 3.5, is fully equivalent to the dispersion analysis

performed using a scattering matrix normalized in terms of power amplitudes, used in [63].

The need to normalize the scattering matrix is due to the reason that in a general SCN, unlike the basic 12-port SCN, the scattering matrix is not unitary, i.e. $\mathbf{S}^T\mathbf{S} \neq \mathbf{I}$. The equivalent condition in this case is described by [6]:

$$\mathbf{S}^T\mathbf{Y}\mathbf{S} = \mathbf{Y}$$

where $\mathbf{Y}$ is a diagonal matrix consisting of the characteristic admittance of link and stub lines. By multiplying both sides of this equation with $\mathbf{Y}^{-\frac{1}{2}}$ on the left and right-hand side, we obtain:

$$(\mathbf{Y}^{-\frac{1}{2}}\mathbf{S}^T\mathbf{Y}^{\frac{1}{2}})(\mathbf{Y}^{\frac{1}{2}}\mathbf{S}\mathbf{Y}^{-\frac{1}{2}}) = \mathbf{I}$$

and after introducing a normalized scattering matrix as $\mathbf{S}_n = \mathbf{Y}^{\frac{1}{2}}\mathbf{S}\mathbf{Y}^{-\frac{1}{2}}$ we write:

$$\mathbf{S}_n^T\mathbf{S}_n = \mathbf{I}$$

which shows that $\mathbf{S}_n$ is a unitary matrix. Normalized in terms of power amplitudes, the matrix $\mathbf{S}_n$ in fact directly obeys the energy conservation law.

The normalized matrix $\mathbf{S}_n$ was used in the dispersion analysis in [63], while original matrix $\mathbf{S}$ was used, for example, in [57, 58]. We will now prove formally, that as far as the dispersion analysis is concerned, these two approaches are equivalent.

First, it can be easily confirmed that for a balanced node, with $Y_{inj} = Y_{ipj}$, the matrices $\mathbf{P}$ and $\mathbf{Y}^{\frac{1}{2}}$ commute, i.e. $\mathbf{P}\mathbf{Y}^{\frac{1}{2}} = \mathbf{Y}^{\frac{1}{2}}\mathbf{P}$. Using this property and the definition of $\mathbf{S}_n$ we can write:

$$\mathbf{P}\mathbf{S}_n = \mathbf{P}\mathbf{Y}^{\frac{1}{2}}\mathbf{S}\mathbf{Y}^{-\frac{1}{2}} = \mathbf{Y}^{\frac{1}{2}}\mathbf{P}\mathbf{S}\mathbf{Y}^{-\frac{1}{2}}$$

Since $\mathbf{Y}^{\frac{1}{2}}$ is non-singular, the matrix $\mathbf{P}\mathbf{S}_n$ is called the *transform* of the matrix $\mathbf{P}\mathbf{S}$ by the matrix $\mathbf{Y}^{-\frac{1}{2}}$ [64]. Matrices $\mathbf{P}\mathbf{S}_n$ and $\mathbf{P}\mathbf{S}$ are also called *similar* matrices. A property for similar matrices is that they have identical eigenvalues [64]. Therefore, it follows that the solutions to the general dispersion relation (7.4) are identical for both representations of the scattering matrix.

7.3 Dispersion relation of the 12-port SCN

7.3.1 Derivation using new scattering matrix formulation

The analytical expansion of the general dispersion relation from the implicit form given by (7.4) requires considerable algebraic effort as finding the eigenvalues of

a matrix of 12th and higher orders, analytically, is not an easy task. The original investigations of the dispersion behaviour of the SCN were carried out mainly numerically [52, 54] and only very recently was the closed-form dispersion relation for the 12-port SCN derived [62]. Here, an interesting approach for deriving the dispersion relation of the 12-port SCN is presented, based on a new formulation of the scattering matrix. A systematic procedure of deriving dispersion relations algebraically for other available nodes will be presented in the next section.

Since the basic 12-port SCN allows only modelling of a homogeneous lossless medium on a uniform mesh, its scattering matrix can be obtained by removing stubs and lossy elements from the GSCN scattering matrix (shown in Figure 3.5) and setting $Z_{ij} = Z_0$. The top 12×12 partition of this matrix then becomes the original 12-port SCN matrix [9] with the elements $a_{ij} = c_{ij} = 0$ and $b_{ij} = d_{ij} = 1/2$. The order of the twelve node ports in this matrix is arranged in an apparently arbitrary manner which does not allow partitioning and expressing in a compact form. Although recently more systematic re-numbering schemes were proposed [44, 65], they do not offer an easier analytical solution to the general dispersion relation.

In the approach presented here, the node ports in the scattering matrix are rearranged so as to allow its partitioning with 6×6 zero blocks on the main diagonal. Voltage ports are ordered according to their direction and polarization indices, using cyclic permutations of indices, i.e. xy, yz and zx for the first six locations, and xz, yx and zy for the rest. A similar right-hand rule technique was used in the numbering scheme presented in [65].

The order of node ports for the new matrix representation is given in Table 7.1. The original scheme numbering is given in the third column for reference. Rearranging the rows and columns of the original scattering matrix according to Table 7.1 yields a new matrix with 6×6 blocks as:

$$\mathbf{S} = \begin{bmatrix} \mathbf{0}^{(6\times6)} & \mathbf{S}_0 \\ \mathbf{S}_0^T & \mathbf{0}^{(6\times6)} \end{bmatrix} \tag{7.6}$$

where

$$\mathbf{S}_0 = \begin{bmatrix} \mathbf{S}_1 & \mathbf{S}_2 \\ \mathbf{S}_2 & \mathbf{S}_1 \end{bmatrix} \tag{7.7}$$

with

$$\mathbf{S}_1 = \frac{1}{2}\begin{bmatrix} 0 & 1 & 1 \\ 1 & 0 & 1 \\ 1 & 1 & 0 \end{bmatrix} \qquad \mathbf{S}_2 = \frac{1}{2}\begin{bmatrix} 0 & -1 & 1 \\ 1 & 0 & -1 \\ -1 & 1 & 0 \end{bmatrix} \tag{7.8}$$

New row/column position	Voltage index	Original port notation [9]
1	xny	3
2	ynz	5
3	znx	2
4	xpy	11
5	ypz	7
6	zpx	9
7	xnz	6
8	ynx	1
9	zny	4
10	xpz	10
11	ypx	12
12	zpy	8

Table 7.1 *Order of node ports in the reorganized scattering matrix*

As a result of the transformation applied to matrix $\mathbf{S}$, matrix $\mathbf{P}$ needs also to be reorganized to reflect the new order of node ports. Moreover, the new form of the matrix $\mathbf{P}$ is compact and can be written as:

$$\mathbf{P} = \begin{bmatrix} \mathbf{P}_0 & \mathbf{0}^{(6\times6)} \\ \mathbf{0}^{(6\times6)} & \mathbf{P}_0 \end{bmatrix} \tag{7.9}$$

where

$$\mathbf{P}_0 = \begin{bmatrix} \mathbf{0}^{(3\times3)} & \mathbf{P}_1 \\ \mathbf{P}_1^* & \mathbf{0}^{(3\times3)} \end{bmatrix} \tag{7.10}$$

with

$$\mathbf{P}_1 = \begin{bmatrix} X & 0 & 0 \\ 0 & Y & 0 \\ 0 & 0 & Z \end{bmatrix} \tag{7.11}$$

and

$$X = e^{jk_x\Delta x} \qquad Y = e^{jk_y\Delta y} \qquad Z = e^{jk_z\Delta z}$$

$\mathbf{P}_1^*$ stands for the Hermitian transpose of $\mathbf{P}_1$ [64].

Solutions to the general dispersion relation (7.4) applied to the basic 12-port node can be found by finding eigenvalues $\lambda_i = \exp(j\theta_i) = \exp(j\omega_i\Delta t)$ of the matrix $\mathbf{PS}$

which is of order 12×12. The eigenvalue equation (7.4) can be written in the form:

$$\mathbf{PS}\vec{X}_i = \lambda_i \vec{X}_i \tag{7.12}$$

Using the partitioned forms of the matrix $\mathbf{S}$ given by (7.6) and the matrix $\mathbf{P}$ given by (7.9) and by partitioning the eigenvector $\vec{X}_i = [\mathbf{X}_{1i}\mathbf{X}_{2i}]^T$ we can write (7.12) in the form:

$$\begin{bmatrix} \mathbf{0}^{(6\times6)} & \mathbf{P}_0\mathbf{S}_0 \\ \mathbf{P}_0\mathbf{S}_0^T & \mathbf{0}^{(6\times6)} \end{bmatrix} \begin{bmatrix} \mathbf{X}_{1i} \\ \mathbf{X}_{2i} \end{bmatrix} = \lambda_i \begin{bmatrix} \mathbf{X}_{1i} \\ \mathbf{X}_{2i} \end{bmatrix} \tag{7.13}$$

which leads to a system of two matrix equations:

$$\mathbf{P}_0\mathbf{S}_0\vec{X}_{2i} = \lambda_i \vec{X}_{1i} \tag{7.14}$$

$$\mathbf{P}_0\mathbf{S}_0^T\vec{X}_{1i} = \lambda_i \vec{X}_{2i} \tag{7.15}$$

Combining these two equations by eliminating $\vec{X}_{2i}$ we obtain:

$$\mathbf{P}_0\mathbf{S}_0\mathbf{P}_0\mathbf{S}_0^T\vec{X}_{1i} = (\lambda_i)^2\vec{X}_{1i} \tag{7.16}$$

This equation has the form of an eigenvalue equation for a 6×6 matrix given by $\mathbf{S}' = \mathbf{P}_0\mathbf{S}_0\mathbf{P}_0\mathbf{S}_0^T$ with eigenvectors $\vec{X}_{1i}$ and eigenvalues $\psi_i = (\lambda_i)^2 = \exp(j2\theta_i)$, thus requiring:

$$\det(\mathbf{S}' - \psi_i\mathbf{I}) = 0 \tag{7.17}$$

Therefore, by solving the eigenvalue equation (7.17) of 6th order for ψ_i we can obtain the eigenvalues λ_i of the 12×12 matrix $\mathbf{PS}$ as $\lambda_i = \pm\sqrt{\psi_i}$.

Having reduced the size of the eigenvalue problem (7.4) involving 12×12 matrices to the equivalent one (7.17) with 6×6 matrices, its analytical solution is relatively simple. The six eigenvalues ψ_i of the matrix $\mathbf{S}'$ can be found from (7.17) as:

$$\psi_1 = \psi_2 = 1 \tag{7.18}$$

$$\psi_3 = \psi_4 = C_1 + \sqrt{C_1^2 - 1} \tag{7.19}$$

$$\psi_5 = \psi_6 = C_1 - \sqrt{C_1^2 - 1} \tag{7.20}$$

where

$$C_1 = \frac{\cos(\chi)\cos(\eta) + \cos(\eta)\cos(\xi) + \cos(\xi)\cos(\chi) - 1}{2} \tag{7.21}$$

with $\chi = k_x\Delta l$, $\eta = k_y\Delta l$ and $\xi = k_z\Delta l$. Note that the calculations were performed for a uniform mesh ($\Delta x = \Delta y = \Delta z = \Delta l$).

From (7.18) we can calculate four eigenvalues $\lambda_{1,2} = 1$ and $\lambda_{3,4} = -1$. Since $\lambda = 1$ implies $\omega = 0$ and $\lambda = -1$ implies $\omega\Delta t = \pi$, the eigenvalues $\lambda_{1,2}$ correspond to

the electrostatic and magnetostatic solutions, whereas $\lambda_{3,4}$ correspond to unphysical solutions oscillating with the frequency $f = 1/(2\Delta t)$ [62]. It can be readily confirmed that $\psi_3 = \psi_5^{-1}$, hence expressions (7.19) and (7.20) represent solutions for waves propagating in positive and negative directions, respectively.

Grouping the reciprocal solutions as:

$$\psi_3 + \psi_5 = e^{j2\theta} + e^{-j2\theta} = 2\cos(2\theta)$$

we obtain from (7.19) and (7.20):

$$2\cos(2\theta) = 2C_1$$

which after using the indentity:

$$cos(2\theta) = 2\cos^2(\theta) - 1$$

and substituting for C_1 and θ gives:

$$4\cos^2(\omega\Delta t) = \cos(\chi)\cos(\eta) + \cos(\eta)\cos(\xi) + \cos(\xi)\cos(\chi) + 1 \tag{7.22}$$

This formula has also been derived in [62].

7.3.2 Analysis of solutions

The dispersion relation (7.22) can be now compared to the dispersion relation of Maxwell's equations given by (7.1). By applying the approximation $\cos(x) \approx 1 - x^2/2$ for small arguments in the case when the temporal frequency approaches zero, i.e. $\omega \to 0$, and for small wave numbers $k \to 0$, the dispersion relation (7.22) yields:

$$\left(\frac{2\omega\Delta t}{\Delta l}\right)^2 = k_x^2 + k_y^2 + k_z^2 \tag{7.23}$$

which is equivalent to the dispersion relation (7.1) of a wave equation with propagation velocity $v = \Delta l/(2\Delta t)$.

Dispersion relation (7.22) has other solutions which do not correspond to the linear dispersion relation of Maxwell's equations. The ambiguity arises from the fact that cosines factors in (7.22) always appear in products and therefore, using the identity $\cos(\pi \pm x) = -\cos(x)$, it follows that:

$$\cos^2(\omega\Delta t) = \cos^2(\pi \pm \omega\Delta t) \tag{7.24}$$

or, for example,

$$\cos(\chi)\cos(\eta) = \cos(\pi \pm \chi)\cos(\pi \pm \eta) \tag{7.25}$$

This shows that every solution to (7.22) which is valid for a particular ω and a wave vector (k_x, k_y, k_z) will also be valid for frequencies $\pi/\Delta t \pm \omega$ and wave vectors $(\pi/\Delta l \pm k_x, \pi/\Delta l \pm k_y, \pi/\Delta l \pm k_z)$. Using (7.24) it can be seen that for every low-frequency solution $(0 \leq \omega\Delta t \leq \pi/2)$ obtained from (7.22) as:

$$\omega\Delta t = \arccos\left(\frac{1}{2}\sqrt{\cos(\chi)\cos(\eta) + \cos(\eta)\cos(\xi) + \cos(\xi)\cos(\chi) + 1}\right) \tag{7.26}$$

there exists another high-frequency solution $(\pi/2 \leq \omega\Delta t \leq \pi)$ given by:

$$\omega\Delta t = \pi - \arccos\left(\frac{1}{2}\sqrt{\cos(\chi)\cos(\eta) + \cos(\eta)\cos(\xi) + \cos(\xi)\cos(\chi) + 1}\right) \tag{7.27}$$

Furthermore, by taking into account (7.25) it follows that for each of the two solutions (7.26) and (7.27) corresponding to, say, low wave numbers (k_x, k_y, k_z), there are solutions in identical form but corresponding to high wave numbers $(\pi/\Delta l \pm k_x, \pi/\Delta l \pm k_y, \pi/\Delta l \pm k_z)$, as originally found by Nielsen [54].

The low-frequency solutions (7.26) with low wave numbers (k_x, k_y, k_z) are physical propagating solution corresponding to Maxwell's equations. The high-frequency solutions (7.27) with both low and high wave numbers are referred to as unphysical solutions (after Krumpholz [66]) or high-frequency spurious solution (after Nielsen and Hoefer [40]) and can be easily suppressed by temporal low-pass filtering or using an excitation with a frequency spectrum sufficiently below $\omega = \pi/\Delta t$.

The most troublesome spurious solutions are those given by (7.26) corresponding to high wave numbers. When $\omega \to 0$, these solutions have an identical dispersion relation to the physical solutions, given by (7.23). The modes with high spatial frequency (that is with high wave numbers) are not easily excited, but they can sometimes occur, for example, generated by an isolated source. Instead of normally being attenuated quickly with distance away from the source, these modes can in a TLM simulation be represented by spurious solutions and propagate without loss with the same speed as physical ones [40, 54]. These spurious modes cannot easily be suppressed, although some investigations into their suppression have been recently reported [67, 68, 69].

Perhaps the best way to illustrate different solutions to the dispersion relation of the SCN is to plot the dispersion diagrams for the propagation along the main space diagonal, that is for $k_x = k_y = k_z$. In this case, assuming the velocity of propagation $v = \Delta l/(2\Delta t)$, the linear dispersion relation (7.1) becomes:

$$\omega = \frac{\Delta l}{2\Delta t}\, k_x\sqrt{3}$$

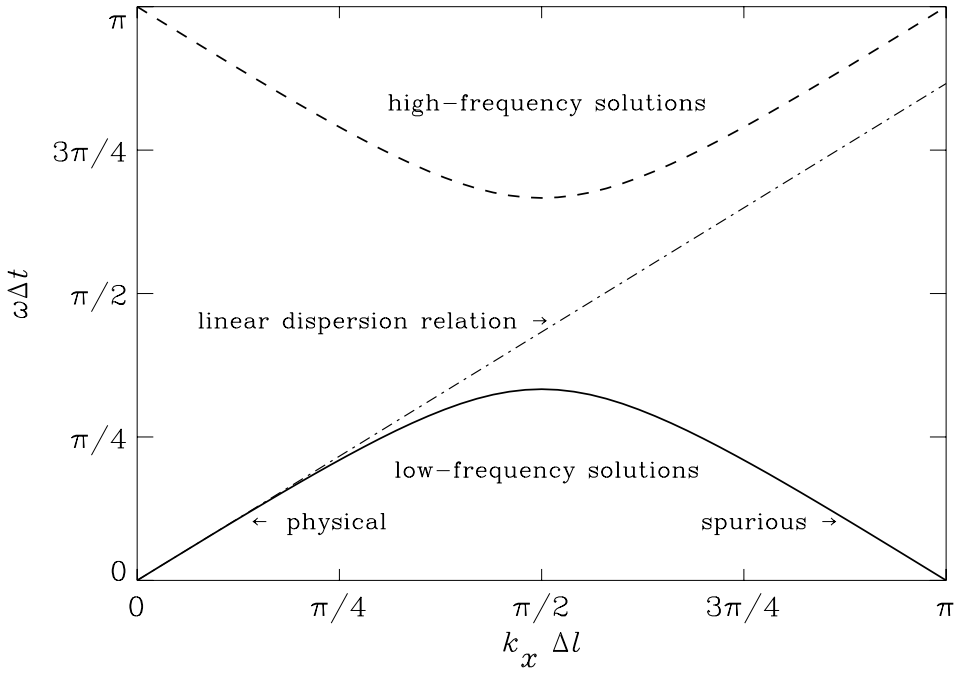

Figure 7.1 *Propagating solutions of the SCN dispersion relation compared to the solution of linear dispersion relation for* $k_x = k_y = k_z$

while the SCN dispersion relation (7.22) yields:

$$4\cos^2(\omega\Delta t) = 3\cos^2(k_x\Delta l) + 1$$

Figure 7.1 show solutions to the linear dispersion relation and the SCN dispersion relation in this case. The high-frequency solutions for the SCN dispersion relation, plotted using a broken line in Figure 7.1, complement low-frequency solutions plotted using a solid line. Only the low frequency solutions with low wave numbers (that is $k_x\Delta l < \pi/2$) follows the linear dispersion relation and they correspond to physical propagating modes of a TLM mesh. The low-frequency solutions with high wave numbers, appearing on the bottom right-hand corner of the plot, represent spurious (parasitic) propagating modes of a TLM mesh [55]. By applying a low-pass temporal filter well below $\omega = \pi/\Delta t$, the high frequency spurious solutions can be eliminated, but low-frequency modes with high wave numbers (around $k_x = \pi/\Delta l$) will, if excited, propagate together with physical modes, as can be seen from Figure 7.1.

The low-frequency spurious solutions also appear for directions of propagation different from the main space diagonal. Figure 7.2 shows solutions to the linear

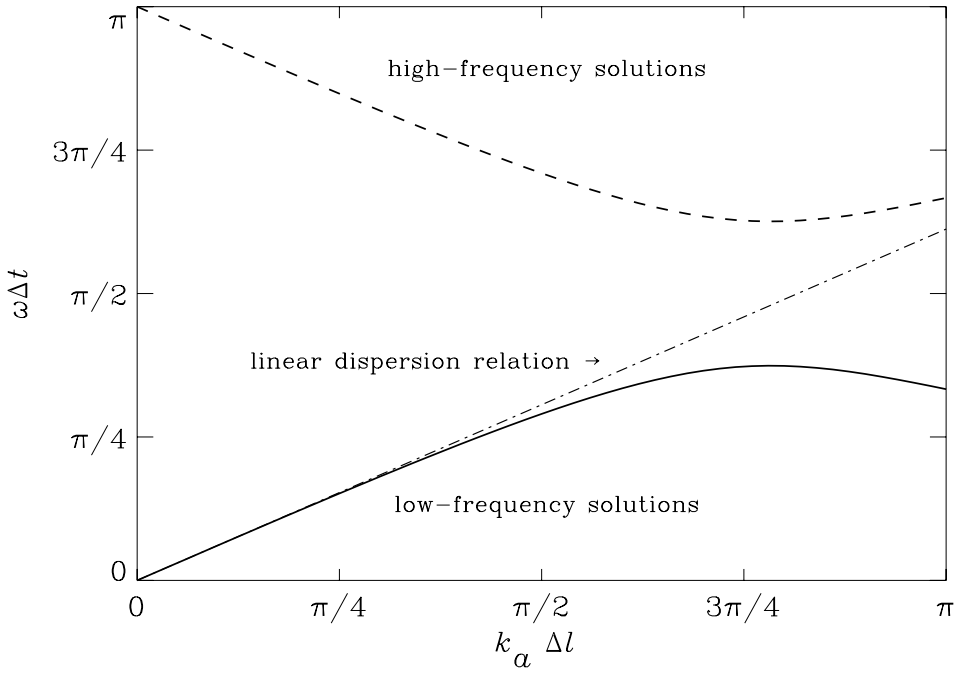

Figure 7.2 *Propagating solutions of the SCN dispersion relation for wave vectors* $(k_a,\ \frac{k_a}{2},\ \frac{k_a}{2})$ *or wave vectors* $(\frac{\pi}{\Delta l} - k_a,\ \frac{\pi}{\Delta l} - \frac{k_a}{2},\ \frac{\pi}{\Delta l} - \frac{k_a}{2})$

dispersion relation and the SCN dispersion relation for propagation with either a wave vector $(k_a, k_a/2, k_a/2)$ or a wave vector $(\pi/\Delta l - k_a, \pi/\Delta l - k_a/2, \pi/\Delta l - k_a/2)$. Both the wave vectors, with low and high wave numbers, have the same dispersion relation and contribute to the identical low- and high-frequency propagation solutions, leading therefore to the appearance of low-frequency spurious solutions with high wave numbers.

It should be noted that the propagation velocities of both low and high frequency solutions when $\vec{k}$ approaches $(0, 0, 0)$ or $(\pi/\Delta l, \pi/\Delta l, \pi/\Delta l)$ have identical absolute values. This can be seen from Figure 7.1, for example, by observing the gradients of curves approaching corners of the plot. This can be also derived analytically from the SCN dispersion relation (7.22) using differential calculus. By expressing the Cartesian components of $\vec{k}$ through a parameter r, such that $k \to 0$ when $r \to 0$, i.e.

$$k_x = \hat{k}_x r \qquad k_y = \hat{k}_y r \qquad k_z = \hat{k}_z r$$

and differentiating low- and high-frequency solutions given by equations (7.26) and (7.27), the propagation velocity for wave vectors approaching zero can be

derived as:

$$v = \lim_{k\to 0} \frac{\partial \omega}{\partial k} = \lim_{r\to 0} \frac{\partial \omega}{\partial r}\frac{\partial r}{\partial k} = \pm\frac{\Delta l}{2\Delta t}$$

where the upper and lower sign apply to solutions (7.26) and (7.27) respectively. Also, since the propagating modes with high wave numbers have dispersion relations identical to the corresponding physical modes with low wave numbers, due to the identity (7.25), it follows that physical and spurious modes propagate with the same velocity (in absolute value).

The accuracy of the TLM scheme with the SCN, for physical propagating modes, can be roughly estimated from, for example, Figure 7.1, where it can be seen that the discrepancy between the linear dispersion relation and the SCN dispersion relation is almost indistinguishable for $k_x\Delta l < \pi/4$ which is equivalent to $\Delta l/\lambda = \sqrt{3}/8 \approx 0.21$, i.e. for a discretization of five nodes per wavelength. It should be pointed out that for axial propagation, for example when $k_y = k_z = 0$ and $k_x = k$, the dispersion relation (7.22) simplifies to:

$$\cos^2(\omega\Delta t) = \cos^2\left(\frac{k\Delta l}{2}\right) \tag{7.28}$$

which means that in this case physical modes propagate with velocity $\Delta l/(2\Delta t)$ at all frequencies, hence without dispersion, as noticed by Johns [9]. A more detailed quantitative analysis of numerical dispersion and the accuracy of different condensed node schemes will be presented in Chapter 8.

7.4 Analytical expansion of the general dispersion relation

The new numbering scheme introduced in the previous section allowed the reduction of the eigenvalue problem in the 12-port SCN. This approach, however, cannot be used for the algebraic derivation of dispersion relations for other available condensed nodes, as an appropriate partitioning of the full GSCN matrix cannot be achieved successfully. We therefore resort to a new methodology, which is explained in this section.

7.4.1 Basic concepts

The general TLM dispersion relation (7.4) can be solved as an eigenvalue problem. The left-hand side of (7.4) represents the characteristic polynomial of the matrix **PS**, where $\lambda = \exp(j\theta)$ are its characteristic values (or eigenvalues). By formulating this N-th order polynomial in a normal form with coefficients $C_{i,\, i=1\ldots N}$, we

can write (7.4) as:

$$\mathcal{P}^{(N)}(\lambda) = \lambda^N + \sum_{i=1}^{N} C_i \lambda^{N-i} = 0 \tag{7.29}$$

where N is equal to the number of node ports.

The analytical expansion of the general dispersion relation (7.4) can be accomplished by finding the N coefficients $C_{i,\ i=1\ldots N}$ of the characteristic polynomial $\mathcal{P}^{(N)}(\lambda)$. In a general case, analytical determination of the coefficients of a characteristic polynomial of a matrix of high order (e.g. $N = 12, 15, 18$) is a lengthy algebraic process, which requires matrix diagonalization.

However, the size of the problem can be reduced if some of the roots of the characteristic polynomial are known *a priori*. For example, in the derivation of the dispersion relation for the 12-port SCN, performed in previous section and in [62], it was found that two of the eigenvalues are $\lambda = 1$ and two are $\lambda = -1$, representing respectively, non-propagating static solutions and solutions oscillating at a high frequency. It was also found that propagating eigenvectors of the SCN are repeated twice (degenerate solutions).

For a general symmetrical condensed node, assuming the presence of h non-propagating solutions, l high-frequency oscillating solutions and r possible degeneracies of propagating solutions, equation (7.29) can be written as:

$$\mathcal{P}^{(N)}(\lambda) = (\lambda - 1)^h (\lambda + 1)^l (\mathcal{Q}^{(n)}(\lambda))^r = 0 \tag{7.30}$$

where $n = (N - h - l)/r$, the order of the polynomial $\mathcal{Q}^{(n)}(\lambda)$.

Roots of the polynomial $\mathcal{Q}^{(n)}(\lambda)$ are also roots of $\mathcal{P}^{(N)}(\lambda)$ and they describe the propagation solutions to the dispersion relation (7.30). Equation (7.30) can be simplified to:

$$\mathcal{Q}^{(n)}(\lambda) = \lambda^n + \sum_{i=1}^{n} B_i \lambda^{n-i} = 0 \tag{7.31}$$

where $B_{i,\ i=1\ldots n}$ are coefficients to be determined.

In the previous section it was shown that propagation solutions appear in reciprocal pairs (λ, λ^{-1}). This is due to symmetry, as they correspond to eigenvectors describing wave propagation in positive and negative directions. As a result of this, it follows that the order of $\mathcal{Q}^{(n)}(\lambda)$, n, is an even number and it can be easily shown that the coefficients of $\mathcal{Q}^{(n)}(\lambda)$ must be symmetrical, i.e. $B_i = B_{n-i}$ and B_n=1. Therefore, only $m = n/2$ coefficients B_i need to be determined to completely describe the dispersion relation (7.31).

Dividing equation (7.31) by $2\lambda^m$ (where $m = n/2$), and substituting $B_n = 1$, $B_{n-i} = B_i$ and $\lambda^i + \lambda^{-i} = 2\cos(i\theta)$ for $i = 1...m$ (note that $\lambda = e^{j\theta}$), it simplifies to:

$$\cos(m\theta) + \sum_{i=1}^{m-1} B_i \cos\left[(m-i)\theta\right] + \frac{B_m}{2} = 0 \tag{7.32}$$

Expression (7.32) is a general algebraic form of the dispersion relation for propagating solutions. By raising the polynomial $\mathcal{Q}^{(n)}(\lambda)$ to the power of r and multiplying by $(\lambda-1)^h(\lambda+1)^l$, the coefficients B_i can be related to the coefficients C_i of the polynomial $\mathcal{P}^{(N)}(\lambda)$. Since only m coefficients B_i are unknown, it is sufficient to obtain the first m coefficients C_i of the characteristic polynomial $\mathcal{P}^{(N)}(\lambda)$ to derive the dispersion relation (7.32).

A conventional method for obtaining coefficients of the characteristic polynomial consists of matrix diagonalization using Gaussian elimination or a similar technique. Using this method, all coefficients of the characteristic polynomial are computed simultaneously and we cannot derive only the first m coefficients, hence we cannot benefit from our *a priori* knowledge on the structure of the characteristic polynomial. Therefore, a method which allows separate computation of the coefficients should be used.

An efficient method for the computation of leading coefficients of the characteristic polynomial is the method of Faddeev [70]. Here, the coefficients C_i are simply obtained by computing sums of diagonal elements of appropriate matrices and using an iterative procedure consisting of matrix additions and multiplications [70]. The algorithm can be described in a pseudo-code as:

Algorithm 1 (Faddeev Method)

$\mathbf{A} := \mathbf{PS}$;
for $i := 1$ **to** N
begin
  $C_i := -(\sum_{j=1}^{N} \mathbf{A}_{j,j})/i$;
  $\mathbf{A} := \mathbf{PS}\,(\mathbf{A} + C_i\mathbf{I})$
end;

This method has the advantage over conventional diagonalization methods that it can be terminated when the desired number of coefficients is computed. As

indicated before, only m iterations are needed to obtain the coefficients needed for the relation (7.32).

In order to establish the relationships between the coefficients B_i of the polynomial $\mathcal{Q}^{(n)}(\lambda)$ and the coefficients C_i of the polynomial $\mathcal{P}^{(N)}(\lambda)$, parameters h, l, r and n, appearing in (7.30), must be known. A particular case can be considered, by setting fixed, arbitrary numerical values for the propagation vector components k_x, k_y, k_z, material properties and node spacings, so as to obtain numerical matrices $\mathbf{P}$ and $\mathbf{S}$. Then, numerical values for all (N) coefficients C_i can be obtained using for example, the Faddeev method. After obtaining the coefficients of $\mathcal{P}^{(N)}(\lambda)$ for this particular case, the roots can be found numerically and solutions of the form $\lambda = \pm 1$ and possible degeneracies can be identified.

The complete procedure of an analytical expansion of the general TLM dispersion relation is demonstrated for the example of the 12-port SCN. Using fixed numerical values for k_x, k_y, k_z and Δl, we find two solutions $\lambda = 1$, two solutions $\lambda = -1$ and that all remaining numerical solutions are degenerate. Therefore $h = 2$, $l = 2$, $r = 2$ and $n = (12 - h - l)/r = 4$ and we write (7.30) as:

$$\mathcal{P}^{(12)}(\lambda) = (\lambda - 1)^2(\lambda + 1)^2(\mathcal{Q}^{(4)}(\lambda))^2 = 0 \tag{7.33}$$

Since $m = n/2 = 2$, only the first two coefficients of the polynomial $\mathcal{P}^{(12)}(\lambda)$ need to be calculated. Using the Faddeev method, now applied to the matrices $\mathbf{P}$ and $\mathbf{S}$ in analytical forms, coefficients C_1 and C_2 are obtained as

$$C_1 = 0 \qquad C_2 = -2\Sigma \tag{7.34}$$

where

$$\Sigma = \cos(\chi)\cos(\eta) + \cos(\eta)\cos(\xi) + \cos(\xi)\cos(\chi) \tag{7.35}$$

with $\chi = k_x\Delta l$, $\eta = k_y\Delta l$ and $\xi = k_z\Delta l$. Relationships between C_1, C_2 and B_1, B_2 are found by expanding $\mathcal{P}^{(12)}(\lambda)$ from equation (7.33):

$$C_1 = 2B_1 \qquad C_2 = B_1^2 + 2B_2 - 2 \tag{7.36}$$

which leads to

$$B_1 = 0 \qquad B_2 = 1 - \Sigma$$

By inserting B_1, B_2 and $m = 2$ into (7.32) and expanding cosines of multiple angles the dispersion relation for the SCN is obtained as:

$$\cos^2(\theta) = \frac{\Sigma + 1}{4} \tag{7.37}$$

which is identical to the relation (7.22) derived in the previous section.

This procedure can also be applied to derive the dispersion relation for other nodes. Parameters h, l, r, n of the characteristic polynomial in equation (7.30) and hence the required number of coefficients, m, differ in each case. These parameters have been obtained for presently available nodes and are shown in Table 7.2. Note that the analysis of the stub-loaded SCN is separated into three different cases.

Node	Case	N	h	l	r	n	m
SCN	—	12	2	2	2	4	2
SSCN	all	12	2	2	2	4	2
HSCN	all	15	2	3	1	10	5
Stub-loaded SCN	1	15	2	3	1	10	5
	2	18	2	0	2	8	4
	3	18	2	0	1	16	8

Case 1: uniform mesh: $\varepsilon_r > 1$, $\mu_r = 1$ or $\mu_r > 1$, $\varepsilon_r = 1$
Case 2: uniform or graded mesh: $\varepsilon_r = \mu_r$
Case 3: uniform or graded mesh: $\varepsilon_r \neq \mu_r$.

Table 7.2 *Parameters of the characteristic polynomial*

It can be seen from Table 7.2 that the structure of the characteristic polynomial for the SSCN is the same as for the SCN, thus requiring only two coefficients to be determined. The most demanding is the analysis of the stub-loaded SCN in a general case (Case 3). It should be pointed out that in all nodes for all cases $h = 2$, i.e. the two non-propagating solutions $\lambda = 1$, corresponding to the electrostatic and magnetostatic case, always exist. Also, the propagation solutions are degenerate ($r = 2$) in the SCN, the SSCN and the stub-loaded SCN in Case 2, which greatly reduces the required number of coefficients in these cases.

The analytical expansion of the general dispersion relation (7.4) will be applied in the following subsections to these different condensed nodes modelling isotropic media on a uniform and a graded mesh. The methodology described above and the parameters in Table 7.2 will be used.

7.4.2 Symmetrical super-condensed node

It can be seen from Table 7.2 that the parameters of the characteristic polynomial for the SSCN are the same as for the 12-port SCN. Hence, the relationships between B_1, B_2 and C_1, C_2 are given by equation (7.36). Here, separate analyses are performed for uniform and graded meshes, modelling isotropic media with arbitrary ε_r, μ_r.

The scattering matrix for the isotropic lossless SSCN is derived from the GSCN scattering matrix (shown in Figure 3.5) by eliminating row/columns $13 \ldots 24$ and setting $Y_{oj} = Z_{sk} = G_{ej} = R_{mk} = 0$ in equations (3.45)–(3.48). The top 12×12 submatrix $\mathbf{S}_{ln}$ defined by equation (3.49) becomes the scattering matrix of the SSCN. The scattering coefficients of this matrix can be found from expressions (3.42)–(3.48) and are:

$$\begin{aligned} a_{ij} &= 1 - b_{ij} - d_{ij} & b_{ij} &= \hat{C}_{kj} \\ c_{ij} &= d_{ij} - b_{ij} & d_{ij} &= \hat{L}_{ij} = \hat{C}_{ik} \end{aligned} \tag{7.38}$$

where the expressions for normalized capacitances $\hat{C}_{ij}$ can be found in § 5.2.1.

Using the properties of the SSCN for the uniform mesh, derived in § 5.2.3, namely $C_{xy} = C_{yz} = C_{zx} = C_p = 1 - C_n$ and $C_{xz} = C_{yx} = C_{zy} = C_n$, the scattering coefficients (7.38) can be expressed in this case through a single parameter q as:

$$\begin{aligned} a_{p,n} &= \pm(1 - 2q) & b_p &= d_p = q \\ c_{p,n} &= 0 & b_n &= d_n = 1 - q \end{aligned} \tag{7.39}$$

where

$$q = C_n = \frac{1 \mp \sqrt{1 - \dfrac{1}{\varepsilon_r \mu_r}}}{2} \tag{7.40}$$

The first and second subscripts in (7.39) correspond to the upper and lower sign, respectively. Subscript p corresponds to lines xy, yz and zx, while subscript n corresponds to lines xz, yx and zy. Note from the definition of q given by (7.40) that two sets of coefficients can be chosen. When $\varepsilon_r = \mu_r = 1$, then $q = 1/2$ and the coefficients in (7.39) reduce to those of the basic 12-port SCN, namely $a = c = 0$ and $b = d = 1/2$.

Applying the Faddeev method on the matrix **PS** for the uniform mesh SSCN with node spacing Δl, the leading two coefficients of the characteristic polynomial $\mathcal{P}^{(12)}(\lambda)$ can be obtained as:

$$C_1 = 0 \qquad C_2 = 8(q - q^2)(3 - \Sigma) - 6$$

where Σ is defined in the previous subsection by (7.35). Using the relationships (7.36) the coefficients required for the dispersion relation are obtained as:

$$B_1 = 0 \qquad B_2 = 4(q - q^2)(3 - \Sigma) - 2 \tag{7.41}$$

It can be readily shown from (7.40) that

$$4(q - q^2) = \frac{1}{\varepsilon_r \mu_r}$$

which is independent of the sign chosen for the definition of q in (7.40). By inserting B_1, B_2 and $m = 2$ into (7.32), taking into account the above expression, then substituting Σ from (7.35) and applying simple manipulations with basic trigonometric identities, the dispersion relation for the SSCN (uniform mesh) can be derived as:

$$4\varepsilon_r \mu_r \sin^2(\omega \Delta t) = 3 - \cos(\chi)\cos(\eta) - \cos(\eta)\cos(\xi) - \cos(\xi)\cos(\chi) \tag{7.42}$$

The dispersion relation for the SSCN is therefore dependent on the material properties ε_r, μ_r but not on the sign chosen in the definitions of the SSCN's scattering parameters (eqn. 7.40). For the special case $\varepsilon_r = \mu_r = 1$ equation (7.42) simplifies to the dispersion relation for the 12-port node (7.37) obtained earlier.

By approximating cosine and sine terms in (7.42) for small ω and small $\vec{k}$ using $\sin(x) \approx x$ and $\cos(x) \approx 1 - x^2/2$, we derive

$$\left(\frac{2\sqrt{\varepsilon_r \mu_r}\omega \Delta t}{\Delta l} \right)^2 = k_x^2 + k_y^2 + k_z^2 \tag{7.43}$$

which is equivalent to the dispersion relation (7.1) of a wave equation with propagation velocity $v = \Delta l / (2\sqrt{\varepsilon_r \mu_r}\Delta t)$.

Similarly as in the case of the dispersion relation of the SCN, there are different combinations of solutions with low/high temporal frequencies (ω) and low/high wave numbers (k). It follows from (7.42), since $\sin^2(\omega \Delta t) = \sin^2(\pi - \omega \Delta t)$ and, for example, $\cos(\chi)\cos(\eta) = \cos(\pi - \chi)\cos(\pi - \eta)$, that for any given temporal frequency ω, propagation vectors (k_x, k_y, k_z) which satisfy the dispersion relation (7.42) are complemented by propagation vectors $(\pi/\Delta l - k_x, \pi/\Delta l - k_y, \pi/\Delta l - k_z)$, as discussed earlier.

Figure 7.3 shows the propagating solutions of the dispersion relation (7.42) for $\varepsilon_r \mu_r = 2$ and the linear dispersion relation for the velocity of $v = \Delta l / (2\sqrt{\varepsilon_r \mu_r}\Delta t)$ and propagation direction determined by $k_x = k_y = k_z$. Unphysical high-frequency

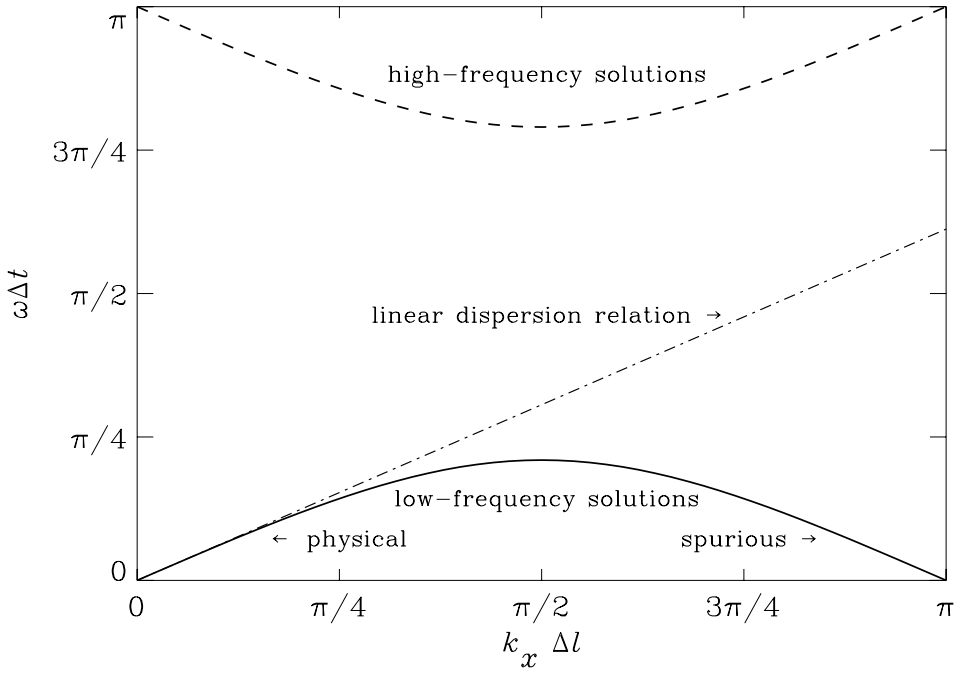

Figure 7.3 *Propagating solutions of the SSCN dispersion relation for uniform mesh and* $\varepsilon_r\mu_r = 2$ *(*$k_x = k_y = k_z$*)*

and spurious low-frequency solutions can be identified as in the case for the SCN depicted earlier in Figure 7.1. The velocities of physical and unphysical solutions are identical, since by using the same procedure described earlier for the SCN, it can be shown from (7.42) that:

$$|v| = \left|\lim_{k\to 0}\frac{\partial\omega}{\partial k}\right| = \frac{\Delta l}{2\sqrt{\varepsilon_r\mu_r}\Delta t}$$

When using the SSCN on a graded mesh, the scattering matrix can be expressed in terms of three normalized capacitances, for example $\hat{C}_{xz}$, $\hat{C}_{yx}$ and $\hat{C}_{zy}$, as the remaining three can be found using $\hat{C}_{ij} = 1 - \hat{C}_{kj}$. Scattering coefficients are described by (7.38) whereas definitions for normalized capacitances can be found in § 5.2.1.

Using the Faddeev method to compute C_1 and C_2 and by applying relationships (7.36) we obtain:

$$\begin{aligned} B_1 &= 2\left[\cos(\chi)(q_y - q_z) + \cos(\eta)(q_z - q_x) + \cos(\xi)(q_x - q_y)\right] \\ B_2 &= 4\left[s_x(\cos(\eta)\cos(\xi) - 1) + s_y(\cos(\xi)\cos(\chi) - 1)\right. \\ &\quad \left. + s_z(\cos(\chi)\cos(\eta) - 1)\right] - 2 \end{aligned} \tag{7.44}$$

where

$$s_i = s_0 - 2q_jq_k - q_i \qquad (i,j,k) \in \{(x,y,z),(y,z,x),(z,x,y)\}$$

with

$$s_0 = q_xq_y + q_yq_z + q_zq_x$$

and $q_x = \hat{C}_{yx}$, $q_y = \hat{C}_{zy}$ and $q_z = \hat{C}_{xz}$. Note that now $\chi = k_x\Delta x$, $\eta = k_y\Delta y$ and $\xi = k_z\Delta z$.

Subsequently, the dispersion relation for the SSCN (graded mesh) is written as:

$$\cos(2\theta) + B_1\cos(\theta) + \frac{B_2}{2} = 0 \tag{7.45}$$

where B_1 and B_2 are defined by (7.44). In the special case when $\Delta x = \Delta y = \Delta z = \Delta l$ it follows that $q_x = q_y = q_z = q$, the coefficients B_1 and B_2 simplify to those obtained for the uniform mesh given by (7.41) and the dispersion relation (7.45) becomes equivalent to the relation (7.42).

It should be pointed out that two sets of the link line parameters of the graded SSCN are possible, except when it operates on its maximum time-step (see §5.2.1 and §5.2.2) and each of them contributes to different coefficients B_1 and B_2 appearing in the dispersion relation (7.45). By approximating cosine factors in (7.45) for small ω and small $\vec{k}$ using $\cos(x) \approx 1 - x^2/2$, both sets of SSCN parameters yield:

$$\left(\frac{2\omega\Delta t}{\Delta l}\right)^2 = k_x^2 + k_y^2 + k_z^2 \tag{7.46}$$

Taking into account that the equivalent cubic cell parameter Δl used in the derivation of the SSCN was defined by $\Delta l = 2\Delta t/\sqrt{\varepsilon\mu}$, equation (7.46) becomes identical to the linear dispersion relation (7.1) with a propagation velocity $v = 1/\sqrt{\varepsilon\mu}$, thus confirming the validity of the graded SSCN for modelling an isotropic medium.

By expanding multiple angles and solving for $\cos(\omega\Delta t)$, two solutions of (7.45), corresponding to low and high frequencies, respectively ω_1 and ω_2, are obtained as:

$$\cos(\omega_1\Delta t) = \frac{-B_1 + \sqrt{B_1^2 - 4B_2 + 8}}{4} \tag{7.47}$$

$$\cos(\omega_2\Delta t) = \frac{-B_1 - \sqrt{B_1^2 - 4B_2 + 8}}{4} \tag{7.48}$$

The two solutions are illustrated in Figure 7.4 for the case when $\Delta x = \Delta y = 2\Delta z$, for the maximum time step and for wave vectors with $k_x = k_y = k_z$. It can be seen

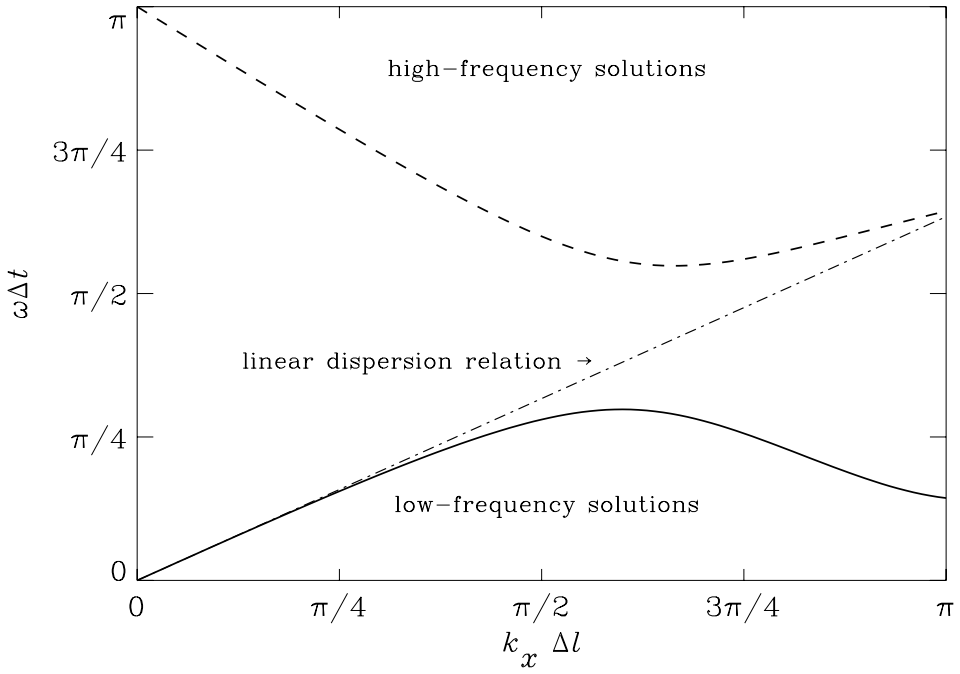

Figure 7.4 *Propagating solutions of the SSCN dispersion relation for graded mesh with* $\Delta x = \Delta y = 2\Delta z$ *and* $k_x = k_y = k_z$

that the gradients of the low and high frequency dispersion characteristics of the graded SSCN are different, i.e. the physical and unphysical modes have different velocities. This can be also confirmed analytically, by finding the derivatives of the two solutions when $k \to 0$. It follows from (7.47) that:

$$v = \lim_{k \to 0} \frac{\partial \omega_1}{\partial k} = \frac{\Delta l}{2\Delta t} \tag{7.49}$$

but a similar procedure for obtaining the propagation velocity for solutions corresponding to ω_2 given by (7.48) does not yield a simple expression in the general case.

Investigating the form of the dispersion relation (7.45) it can be seen that the existence of the term $B_1 \cos(\omega \Delta t)$ disallows, in the general case, the appearance of complementary x and $\pi - x$ solution pairs found in the SCN and the SSCN for the uniform mesh. This means that propagation modes given by low wave numbers (k_x, k_y, k_z) will not have identical dispersion properties as modes with high wave numbers $(\pi/\Delta x - k_x, \pi/\Delta y - k_y, \pi/\Delta z - k_z)$.

However, propagating modes with low frequencies and high wave numbers exist. Analysing temporal and spatial cosine factors in the dispersion relation (7.45) it

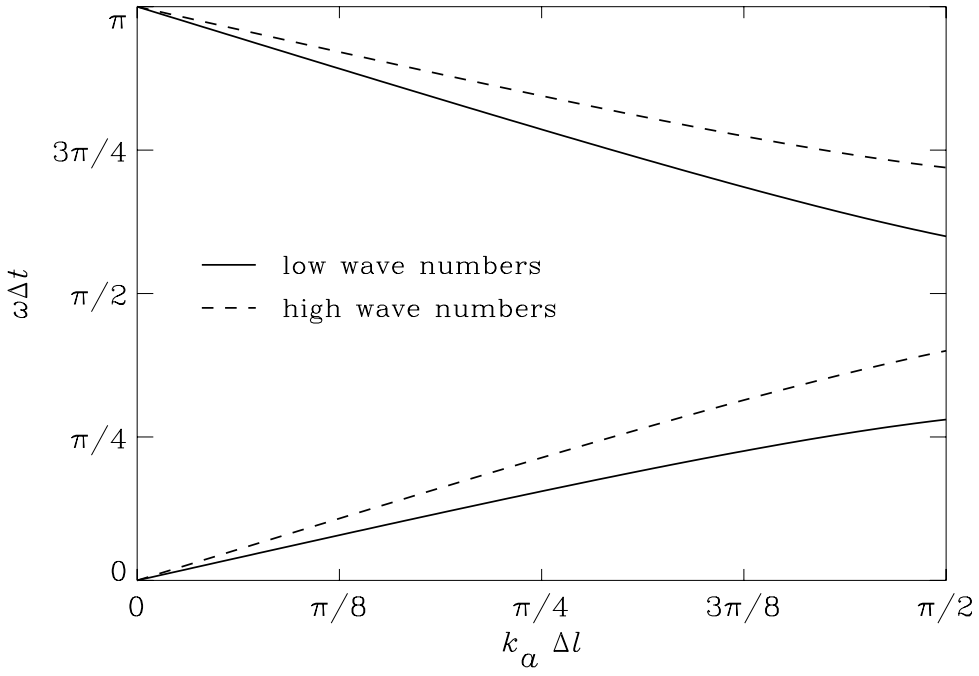

Figure 7.5 *Solutions of the SSCN dispersion relation for graded mesh with* $\Delta x = \Delta y = 2\Delta z$ *for low wave numbers* (k_a, k_a, k_a) *and high wave numbers* $(\pi/\Delta x - k_a,\ \pi/\Delta y - k_a,\ \pi/\Delta z - k_a)$

can be shown, using, for example, the indentity

$$\cos(\pi - \omega\Delta t)\cos(\chi) = \cos(\omega\Delta t)\cos(\pi \pm \chi) \tag{7.50}$$

and identities given by (7.24) and (7.25), that if the dispersion relation has solutions for a high frequency $\pi/\Delta t - \omega$ and low wave numbers (k_x, k_y, k_z) it will have identical solution for a low frequency ω and high wave numbers $(\pi/\Delta x \pm k_x, \pi/\Delta y \pm k_y, \pi/\Delta z \pm k_z)$. It is shown by plotting the solutions (7.47) and (7.48) in Figure 7.4, that high frequency solutions for low wave numbers exist. It therefore follows that complementary solutions with low frequency and high wave numbers also exist.

As an example, dispersion characteristics, for propagation along the main space diagonal, for solutions with low wave numbers (k_a, k_a, k_a) and high wave numbers $(\pi/\Delta x - k_a, \pi/\Delta y - k_a, \pi/\Delta z - k_a)$, are shown in Figure 7.5 for a grading set at $\Delta x = \Delta y = 2\Delta z$ and maximum time step. It can be seen that the magnitude of the gradient of the curve corresponding to high frequency and low wave numbers solutions is identical to that corresponding to low frequency and high wave numbers solutions, and vice versa.

A more detailed quantitative analysis of the dispersion relations of the SSCN is presented in Chapter 8.

7.4.3 Hybrid symmetrical condensed node

The analytical expansion of the dispersion relation for the hybrid node (HSCN) is more complex; as can be seen from Table 7.2 no degenerate solutions exist and $m = 5$ coefficients must be determined. Here, separate analyses are performed for uniform and graded meshes, modelling isotropic media with arbitrary ε_r, μ_r. In both cases, the characteristic polynomial has the structure:

$$\mathcal{P}^{(15)}(\lambda) = (\lambda - 1)^2(\lambda + 1)^3\mathcal{Q}^{(10)}(\lambda) \tag{7.51}$$

The relationships between the five leading coefficients B_i of the polynomial $\mathcal{Q}^{(10)}(\lambda)$ and C_i of $\mathcal{P}^{(15)}(\lambda)$ can be found after expanding (7.51) and they are:

$$\begin{aligned} B_1 &= C_1 - 1 \\ B_2 &= C_2 - B_1 + 2 \\ B_3 &= C_3 + 2B_1 - B_2 + 2 \\ B_4 &= C_4 + 2B_1 + 2B_2 - B_3 - 1 \\ B_5 &= C_5 - B_1 + 2B_2 + 2B_3 - B_4 - 1 \end{aligned} \tag{7.52}$$

The scattering matrix for the lossless HSCN can be derived from the GSCN scattering matrix as explained in § 3.3.6. It was shown in [60] that the dispersion characteristics of the Type I HSCN and Type II HSCN are complementary, hence the derivation here will be performed only for the Type I formulation [19].

When using a uniform mesh, the scattering coefficients of the Type I HSCN are found from expressions (3.42)–(3.48) and definitions (2.59)–(2.60) as

$$\begin{aligned} a = c &= \frac{1 - \varepsilon_r\mu_r}{2\varepsilon_r\mu_r} & b = e &= \frac{1}{2\varepsilon_r\mu_r} \\ d &= \frac{1}{2} & g &= \frac{2(\varepsilon_r\mu_r - 1)}{\varepsilon_r\mu_r} \\ h = g - 1 &= \frac{\varepsilon_r\mu_r - 2}{\varepsilon_r\mu_r} \end{aligned} \tag{7.53}$$

It can be seen that the scattering coefficients are functions of the product $\varepsilon_r\mu_r$ and not separate functions of ε_r and μ_r. This result is somewhat surprising, bearing in mind that the definitions of the characteristic admittances of link lines and stubs in the HSCN, given by (2.59) and (2.60), do not contain products $\varepsilon_r\mu_r$. Having the

scattering coefficients formulated in such a manner is desirable since it means that solutions to the dispersion relation will be identical for $\varepsilon_r\mu_r = const$ regardless of the ratio ε_r/μ_r. It is indicated in Table (7.2) that this is not case with the stub-loaded SCN, which will be further discussed in the following subsection.

To facilitate manipulation of the scattering coefficients, it is convenient to remove the variable $\varepsilon_r\mu_r$ appearing in the denominators of the rational expressions in definitions (7.53). By introducing a parameter p defined by

$$p = 1 - \frac{1}{\varepsilon_r\mu_r} \tag{7.54}$$

the scattering coefficients for the cubic HSCN simplify to:

$$\begin{aligned} a = c &= -\frac{p}{2} & b = e &= \frac{1-p}{2} \\ d &= \frac{1}{2} & g &= 2p \\ h &= 2p-1 \end{aligned} \tag{7.55}$$

The five coefficients B_i required for the dispersion relation (7.32) can be computed as before by using the Faddeev method and relationships (7.52) to give:

$$\begin{aligned} B_1 &= 2\,(p\,s_1 + 1) \\ B_2 &= p^2(s_4 + 3s_2) + 2p\,(s_2 + 2s_1) - 2s_2 - 4s_1 - 3 \\ B_3 &= p^3(s_5 + 2s_3) + 2p^2(s_5 + s_4 + 6s_3 + 3s_2) \\ &\quad -2p\,(s_5 + 2s_4 + 6s_3 + 4s_2) - 4\,(s_2 + 2s_1 + 2) \\ B_4 &= 2p^3(3s_7 + s_6 + s_5 + 2s_3) - p^2(4s_7 + s_6 + 2s_5 - 3s_4 - 5s_2) \\ &\quad -2p\,(2s_7 + s_6 + 4s_5 + 4s_4 + 12s_3 + 9s_2 + 2s_1) \\ &\quad +2s_7 + s_6 + 4s_5 + 4s_4 + 12s_3 + 10s_2 + 4s_1 + 2 \\ B_5 &= 2p^3(3s_8 + 4s_7 + s_5 + 6s_3) \\ &\quad -2p^2(6s_8 + 12s_7 + s_6 - 2s_4 + 12s_3 - 2s_2) \\ &\quad +2p\,(3s_8 + 6s_7 - 2s_5 - 4s_4 - 8s_2 - 2s_1) \\ &\quad +2\,(2s_7 + s_6 + 4s_5 + 4s_4 + 12s_3 + 12s_2 + 8s_1 + 6) \end{aligned} \tag{7.56}$$

where

$$\begin{aligned} s_1 &= c_x + c_y + c_z & s_5 &= s_1 s_2 - 3s_3 \\ s_2 &= c_x c_y + c_y c_z + c_z c_x & s_6 &= s_2^2 - 2s_1 s_3 \\ s_3 &= c_x c_y c_z & s_7 &= s_1\,s_3 \\ s_4 &= s_1^2 - 2s_2 & s_8 &= s_2\,s_3 \end{aligned} \tag{7.57}$$

with $c_x = \cos(\chi) - 1$, $c_y = \cos(\eta) - 1$ and $c_z = \cos(\xi) - 1$.

The dispersion relation for the HSCN (uniform mesh) can be written as:

$$\cos(5\theta) + B_1 \cos(4\theta) + B_2 \cos(3\theta) + B_3 \cos(2\theta) + B_4 \cos(\theta) + \frac{B_5}{2} = 0 \qquad (7.58)$$

where $B_1 \dots B_5$ are defined by (7.56). By performing a similar analysis for the Type II HSCN the same coefficients $B_1 \dots B_5$ are found in this case too.

By expanding cosines of multiple angles, the dispersion relation for the HSCN becomes a polynomial of 5th order in $\cos(\omega\Delta t)$. This means that a full analytical analysis of the propagating solutions cannot be performed as in the case of the SCN and the SSCN. Here, analyses are given for particular propagation directions, namely along a coordinate plane diagonal $[\mathbf{1}, \mathbf{1}, \mathbf{0}]$ defined by $k_y = k_x$ and $k_z = 0$ and along main space diagonal $[\mathbf{1}, \mathbf{1}, \mathbf{1}]$ defined by $k_y = k_z = k_x$.

For propagation along the direction $[\mathbf{1}, \mathbf{1}, \mathbf{0}]$, the dispersion relation (7.58) can be factorized and split into four relations given by:

$$2\cos(\omega\Delta t) + \cos(\chi) + 1 = 0 \qquad (7.59)$$

$$2\cos(\omega\Delta t) + \cos(\chi)(p+1) - p + 1 = 0 \qquad (7.60)$$

$$2\cos(\omega\Delta t) + \cos(\chi)(p-1) - p - 1 = 0 \qquad (7.61)$$

$$2\cos^2(\omega\Delta t) + (2p-1)(\cos(\chi) - 1)\cos(\omega\Delta t) - \cos(\chi) - 1 = 0 \qquad (7.62)$$

The first two of these relations contribute to the unphysical solutions propagating at a high-frequency. The relation (7.61) describes a physical solution, propagating with the correct velocity at low frequencies:

$$v = \left(\lim_{\omega \to 0} \frac{\partial k}{\partial \omega} \right)^{-1} = \frac{\Delta l}{2\sqrt{\varepsilon_r \mu_r}\Delta t} \qquad (7.63)$$

There are two possible solutions to the relation (7.62). One is unphysical, whereas the other corresponds to modes propagating with the low-frequency velocity given by (7.63). Therefore, two low-frequency propagating solutions, both physical, are described by equations (7.61) and (7.62). Although not immediately clear at this stage, this phenomenon has the interpretation that two different orthogonal polarizations of the electric field propagate in a TLM mesh based on the HSCN (and also the stub-loaded SCN) with different dispersion characteristics [60]. This ambiguity, called *mesh anisotropy* [60], arises from the fact that only one type of stub, either open- or short-circuit, is used in the HSCN, and because of this

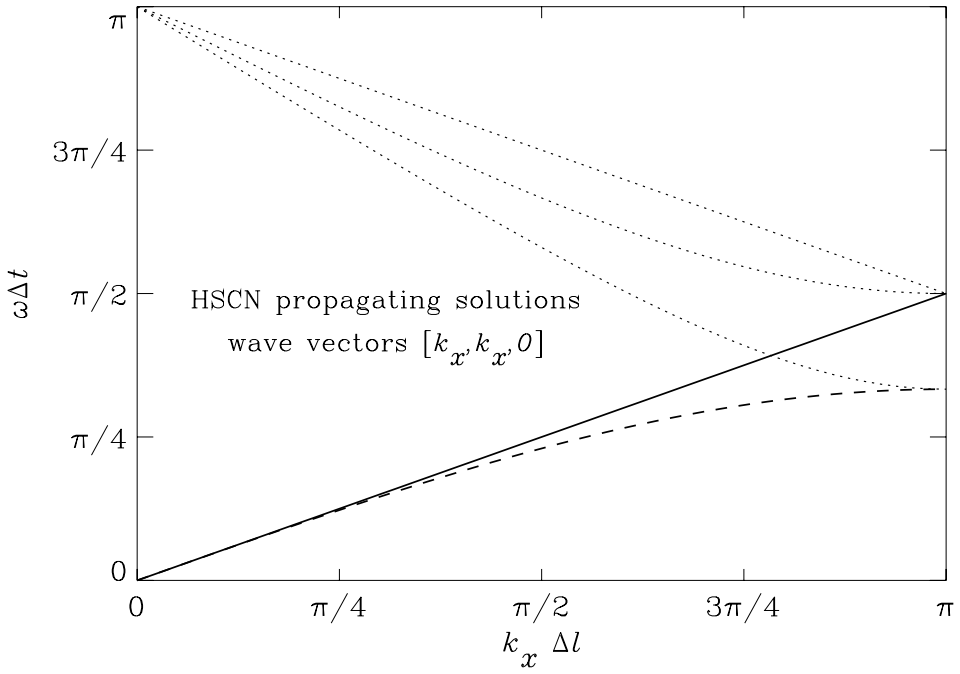

Figure 7.6 *Solutions of the HSCN dispersion relation for wave vectors* $(k_x, k_x, 0)$ *and* $\varepsilon_r \mu_r = 2$

the overall coupling of stub and link lines with the electric and magnetic field is asymmetrical. The mesh anisotropy will be further investigated and quantified in the following chapter.

Five possible solutions to the dispersion relations (7.59)–(7.62) are plotted in Figure 7.6 for the case when $\varepsilon_r \mu_r = 2$. The physical solutions corresponding to (7.61) and (7.62) are plotted with broken and solid lines, respectively, whereas the three unphysical solutions are plotted by dotted lines. It is interesting to note that in this particular case, when $\varepsilon_r \mu_r = 2$, one of the physical solutions, given by (7.62) corresponds exactly to the linear dispersion relation. This can be confirmed by analysing equation (7.62) after substituting for $p = 1 - 1/(\varepsilon_r \mu_r) = 1/2$.

The existence of low-frequency propagating solutions with high wave numbers (spurious modes) can be studied for a complementary propagation direction defined by a wave vector $(\pi/\Delta l - k_a,\ \pi/\Delta l - k_a,\ \pi/\Delta l)$. Factorizing the dispersion relation (7.58) as before, analytical expressions for the five solutions can be found, two of them yielding a low-frequency propagation velocity:

$$v = \left(\lim_{\omega \to 0} \frac{\partial k}{\partial \omega} \right)^{-1} = \frac{\Delta l}{2\Delta t} \tag{7.64}$$

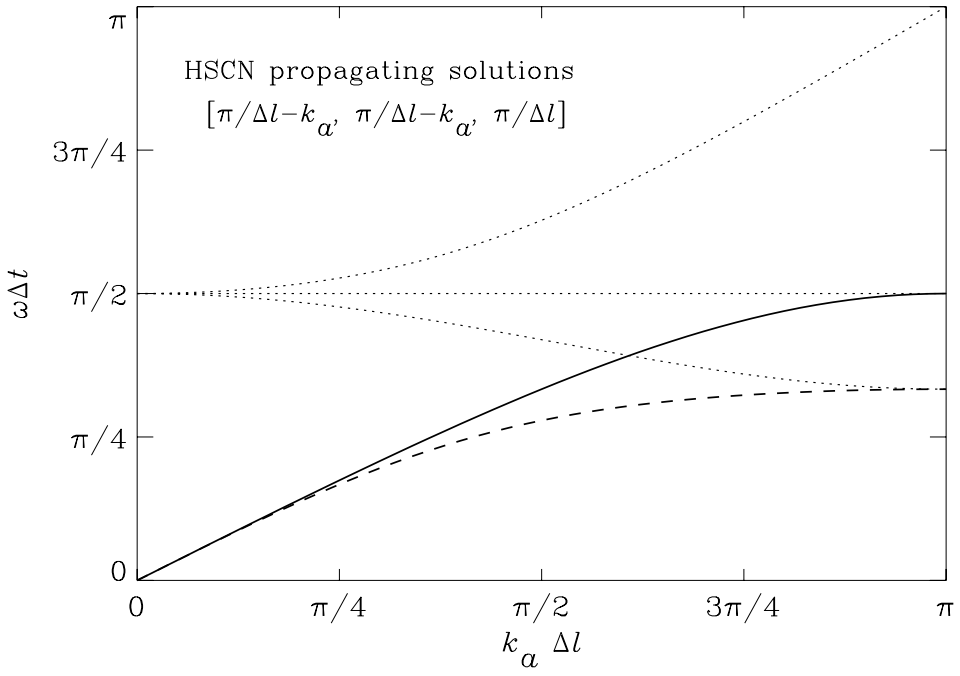

Figure 7.7 *Solutions of the HSCN dispersion relation for wave vectors* $(\pi/\Delta l - k_a, \pi/\Delta l - k_a, \pi/\Delta l)$ *and* $\varepsilon_r\mu_r = 2$

This means that, in this case, spurious modes in the HSCN propagate with the velocity of free space, different from the velocity of modelled medium. Five possible solutions for these wave numbers are plotted in Figure 7.7.

For propagation along the direction $[\mathbf{1},\mathbf{1},\mathbf{1}]$, by imposing $k_x = k_y = k_z$, the dispersion relation (7.58) simplifies to:

$$\Big(4\cos^2(\theta) + 4p\,(\cos(\chi) - 1)\cos(\theta) + (p-1)(3\cos^2(\chi) + 1) - 4p\cos(\chi)\Big)^2$$
$$(p\cos(\theta) + \cos(\chi) - p + 1) = 0 \tag{7.65}$$

By analysing propagating solutions as before, it can be found that the two physical solutions, representing orthogonal wave polarizations, are degenerate for propagation along the main space diagonal $[\mathbf{1},\mathbf{1},\mathbf{1}]$. This is a consequence of the square term in (7.65).

The low-frequency solutions of the dispersion relation (7.65) are plotted in Figure 7.8 for $\varepsilon_r\mu_r = 1, 2, 4$. It can be seen from the gradients of curves approaching corners of the plot that physical modes (with low wave numbers) in different media propagate with different velocities, as expected, whilst the spurious modes (with high wave numbers) propagate in all cases with the same, free-space, velocity.

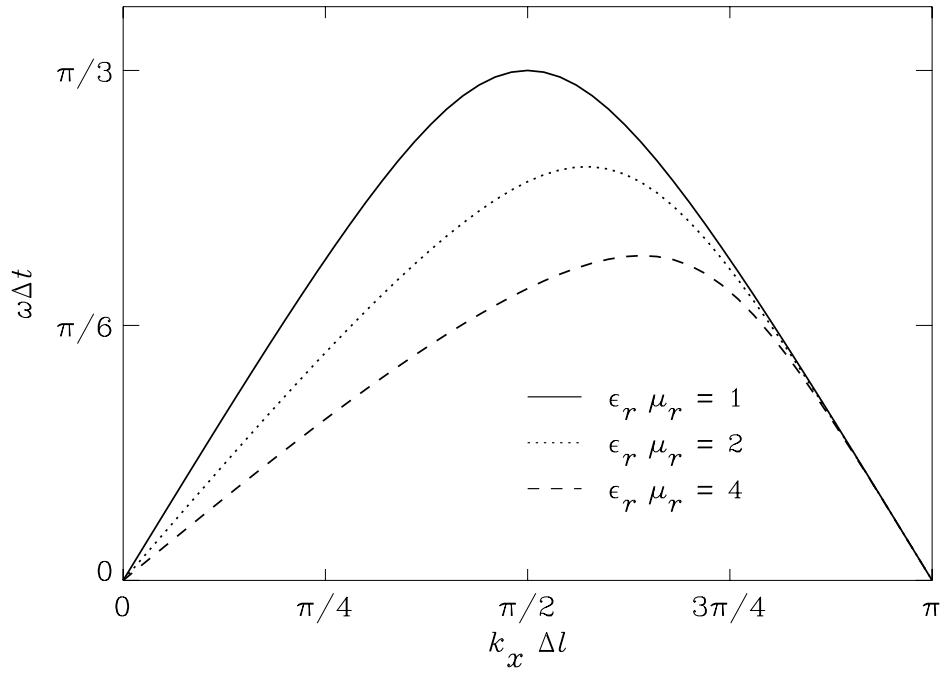

Figure 7.8 *HSCN dispersion characteristics for low-frequency propagating modes along the main space diagonal* $[\mathbf{1},\mathbf{1},\mathbf{1}]$

Finally, it should be pointed out that for axial propagation, for example along the $[\mathbf{1},\mathbf{0},\mathbf{0}]$ direction, the dispersion relation (7.58) simplifies to:

$$4\left(\cos(\chi)+1\right)\left(2\cos^2(\theta)+p\,\cos(\theta)(\cos(\chi)-1)-\cos(\chi)-1\right)^2 \tag{7.66}$$

It produces, as in the case for $[\mathbf{1},\mathbf{1},\mathbf{1}]$ propagation, degenerate dispersion characteristics for both orthogonal wave polarizations. Also, for $p=0$, that is for $\varepsilon_r\mu_r=1$, it can be found that physical modes propagate along the axes without dispersion, as expected, since the HSCN simplifies to the SCN in this case. Dispersion characteristics of the HSCN for other propagating directions and different material properties will be further explored in Chapter 8.

When using the HSCN on a graded mesh, the scattering matrix can be expressed in terms of three parameters p_x, p_y and p_z as:

$$\begin{aligned} a_{ij} &= c_{ij} = -\frac{p_i}{2} & b_{ij} &= e_{kj} = \frac{1-p_k}{2} \\ d_{ij} &= \frac{1}{2} & g_i &= p_j + p_k \\ h_i &= p_j + p_k - 1 \end{aligned} \tag{7.67}$$

where p_x, p_y and p_z are described as:

$$p_i = 1 - \frac{1}{\varepsilon_r \mu_r} \left(\frac{2c\Delta t}{\Delta i} \right)^2 \tag{7.68}$$

with $i, j, k \in \{x, y, z\}$ and $c = 1/\sqrt{\varepsilon_0 \mu_0}$.

The coefficients $B_1 \ldots B_5$ for the graded HSCN dispersion relation can be obtained by the Faddeev method and using relationships (7.52) as:

$$\begin{aligned}
B_1 &= 2\,(u_1 + 1) \\
B_2 &= -2s_2 + s_1\,(u_1 - 4) + u_4 + 3u_2 + 4u_1 - v_1 - 3 \\
B_3 &= -2s_2\,(u_1 + 2) + s_1\,(u_4 + u_2 - 4u_1 - 8) \\
&\quad u_5 + 2u_4 + 2u_3 + 6u_2 - 2v_2 + 3v_3 - v_4 - 8 \\
B_4 &= 2s_7 + s_6 - s_5\,(u_1 - 4) - s_4\,(2u_1 - 4) - s_3(2u_1 - 12) \\
&\quad -s_2(2u_2 + 6u_1 - 10) - s_1\,(2u_2 + 9u_1 - 4) + 2u_5 + 3u_4 \\
&\quad +4u_3 + 5u_2 - 4u_1 + v_1 - 2v_2 + 2v_3\,(1 + u_1) \\
&\quad +2v_5 + v_6 + v_7 + v_8 - v_9 + v_{10} + 2 \\
B_5 &= 2\,[s_7\,(u_1 + 2) + s_6 + 4s_5 + 4s_4 + 2s_3\,(u_1 - u_2 + 6) \\
&\quad +s_2\,(u_3 - 4u_2 - 2u_1 + 12) + s_1\,(u_4 + u_3 - u_2 - 4u_1 + 8) \\
&\quad +u_5 + 2u_4 + 6u_3 + 2u_2 - 2u_1 - v_1 s_3 + 2v_2 + v_3(u_1 - 3) \\
&\quad -v_4 - 3v_7 + 3v_8 - v_9 + v_{11} + 6] + v_{12}
\end{aligned} \tag{7.69}$$

where

$$\begin{aligned}
u_1 &= d_x + d_y + d_z & \qquad u_4 &= u_1^2 - 2u_2 \\
u_2 &= d_x d_y + d_y d_z + d_z d_x & \qquad u_5 &= u_1 u_2 - 3u_3 \\
u_3 &= d_x d_y d_z
\end{aligned} \tag{7.70}$$

and

$$\begin{aligned}
v_1 &= c_x d_x + c_y d_y + c_z d_z \\
v_2 &= c_x c_y d_z + c_y c_z d_x + c_z c_x d_y \\
v_3 &= c_x d_y d_z + c_y d_z d_x + c_z d_x d_y \\
v_4 &= d_x^2 c_x + d_y^2 c_y + d_z^2 c_z \\
v_5 &= d_x c_x^2 + d_y c_y^2 + d_z c_z^2 \\
v_6 &= c_x^2 d_x (c_y + c_z) + c_y^2 d_y (c_z + c_x) + c_z^2 d_z (c_x + c_y) \\
v_7 &= c_x^2 d_y d_z + c_y^2 d_z d_x + c_z^2 d_x d_y
\end{aligned}$$

$$
\begin{aligned}
v_8 &= c_x c_y d_x d_y + c_y c_z d_y d_z + c_z c_x d_z d_x \\
v_9 &= c_x c_y d_z^2 + c_y c_z d_x^2 + c_z c_x d_y^2 \\
v_{10} &= c_x d_x (d_y^2 + d_z^2) + c_y d_y (d_z^2 + d_x^2) + c_z d_z (d_x^2 + d_y^2) \\
v_{11} &= c_x^2 c_y^2 d_z + c_y^2 c_z^2 d_x + c_z^2 c_x^2 d_y \\
v_{12} &= (c_x + c_y)(d_z^2(-c_x c_y + d_x c_y + c_x d_y) + 4 d_z c_x c_y - 3 d_x d_y c_z^2) + \\
&\quad (c_y + c_z)(d_x^2(-c_y c_z + d_y c_z + c_y d_z) + 4 d_x c_y c_z - 3 d_y d_z c_x^2) + \\
&\quad (c_z + c_x)(d_y^2(-c_z c_x + d_z c_x + c_z d_x) + 4 d_y c_z c_x - 3 d_z d_x c_y^2)
\end{aligned} \tag{7.71}
$$

with terms $s_1 \dots s_8$ defined by (7.57) and

$$
\begin{aligned}
c_x &= \cos(\chi) - 1 & c_y &= \cos(\eta) - 1 & c_z &= \cos(\xi) - 1 \\
d_x &= p_x c_x & d_y &= p_y c_y & d_z &= p_z c_z
\end{aligned}
$$

The dispersion relation for the HSCN (graded mesh) is given by (7.58) with $B_1 \dots B_5$ defined by (7.69). Similar analysis of the physical and unphysical solutions can be performed as in the case of the uniform mesh. It is interesting to note that for axial propagation the dispersion relation for the graded mesh simplifies to the same form derived for the uniform mesh and given by (7.66), but with the factor p_x (for $[\mathbf{1}, \mathbf{0}, \mathbf{0}]$ direction) instead of p. In order to achieve dispersionless propagation along the x-axis using the graded HSCN, it is required that p_x is equal to zero. From the definition of p_x given by (7.68) it follows, for the example of free-space, that for dispersionless propagation, the time step has to be chosen as $\Delta t = \Delta x/(2c)$, which explains the simulation results obtained in [19].

7.4.4 Stub-loaded symmetrical condensed node

It can be seen from Table 7.2 that in a general case, the analytical expansion of the dispersion relation for the stub-loaded SCN requires determination of eight coefficients. Due to this complexity, two simpler cases will be first considered: Case 1 corresponding to modelling only dielectric ($\varepsilon_r > 1,\ \mu_r = 1$) or only magnetic ($\mu_r > 1,\ \varepsilon_r = 1$) materials on a uniform mesh; and Case 2 corresponding to modelling materials with $\mu_r = \varepsilon_r$ on a uniform or a graded mesh.

Case 1: $(\varepsilon_r > 1, \mu_r = 1)$ or $(\mu_r > 1, \varepsilon_r = 1)$

When modelling a local increase in the dielectric constant, only open-circuit stubs are required in the stub-loaded node [9]. Similarly, for modelling an increase in the magnetic permeability, only short-circuit stubs are required. In either case, the

scattering matrix for the stub-loaded SCN (the lossless case) will have only $N = 15$ rows and columns. By using the definitions of the parameters for the stub-loaded SCN derived in § 2.4.1 and the GSCN scattering coefficients expressed by (3.42)–(3.48), we derive the scattering coefficients for the stub-loaded node modelling a dielectric with relative permittivity ε_r on a uniform mesh as:

$$\begin{aligned} a = c &= \frac{1-\varepsilon_r}{2\varepsilon_r} & b = e &= \frac{1}{2\varepsilon_r} \\ d &= \frac{1}{2} & g &= \frac{2(\varepsilon_r - 1)}{\varepsilon_r} \\ h = g - 1 &= \frac{\varepsilon_r - 2}{\varepsilon_r} \end{aligned} \tag{7.72}$$

Comparing the definition (7.72) with that for the HSCN given by (7.53) we can see that they are identical when $\mu_r = 1$ in (7.53). This is expected, as the Type I HSCN and the stub-loaded SCN are identical when modelling a dielectric on a uniform mesh. Following this analogy, it becomes obvious that the dispersion relation for the stub-loaded SCN in Case 1 is the same as that derived for the HSCN (uniform mesh), given by (7.58), provided that the coefficients $B_1 \dots B_5$ are defined by (7.56) when $\mu_r = 1$.

Performing a similar analysis for the case when modelling magnetic materials, we find that the scattering matrix of the stub-loaded SCN and the HSCN Type II are the same and therefore their dispersion characteristics are identical. Since the analytical form of the dispersion relation for the Type II and Type I HSCN is identical, it follows that the dispersion relation for the stub-loaded SCN in this case is given by (7.58), provided that coefficients $B_1 \dots B_5$ are defined by (7.56) when $\varepsilon_r = 1$.

Since the dispersion relations for the stub-loaded node in Case 1 are equivalent to that of the HSCN, the mesh anisotropy experienced in the HSCN (i.e. the existence of different solutions for two orthogonal wave polarizations) is found in the stub-loaded SCN in Case 1, too.

Case 2: $(\mu_r = \varepsilon_r)$

When using the stub-loaded SCN for modelling any material with $\varepsilon_r = \mu_r$ on either a uniform or a graded mesh, the structure of the characteristic polynomial is somewhat simplified, as the propagating solutions appear in degenerate pairs. The characteristic polynomial has the structure:

$$\mathcal{P}^{(18)}(\lambda) = (\lambda - 1)^2 (\mathcal{Q}^{(8)}(\lambda))^2 \tag{7.73}$$

and only $m = 8/2 = 4$ coefficients need to be calculated. The relationships between the four leading coefficients B_i of the polynomial $\mathcal{Q}^{(8)}(\lambda)$ and C_i of $\mathcal{P}^{(18)}(\lambda)$ can be found after expanding (7.73) and they are:

$$\begin{aligned} B_1 &= \frac{C_1}{2} + 1 \\ B_2 &= \frac{C_2 - B_1^2 + 4B_1 - 1}{2} \\ B_3 &= \frac{C_3}{2} + B_1^2 - B_1 B_2 - B_1 + 2B_2 \\ B_4 &= \frac{C_4 - B_1^2 + 4B_1 B_2 - 2B_1 B_3 - B_2^2 - 2B_2 + 4B_3}{2} \end{aligned} \tag{7.74}$$

When using a uniform mesh, the scattering coefficients of the stub-loaded SCN in Case 2 are found from expressions (3.42)–(3.48) and definitions (2.49)–(2.50) as:

$$\begin{aligned} a &= 0 & b &= e = d = i = \frac{1-r}{2} \\ c &= -r & f &= g = 2r \\ h &= 2r - 1 & j &= 1 - 2r \end{aligned} \tag{7.75}$$

where

$$r = 1 - \frac{1}{\varepsilon_r} = 1 - \frac{1}{\mu_r} = 1 - \frac{1}{\sqrt{\varepsilon_r \mu_r}}$$

The four coefficients B_i required for the dispersion relation (7.32) can be computed as before by using the Faddeev method and relationships (7.74) to give:

$$\begin{aligned} B_1 &= 2\,(r\,s_1 + 2) \\ B_2 &= r^2\,(3s_2 - 2s_1) + 2r\,(s_2 + 4s_1) - s_2 - 2s_1 + 4 \\ B_3 &= 2r^3\,(s_3 - 2s_2) + 4r^2\,(3s_3 + s_2 - 2s_1) \\ &\quad + 2r\,(-3s_3 + 2s_2 + 7s_1) - 4\,(s_2 + 2s_1 + 1) \\ B_4 &= 4r^3\,(-7s_3 - 2s_2) + 2r^2\,(12s_3 + s_2 - 6s_1) \\ &\quad + 4r\,(-3s_3 + s_2 + 4s_1) - 2\,(3s_2 + 6s_1 + 5) \end{aligned} \tag{7.76}$$

where s_1, s_2 and s_3 are defined by (7.57).

The dispersion relation for the stub-loaded SCN in Case 2 (uniform mesh) can be written as:

$$\cos(4\theta) + B_1 \cos(3\theta) + B_2 \cos(2\theta) + B_3 \cos(\theta) + \frac{B_4}{2} = 0 \tag{7.77}$$

where $B_1 \dots B_4$ are defined by (7.76).

When using the stub-loaded SCN in Case 2 on a graded mesh, the scattering matrix can be expressed in terms of three parameters r_x, r_y and r_z as:

$$\begin{aligned} a_{ij} &= \frac{r_k - r_j}{2} & b_{ij} &= e_{ij} = \frac{1 - r_j}{2} \\ c_{ij} &= -\frac{r_j + r_k}{2} & d_{ij} &= i_{ij} = \frac{1 - r_k}{2} \\ f_j &= g_j = 2r_j & h_j &= -j_j = 2r_j - 1 \end{aligned} \tag{7.78}$$

where r_x, r_y and r_z are described as:

$$r_i = 1 - \frac{2c\Delta t \Delta i}{\Delta j \Delta k \sqrt{\varepsilon_r \mu_r}} \tag{7.79}$$

with $i, j, k \in \{x, y, z\}$ and $c = 1/\sqrt{\varepsilon_0 \mu_0}$.

The coefficients $B_1 \dots B_4$ for the graded stub-loaded SCN dispersion relation in Case 2 can be obtained by the Faddeev method and using relationships (7.74) as:

$$\begin{aligned} B_1 &= s_1 u_1 - u_1 + 4 \\ B_2 &= s_2 (u_2 - 1) + 2s_1 (2u_1 - 1) + 4 + 2v_2 - 4v_1 - 2v_3 \\ B_3 &= 2s_3 (u_3 + 2u_2 - u_1) - 4s_2 (u_3 + 1) + s_1 (7u_1 - 8) \\ &\quad +4 (v_8 + v_2) - 7v_1 - 8v_3 - 4 \\ B_4 &= 4s_3 (-7u_3 + 2u_2 - u_1) - 2s_2 (4u_3 + u_2 + 3) + 4s_1 (2u_1 - 3) \\ &\quad +8v_8 + 4v_2 - 8v_1 - 12v_3 - 10 \end{aligned} \tag{7.80}$$

where s_1, s_2, s_3, u_1, u_2, u_3, v_1, v_3 and v_8 are defined by (7.57), (7.70) and (7.71) with $d_x = r_x$, $d_y = r_y$ and $d_z = r_z$.

The dispersion relation for the Case 2 stub-loaded SCN (graded mesh) is given by (7.77) with $B_1 \dots B_4$ defined by (7.80).

Analyses of the dispersion relations can be performed in a similar manner as before and physical and unphysical propagation modes can be studied for particular directions of propagation. However, the most interesting result in this case is the absence of mesh anisotropy, like in the 12-port SCN and the SSCN and unlike the HSCN and the stub-loaded SCN in Case 1. This can be explained by the fact that in Case 2, the introduced open- and short-circuit stubs model the same amount of additional capacitance and inductance, thus securing a symmetrical coupling with electric and magnetic fields. This will be further exploited in Chapter 9 for deriving new stub-loaded nodes with advantageous dispersion characteristics.

Case 3: $(\varepsilon_r \neq \mu_r)$

The dispersion relation for the stub-loaded SCN in the general case when $\varepsilon_r \neq \mu_r$ contains eight coefficients B_i. The complexity of the derivation is due to a feature of the stub-loaded SCN that its scattering coefficients are dependent separately on ε_r and μ_r, rather then on their product, $\varepsilon_r \mu_r$, which is the case in the SSCN and the HSCN. As the efficiency of the stub-loaded SCN for a graded mesh is in any case degraded by the unfavourable time-step, the derivation of the dispersion relation for Case 3 will be presented here only for the uniform mesh and for propagation in planes which will be analysed in the next chapter, namely for a coordinate plane defined by $k_z = 0$ (subcase a), and a diagonal plane where $k_x = k_y$ (subcase b).

The scattering matrix in Case 3 can be expressed in terms of two parameters, r_e and r_m as:

$$\begin{aligned} a &= \frac{r_m - r_e}{2} & b &= e = \frac{1 - r_e}{2} \\ c &= -\frac{r_m + r_e}{2} & d &= i = \frac{1 - r_m}{2} \\ f &= 2r_m & h &= 2r_e - 1 \\ g &= 2r_e & j &= 1 - 2r_m \end{aligned} \tag{7.81}$$

where r_e and r_m are defined by:

$$r_e = 1 - \frac{1}{\varepsilon_r} \qquad r_m = 1 - \frac{1}{\mu_r} \tag{7.82}$$

By using a similar procedure to that used before, eight coefficients of the polynomial $\mathcal{Q}^{(16)}(\lambda)$ can be obtained. For propagation along a coordinate plane, defined by $k_z = 0$, this polynomial factorizes as:

$$\mathcal{Q}^{(16)}(\lambda) = (\lambda + 1)^2 \mathcal{R}_1^{(6)}(\lambda) \mathcal{R}_2^{(6)}(\lambda) \tag{7.83}$$

The coefficients of the polynomial $\mathcal{R}_1^{(6)}(\lambda)$ can be obtained as:

$$\begin{aligned} B_1 &= s_1 (r_e + r_m) + 2 \\ B_2 &= 2r_e r_m (s_2 - s_1) + 2r_e (s_1 + s_2) + r_m^2 s_2 + 2r_m s_1 - 2s_1 - s_2 - 1 \\ B_3 &= 2 (-2r_e r_m^2 s_2 - 2r_e r_m (s_1 + s_2) + r_e s_1 + r_m^2 s_2 + r_m s_1 - 2s_1 - s_2 - 2) \end{aligned} \tag{7.84}$$

where s_1 and s_2 are defined as before (eqn. 7.57), but with k_z=0. The coefficients of the polynomial $\mathcal{R}_2^{(6)}(\lambda)$ are identical to (7.84) provided that r_e and r_m swap

places. The dispersion relation for the stub-loaded SCN in Case 3a can be written as:

$$\cos(3\theta) + B_1 \cos(2\theta) + B_2 \cos(\theta) + \frac{B_3}{2} = 0 \tag{7.85}$$

where $B_1 \dots B_3$ are defined by (7.84). A complementary dispersion relation, corresponding to another orthogonal polarization, can be derived by swapping r_e and r_m.

For propagation along a diagonal, defined by $k_x = k_y$, the polynomial $\mathcal{Q}^{(16)}(\lambda)$ factorizes as:

$$\mathcal{Q}^{(16)}(\lambda) = \mathcal{R}_1^{(8)}(\lambda)\mathcal{R}_2^{(8)}(\lambda) \tag{7.86}$$

The coefficients of the polynomial $\mathcal{R}_1^{(8)}(\lambda)$ can be obtained as:

$$\begin{aligned}
B_1 &= r_e\,(c_x + c_z) + r_m\,(3c_x + c_z) + 4 \\
B_2 &= r_e r_m\,(c_x^2 + 4c_x c_z - 4c_x - 2c_z) + (r_e + r_m)\,(c_x^2 + 2c_x c_z + 6c_x + 4c_z) \\
&\quad + 2r_m^2 c_x\,(c_x + c_z) + 4r_m c_x - c_x^2 - 2c_x c_z - 4c_x - 2c_z + 4 \\
B_3 &= 2r_e r_m^2 c_x\,(c_x c_z - 2c_x - 4c_z) + 2r_e r_m\,(3c_x^2 c_z - 8c_x - 4c_z) \\
&\quad + r_e\,(4c_x^2 + 8c_x c_z + 15c_x + 7c_z) + 2r_m^2 c_x\,(3c_x c_z + 2c_x + 4c_z) \\
&\quad + r_m\,(-6c_x^2 c_z + 13c_x + 7c_z) + 4\,(-c_x^2 - 2c_x c_z - 4c_x - 2c_z - 1) \\
B_4 &= 4r_e r_m^2 c_x\,(-7c_x c_z - 2c_x - 4c_z) + 2r_e r_m\,(6c_x^2 c_z - c_x^2 \\
&\quad - 4c_x c_z - 12c_x - 6c_z) + 2r_e\,(3c_x^2 + 6c_x c_z + 10c_x + 4c_z) \\
&\quad + 4r_m^2 c_x\,(3c_x c_z + c_x + 3c_z) + 2r_m\,(-6c_x^2 c_z - c_x^2 - 2c_x c_z \\
&\quad + 6c_x + 4c_z) + 2\,(-3c_x^2 - 6c_x c_z - 12c_x - 6c_z - 5)
\end{aligned} \tag{7.87}$$

where $c_x = \cos(k_x \Delta l) - 1$ and $c_z = \cos(k_z \Delta l) - 1$. The coefficients of the polynomial $\mathcal{R}_2^{(8)}(\lambda)$ are identical to (7.87) provided that r_e and r_m are swapped. The dispersion relation for the stub-loaded SCN in Case 3b is given by (7.77) with $B_1 \dots B_4$ defined by (7.87). A complementary dispersion relation can be derived by swapping r_e and r_m.

Mesh anisotropy exists in Case 3, as in Case 1, due to unequal proportions of extra capacitance modelled by open-circuit stubs and extra inductance modelled by short-circuit stubs. Hence asymmetrical coupling with electric and magnetic fields occurs for different wave polarizations.

In order to show the existence of different dispersion characteristics for the stub-loaded SCN when $\varepsilon_r \mu_r = const$ but ε_r / μ_r varies, the physical solutions to the

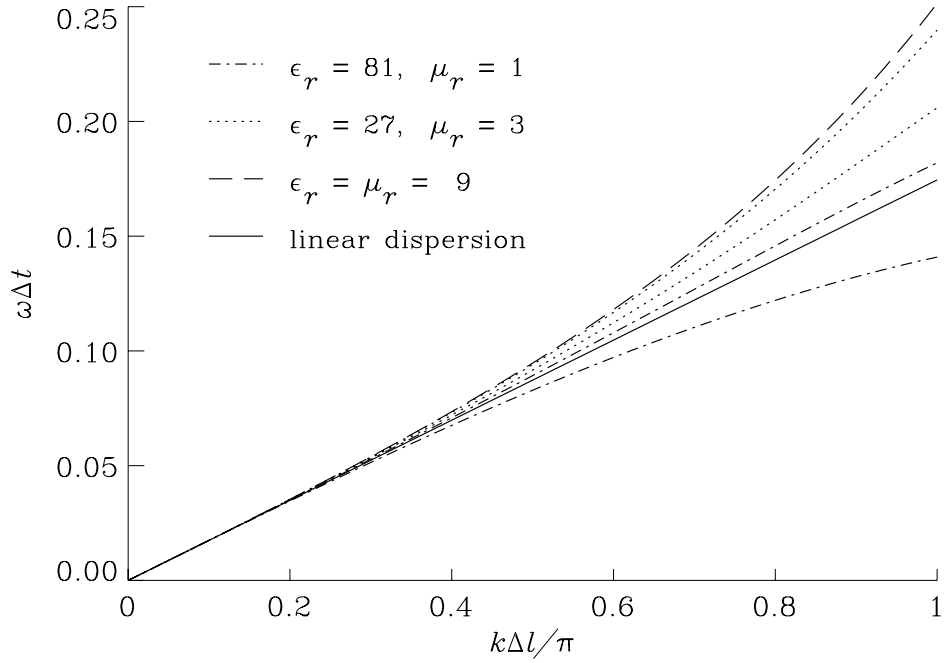

Figure 7.9 *Stub-loaded SCN dispersion characteristics along direction* $[\mathbf{1}, \mathbf{1}, \mathbf{0}]$

dispersion relations derived in this subsection for different cases are plotted in Figure 7.9 for $\varepsilon_r \mu_r = 81$ and different values of ε_r, for propagation in the direction $[\mathbf{1}, \mathbf{1}, \mathbf{0}]$. It can be seen that two curves exist when $\varepsilon_r \neq \mu_r$, related to the two different wave polarizations [58, 60]. However, it can also be seen that all curves approach the linear dispersion curve for frequencies and wave numbers approaching zero. Note that for $k\Delta l \leq 0.2\pi$, that is when the spatial discretization does not exceed ten nodes per wavelength, the deviations from the linear dispersion characteristics are practically unobservable in Figure 7.9.

It should be pointed out after analysing the dispersion relations derived for the stub-loaded node, that if mesh anisotropy exists, then two dispersion curves calculated when $\varepsilon_r = a$, $\mu_r = b$ coincide with curves calculated for $\varepsilon_r = b$, $\mu_r = a$. Intuitively, based on the principle of duality in electromagnetics, one can conclude that the dispersion characteristics for complementary values of ε_r and μ_r would complement each other; that is the dispersion characteristics for horizontal electric field polarization and $\varepsilon_r = a$, $\mu_r = b$ should be the same as the dispersion characteristics for vertical electric field polarization and $\varepsilon_r = b$, $\mu_r = a$, and vice versa. This was suggested in [58, 60] and will be further checked by performing numerical simulations in Chapter 8.

7.5 Discussion

Using a systematic algebraic procedure, analytical expansion of the general TLM dispersion relation was made possible for different symmetrical condensed nodes capable of modelling media with arbitrary electromagnetic parameters. Simple closed-form algebraic expressions were obtained for the SCN and the SSCN. For other nodes (the stub-loaded SCN and the HSCN), the general matrix-form dispersion relation (7.4) was expanded into forms of implicit polynomial equations. Since these polynomials are of 5th to up to 8th order in $\cos(\omega\Delta t)$, closed form solutions in the form $\omega = F(k)$ are not possible.

However, the dispersion relations derived here in algebraic forms are either linear or quadratic expressions in terms of $\cos(k_x\Delta x)$, $\cos(k_y\Delta y)$ or $\cos(k_z\Delta z)$. A closed form solution in the form $k = F^{-1}(\omega)$ is not yet possible, since the cosine factors contain Cartesian components but not the amplitude of the wave vector $\vec{k}$. However, for a given excitation frequency ω ($0 < \omega\Delta t < \pi/2$), and two wave vector components, say k_y and k_z, the third, unknown component k_x, and therefore the wave vector $\vec{k}$ can be computed **exactly** from the dispersion relations, by solving a linear or quadratic equation analytically in terms of $\cos(k_x\Delta x)$, hence a numerical solver is not needed.

It may appear that the analytical forms of the dispersion relations obtained here for the HSCN and the stub-loaded SCN are too complicated and that a manipulation with such lengthy expressions may be less efficient than numerically solving the general dispersion relation in the matrix form (7.4). However, in cases when there are two physical solutions close to each other, the numerical solution is not always easy [60] or accurate [57]. The separation of the two, usually very close, physical solutions requires, in a numerical solver, high precision arithmetic and is very sensitive to the initial (approximate) values needed to start the computation. It will be shown in the next chapter that using the algebraic form of dispersion relations derived here, this problem is not experienced. Of course, modern computer-based symbolic algebra packages, such as *Maple* or *Mathematica* could be used to assist the handling and analytical solution of lengthy algebraic expressions.

In this chapter, a mathematical analysis of the dispersion relations was pursued, including the characterization of physical and spurious solutions. Further discussion on the physical solutions will be provided in the following chapter, after performing a detailed quantitative analysis.

Chapter 8 Quantitative analysis and validation of dispersion relations

8.1 Introduction

In the previous chapter, the dispersion relations for the currently available TLM condensed nodes were derived in implicit polynomial forms and, where possible, explicit closed forms, from the general TLM dispersion relation (7.4) given in an eigenvalue matrix form. In addition to the solutions converging to the linear dispersion characteristics of the wave equation, additional unphysical solutions were also identified. While mainly a qualitative analysis of different solutions was performed in the previous chapter, in this chapter the quantitative analysis and validation of the physical solutions to the TLM dispersion relations, i.e. those which converge to solutions of Maxwell's equation, is pursued.

The analysis in the previous chapter was performed for a continuous frequency range, and for propagation vectors with small as well as with high wave numbers. Here, an analysis is performed when the frequency or the wave vector are set to a fixed value which is of practical interest, usually corresponding to a benchmark discretization of ten nodes per wavelength, i.e. $\Delta l/\lambda = 0.1$, while other input parameters, such as direction of propagation, material properties, aspect ratio of cells and time step are altered. This analysis makes possible a comparison of the accuracy of different nodal structures, thus allowing the modeller to gain more insight into the suitability of available TLM condensed node schemes in solving a particular problem accurately and efficiently.

The deviation in the wave velocity from its theoretical value due to numerical dispersion can be studied in two ways [56]. In *deterministic problems*, a wave of particular frequency f_0 is excited in the model, and it propagates with a wavelength λ, different from the theoretical value $\lambda_0 = v/f_0$. The deviation of the wave velocity can be analysed through the deviation of the wavelength λ from λ_0. The difference between the amplitude of the modelled propagation vector $\vec{k}$,

given by $k = 2\pi/\lambda$ and the theoretical medium propagation constant defined by $k_m = 2\pi f_0\sqrt{\varepsilon\mu}$ can be also studied in this way.

In *eigenvalue problems*, the wavelength λ_0 is forced to the correct value by the boundary conditions and therefore the modelled frequency f differs from the theoretical one $f_0 = v/\lambda_0$. In this way, the deviation in the wave velocity can be studied through the deviation in frequency. The difference between the amplitude of the modelled propagation vector $\vec{k}$, computed now as $k = 2\pi f\sqrt{\varepsilon\mu}$, and the theoretical medium propagation constant defined by $k_m = 2\pi/\lambda_0$ can again be studied in this way.

By analysing the algebraic expressions of the dispersion relations derived in the previous chapter it should be noticed that the coefficients B_i, appearing in the dispersion relations, contain factors $\cos(k_x\Delta x)$, $\cos(k_y\Delta y)$ and $\cos(k_z\Delta z)$ and their squares, hence the dispersion relations are polynomials in $\cos(k_i\Delta i)$ of at most 2nd order. For deterministic problems, where the frequency excitation f_0 is fixed, this means that solutions to the wave vector components (k_x, k_y, k_z) can always be found analytically from the dispersion relations.

This is not the case when analysing dispersion relations in eigenvalue problems, as after expanding cosines of multiple angles, they become polynomials in $\cos(\theta)$ of up to 8th order, where the order of the polynomial is determined by the coefficient m defined in the previous chapter. This means, that for a chosen wave vector $\vec{k}$, the modelled frequency f (note that $\theta = 2\pi f\Delta t$) cannot be obtained analytically in all cases since the closed-form solution of a polynomial with order $m > 4$ cannot be guaranteed. In fact, for most practical cases, only roots of linear and quadratic polynomials ($m = 2$) can be found in simple closed forms, whilst equations of a higher order are most efficiently solved numerically. Following this reasoning, it appears that the analysis of the dispersion relations can be more efficiently performed using the deterministic approach.

On the other hand TLM simulations of deterministic problems, which assume the wave propagating over several wavelengths in unbounded media, are difficult to perform without introducing additional errors due to the modelling of absorbing boundaries [71], which is necessary in this case. In contrast to this, the eigenvalue problems are easier to model with TLM method, as they are associated with propagation in resonators bounded by appropriate electric and magnetic walls. Numerical simulations of the wave propagation in resonators can be carried out 'exactly', i.e. the only error introduced into the calculations would be due to numerical dispersion (and not due to imperfect modelling of the absorbing

boundaries). The eigenvalue approach is therefore more convenient from the validation point of view, since the frequency error obtained from TLM simulations can be compared to the error predicted by the dispersion relation. In the following section, it will be shown how the two approaches can be combined, in order to facilitate an efficient validation of the TLM dispersion relations.

8.2 Relationships between eigenvalue and deterministic problems

In the 3D TLM method, the velocity of voltage pulses travelling along constituent transmission lines, v_l, is twice the velocity of waves propagating in the medium with background parameters ε_0, μ_0 and is given by:

$$v_l = 2c = \frac{2}{\sqrt{\varepsilon_0 \mu_0}}$$

In a non-dispersive isotropic medium with parameters ε_r, μ_r waves propagate with speed

$$v_m = \frac{1}{\sqrt{\varepsilon \mu}} = \frac{c}{\sqrt{\varepsilon_r \mu_r}}$$

and therefore it follows that:

$$v_m = \frac{v_l}{2\sqrt{\varepsilon_r \mu_r}}$$

The medium propagation constant is determined from the dispersion relation of Maxwell's equations (7.1) as:

$$k_m = \frac{\omega_0}{v_m}$$

Following the above definitions, the anticipated phase shift θ_0 along the constituent TLM lines would be:

$$\theta_0 = \omega_0 \Delta t = k_m v_m \Delta t = k_m \frac{v_l \Delta t}{2\sqrt{\varepsilon_r \mu_r}} = k_m \frac{\Delta l}{2\sqrt{\varepsilon_r \mu_r}} \tag{8.1}$$

Factor $k_m \Delta l$ appearing in the formulation of θ_0 describes the level of spatial discretization, as by definition it follows that:

$$k_m \Delta l = 2\pi \frac{\Delta l}{\lambda_0}$$

In numerical schemes, the discretization is usually set at a minimum of ten nodes per wavelength, that is $\Delta l / \lambda_0 = 0.1$. For this value it follows that $k_m = 0.2\pi$.

In deterministic problems, the initial value of phase shift θ_0 can be chosen according to equation (8.1) to satisfy a desirable discretization level, set through $k_m \Delta l$. The amplitude of the modelled propagation vector, $k = (k_x^2 + k_y^2 + k_z^2)^{-1/2}$, can be

computed from the dispersion relation, for different propagation directions, and compared to the chosen propagation constant k_m. A quantitative measure of the dispersion can be introduced through a relative *propagation error* as:

$$\delta k' = \frac{k - k_m}{k_m} \tag{8.2}$$

In eigenvalue problems the theoretical value of the phase shift, denoted by θ_0 is obtained again from (8.1) for a certain $k_m \Delta l$. However, the numerical phase shift θ is computed from the dispersion relation, for different values of k_x, k_y, k_z, where $(k_x^2 + k_y^2 + k_z^2)^{-1/2} = k_m$ and can be compared to θ_0. Therefore, another measure of the dispersion can be introduced through a relative *frequency error* as:

$$\delta f = \frac{f - f_0}{f_0} = \frac{\omega - \omega_0}{\omega_0} = \frac{\theta - \theta_0}{\theta_0} \tag{8.3}$$

It would be convenient to somehow relate the propagation error defined by (8.2) to the frequency error defined by (8.3) so as to allow validation of the dispersion relations using the deterministic approach in solving the dispersion relation and the eigenvalue approach in obtaining results from numerical simulations. This can be achieved by making use of the fact that TLM is accurate to second order [42, 58] which was also confirmed in Chapter 4 where the GSCN was derived from Maxwell's equation using the central differencing and averaging, two approximation techniques which each have 2nd order accuracy. The second order accuracy of TLM suggests that the relative deviations at different spatial discretization levels are related by [58]:

$$\frac{\delta k_2}{\delta k_1} = \left(\frac{\Delta l / \lambda_2}{\Delta l / \lambda_1} \right)^2 \tag{8.4}$$

The errors associated with the deterministic and eigenvalue problems are depicted in Figure 8.1. The propagation vector is plotted for the example of propagation in the coordinate plane xy. Solid lines correspond to the dispersion relation of Maxwell's equations and broken lines correspond to the dispersion relation of the SCN.

In the deterministic problems, with a fixed excitation frequency ω_0, the amplitude k of propagation vector $\vec{k}$ is computed from the dispersion relation for an angle of propagation and is generally different from the correct physical value k_m, as shown in Figure 8.1. The relative error between the two values is denoted by $\delta k'$ and is defined by (8.2). In order to obtain an amplitude of the propagation vector, for the same angle, identical to k_m, from the dispersion relation of the SCN,

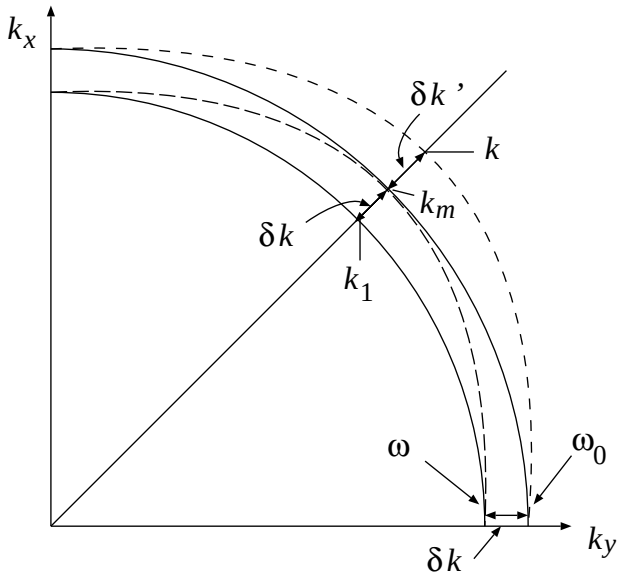

$$\delta k' = \frac{k - k_m}{k_m}$$

$$\delta k = \frac{k_m - k_1}{k_1} = \frac{\omega_0 - \omega}{\omega}$$

Figure 8.1 *Errors associated with deterministic and eigenvalue problems*

the excitation frequency has to be decreased from ω_0 to ω. The new frequency ω corresponds, according to the dispersion relation of Maxwell's equation, to another propagation vector $\vec{k}_1$. Determination of ω is, in fact, an eigenvalue problem, where the propagation constant k_m is chosen *a priori*. If the wave velocity in the medium is v_m, then $k_m = \omega_0/v_m$ and $k_1 = \omega/v_m$, and a relative error can be defined as:

$$\delta k = \frac{k_m - k_1}{k_1} = \frac{\omega_0 - \omega}{\omega} \tag{8.5}$$

which is illustrated in Figure 8.1.

The original relative error $\delta k'$ corresponds to $k = 2\pi/\lambda$ and therefore to the discretization level of $\Delta l/\lambda$, whereas the relative error δk corresponds to $k_m = 2\pi/\lambda_0$ and therefore to $\Delta l/\lambda_0$. Taking into account the second order accuracy of TLM expressed by equation (8.4) and using equation (8.2), it follows that:

$$\delta k = \delta k' \left(\frac{\Delta l/\lambda_0}{\Delta l/\lambda}\right)^2 = \delta k' \left(\frac{k_m}{k}\right)^2 = \frac{k - k_m}{k_m} \left(\frac{k_m}{k}\right)^2 \tag{8.6}$$

Formula (8.6) shows how a new normalized propagation error δk can be computed from the dispersion relations using a deterministic approach. The same error can be computed from an eigenvalue approach by exploiting equations (8.5) and (8.1) as:

$$\delta k = \frac{\theta_0 - \theta}{\theta} = \frac{k_m \Delta l}{2\theta\sqrt{\varepsilon_r \mu_r}} - 1 \tag{8.7}$$

Finally, this error can be computed by obtaining resonant frequencies of homogeneous resonators by performing numerical simulation as:

$$\delta k = \frac{f_0 - f}{f} \tag{8.8}$$

Because δk can be accurately obtained theoretically as well as from numerical simulations, the results from the dispersion relations and numerical simulations in the following analysis will be compared by calculating δk. In order to validate dispersion relations, results obtained from numerical calculations for an arbitrary node spacing may need to be further normalized to a benchmark discretization level of $\Delta l/\lambda = 0.1$, by making use of (8.4) as:

$$\overline{\delta k} = \delta k \left(\frac{0.1}{\Delta l/\lambda} \right)^2 \tag{8.9}$$

The normalized propagation error $\overline{\delta k}$ can be computed directly from the dispersion relations by choosing $k_m \Delta l = 0.2\pi$ and using (8.6) or (8.7).

It should be noted that a relationship between δk and δf can be found from (8.3) and (8.5) as:

$$(1 + \delta k)(1 + \delta f) = 1 \tag{8.10}$$

This equation shows that the two relative errors, δk and δf must have opposite sign and approximately the same absolute value (for small values). This is important to notice in order to make comparisons between results obtained in this chapter in terms of δk and results obtained in [56, 58] in terms of δf. Equations (8.8) and (8.10) show that δk has a physical interpretation as an underestimation of a modelled frequency due to the numerical dispersion.

Deviation in the wave velocity due to dispersion is generally anisotropic, i.e. it is dependent on the direction of propagation. Bearing this in mind, the relative error δk will be investigated for different angles of propagation φ, ϑ defined as $\varphi = \arccos(k_z/k)$ and $\vartheta = \arctan(k_y/k_x)$ and illustrated in Figure 8.2. Note that the relative error δk is, in fact, the magnitude of an error vector $\vec{\delta k}$ which have spherical coordinates $(\delta k, \varphi, \vartheta)$.

In the following sections, possible ways of visualizing dispersion errors in three-dimensional space and of extracting information of interest, will be presented, followed by systematic comparisons of the dispersion errors in available symmetrical condensed nodes when modelling arbitrary electromagnetic properties of media.

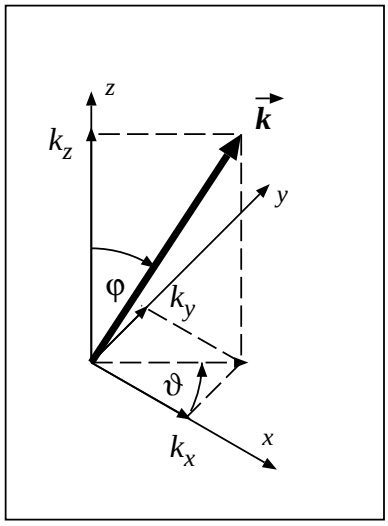

$$\vartheta = \arctan\left(\frac{k_y}{k_x}\right)$$

$$\varphi = \arccos\left(\frac{k_z}{k}\right)$$

$$k_x = k\sin(\varphi)\cos(\vartheta)$$

$$k_y = k\sin(\varphi)\sin(\vartheta)$$

$$k_z = k\cos(\varphi)$$

$$k = \sqrt{k_x^2 + k_y^2 + k_z^2}$$

Figure 8.2 *Components of the propagation vector*

8.3 Visualization of dispersion errors

By using the dispersion relations for different condensed nodes, derived in the previous chapter, analyses of physical solutions and calculation of δk can be performed by using either a deterministic or an eigenvalue approach. As discussed before, if only analytical tools are used, the eigenvalue approach can be applied for a general direction of propagation only in the case of the 12-port SCN and the SSCN, while for the other cases the deterministic approach must be used.

When using the eigenvalue approach, the mesh discretization is set by choosing an appropriate $k_m\Delta l$, while the components of the theoretical propagation vector are calculated for different angles (see Figure 8.2) as:

$$\begin{aligned} k_x &= k_m\sin(\varphi)\cos(\vartheta) \\ k_y &= k_m\sin(\varphi)\sin(\vartheta) \\ k_z &= k_m\cos(\varphi) \end{aligned}$$

so that a modelled phase shift $\theta = \omega\Delta t$ can be obtained analytically using dispersion relations obtained in the previous chapter. A modelled value of the propagation constant can be then calculated as

$$k = \omega\sqrt{\varepsilon\mu} = \frac{2\omega\Delta t\sqrt{\varepsilon_r\mu_r}}{\Delta l} = \frac{2\theta\sqrt{\varepsilon_r\mu_r}}{\Delta l}$$

and compared to the initially chosen k_m.

Using this procedure for the SCN dispersion relation, a normalized wave vector $\vec{k}/k_m$ has been obtained for different angles of propagation in 3D space and plotted as a parametric plot in Figure 8.3, in which the distance from the coordinate origin corresponds to the amplitude of the normalized wave vector in the particular direction. Typical discretization values chosen are $k_m\Delta l = 0.2\pi$ and $k_m\Delta l = \pi$, corresponding, respectively, to the benchmark discretization ratio of $\Delta l/\lambda = 0.1$ and to the coarsest possible discretization where only two nodes per wavelength are used.

Since electromagnetic waves in an isotropic medium propagate with the same amplitude of the wave vector in all directions, the parametric plot should describe a perfect sphere. It can be seen from Figure 8.3 that for a sufficiently fine discretization, $k_m\Delta l = 0.2\pi$, the wave vector calculated from the SCN dispersion relation do indeed describe a spherical dispersion surface, but this sphere becomes distorted at higher frequencies, as can be seen for the case when $k_m\Delta l = \pi$.

A more convenient way of looking at this distorsion is to measure the deviation from a perfect sphere. The percentage error δk, defined in the previous section and computed here by using equation (8.7), is plotted in Figure 8.4, as a parametric surface whose distance from the coordinate origin corresponds to the magnitude of the error in the particular direction. In the case of the SCN, where axial propagation is dispersionless (see eqn. 7.28), the plot represents a three dimensional shape with nulls along the axes and lobes on main diagonals. Note that even for very coarse discretization of $k_m\Delta l = \pi$ the error along principal axes is zero.

Similar plots can be obtained for the SSCN modelling media with arbitrary electromagnetic parameters. For example, the parametric plot of the percentage error in the SSCN where $\varepsilon_r\mu_r = 2$ is shown in Figure 8.5. It indicates that dispersion for axial propagation exists, unlike the case of the 12-port SCN modelling free-space, shown in Figure 8.4, where the propagation error along axes was zero.

From the plots shown in Figures 8.3–8.5 it can be seen that an axial symmetry exist, which is expected since the TLM method models propagation in positive and negative directions equally. By exploiting this fact, we can consider only one octant of 3D space, for example, for $x, y, z > 0$. The percentage error shown in Figure 8.4 can be, for example, plotted as a projection of the first octant onto the xz-plane, as shown in Figure 8.6 for $k_m\Delta l = 0.2\pi$.

The inner curve (lobe) of the parametric plot from Figure 8.6 represents a trajectory of the error vector for propagation in a coordinate plane, while the outer

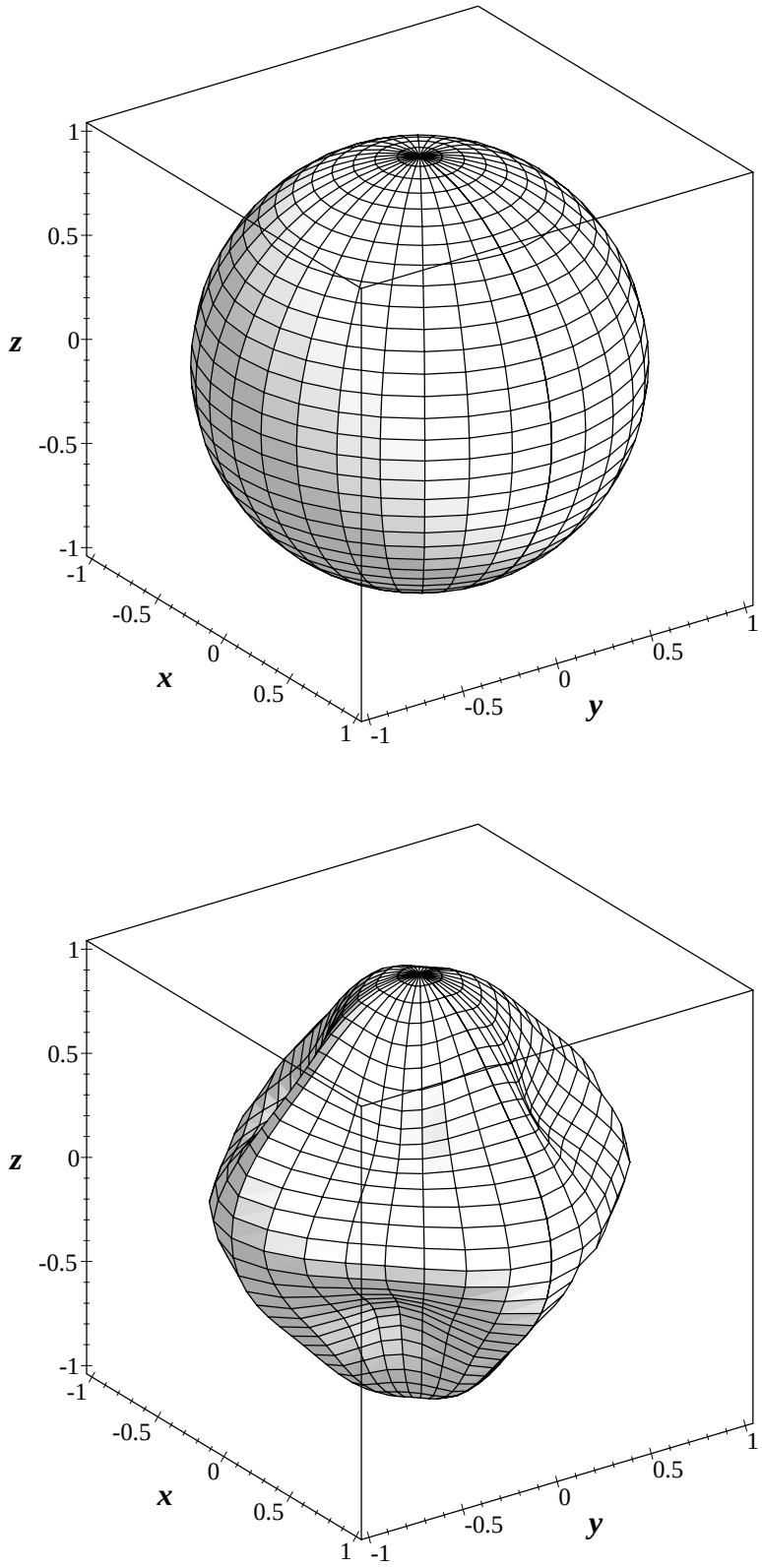

Figure 8.3 *Parametric plot of the normalized wave vector $\vec{k}/k_m$ in SCN mesh for $k_m\Delta l = 0.2\pi$ (top) and $k_m\Delta l = \pi$ (bottom)*

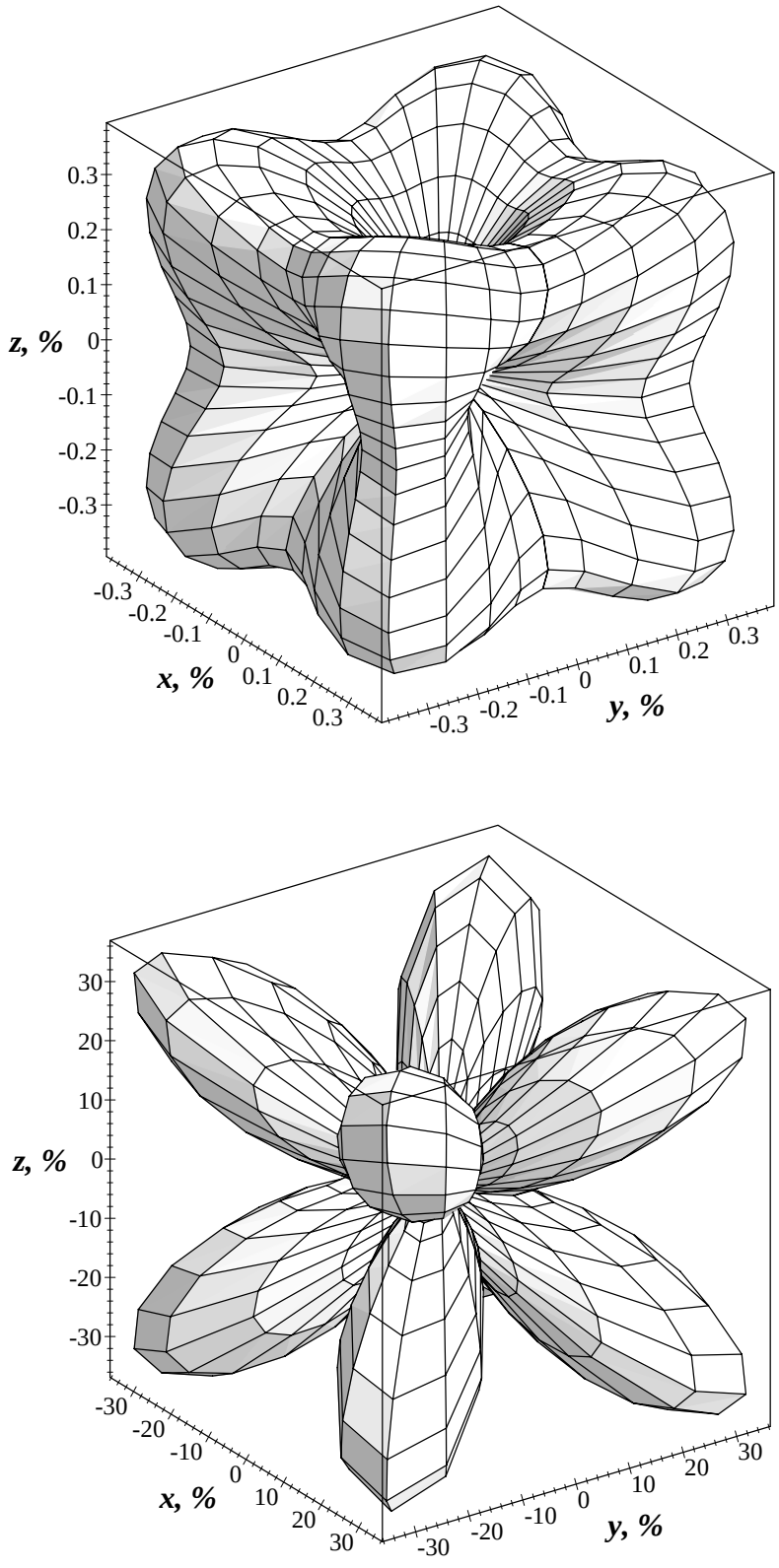

Figure 8.4 *Parametric plot of the percentage propagation error δk in SCN mesh for $k_m \Delta l = 0.2\pi$ (top) and $k_m \Delta l = \pi$ (bottom)*

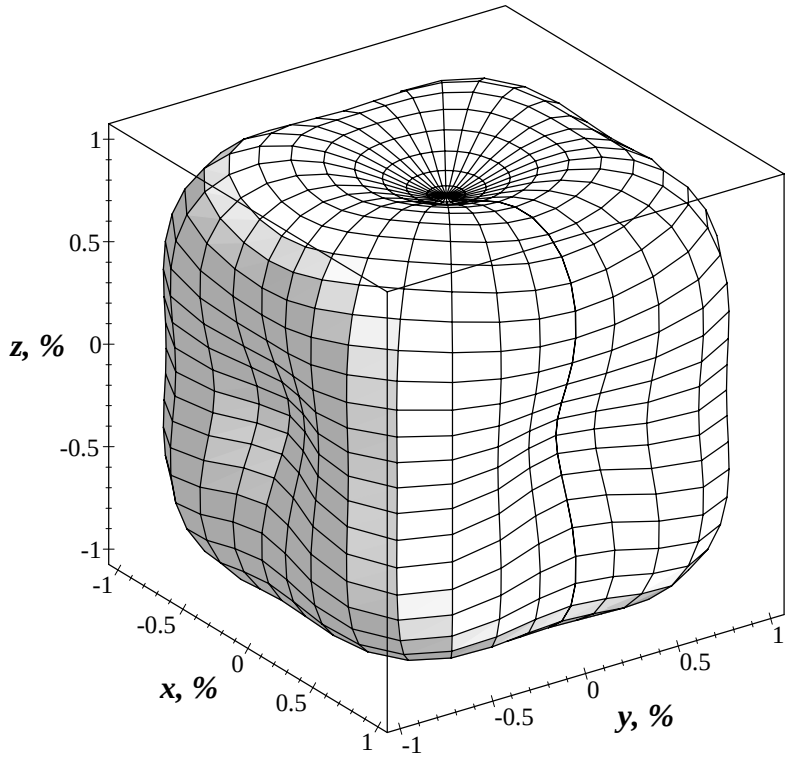

Figure 8.5 *Parametric plot of the percentage propagation error δk in SSCN mesh for $k_m \Delta l = 0.2\pi$ and $\varepsilon_r \mu_r = 2$*

lobe contains information about the error along main and coordinate diagonals. From this plot we can also notice a symmetry with respect to the diagonal, since, for the uniform mesh ($\Delta x = \Delta y = \Delta z$) the propagation characteristics should be invariant with respect to the order of coordinates determining the propagation direction. This means, for example, that dispersion characteristics for propagation directions **[1,2,0]** and **[2,1,0]** are equal when modelling isotropic media on a uniform mesh. This is not the case, however, in cuboid nodes with arbitrary aspect ratio ($\Delta x \neq \Delta y \neq \Delta z$) which will be shown later in this chapter.

Parametric plots of the wave vectors and percentage errors in Figures 8.3–8.6 provide valuable physical insight into the spatial distribution of propagation errors due to dispersion, however more quantitative data can be extracted by presenting the percentage error as an explicit function of the two spherical coordinates φ and ϑ, but plotted in the Cartesian coordinate system. For example, the propagation error in the SCN for $\Delta l/\lambda = 0.1$ is illustrated in Figure 8.7 using contour and surface plots. The contour plot shows this error for angles $0 \leq \varphi, \vartheta \leq 90°$, which correspond to the first octant of a 3D coordinate system. Positions of main axial and diagonal propagation directions are indicated in the contour plot of Figure 8.7,

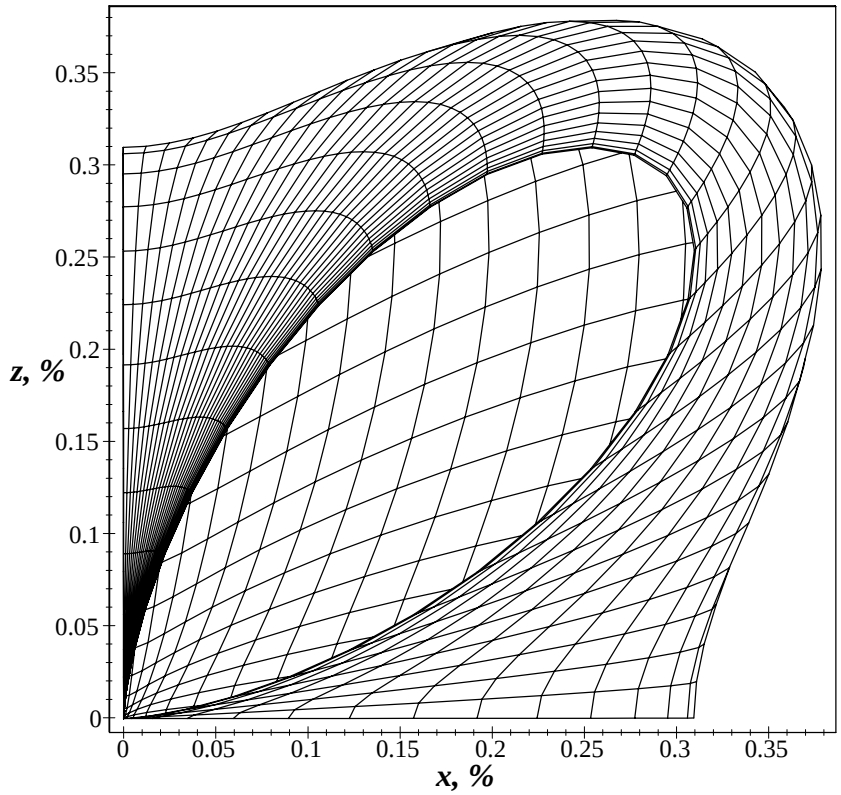

Figure 8.6 *Projection of the first octant of SCN percentage error onto the xz-plane, for* $k_m \Delta l = 0.2\pi$

from which can be seen that maximum error occurs for propagation along the main space diagonal **[1,1,1]**.

Because of the symmetry experienced in the uniform mesh, δk is shown in the surface plot of Figure 8.7 only for angles $0 \leq \vartheta \leq 45°$. A cross-section of the surface plot for $\vartheta = 0$ gives the information on the propagation errors along a coordinate plane, in this case $y = 0$, and contains directions **[u,0,v]**, where $\mathbf{u}, \mathbf{v}$ are integers. A cross-section for $\vartheta = 45°$ gives these errors for propagation along a diagonal plane, in this case $x = y$, and contains directions **[u,u,v]**.

Figure 8.8 shows the propagation errors in the TLM mesh using the 12-port SCN, along these two planes, for different levels of discretization. It can be seen from Figure 8.8 that by using a coarser mesh, or equivalently by decreasing the wavelength, the propagation error increases superlinearly, as a function of second order, thus confirming that the TLM method is second order accurate. For example, it can be seen that propagation errors for a discretization $\Delta l/\lambda = 0.2$ are around four times higher than for the discretization $\Delta l/\lambda = 0.1$, for all propagating directions.

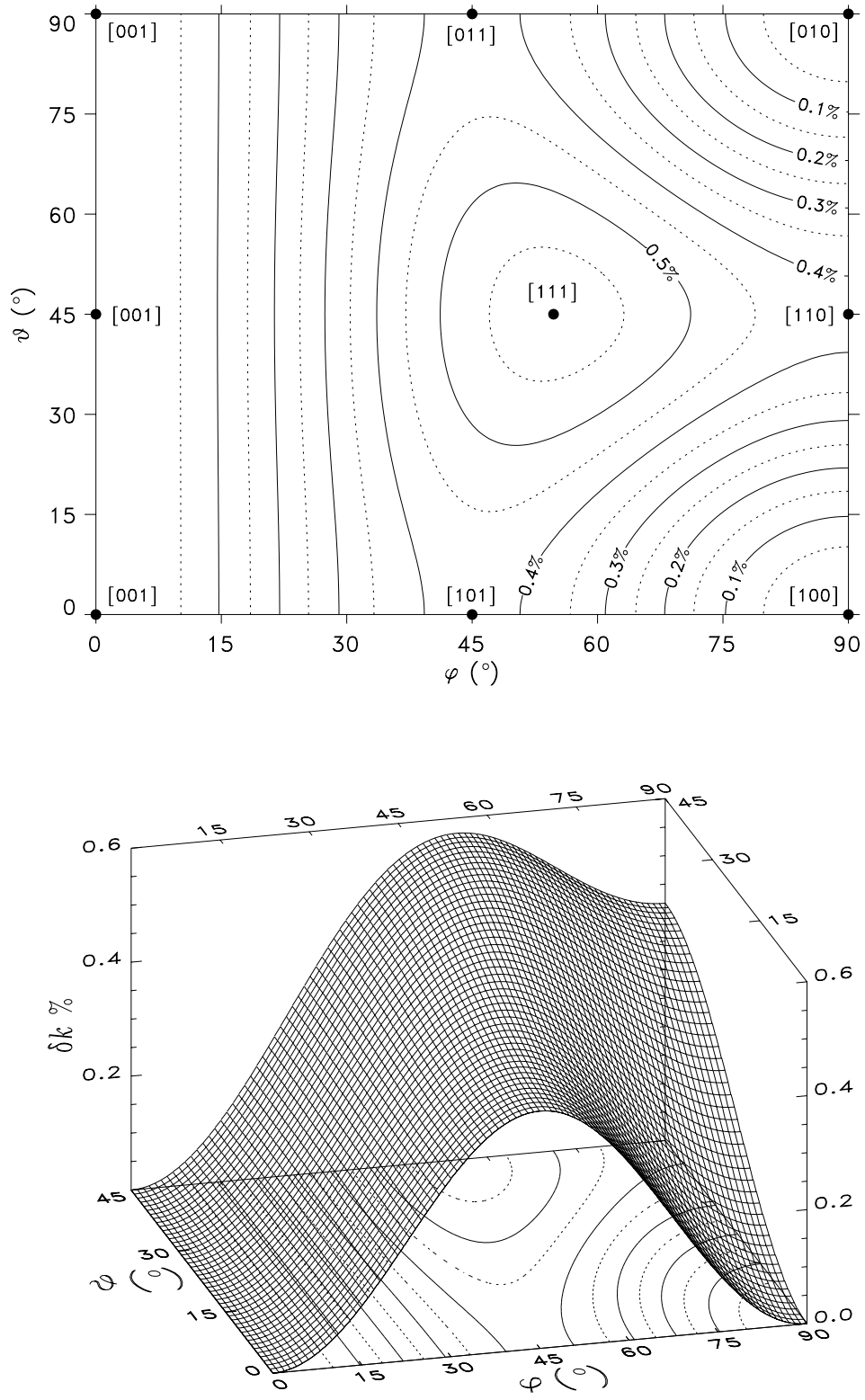

Figure 8.7 *Percentage propagation error in SCN for* $\Delta l/\lambda = 0.1$

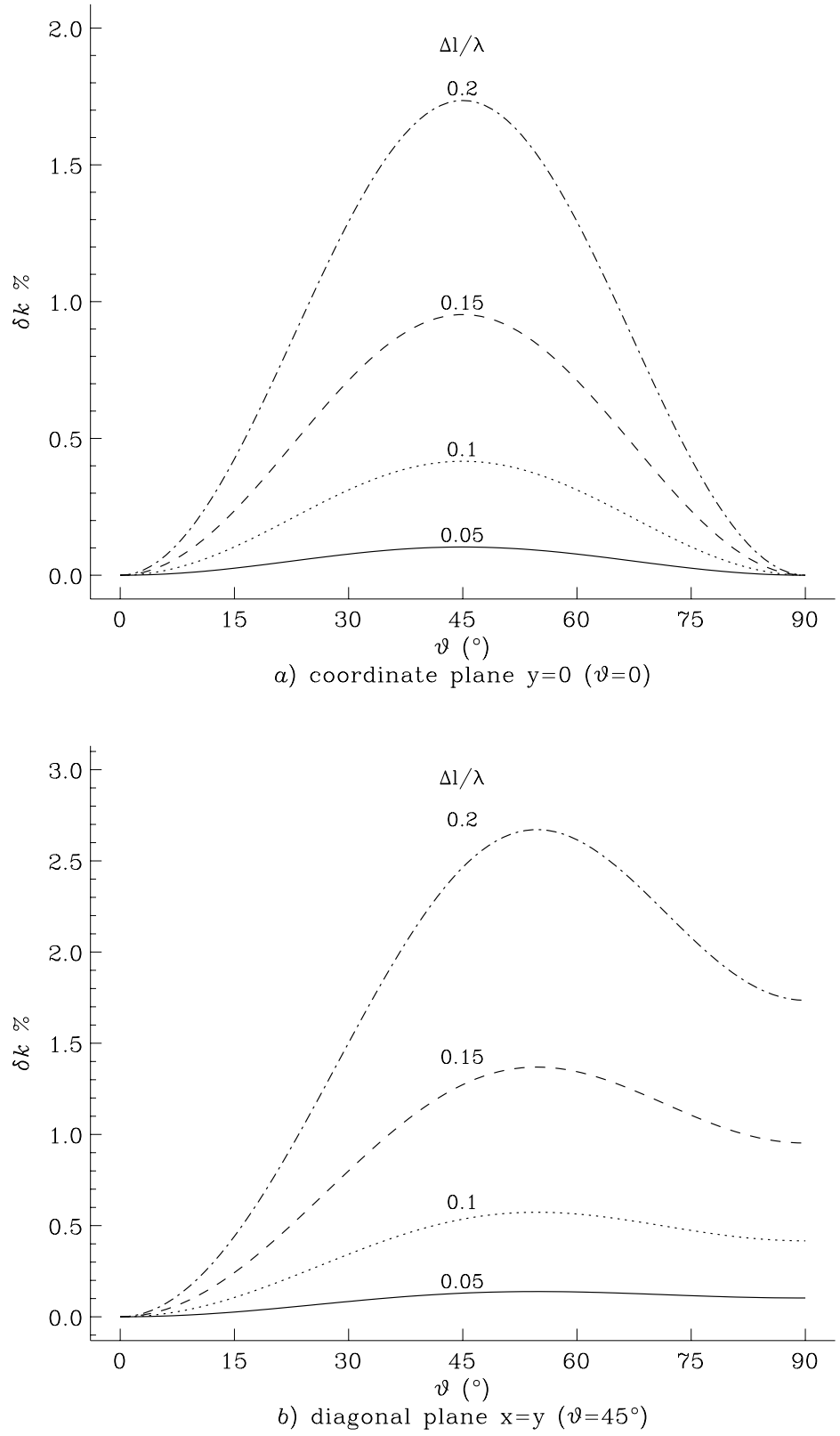

Figure 8.8 *Percentage propagation error in the SCN along a coordinate and a diagonal plane, for different discretization levels*

8.4 Dispersion in uniform meshes

In this section the deterministic approach is used to compare propagation errors in uniform TLM meshes modelling media with arbitrary ε, μ with different available nodes (stub-loaded SCN, HSCN, SSCN). The phase shift θ, and two of the components of the propagation vector are chosen initially, while the third component of the propagation vector is computed from the algebraic form dispersion relations derived in the previous chapter. It should be pointed out that in this case, the exact angle of the propagation direction is not known before determining the remaining component of the modelled wave vector. This means that along with the calculation of the propagation error and its normalization using equation (8.6), the propagation angles are also calculated and stored to facilitate accurate plots of error diagrams.

The initial value of θ will be chosen in all calculations performed in this section according to equation (8.1) for $k_m \Delta l = 0.2\pi$, which is equivalent to a discretization of 10 nodes per wavelength. Accordingly, the propagation error for this case will be denoted as $\overline{\delta k}$.

In order to validate results obtained from the dispersion relations, simulations of resonant frequencies in homogeneous cubic resonators will be performed [58]. The propagation error will be computed from modelled and theoretical frequencies using equation (8.8) and normalized to $\overline{\delta k}$ using equation (8.9). Numerical data obtained from simulations will be represented in the error diagrams shown in this section by diamond symbols.

Using the dispersion relation obtained in the previous chapter, the propagation errors in all directions can be obtained and plotted for the SSCN, the HSCN and the stub-loaded SCN in Cases 1 and 2. The propagation errors for propagation along the coordinate planes, denoted as subcase (a), and along the diagonal planes, denoted as subcase (b), can be performed for all available nodes, including the stub-loaded SCN in Case 3. (Cases 1, 2 and 3 are explained in Table 7.2.)

8.4.1 Propagation in 3D space

The analysis starts with plotting propagation errors using three-dimensional surface plots, for the example of modelling a material with $\varepsilon_r \mu_r$=8. The error diagrams for different condensed nodes are shown in Figures 8.9–8.11.

As already found in the previous chapter, the TLM mesh with the HSCN and the stub-loaded SCN in Case 1 produces two physical solutions, corresponding to

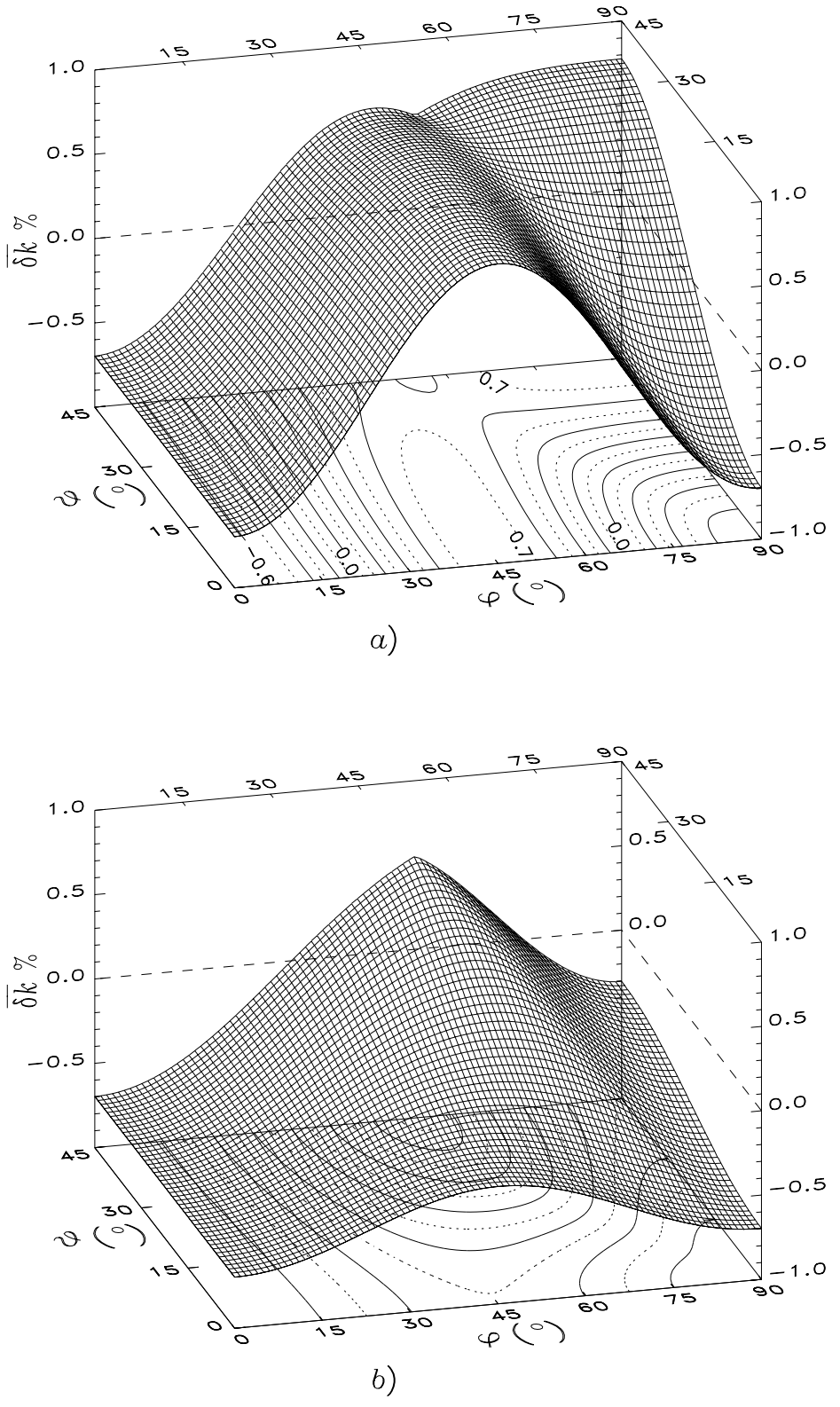

Figure 8.9 *Two solutions for percentage propagation error in the HSCN and the stub-loaded SCN in Case 1, for $\varepsilon_r \mu_r = 8$, with an interpretation given in Table 8.1*

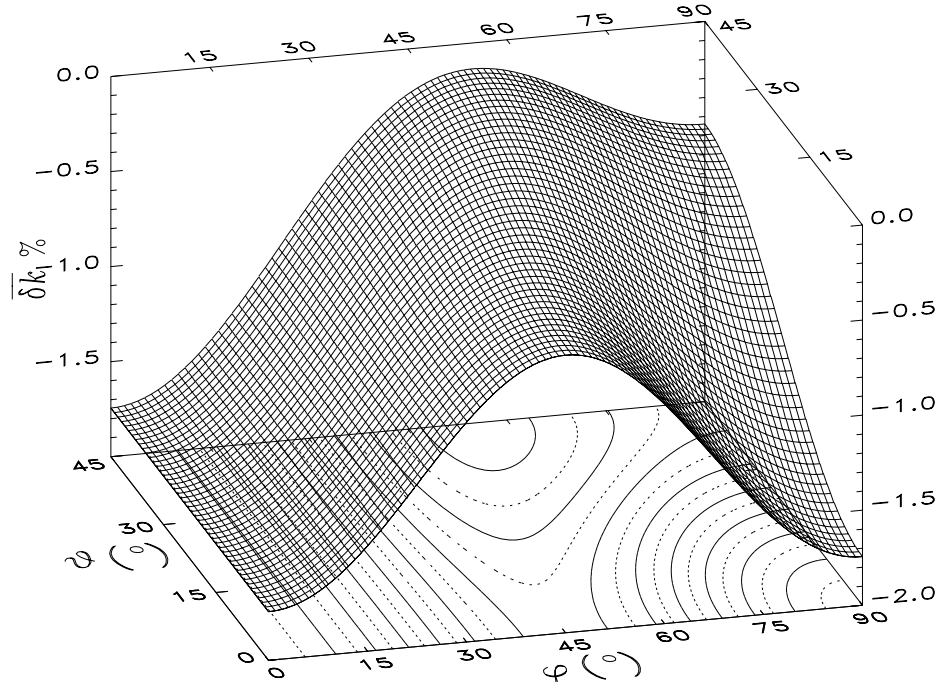

Figure 8.10 *Percentage propagation error in the stub-loaded SCN in Case 2 for* $\varepsilon_r \mu_r = 8$

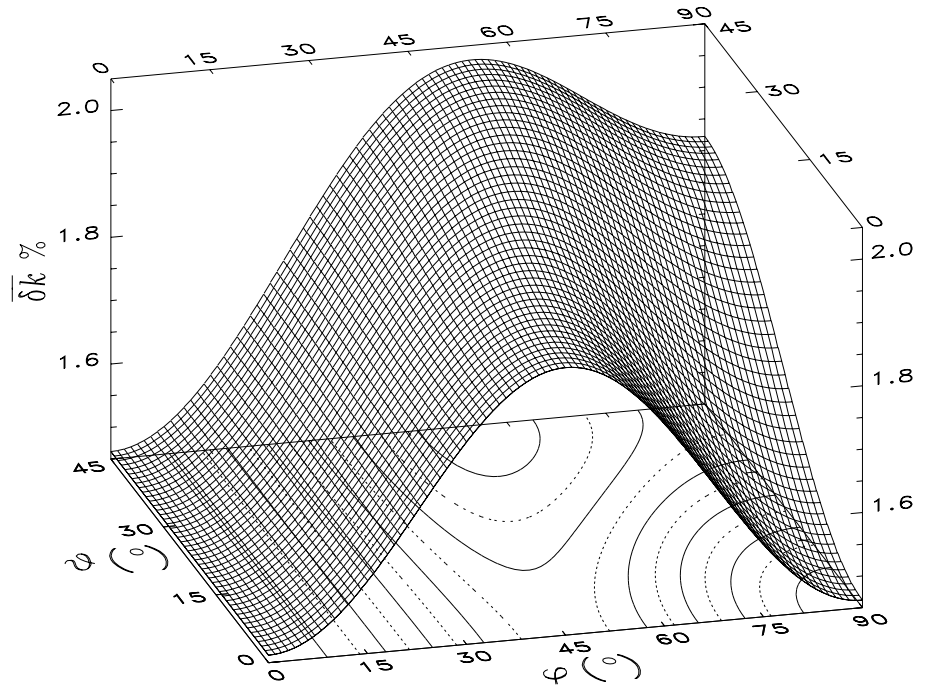

Figure 8.11 *Percentage propagation error in the SSCN for* $\varepsilon_r \mu_r = 8$

the two orthogonal wave polarizations. In the case of propagation in a coordinate plane, for example xy-plane, these solutions have physical interpretation of the modes containing either the field components E_z, H_x, H_y or H_z, E_x, E_y [58]. Further in the text, the former modes are referred to as transverse electric, or TE modes, whereas the latter are referred to as transverse magnetic, or TM modes. For propagation along arbitrary directions in 3D space, a clear interpretation of these modes is difficult to present. For this reason, the two orthogonal solutions of the dispersion relations in an arbitrary direction will be associated to the corresponding modes obtained for propagation in a coordinate plane and, for brevity, will be referred to as TE and TM modes.

Analytically, it is not possible to determine which solution correspond to which particular mode. However, by computing errors from TLM simulations modelling wave propagation in a coordinate plane, the solutions plotted in Figures 8.9a,b can be identified with the corresponding TE and TM modes as summarized in Table 8.1.

Case/Mode	TE	TM
Stub-loaded SCN for $\varepsilon_r = 8$, $\mu_r = 1$	8.9b	8.9a
Stub-loaded SCN for $\varepsilon_r = 1$, $\mu_r = 8$	8.9a	8.9b
HSCN Type I, $\varepsilon_r \mu_r = 8$	8.9b	8.9a
HSCN Type II, $\varepsilon_r \mu_r = 8$	8.9a	8.9b

Table 8.1 *Interpretation of errors plotted in Figures 8.9a,b*

Apart from the two different solutions encountered in the HSCN and the stub-loaded SCN in Case 1, Figure 8.9 also shows the coexistence of positive and negative propagation errors for different angles of propagation, a condition which is described as *bilateral dispersion* in [58].

From Figure 8.10 it can be seen that in the stub-loaded SCN in Case 2 ($\varepsilon_r = \mu_r$), the absolute values of the errors are generally higher than in the Case 1 and in the HSCN. However, the difference between a maximum and a minimum error, taken for all possible directions, is approximately the same in both cases (around 1.5%). The error surface $\overline{\delta k}(\vartheta, \varphi)$ in Case 2 is shifted towards negative values, but its shape is similar to that of the 12-port SCN modelling free-space, plotted in Figure 8.7.

Finally, Figure 8.11 shows that propagation errors are positive in the SSCN and

they are higher than in the previous cases. However, the difference between the minimum and maximum error is smaller then in the previous cases (around 0.6%, similar to the 12-port SCN). The error surface $\overline{\delta k}(\vartheta, \varphi)$ is now shifted towards positive values, but its shape is almost identical to that of the 12-port SCN modelling free-space, plotted in Figure 8.7.

8.4.2 Propagation in coordinate and diagonal planes

As indicated before, the cross-section of the surface plots in Figures 8.9–8.11 for $\vartheta = 0$ gives information on the propagation errors along a coordinate plane, in this case $y = 0$, containing directions **[u,0,v]**. Cross-section for $\vartheta = 45°$ gives these errors for propagation along a diagonal plane, in this case $x = y$, containing directions **[u,u,v]**. Since these two planes contain most of the directions of practical interest, such as for example **[1,0,0]**, **[1,1,0]** , **[1,1,1]**, **[1,0,2]**, and **[1,1,2]**, for which equivalent resonant frequencies can be easily simulated in cubic resonators, they will be given particular consideration here.

The analysis that follows is performed for the benchmark discretization of $\Delta l/\lambda = 0.1$. The propagation error $\overline{\delta k}$ is given in percentages. The results for the two orthogonal solutions occurring in the HSCN and the stub-loaded SCN in Case 1 are interpreted with respect to the stub-loaded SCN modelling dielectric materials ($\mu_r = 1$) or equivalently with respect to the Type I HSCN modelling any ratio of ε_r/μ_r. The complementary interpretation of these solutions applies for the stub-loaded SCN when $\varepsilon_r = 1$ and for the Type II HSCN. The error diagrams for propagation along the coordinate and diagonal planes are shown in Figures 8.12–8.15 on pages 160–163 for different condensed nodes.

Figure 8.12(a) shows the propagation error $\overline{\delta k}$ in the stub-loaded SCN in Case 1 and the HSCN for propagation along the coordinate plane $y = 0$. Figure 8.12(b) shows the propagation error in the same nodes for propagation along the diagonal plane $x = y$. The upper and lower sets of curves in Figures 8.12(a),(b) correspond to the two orthogonal wave polarizations described earlier as TM and TE modes, respectively. Both parts of Figure 8.12 show the coexistence of positive and negative propagation errors, described as bilateral dispersion in [58]. They show that dispersion solutions at a given frequency converge as $\varepsilon_r\mu_r \to \infty$ and that the maximum positive propagation error occurs for a direction **[1,0,1]** (the diagonal in a coordinate plane), whereas the maximum negative error occurs for axial propagation. The two sets of curves representing orthogonal solutions of (7.58) converge for axial propagation (Fig. 8.12(a)) and propagation along the main space diago-

nal (Fig. 8.12(b)). Note from Figures 8.12(a),(b) that the error $\overline{\delta k}$ for TM modes in directions **[1,0,2]** and **[1,1,2]** as well as for both modes in direction **[1,1,1]** is virtually independent of ε_r, μ_r.

Figures 8.13(a),(b) show the propagation error in the stub-loaded SCN Case 2, for propagation along the coordinate and the diagonal planes, respectively. They show that this error is significantly higher than in Case 1 and in the HSCN, and that the highest error occurs for axial propagation. The solutions at a given frequency converge when $\varepsilon_r\mu_r \to \infty$ but at a slower rate than in the previous case. The propagation error is bilateral for smaller $\varepsilon_r\mu_r$ and negative for higher $\varepsilon_r\mu_r$.

Figures 8.14(a),(b) show the propagation error in the stub-loaded SCN Case 3, for propagation along the coordinate and the diagonal planes, respectively, for $\varepsilon_r\mu_r = const = 8$. Note that the three curves corresponding to values $\varepsilon_r, \mu_r \geq 2$ are very close, indicating that the propagation error for Case 3 for higher values of ε_r, μ_r is similar to that in Case 2, unless $\varepsilon_r \to 1$ or $\mu_r \to 1$ when Case 3 converges to Case 1. As in Case 1, swapping values of ϵ_r and μ_r swaps dispersion solutions for TE and TM modes.

Finally, Figures 8.15(a),(b) show the propagation error in the SSCN, for the same propagation planes as in the previous figures. It can be seen from Figures 8.15(a),(b) that the propagation error for the SSCN is always positive, for all propagation directions and for all materials, hence it is referred to as *unilateral dispersion*, to distinguish from the bilateral dispersion experienced in the stub-loaded SCN and the HSCN. Note that here the highest error occurs on the main space diagonal, as in the case of the 12-port SCN modelling free-space. Note also that curves for different $\varepsilon_r\mu_r$ are uniformly shifted which means that the range of propagation error, that is the difference between the maximum and minimum error considering all directions, is constant within an individual medium. The equal shifting of curves in the plots from Figure 8.15 also suggests that a surface $\overline{\delta k}(\vartheta, \varphi)$, plotted earlier for the example of $\varepsilon_r\mu_r = 8$ on Figure 8.11, will have the same shape as the related surface for the 12-port SCN, for any value of $\varepsilon_r\mu_r$.

Numerical results obtained by performing TLM simulations of homogeneous cubic resonators are marked with diamond symbols and plotted in Figures 8.12–8.15(a) for directions **[0,0,1]**, **[1,0,2]**,**[1,0,1]**,**[2,0,1]**,**[1,0,0]** and in Figures 8.12–8.15(b) for directions **[0,0,1]**, **[1,1,2]**, **[1,1,1]**,**[1,1,0]**. They are found to be in excellent agreement with the analytical plots. Spurious propagating solutions described in the previous chapter do not show a significant impact on the results obtained from these simulations.

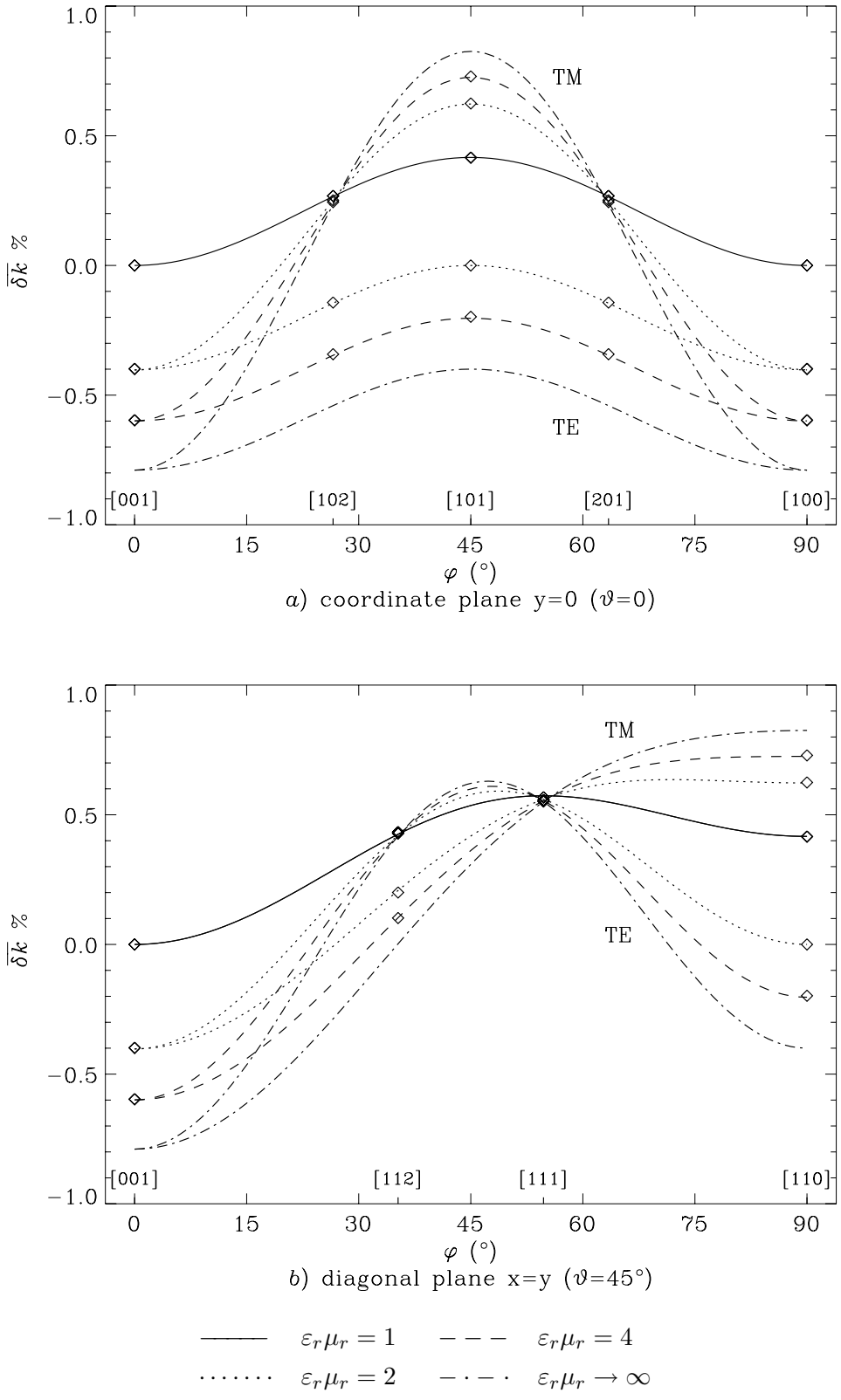

Figure 8.12 *Percentage propagation error in the HSCN and the stub-loaded SCN, Case 1*

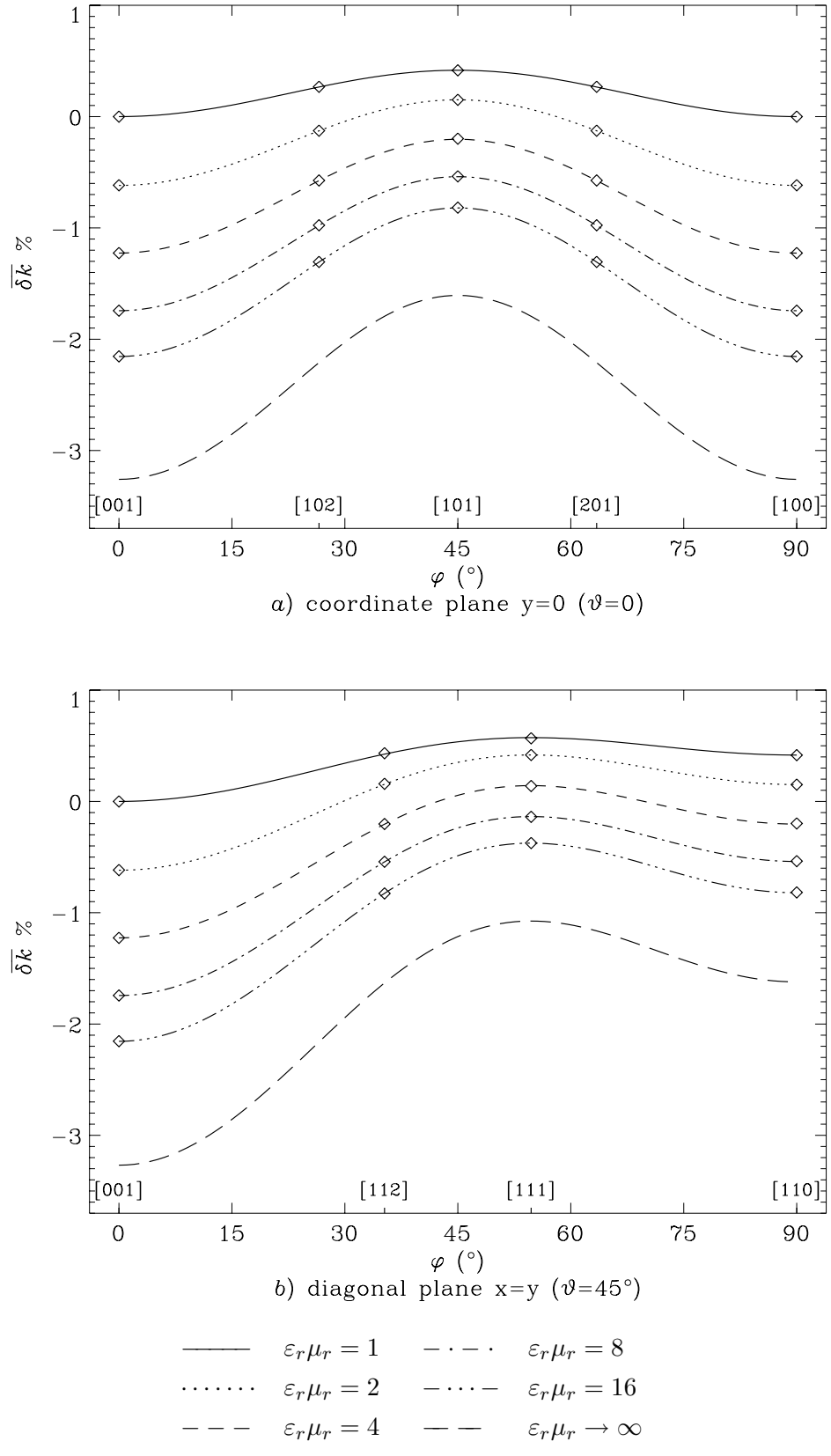

Figure 8.13 *Percentage propagation error in stub-loaded SCN, Case 2*

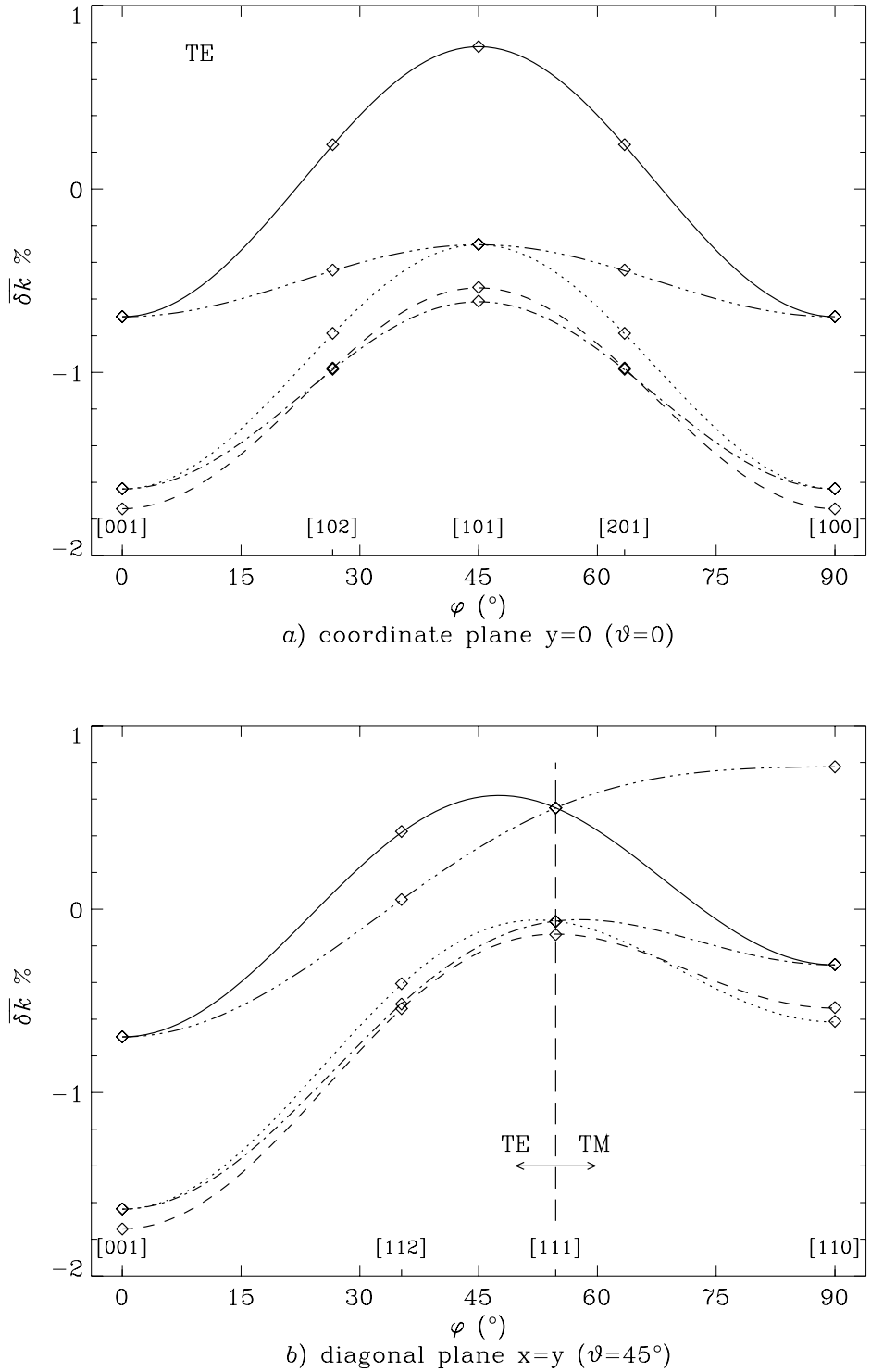

Figure 8.14 *Percentage propagation error in stub-loaded SCN, Case 3*

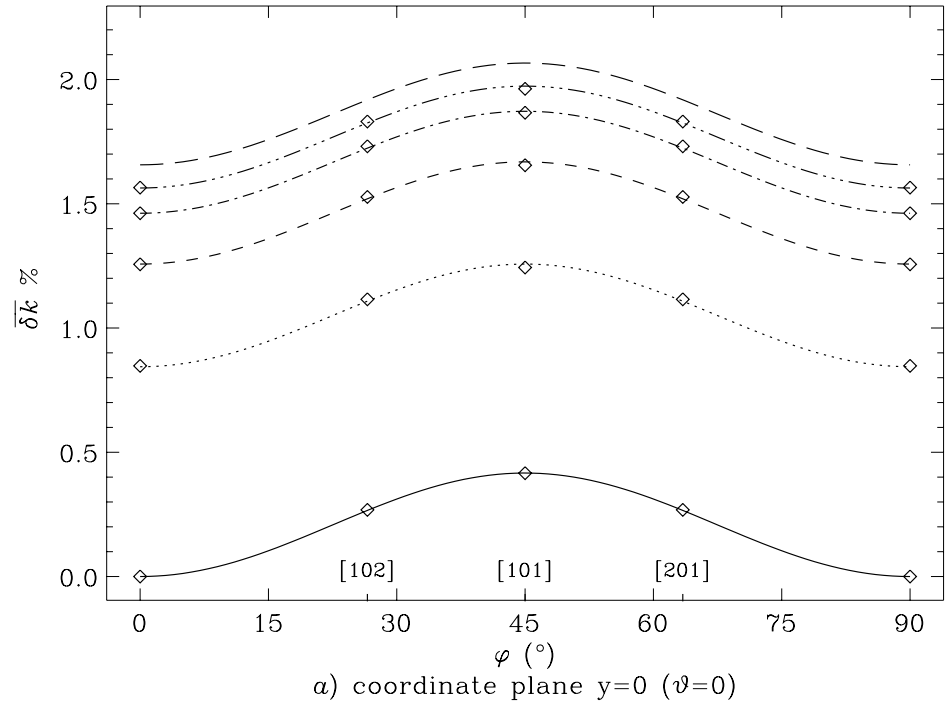

a) coordinate plane y=0 (ϑ=0)

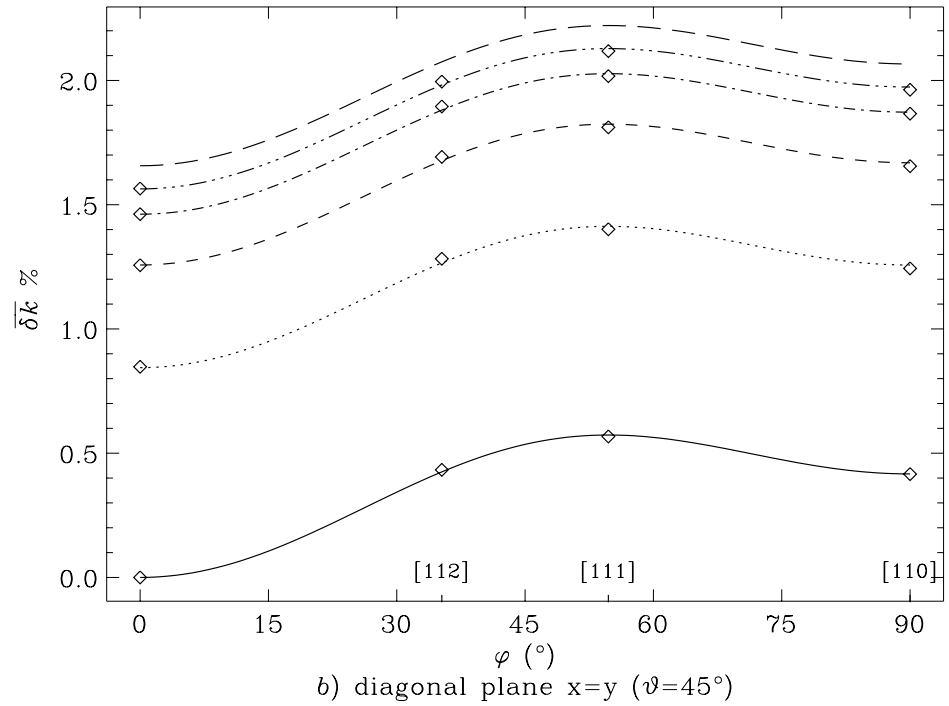

b) diagonal plane x=y (ϑ=45°)

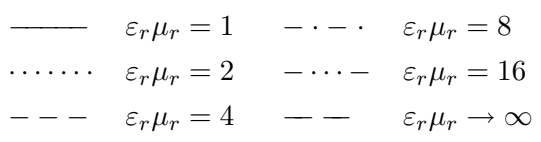

Figure 8.15 *Percentage propagation error in the SSCN*

Node	SCN	Stub-loaded SCN			HSCN	SSCN
		Case 1	Case 2	Case 3		
Error independ. of wave polarization	Yes	No	Yes	No	No	Yes
Error independ. of medium impedance	Yes	No	Yes	No	Yes	Yes
Unilateral propagation error	Yes	No	No	No	No	Yes
Max. positive error $\overline{\delta k}_{\max+}$ (%)	0.57	0.83	0.57	0.83	0.83	2.22
Max. negative error $\overline{\delta k}_{\max-}$ (%)	0.00	0.79	3.26	3.26	0.79	0.00
Error range, $\overline{\delta k}_t = \overline{\delta k}_{\max+} + \overline{\delta k}_{\max-}$	0.57	1.62	3.83	4.09	1.62	2.22
Storage N (node ports)	12	15	18	18	15	12
Normalized error range, $\overline{\delta k}_{t,18}$ (%)	0.44	1.43	3.83	4.09	1.43	1.69
MUL operations per node, M	6	9	12	12	12	6
ADD/SUB operations per node	24	48	54	54	48	48
Theoretical performance index P_t	12.39	3.18	1.07	1.00	2.38	3.23
Same line and medium impedances	Yes	No	Yes	No	No	No
Simple connection procedure	Yes	Yes	Yes	Yes	No	No

Table 8.2 *Numerical characteristics of various TLM condensed node schemes for uniform mesh*

8.4.3 Summary of results

A summary of the numerical characteristics of the existing condensed nodes for modelling isotropic media on a uniform mesh is shown in Table 8.2. The properties of the 12-port SCN are also shown for reference, although this node cannot model inhomogeneous configurations.

The first set of rows of Table 8.2 concerns the nature of the dispersion. In TLM, errors due to dispersion depend normally on the discretization ($\Delta l/\lambda$), wave velocity in media ($1/\sqrt{\varepsilon\mu}$) and direction of propagation (ϑ, φ). However, the two orthogonal solutions of the dispersion relation for the stub-loaded SCN and the HSCN reveal that dispersion for these nodes is further dependent on the wave polarization. This can have the effect of splitting degenerate modes, which otherwise would have the same resonant frequencies, and changing the polarization of propagating waves, as shown in [56]. The dispersion in the stub-loaded SCN is also function of the medium impedance, i.e. it depends on μ_r/ε_r for $\mu_r\varepsilon_r = const.$ Both the stub-loaded SCN and the HSCN experience bilateral dispersion [58]. In contrast, the nature of the dispersion errors in the SSCN is identical to that of the basic SCN, i.e. dispersion is independent of the wave polarization and of the medium impedance (for $\mu_r\varepsilon_r = const$) and the propagation error is unilateral. These are regarded as advantageous features of the SSCN.

The second set of rows of Table 8.2 shows maximum propagation errors calculated for the discretization of $\Delta l/\lambda = 0.1$, assuming all propagation angles and all media with properties $1 \leq \varepsilon_r \mu_r < \infty$. Table 8.2 shows that the total error range $\overline{\delta k}_t$, defined as the sum of the maximum positive error $\overline{\delta k}_{\max +}$ and the maximum negative error $\overline{\delta k}_{\max -}$, is the highest in the stub-loaded SCN in Cases 2 and 3 and smallest in the HSCN.

In order to compare further the performance of various nodes, the error range $\overline{\delta k}_t$ should be combined with the memory storage expressed by number of node ports, N, to produce a figure of merit. Assuming that the total available memory is N_t, and if the two different nodal structures contain N_1 and N_2 node ports, where say $N_1 < N_2$, it follows that total number of nodes which can be used in the mesh for the two cases is, respectively, $n_1 = N_t/N_1$ and $n_2 = N_t/N_2$. It follows further that, assuming a three dimensional cubic mesh, the node spacing for the first node type can be chosen to be smaller by a factor $A = (n_2/n_1)^{1/3} = (N_1/N_2)^{1/3}$ than for the second node type, thus effectively increasing the accuracy by a factor A^2 in the mesh formed using the first type of nodes (assuming second order accuracy). Choosing $N_2 = 18$, a normalized error range can be defined, according to the above reasoning as:

$$\overline{\delta k}_{t,18} = \overline{\delta k}_t \left(\frac{N}{18} \right)^{2/3} \tag{8.11}$$

Effectively, $\overline{\delta k}_{t,18}$ represents the error range for each node assuming the same total storage and it can be seen from Table 8.2 that it is smallest for the HSCN.

As discussed in Chapter 6, run-time depends critically on the number of multiplicative operations (MUL) per node per time step, designated here by the letter M. Assuming that the total number of available memory locations is N_t then the total number of MUL operations per time step in the whole mesh is $M_t = MN_t/N$. Since an increase in M_t and an increase in $\overline{\delta k}_{t,18}$ both degrade the overall computational efficiency in the same way, a product of these two values should be computed to relate the propagation error, storage requirements and run-time requirements in a single number. By calculating the inverse of $\overline{\delta k}_{t,18} M_t$ normalized to the smallest value, that is for the stub-loaded SCN in Case 3, a theoretical performance index P_t may be introduced and computed for different nodes, which is shown in Table 8.2. Index P_t suggests that the SSCN is the superior node for modelling general cases.

Further consideration should be given to dispersive effects at interfaces between nodes modelling different materials. Preliminary studies, presented in the following chapter, and also results reported in [56, 58] indicate that these effects indeed

exist but may not be significant, however a more thorough study is necessary to describe these effects analytically. It should be noticed from Table 8.2 that, apart from the basic 12-port SCN, only in the stub-loaded SCN Case 2, does the characteristic impedance of link lines equal the intrinsic impedance of medium. As will be shown in Chapter 9, this feature is important in minimizing dispersive effects at interfaces.

In general, the optimum TLM scheme for uniform mesh is problem dependent. Data in Table 8.2 offer guidance as to what may be achievable in each case. To summarize this information further, it appears that when modelling dielectric materials (Case 1), the stub-loaded SCN and the HSCN are the most accurate and are reasonably computationally efficient, but degenerate propagation modes are likely to be split. For the general case ($\varepsilon_r, \mu_r > 1$), the HSCN offers the best accuracy, but the higher efficiency and the identical dispersion for orthogonal wave polarizations arguably makes the SSCN a better choice.

8.5 Dispersion in graded meshes

Dispersion relations of the presently available nodes for graded meshes can be studied in a similar way as in the case of the uniform mesh. However, there is a greater range of input parameters, hence, apart from studying propagation error as a function of the material properties, it can be, in the case of a graded mesh, studied as function of node aspect ratio and time step. Since a big disadvantage of the graded stub-loaded SCN is that the allowable time step is generally prohibitively small, for practical reasons the analysis presented in this section considers only the HSCN and the SSCN.

The same methodologies used in the analysis of the uniform mesh are used here with some minor differences in the interpretation of the node spacing Δl. Since the node spacing in a graded node differs in the three principal directions, Δl will be regarded as an equivalent cubic cell parameter, related to the time step as $\Delta l = 2c\Delta t$, where c is the wave velocity in the background medium. Also, the discretization level described earlier by $k_m \Delta l$ has now to be described with respect to a particular node dimension, for example, $k_m \Delta x$.

The analysis starts with the investigation of the spatial distribution of propagation error as a function of angles ϑ and φ described in Figure 8.2. It should be pointed out that spherical coordinates $(\varphi, \vartheta) = (90°, 0°)$ describes propagation along the x-axis, $(\varphi, \vartheta) = (90°, 90°)$ describes propagation along the y-axis, and

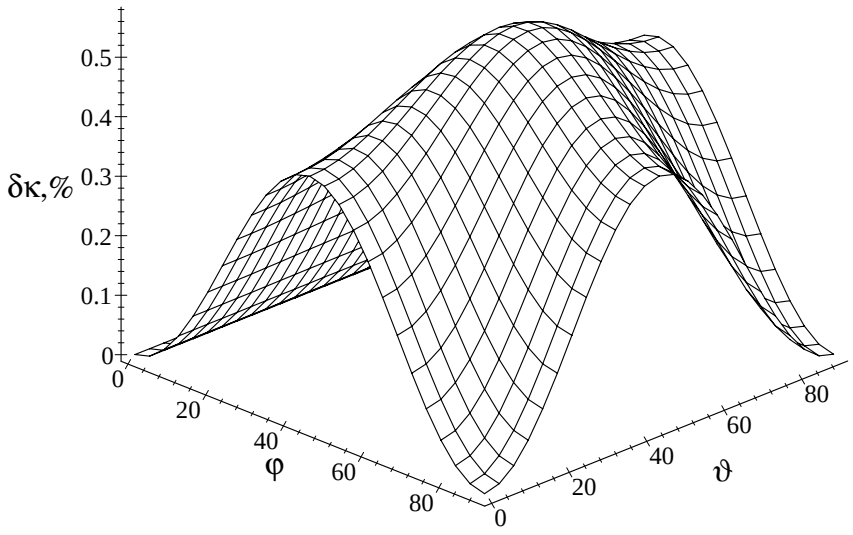

Figure 8.16 *Percentage propagation error in a cubic SCN for* $k_m\Delta x = 0.2\pi$

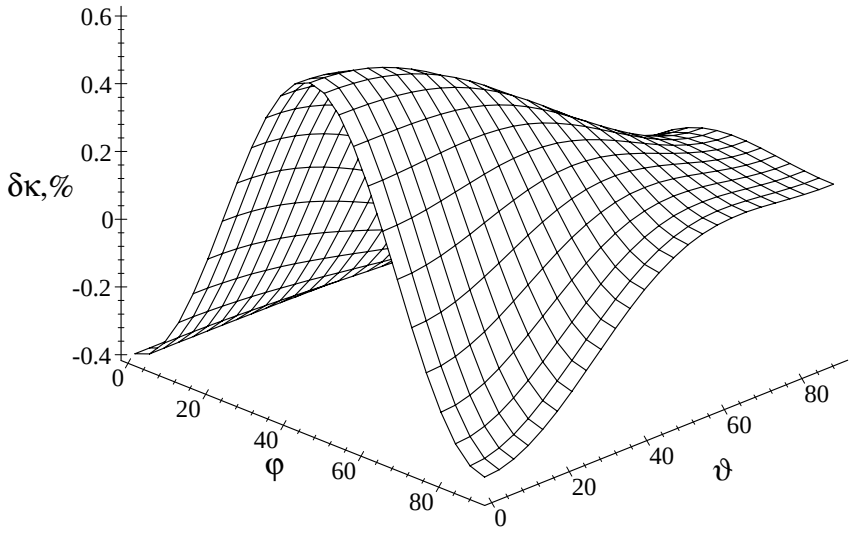

Figure 8.17 *Percentage propagation error in the SSCN with grading set at* $\Delta x = 2\Delta y = \Delta z$ *(for* $k_m\Delta x = 0.2\pi$*)*

$\varphi = 0°$ describes propagation along the z-axis. Accordingly, $\varphi = 90°$ describes propagation in the xy coordinate plane, whereas $\vartheta = 0°$ describes propagation in the xz coordinate plane.

Figures 8.16–8.18 show the percentage error in a uniform mesh with the SCN, and in graded meshes with the SSCN and the HSCN of aspect ratio $\Delta x = 2\Delta y = \Delta z$, each for the discretization level of $k_m\Delta x = 0.2\pi$, i.e. for 10 Δx node spacings

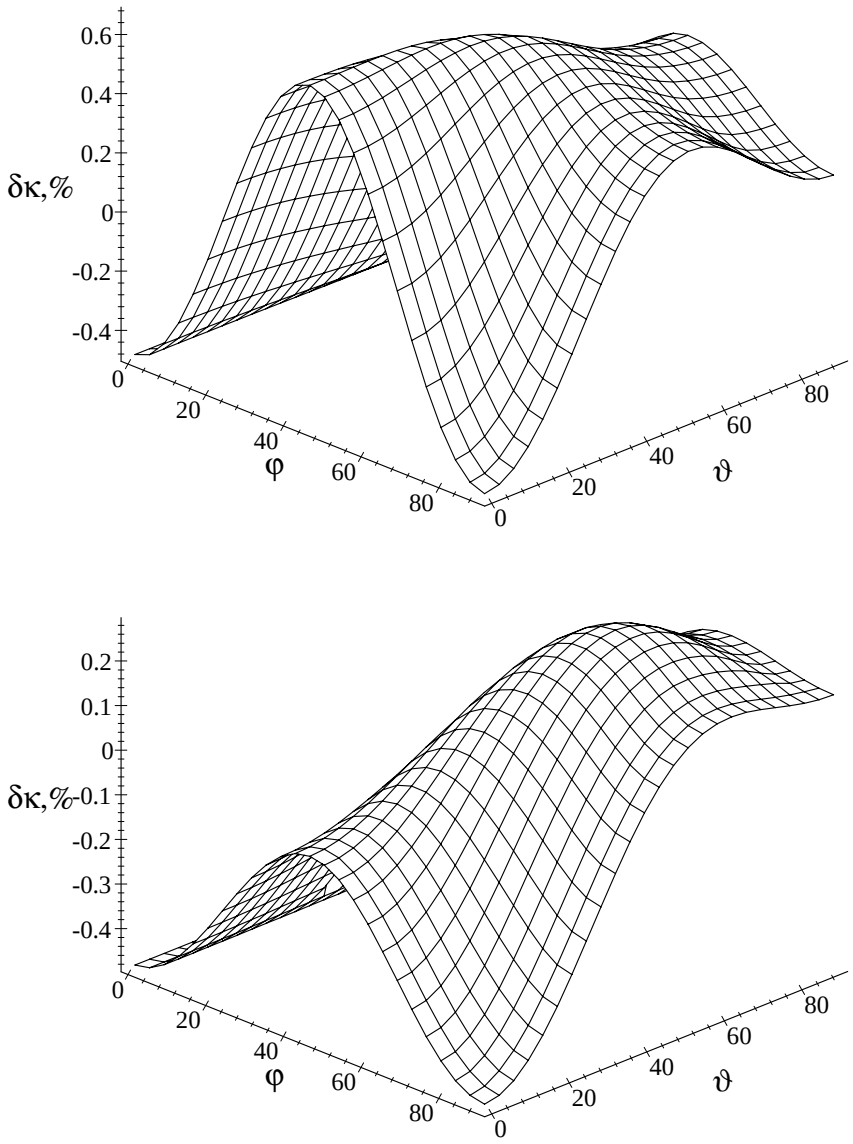

Figure 8.18 *Percentage propagation error in the HSCN for two different polarizations with grading set at* $\Delta x = 2\Delta y = \Delta z$ *(for* $k_m \Delta x = 0.2\pi$*)*

per wavelength. The time step for graded nodes is chosen to be the maximum permissible, in this case $\Delta t = 1.46\Delta t_0$ for the SSCN and $\Delta t = 1.26\Delta t_0$ for the HSCN, where $\Delta t_0 = \Delta y/(2c)$ corresponds to the time step of a cubic node with node spacing Δy. Note that two solutions for the HSCN are plotted in Figure 8.18.

Comparing the plots in Figures 8.16–8.18, it can be seen that the symmetry found in the cubic SCN with respect to the plane $\vartheta = 45°$ (Figure 8.16) is removed when grading is introduced (Figures 8.17–8.18). This means that contrary to the

analysis performed for the uniform mesh, where it was sufficient to study the error distribution for angles $0° \leq \vartheta \leq 45°$ and $0° \leq \varphi \leq 90°$, the full analysis in the case of a graded mesh requires a study for $0° \leq \vartheta, \varphi \leq 90°$.

Observing in Figures 8.17–8.18 the two cross-sections corresponding to the xy and xz planes ($\varphi = 90°$ and $\vartheta = 0°$, respectively), it can be seen that, contrary to the cubic SCN, in the cuboid nodes the error distribution in the xy plane differs from that in the xz plane, due to the grading introduced. Also, it can be observed from Figures 8.17–8.18 that in both graded nodes the error is smallest for the propagation directions with small angles to the y-axis, that is for $\varphi, \vartheta \to 90°$. This shows that the most accurate modelling is achieved for a wave propagating along the direction corresponding to the smallest node dimension, in this case Δy, as expected.

Further analyses of the dispersion in graded meshes can be done by studying errors for the propagation along a coordinate plane, namely $z = 0$ (or equivalently $\varphi = 90°$). Figure 8.19 shows the percentage propagation error $\overline{\delta k}$ in the HSCN operating on different time steps with grading set at $\Delta x = 2\Delta y = \Delta z$, calculated for the spatial discretization of $\Delta x/\lambda = 0.1$. Three pairs of curves are plotted, for $\Delta t = \Delta t_{\max} = 1.26\Delta t_0$, $\Delta t = \Delta t_0$ and $\Delta t \to 0$. The upper and lower curves of each pair represent the solutions for different wave polarizations, as indicated in the figure.

To verify that the curves in Figure 8.19 reliably describe the dispersion relation of the HSCN, a number of simulations is performed using the graded HSCN TLM mesh in a cubic resonator, as earlier described. The normalized propagation error $\overline{\delta k}$, computed from the results of TLM simulations for the resonant modes [**100**], [**210**], [**110**], [**120**] and [**010**], is plotted in Figure 8.19 by diamonds for $\Delta t = \Delta t_{\max}$ and by boxes for $\Delta t = \Delta t_0$. It is obvious from Figure 8.19 that the errors $\overline{\delta k}$ obtained from the simulations exactly coincide with those predicted by the dispersion relation.

An important detail which can be noticed from Figure 8.19 is that propagation error depends on the time step and that the total error range is the smallest when using the maximum time step $\Delta t_{\max}$. This is expected, from the following intuitive reasoning. Considering a uniform mesh, the maximum time step of a (cubic) node modelling material $\varepsilon\mu$ is $\Delta t_{\max} = \Delta l\sqrt{\varepsilon\mu}/2$. However, when modelling inhomogeneous problems in time-domain TLM, the node must operate at the time step imposed by the background parameters ε_0, μ_0. Hence, the node in the medium with parameters $\varepsilon_0\varepsilon_r, \mu_0\mu_r$ operates on a time step $\Delta l\sqrt{\varepsilon_0\mu_0}/2$ which is

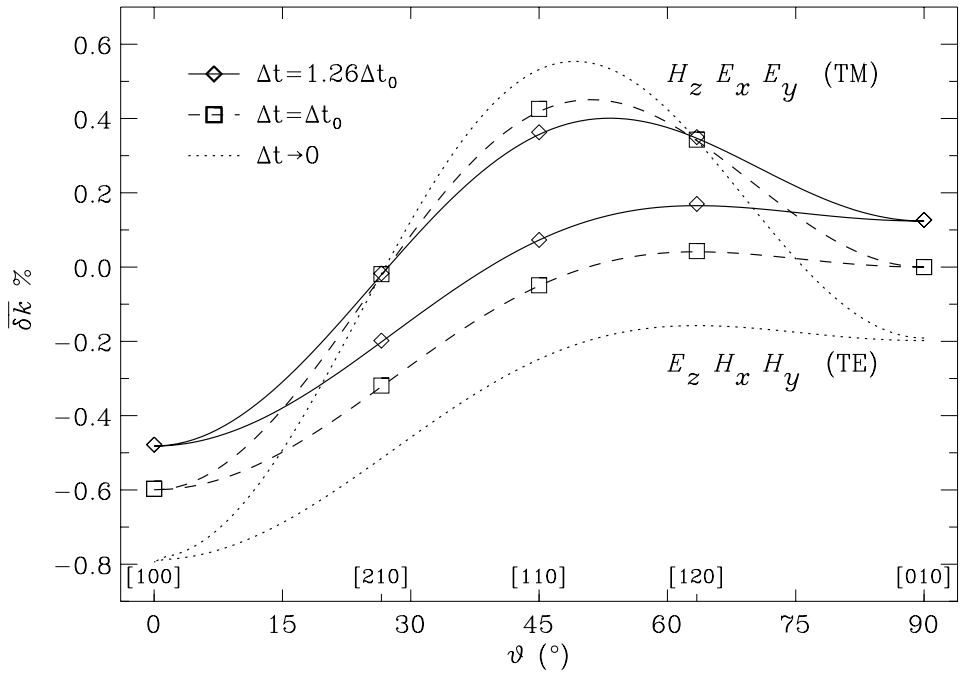

Figure 8.19 *Percentage propagation error in the HSCN for grading set at* $\Delta x = 2\Delta y = \Delta z$

equal to $\Delta t_{\max}/\sqrt{\varepsilon_r \mu_r}$. The increase in $\varepsilon_r \mu_r$ can be therefore interpreted as a decrease in time step. As shown in the analysis of the dispersion relations for the uniform mesh, the propagation error is increased in all types of condensed nodes when modelling materials with higher $\varepsilon_r \mu_r$, hence, this can be now applied to the case of graded mesh as well, to explain the behaviour of errors when decreasing the time step.

Further interesting details can be observed from Figure 8.19. For propagation along the y-axis or at small angles to it, i.e. when $\varphi \rightarrow 90°$, better dispersion properties are observed if Δt_0 is used instead of $\Delta t_{\max}$. From the discussion on the analytical solution of the dispersion relation for graded HSCN in case of propagation along an axis, given in the previous chapter, it follows in fact that the propagation along, say y-axis, will be dispersionless if the HSCN operates on the time step $\Delta y/(2c)$, or Δt_0 in this case. This also confirms the numerical results obtained in [19].

It can be noted from Figure 8.19 that, for a given time step, four different propagation errors, and hence four different resonant frequencies, are obtained for the modes [**120**] and [**210**] with the two different field polarizations. Because of the asymmetrical grading, dispersion is different for these four cases, hence

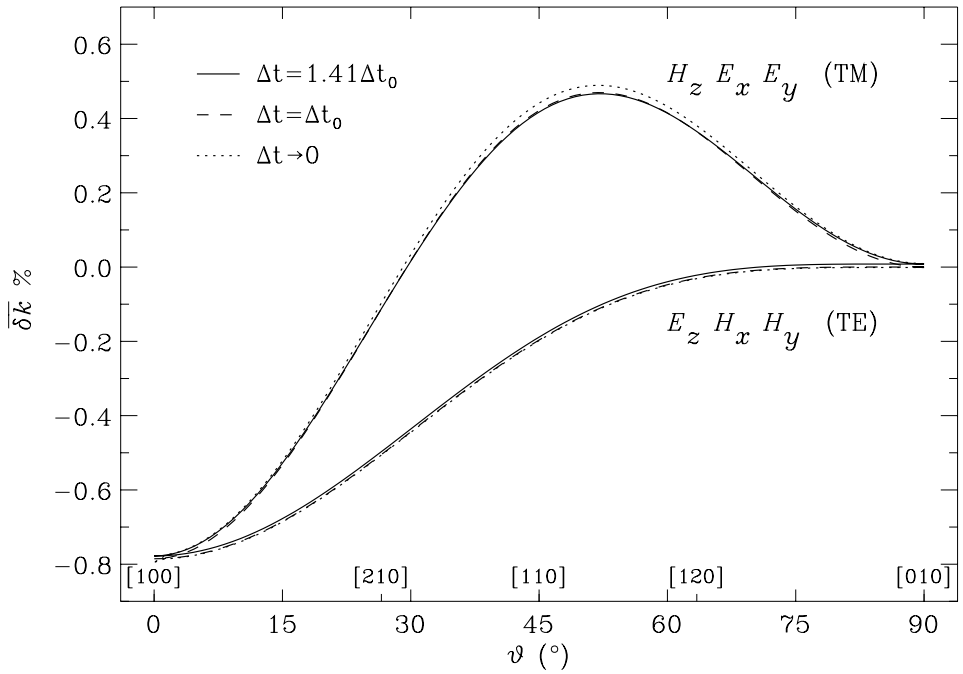

Figure 8.20 *Percentage propagation error in the HSCN for grading set at* $\Delta x = 10\Delta y = \Delta z$

the resonant frequencies are not degenerate as expected for a homogeneous cubic resonator.

A similar set of curves to those plotted in Figure 8.19 is shown in Figure 8.20 for a HSCN with grading set at $\Delta x = 10\Delta y = \Delta z$. Note that in this case $\Delta t_{\max} \approx 1.41\Delta t_0$. Figure 8.20 shows that for a high aspect ratio, in this case $\Delta x/\Delta y = 10$, propagation errors are not very dependent on the time step chosen. Therefore, in such cases any time step can be used with no loss in accuracy, however it should be as high as possible to allow faster completion of a TLM simulation.

The propagation error in a graded TLM mesh with the SSCN of aspect ratio $\Delta x = 2\Delta y = \Delta z$ is studied in Figure 8.21 for different values of time step and propagation along coordinate plane $z = 0$ ($\varphi = 90°$). Note that two sets of parameters are possible for a graded SSCN, hence two error curves appear in Figure 8.21 for $\Delta t \neq \Delta t_{\max}$. It should be noted, however, that the nature of these two solutions is different from those in the HSCN. In the HSCN, two physical solutions of the dispersion relation correspond to different wave polarization. In contrast, the dispersion relation of the SSCN always produces only one physical solution, but the characteristic impedances of link lines in the SSCN can be chosen in two different ways if the time step is smaller than the maximum permissible one.

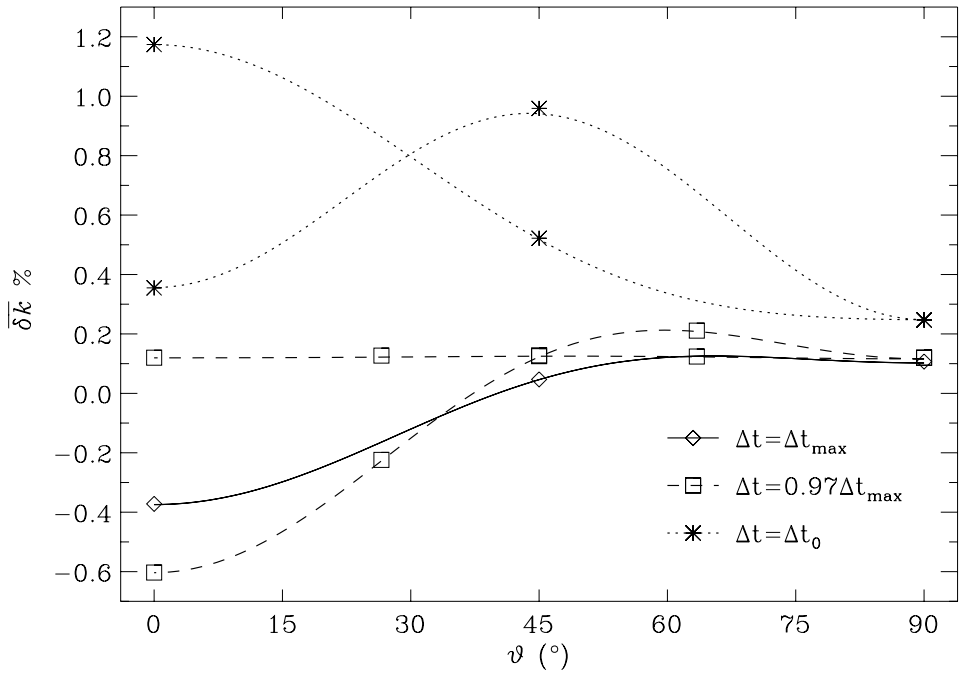

Figure 8.21 *Percentage propagation error in the SSCN for grading set at* $\Delta x = 2\Delta y = \Delta z$

In fact, a choice between the two sets of parameters can be made with respect to the dispersion characteristics, in order to allow a more accurate TLM simulation of a particular problem.

Solutions to the dispersion relation of the graded SSCN plotted in Figure 8.21 in terms of $\overline{\delta k}$ are validated as before, by performing numerical simulations in homogeneous resonators, and results agree well. It can be seen from Figure 8.21 that when decreasing the time step, the propagation error generally increases, as in the case of the HSCN. Note, however, that the margin of errors in the SSCN is higher and more sensitive on changes in the time step than found in the HSCN and shown in Figure 8.19.

A particularly interesting behaviour is found in the SSCN when the time step is just slightly decreased to a value of $0.97\Delta t_{\max}$. In this case, the solutions to the SSCN dispersion relation (for the one set of link line impedances values) produces a flat error curve. This feature, which is not found in the other available nodes, actually means that errors due to dispersion are the same for all angles of propagation in, for this case, the xy plane. This effect will be further explored in the next section to find possible ways of minimizing and eliminating dispersion in TLM simulations.

8.6 Minimization and elimination of dispersion

It has been shown thus far that the dispersion characteristics of a graded TLM condensed node are dependent on the aspect ratio of the node, the time step and the direction of propagation. It will now be shown how the results from the previous analyses can be used in minimizing and eliminating dispersion in the propagation directions of interest.

It follows from Figures 8.17–8.21 that the propagation error is minimal along an axis corresponding to the smallest dimensions of the node and along directions close to it. Hence, the most accurate modelling of wave propagation can be achieved if the aspect ratio of the node is commensurate with the ratio of the wave numbers in the three axial directions. This conclusion is generally valid for other TLM schemes as was shown in [49] for a 'distributed node', which is the counterpart of the SSCN in the expanded node schemes.

Similar results were presented for the SSCN in Chapter 5, when it was shown that modelling of a resonator loaded with dielectric layers is most accurately achieved by adjusting the node aspect ratios to correspond with the direction of wave propagation (Figures 5.6–5.7 and Table 5.2). An intuitive step performed in this example was the use of non-uniform grading in different dielectric layers, to reflect the fact that propagation velocities are different in the different regions. Particular attention is drawn here to the cases of grading depicted in Figures 5.7(c) and (d). In the first case, a uniform grading was used throughout the resonator (Figure 5.7(c)). The time step imposed in the mesh was the one corresponding to the free-space layer and it was, according to Table 5.2, $\Delta t = 0.491\Delta t_0$. The maximum time step for the nodes belonging to the dielectric layer with $\varepsilon_r = 4$ was twice this, namely $\Delta t_\varepsilon = 0.982\Delta t_0$, since $\sqrt{\varepsilon_r} = 2$, but this part of the mesh had to operate on a lower time step to ensure time synchronism. As shown in the previous section, decreasing the time step for a node increases the propagation error, so the deviation in the resonant frequency for the example studied was mainly due to a disparity in the maximum allowable time steps of the two layers.

When a non-uniform grading is introduced, as illustrated in Figure 5.7(d), the maximum time step for the free-space region was increased to $\Delta t = 0.938\Delta t_0$, becoming very close to the maximum time step for the dielectric regions Δt_ε which remained the same as in the previous case. The ratio between the maximum time steps in two regions was now 0.96, hence the accuracy was significantly improved, as was shown in Table 5.2, with the additional benefits of an increased time step and decreased number of cells.

Adjusting of the node aspect ratio in different dielectric layers to achieve commensurating time steps and hence better accuracy, can be called 'smart grading'. This approach was, in fact, fundamental in the derivation of 2D and 3D nodes proposed in [33, 72], where the time step was set for one dielectric region and the grading of other regions was chosen to ensure time synchronism. The results achieved in modelling planar structures with these nodes [73] confirm the high accuracy predicted by the dispersion analysis performed in this chapter.

The way of improving accuracy, discussed so far, was based on the *a priori* setting of the parameters of the mesh to favour propagation directions of interest. Now, *a posteriori* minimization and even total elimination of dispersion effects will be explored, by using 'flattening of dispersion'. It was already indicated in Figure 8.21 that for a particular combination of grading and time step, the error curve may become flat, in other words, the relative propagation error can be made equal at all angles for propagation in a particular plane. A similar effect, but assuming that the time step is always the maximum one, can be seen from the following example.

Assume that we are mainly interested in accurate modelling of waves propagating in a coordinate plane, e.g. xy. In this case, the dimension Δz is of no particular importance and hence can be varied to achieve a 'good' dispersion characteristic. Figure 8.22 shows error curves in the xy-plane, for different values of Δz when $\Delta y = \Delta x$. A flat error curve can be obtained for $\Delta z = \sqrt{3}\Delta x$, hence the error at the coordinate diagonal ($\vartheta = 45°$) is reduced from 0.42% in case of cubic node to 0.28% in case of the graded one. The permissible time step in the graded mesh is 15% greater than the one with the cubic nodes and the number of cells is reduced by a factor $1/\sqrt{3}$. Furthermore, because the numerical errors are uniform in all directions, they can be easily eliminated, for example, when calculating resonant $[N_x N_y 0_z]$ frequencies in a cubic resonator, by using the formula:

$$f_0 = f\left(1 + \overline{\delta k}\left(\frac{\Delta x/\lambda}{0.1}\right)^2\right)$$

which can be derived by combining equations (8.8) and (8.9). Here f and f_0 are simulated and corrected frequency values, respectively, $\overline{\delta k}$ is the relative propagation error obtained for the discretization $\Delta x/\lambda = 0.1$ ($\overline{\delta k} = \delta k = 0.28\%$ in the previous example) and λ is the wavelength of the resonant mode $[N_x N_y 0_z]$, which can be calculated as:

$$\lambda = \frac{2D}{\sqrt{N_x^2 + N_y^2 + N_z^2}}$$

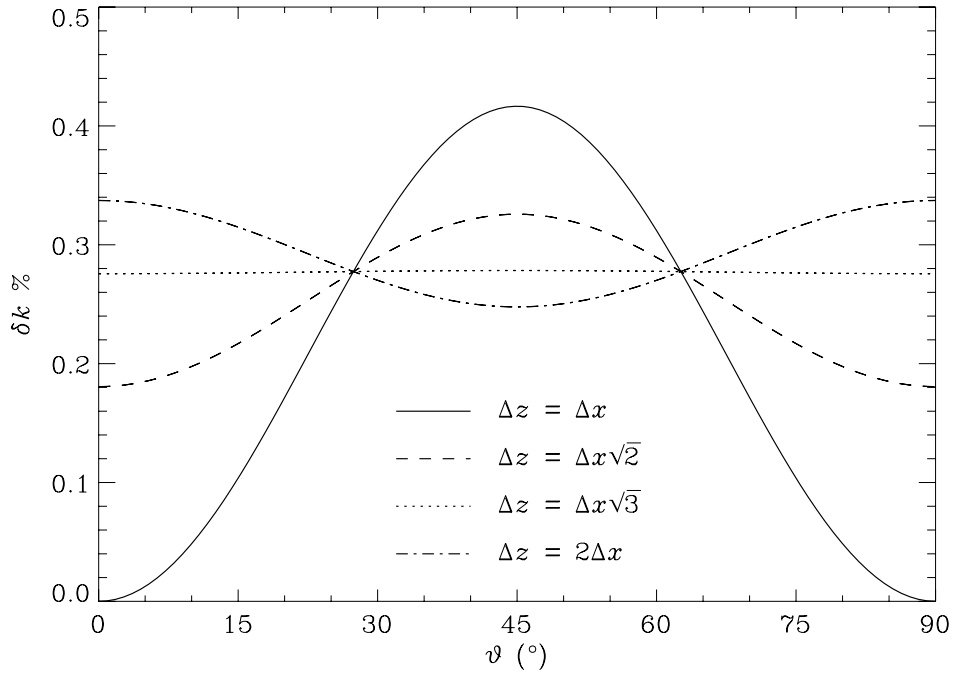

Figure 8.22 *Percentage propagation error in the SSCN for different gradings and* $\Delta x/\lambda = 0.1$

where D is the linear dimension of the cubic resonator, N_x and N_y are the numbers of half wavelengths in the x and y directions, respectively, and $N_z = 0$.

This approach was tested by performing numerical simulation of the propagation within a cubic resonator, for a range of propagation modes $[N_x N_y 0_z]$, namely **[100]**, **[010]**, **[110]**, **[120]**, **[210]**, **[220]**, **[130]** and **[310]**. For the chosen cell dimension of $\Delta x/D = 0.1$, which yields discretization factors $\Delta x/\lambda$ ranging from 0.05 for the **[100]** mode to ≈ 0.16 for the **[310]** mode, the relative deviation of the corrected frequency f_0 from the analytical one was always smaller than 10^{-4}.

It is interesting to observe the distribution of errors in other directions for the SSCN graded as in the previous example. Figure 8.23 depicts the magnitude of the percentage propagation error in 3D space using surface and parametric plots. As expected, the propagation error for angles $\varphi \to 0°$, that is along and close to the z-axis, is rather high, but only errors for $\varphi \to 90°$ were of interest here. From the surface plot of Figure 8.23 it can be seen that, for a given φ, the error is almost independent of ϑ, i.e. of the angles between x and y axes. This can be also seen in the parametric plot of Figure 8.23 through the existence of concentric circles around the z-axis. The constant value of δk for a given φ, may facilitate a minimization and elimination of dispersion in the propagating planes other than

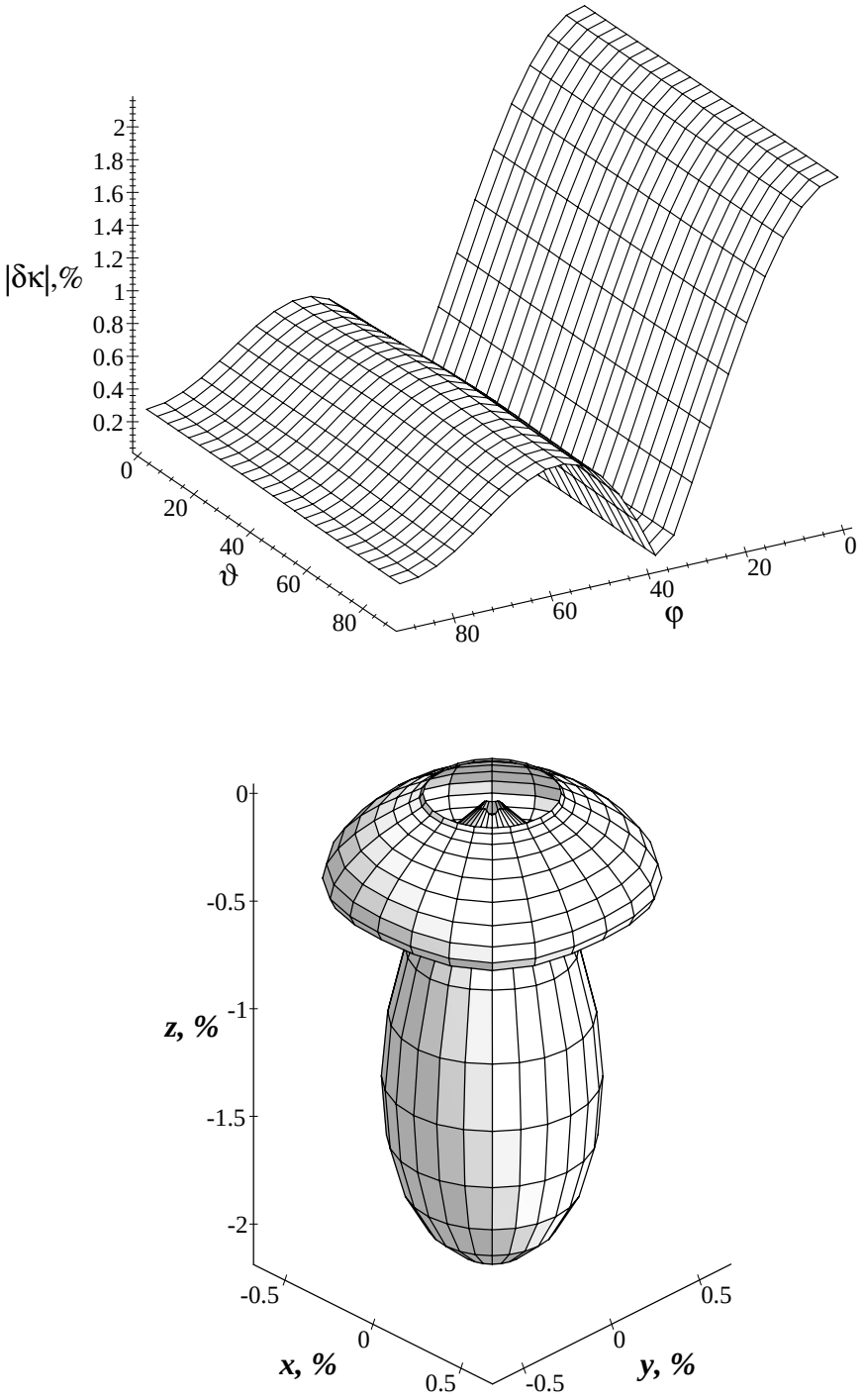

Figure 8.23 *Surface and parametric plot of the propagation error (absolute value) in a graded SSCN for* $\Delta y = \Delta x$, $\Delta z = 1.73\Delta x$ *and* $\Delta x/\lambda = 0.1$

coordinate ones (defined by $\varphi = const \neq 0°$), using a similar *a posteriori* correction procedure as before.

8.7 Summary

Physical solutions of the dispersion relations derived in Chapter 7 were further explored in this chapter. Efficient ways of studying and visualizing dispersion errors were presented and a detailed quantitative analysis of the results was performed. The dispersion errors were studied for uniform and graded meshes formed by presently available condensed nodes and the results were systematically compared and analysed. The analytical results obtained by solving dispersion relations were validated by modelling resonant frequencies in homogeneous cubic resonators. Possible ways of minimizing dispersion errors by selection of the node aspect ratio and time step were also explored.

The dispersion analysis presented in these last two chapters can be combined with the theoretical foundation of the general symmetrical condensed node, described in the first part of the thesis, in order to explore possibilities of deriving new, optimized TLM schemes. Given the theoretical instrument to describe new nodes (Part One) and the systematic procedures to quantify their accuracy and performance (Part Three), in the final part of this thesis some of the several further advanced node developments will be presented.

Part IV

Further Developments

Chapter 9 Advanced nodes with improved dispersion characteristics

9.1 Introduction

The main objective in the derivation of the SSCN performed in Chapter 5 was to reduce storage requirements by eliminating the need for stubs. An additional benefit of this, as it was revealed in Chapter 6, was a higher efficiency in terms of CPU run-time, compared to the previous nodes. In this chapter, however, the main goal will be to derive new nodes which will have more advantageous dispersion properties, and hence, improved numerical accuracy. The theoretical foundation of the general symmetrical condensed node (GSCN), established in Part One, will be used in the derivation of new nodes.

The dispersion analysis performed in Part Three has shown that the alterations made to the basic 12-port SCN, in terms of adding stubs and varying the characteristic impedance of link lines, caused different effects in the dispersion characteristics, depending on how these alterations were done.

In the conventional stub-loaded SCN, where open- and short-circuit stubs were added whilst the characteristic impedance of link lines was kept equal to the intrinsic impedance of the background medium, several features in the solution of the dispersion relation were noticed. In the general case, when $\varepsilon_r \neq \mu_r$, two physical solutions were obtained, corresponding to the two orthogonal wave polarizations. Also, it has been demonstrated that dispersion in a medium with constant $\varepsilon_r \mu_r$ depends on its intrinsic impedance, i.e. on the factor μ_r/ε_r. Both types of behaviour are in contrast to the linear dispersion characteristics of Maxwell's equations and represent numerical errors. In addition, in comparison to the basic 12-port SCN, bilateral dispersion (errors with both positive and negative values) was introduced and the total error range was increased.

In the case of the hybrid SCN (HSCN), where only one type of stub is used while allowing for different link line impedances, the dispersion analysis has shown that

the propagation error is independent of the medium intrinsic impedance for a constant value of $\varepsilon_r\mu_r$. Also the error range is smaller than in the case of the stub-loaded SCN. However, bilateral dispersion and the ambiguity of the two physical solutions remain.

The dispersion analysis of the stubless, super-condensed node (SSCN), where all required adjustments were done through changing of the characteristic impedances of link lines, showed that in this node the dispersion is unilateral and independent of both the wave polarization and the intrinsic impedance of the medium. However, the range of propagation errors in the SSCN is higher than in the HSCN.

The dispersion analysis of the presently available nodes showed different error trends when introducing stubs and when altering link lines. From the error diagrams of the stubless SSCN it can be seen that the relative propagation error $\overline{\delta k}$ increases in the positive direction with increasing $\varepsilon_r\mu_r$ (or equivalently decreasing time step). A contrasting behaviour can be noticed in the case of the stub-loaded SCN (especially in Cases 2 and 3) where the errors are extended mainly to negative values. In the HSCN, where both stubs and altered link lines were used, errors are bilateral, but close to zero.

Intuitively, it is reasonable to expect that an improvement in the accuracy and dispersion behaviour of presently available nodes can be achieved by carefully combining the effects caused by stub loading and changing the impedances of the link lines in the node. However, the dependence on the ratio μ_r/ε_r found in the stub-loaded SCN makes it difficult to interpret error trends in this node. In order to eliminate this undesirable feature of the stub-loaded SCN, a new stub-loaded node, maintaining a constant link line impedance, but equal to the intrinsic impedance of modelled medium rather than to the impedance of the background medium, will be first developed. This node will be referred to as the matched impedance SCN (MSCN).

Comparison of the dispersion characteristics of the MSCN to those of the SSCN will, later in this chapter, lead to the development of a new family of nodes with improved accuracy, referred to as adaptable symmetrical condensed nodes (ASCN). Due to the increased complexity, caused by the great variety of combinations of link lines and stubs possible in the definition of a new node, only nodes for the uniform mesh will be developed. It is, however, hoped that the methodology used here will allow future development of similar advanced nodes for a graded mesh.

9.2 SCN with matched line impedances (MSCN)

9.2.1 Derivation

From the dispersion analysis of the stub-loaded SCN, performed in the previous chapter, it can be seen that the two physical solutions of the dispersion relation become identical only in the case when $\varepsilon_r = \mu_r$. The intrinsic impedance of the medium Z equals in this case the characteristic impedance of the link lines Z_0, since it follows that:

$$Z = \sqrt{\frac{\mu}{\varepsilon}} = \sqrt{\frac{\mu_r \mu_0}{\varepsilon_r \varepsilon_0}} = \sqrt{\frac{\mu_0}{\varepsilon_0}} = Z_0$$

This observation suggests that one may expect that the dispersion characteristics of a node having link lines whose characteristic impedance is equal to the intrinsic impedance of the modelled medium will be similar to those of the stub-loaded SCN when $\varepsilon_r = \mu_r$. The parameters of such a node can be derived from the general TLM constitutive relations described in Chapter 2, as follows.

The system of equations (2.41)–(2.42) with the condition $Z_{ij} = Z$ (or equivalently $Y_{ij} = Y = 1/Z$) reduces in the case of a uniform mesh ($\Delta x = \Delta y = \Delta z = \Delta l$) and an isotropic medium to:

$$2Y + \frac{Y_o}{2} = \varepsilon \frac{\Delta l}{\Delta t} \tag{9.1}$$

$$2Z + \frac{Z_s}{2} = \mu \frac{\Delta l}{\Delta t} \tag{9.2}$$

The characteristic admittance of open-circuit stubs and the impedance of short-circuit stubs, Y_o and Z_s respectively, are obtained from (9.1) and (9.2) as:

$$Y_o = 2Y \left(\frac{\Delta l}{\Delta t} \sqrt{\varepsilon \mu} - 2 \right) \tag{9.3}$$

$$Z_s = 2Z \left(\frac{\Delta l}{\Delta t} \sqrt{\varepsilon \mu} - 2 \right) \tag{9.4}$$

Assuming that the velocity of pulses on the transmission lines is imposed by the parameters of the background medium as [9]:

$$\frac{\Delta l}{\Delta t} = \frac{2}{\sqrt{\varepsilon_0 \mu_0}} \tag{9.5}$$

equations (9.3)–(9.4) simplify to:

$$Y_o = 4Y(\sqrt{\varepsilon_r \mu_r} - 1) \tag{9.6}$$

$$Z_s = 4Z(\sqrt{\varepsilon_r \mu_r} - 1) \tag{9.7}$$

Normalizing the values of Y_o and Z_s to those of the link lines (Y, Z) we obtain:

$$\hat{Y}_o = \hat{Z}_s = 4(\sqrt{\varepsilon_r \mu_r} - 1) \tag{9.8}$$

The scattering matrix for the MSCN can be easily derived from the GSCN scattering matrix shown in Figure 3.5 by using the definitions of the scattering coefficients given by (3.42)–(3.48), taking into account that $Z_{ij} = Z$ and the definitions of stub parameters given by (9.6)–(9.7). In the case of a lossless medium ($G_{ej} = R_{mk} = 0$) the scattering coefficients are found as:

$$\begin{aligned} a &= 0 & b &= d = e = i = \frac{q}{2} \\ c &= q - 1 & f &= g = 2\,(1 - q) \\ h &= 1 - 2q & j &= 2q - 1 \end{aligned} \tag{9.9}$$

where $q = 1/\sqrt{\varepsilon_r \mu_r}$ and the notation of Figure 3.5 is used.

By inspecting the definition of the scattering coefficients for the stub-loaded SCN in Case 2, given by equation (7.75), and the scattering coefficients of the MSCN, given by equation (9.9), they are found to be identical. This is expected, as the MSCN and the stub-loaded SCN are identical in the case when $\varepsilon_r = \mu_r$. Note, however, that for a given $\varepsilon_r \mu_r = const$, equation (7.75) defines scattering coefficients in the stub-loaded SCN **only** when $\varepsilon_r = \mu_r$, whereas equation (9.9) defines scattering coefficients in the MSCN for any ratio of ε_r/μ_r. Accordingly, the dispersion characteristics of the MSCN, in contrast to those of the stub-loaded SCN, will be independent of the ratio ε_r/μ_r for $\varepsilon_r \mu_r = const$. Furthermore, the dispersion relation of the MSCN will have the identical functional form as the dispersion relation of the stub-loaded SCN in Case 2, given by (7.77), yielding the same physical solution for the two orthogonal wave polarizations.

The dispersion characteristics of the MSCN are therefore advantageous compared to the stub-loaded SCN because of: a) the independence on the wave impedance (i.e. the factor μ_r/ε_r) for $\varepsilon_r \mu_r = const$ and b) the existence of a unique propagating solution for any ratio μ_r/ε_r. A disadvantage of the MSCN dispersion characteristics is a high error margin. Namely, the error range in the stub-loaded SCN is the highest in Case 2 and following the equivalence between the dispersion relations of the MSCN and the Case 2 stub-loaded SCN, it follows that the total error range in the MSCN will never be smaller than for the stub-loaded SCN, especially when a dielectric ($\mu_r = 1$) or magnetic ($\varepsilon_r = 1$) material is modelled (Case 1 SCN).

However, when modelling inhomogeneous media, the errors due to dispersion are found to be smaller in the MSCN than predicted from the dispersion analysis for homogeneous problems, as it will be shown later in this chapter. This behaviour can be attributed to the fact that the impedance of link lines always matches the impedance of the modelled medium in the MSCN. Accordingly, the scattering of voltage pulses occurring at the interface between two materials is directly equivalent to the scattering of waves on the boundaries between different media. In the conventional stub-loaded SCN, the voltage pulses pass the interface without 'seeing' the boundary at all, while in the HSCN and the SSCN, a reflection/transmission process occurs due to different values of the link line characteristic impedances which do not generally match the intrinsic impedances of the modelled media.

From the computational point of view, the MSCN is clearly as demanding as the stub-loaded SCN. In cases when only dielectric or only magnetic materials are modelled, where the stub-loaded SCN normally uses only one type of stub, the MSCN is more demanding since it always uses both types of stubs. It appears that a symmetrical use of both types of stubs in the MSCN, expressed through equation (9.8), is a price which must be paid in order to retain identical dispersion characteristics for the two wave polarizations.

There are, however, some cases when the MSCN is more efficient than the stub-loaded SCN. Consider for example the case when modelling two regions with $\varepsilon_r\mu_r = const$, say: region (1) with $\varepsilon_r = 2,\ \mu_r = 2$ and region (2) with $\varepsilon_r = 4,\ \mu_r = 1$. In the conventional stub-loaded SCN, the parameters for the link lines have to be chosen to model free-space and open- and short-circuit stubs need to be introduced in region (1), and open-circuit stubs in region (2). Alternatively, link lines can be chosen to model a hypothetical background medium of $\varepsilon_r = 2,\ \mu_r = 1$, thus introducing short-circuit stubs in region (1) and open-circuit stubs in region (2). It can be shown by analysing equations (9.6)–(9.7) that in the new MSCN, since $\epsilon_r\mu_r = const$ in the two regions, stubs are not needed at all. To summarize, in the conventional SCN the background parameters must be chosen as $(\min(\varepsilon_r), \min(\mu_r))$, where $\min(\varepsilon_r)$ and $\min(\mu_r)$ are the minimum values in all regions, thus imposing in some situations, as shown in the previous example, that stub-loading must be used in the whole mesh. In the MSCN, the background parameters can be chosen as $\min(\varepsilon_r\mu_r)$ which means that one part of the mesh will be always stub-free, while in some particular situations, as in the previous example, the whole mesh can be stub-free.

Due to the impedance matching condition, the connection between neighbouring nodes on different sides of a material interface must be modelled as for the HSCN and the SSCN, as explained in Chapter 6. The extra amount of calculations needed in this case can be justified, however, since the reflections on the interface are in accordance with problem requirements. Finally, the matching impedance condition simplifies the implementation of external boundaries in TLM based on the MSCN, since the line reflection coefficients will always be equal to the medium reflection coefficients [39].

9.2.2 Comparison of error trends in the MSCN and the SSCN

Having eliminated the presence of the two orthogonal solutions of the dispersion relation and their dependence on the wave impedance in the conventional stub-loaded SCN, by developing a new stub-loaded node with the matching impedance condition (MSCN), it is now possible to investigate more closely the effects of stub-loading and link line impedance changing on the numerical accuracy of a general condensed node TLM scheme. It appears most useful to compare the dispersion characteristics of the SSCN and the MSCN, since the former uses exclusively the altering of link lines to model local changes in the material properties, while the later always uses stubs.

Figure 9.1 shows, in the same manner as in Chapter 8, the percentage propagation errors in the SSCN and the MSCN for propagation in a coordinate and a diagonal plane, for the discretization of $\Delta l/\lambda = 0.1$. It can be clearly seen from the plots in Figure 9.1 that, with an increase in $\varepsilon_r \mu_r$ the propagation error is shifted in the positive direction for the SSCN but in the negative direction for the MSCN. Similar observations can be made from Figure 9.2 which shows the propagation error in the two nodes as a function of material properties.

The error trends observed from Figures 9.1 and 9.2 suggest that if a part of the excess material properties is modelled through stubs, as in the MSCN, and a part through varying the characteristic impedances of link lines, as in the SSCN, one may expect that the propagation error in such a combined node might average out, i.e. the error may be small and fluctuate around zero. This possibility is explored in the following section.

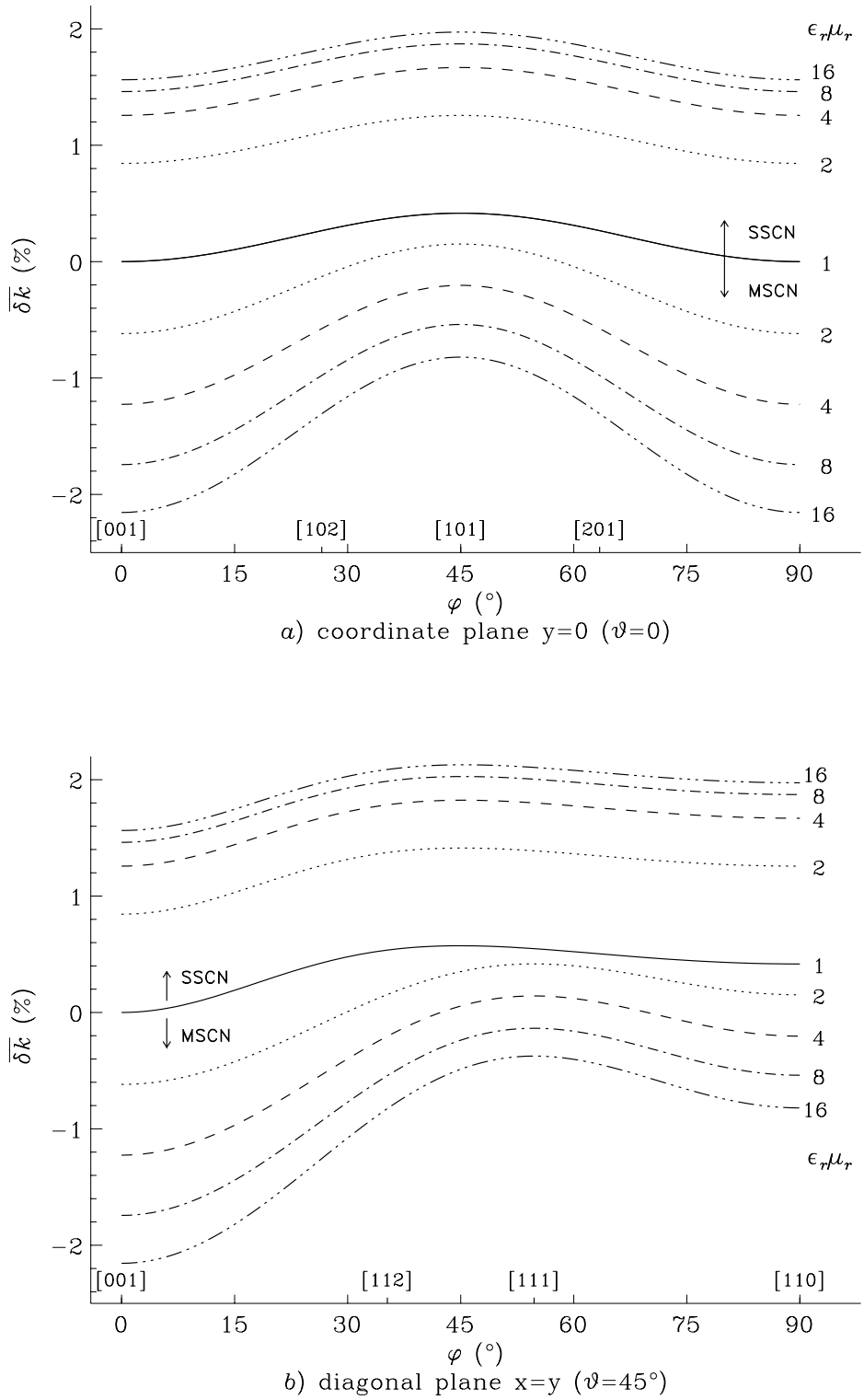

Figure 9.1 *Comparison of the percentage propagation error in the MSCN and the SSCN in different propagation planes for* $\varepsilon_r\mu_r \in \{1, 2, 4, 8, 16\}$ *and* $\Delta l/\lambda = 0.1$

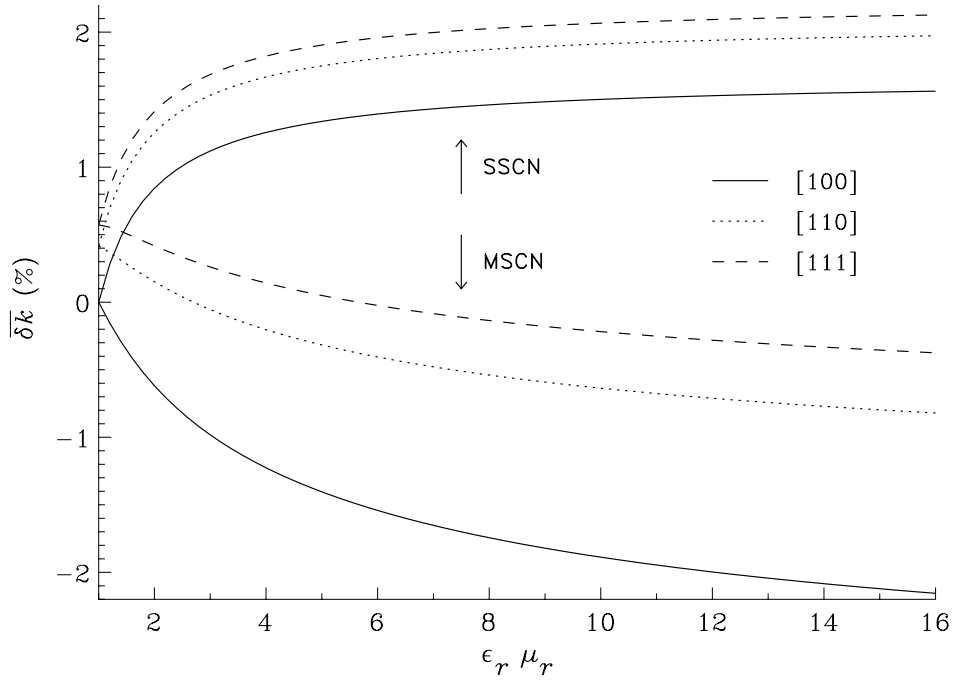

Figure 9.2 *The percentage propagation error in the MSCN and the SSCN, as a function of material properties, for the three principal directions and* $\Delta l/\lambda = 0.1$

9.3 Adaptable symmetrical condensed nodes (ASCN)

9.3.1 Derivation

The TLM constitutive relation for the case when two different link lines (as in the SSCN for uniform mesh) and open and short-circuit stubs (as in the MSCN) are introduced in the node, can be written from equations (2.41)–(2.42) for modelling an isotropic medium with parameters $\varepsilon = \varepsilon_r\varepsilon_0$ and $\mu = \mu_r\mu_0$ as:

$$Y_n + Y_p + \frac{Y_o}{2} = \varepsilon\frac{\Delta l}{\Delta t} \tag{9.10}$$

$$Z_n + Z_p + \frac{Z_s}{2} = \mu\frac{\Delta l}{\Delta t} \tag{9.11}$$

where $Y_n = 1/Z_n$, $Y_p = 1/Z_p$. The characteristic impedances of link lines are denoted, in accordance with the SSCN formulation, as

$$Z_{xy} = Z_{yz} = Z_{zx} = Z_p$$

$$Z_{xz} = Z_{yx} = Z_{zy} = Z_n$$

The system of two equations (9.10)–(9.11) contains four unknowns, namely, Z_n, Z_p, Y_o and Z_s. Additional conditions required for its solution can be imposed by

introducing weighting parameters which describe the proportion of the medium parameters (ε, μ) modelled separately by link lines and by stubs. Let the link lines model a proportion of the medium parameters denoted by ε_1, μ_1 and described by:

$$\varepsilon_1 = w_e\,\varepsilon \tag{9.12}$$

$$\mu_1 = w_m\,\mu \tag{9.13}$$

where w_e and w_m are arbitrary 'weighting' coefficients, non-negative numbers not bigger than unity. Since the parameters ε_1, μ_1 are modelled only by link lines, the general TLM equations (2.41)–(2.42) applied to this 'share' of the medium can be written as:

$$Y_n + Y_p = \varepsilon_1 \frac{\Delta l}{\Delta t} \tag{9.14}$$

$$Z_n + Z_p = \mu_1 \frac{\Delta l}{\Delta t} \tag{9.15}$$

Solving this system of two equations and using equation (9.5), the characteristic impedances of the link lines are obtained as:

$$Z_n = Z_1 A \qquad\qquad Z_p = Z_1/A \tag{9.16}$$

where

$$Z_1 = Z_0\sqrt{\frac{\mu_{r1}}{\varepsilon_{r1}}} \tag{9.17}$$

$$A = \sqrt{\varepsilon_{r1}\mu_{r1}} + \sqrt{\varepsilon_{r1}\mu_{r1} - 1} \tag{9.18}$$

On the other hand, by inserting equations (9.14) and (9.15) respectively in (9.10) and (9.11), and using equations (9.5) and (9.12)–(9.13), the parameters of stubs can be easily obtained as:

$$Y_o = 4Y\sqrt{\varepsilon_r\mu_r}(1 - w_e) \tag{9.19}$$

$$Z_s = 4Z\sqrt{\varepsilon_r\mu_r}(1 - w_m) \tag{9.20}$$

where $Z = 1/Y = \sqrt{\mu/\varepsilon}$.

At this stage two options are open. By choosing w_e and w_m independently, the parameters of open and short-circuit stubs will not be symmetrical, and, as in the case of the stub-loaded SCN and the HSCN, this node will exhibit the ambiguity of producing different solutions to the dispersion relation for the two orthogonal wave polarizations. Alternatively, by choosing $w_e = w_m = w$ and normalizing to

the values Y, Z we obtain, as in the derivation of the MSCN, that the normalized open-circuit stub admittance and short-circuit stub impedance are identical, i.e.:

$$\hat{Y}_o = \hat{Z}_s = 4\sqrt{\varepsilon_r \mu_r}(1 - w) \tag{9.21}$$

Note that in this case:

$$Z_1 = Z_0\sqrt{\frac{\mu_r}{\varepsilon_r}} = Z \tag{9.22}$$

$$A = w\sqrt{\varepsilon_r \mu_r} + \sqrt{w^2 \varepsilon_r \mu_r - 1} \tag{9.23}$$

This node is in fact a combination of the SSCN and the MSCN and intuitively it can be expected that this will ensure the same solution to the dispersion relation irrespective of wave polarization.

The relations (9.21)–(9.23) suggest that if $w = 1$, then $\hat{Y}_o = \hat{Z}_s = 0$, i.e. the stubs disappear and the node reduces the SSCN. On the other side, by choosing $w = 1/\sqrt{\varepsilon_r \mu_r}$, then $A = 1$ and $Z_n = Z_p = Z$, therefore the node reduces to the MSCN. One may expect that for $1/\sqrt{\varepsilon_r \mu_r} < w < 1$, the node behaviour will fall between that of the SSCN and the MSCN.

In this way, a whole class of nodes, referred to as adaptable symmetrical condensed nodes (ASCN) has been derived, whose scattering and dispersion characteristics can be customized (adapted) through a weighting factor w. Note that the SSCN and the MSCN are special cases of the ASCN for particular values of w, as shown above.

The scattering matrix of the ASCN can be derived from the scattering matrix of the GSCN given in Figure 3.5 and through equations (3.42)–(3.48), by using the definitions of the link and stub impedances and admittances derived above. The scattering coefficients for the ASCN modelling a lossless medium can be obtained as:

$$\begin{aligned} a_{p,n} &= \pm wu & b_{n,p} = d_{n,p} = e_{p,n} = i_{n,p} &= \frac{w}{2}(1 \pm u) \\ c_{p,n} &= w - 1 & f = g &= 2(1 - w) \\ h &= 1 - 2w & j &= 2w - 1 \end{aligned} \tag{9.24}$$

where $u = \sqrt{1 - 1/(w^2 \varepsilon_r \mu_r)}$. The first and second subscripts in (9.24) correspond to the upper and lower sign, respectively. Subscript p corresponds to lines xy, yz and zx, while subscript n corresponds to lines xz, yx and zy. The coefficients in (9.24) reduce to those of the MSCN given by (9.9) when $w = 1/\sqrt{\varepsilon_r \mu_r}$. It can

be noticed from (9.24) that the scattering coefficients of the ASCN are functions of $\varepsilon_r\mu_r$ if w is a function of $\varepsilon_r\mu_r$, which guarantees that the dispersion relation will be independent of ε_r/μ_r for $\varepsilon_r\mu_r = const.$ The particular choice of w can be made in a manner to optimize the propagation characteristics of the ASCN, as shown in the following subsection.

9.3.2 Dispersion characteristics

Following the strategy for the analytical expansion of the general TLM dispersion relation explained in Chapter 7, the functional form of the characteristic polynomial of the ASCN was found to be identical to that of the MSCN (or equivalently the stub-loaded SCN in Case 2) and the dispersion relation for the ASCN was derived by using the Faddeev method as:

$$\cos(4\theta) + B_1\cos 3\theta + B_2\cos 2\theta + B_3\cos\theta + \frac{B_4}{2} = 0 \tag{9.25}$$

where $\theta = \omega\Delta t$ and:

$$\begin{aligned}
B_1 &= 2s_1(1-w) + 4 \\
B_2 &= w^2u^2(2s_1+s_2) + w^2(3s_2-2s_1) - 4w(s_1+2s_2) + 4(s_1+s_2+1) \\
B_3 &= -2w^3u^2(3s_3+2s_2) - 2w^3(s_3-2s_2) + 2w^2u^2(3s_3+4s_2+4s_1) \\
&\quad +2w^2(9s_3-4s_2-4s_1) - 2w(12s_3-s_1) + 2(4s_3-s_1-2) \\
B_4 &= -4w^3u^2(3s_3+2s_2) + 4w^3(7s_3+2s_2) + 2w^2u^2(6s_3+7s_2+6s_1) \\
&\quad -2w^2(30s_3+11s_2+6s_1) + 8w(6s_3+2s_2+s_1) \\
&\quad -2(8s_3+4s_2+4s_1+5)
\end{aligned} \tag{9.26}$$

with

$$\begin{aligned}
s_1 &= c_x + c_y + c_z \\
s_2 &= c_xc_y + c_yc_z + c_zc_x \\
s_3 &= c_xc_yc_z
\end{aligned}$$

and $c_x = \cos(k_x\Delta l) - 1$, $c_y = \cos(k_y\Delta l) - 1$ and $c_z = \cos(k_z\Delta l) - 1$.

The dispersion relation for the ASCN given by (9.25) is obtained as function of a coefficient w, $1/\sqrt{\varepsilon_r\mu_r} \leq w \leq 1$, where w describes how close the ASCN definition is to the SSCN or MSCN, as previously discussed. In order to compensate errors experienced in the SSCN and MSCN, a suitable factor w can be chosen as the

mean between the value of $1/\sqrt{\varepsilon_r\mu_r}$, which corresponds to the MSCN definition, and unity, corresponding to the SSCN definition. For example, the arithmetic and geometric means of these values are:

$$w_a = \frac{\frac{1}{\sqrt{\varepsilon_r\mu_r}} + 1}{2} = \frac{\sqrt{\varepsilon_r\mu_r} + 1}{2\sqrt{\varepsilon_r\mu_r}}$$

and

$$w_g = \sqrt{\frac{1}{\sqrt{\varepsilon_r\mu_r}} \cdot 1} = \frac{1}{\sqrt[4]{\varepsilon_r\mu_r}}$$

respectively.

In order to compare propagation characteristics of the ASCN with different values of w, the propagation errors for the three principal directions are obtained from (9.25) for the values of $w = w_a$ and $w = w_g$ and plotted in Figure 9.3. By comparing the propagation errors of the ASCN plotted in Figure 9.3 to those of the SSCN and the MSCN plotted in Figure 9.2, it can be seen that the error in the ASCN is indeed contained between the errors in the MSCN and the SSCN. It can be also seen from Figure 9.3 that the error range in the ASCN with $w = w_a$ is significantly smaller than in the SSCN and MSCN, plotted in Figure 9.2.

It can be noticed from Figure 9.3 that the propagation errors in the ASCN are not monotonic functions of $\varepsilon_r\mu_r$ as in the case of the SSCN and the MSCN, where we have, respectively, monotonically increasing and monotonically decreasing $\overline{\delta k}$ with increasing of $\varepsilon_r\mu_r$, as can be seen from Figure 9.2. In the case of the ASCN, these functions show increase up to the certain values of $\varepsilon_r\mu_r$, after which they decrease. Another feature of the propagation error in the ASCN with $w = w_a$ and $w = w_g$ is that errors are both positive and negative, i.e. the dispersion is bilateral. This is not the case with the propagation errors in the SSCN.

Obviously, a more detailed mathematical analysis on the behaviour of propagation error in the ASCN should be pursued to find an optimal weighting factor. However, it will be shown below how a weighting factor can be obtained to produce unilateral dispersion.

From Figure 9.3 it can be seen that the lowest values of positive errors and negative errors occur for the propagation along the axial direction (i.e. **[1,0,0]**). It appears that the propagation error in other directions will always be positive, if the error along the axial direction is non-negative. Hence, let us impose a condition that the error along the axial direction is zero for any value of $\varepsilon_r\mu_r$. By inserting

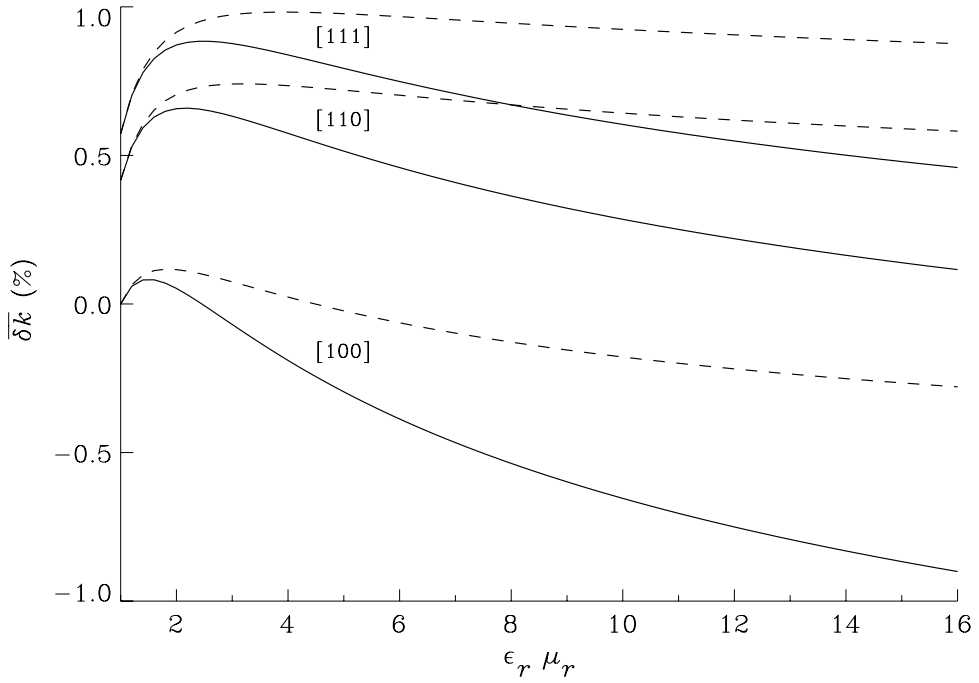

Figure 9.3 *Percentage propagation errors in the ASCN for two different weighting factors w_a (broken lines) and w_g (solid lines) and for $\Delta l/\lambda = 0.1$*

$k_x \Delta l = 2\theta\sqrt{\varepsilon_r \mu_r}$ and $k_y = k_z = 0$ in (9.25) and solving it for w, it is found that:

$$w = \frac{\cos(\theta) + \cos(2\theta\sqrt{\varepsilon_r \mu_r})}{\cos(2\theta\sqrt{\varepsilon_r \mu_r}) - 1} + \frac{1}{2\varepsilon_r \mu_r (1 - \cos(\theta))} \tag{9.27}$$

It can be seen from (9.27) that the solution for w is, of course, dependent on $\theta = \omega \Delta t$, i.e. on the frequency. Since dispersion is investigated here at a relatively low frequency, the limit of (9.27) can be sought when $\theta \to 0$, leading to a somewhat surprisingly simple and elegant result for w given by:

$$w = w_u = \frac{1 + 2\varepsilon_r \mu_r}{3\varepsilon_r \mu_r} \tag{9.28}$$

where subscript u denotes 'unilateral' dispersion.

The percentage error for the ASCN with the weighting factor w_u is plotted in Figure 9.4 (solid lines) and compared to that with $w = w_a$ (broken lines). Indeed, it is clear from Figure 9.4 that the propagation error for all three principal directions and for any value of $\varepsilon_r \mu_r$ is positive and hence unilateral. Note also that the error for axial propagation **[1,0,0]** is virtually zero. Finally, the propagation errors in the three directions are monotonic functions of $\varepsilon_r \mu_r$ although this was not a condition explicitly enforced in the derivation of w_u.

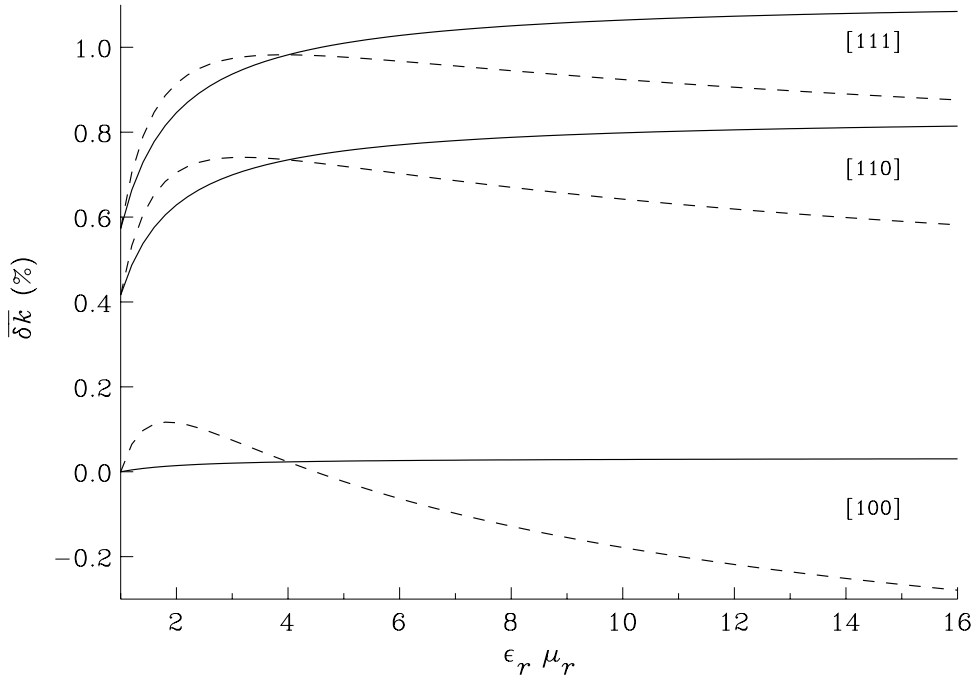

Figure 9.4 *Percentage propagation errors in the ASCN for two different weighting factors w_a (broken lines) and w_u (solid lines) and for $\Delta l/\lambda = 0.1$*

The ASCN with the weighting factor w_u which produces unilateral dispersion is only one example of an 'optimized' node. Note that the dispersion analysis applied here is valid for homogeneous problems, therefore, bilateral dispersion may be introduced in modelling inhomogeneous problems due to spurious reflections on the boundaries between different materials, as will be shown in the following section. More investigations should be pursued to derive other 'optimal' weighting factors. In this chapter, however, further analysis of the ASCN will be performed using the weighting factor $w = w_u$ defined by (9.28).

The normalized propagation error $\overline{\delta k}$ in the ASCN is shown in Figure 9.5 using similar plots to those used previously in the analyses of other nodes. Comparing the plots from Figure 9.5 to those presented in Chapter 8, it can be seen that the total error range in the ASCN is smaller than in the previous nodes and that the dispersion is always unilateral.

Further comparisons of the propagation error in the ASCN to those errors in the MSCN and the SSCN are made in Figure 9.6. From the plots in Figure 9.6 it is clear that the error range for the ASCN is substantially smaller than for all previous nodes.

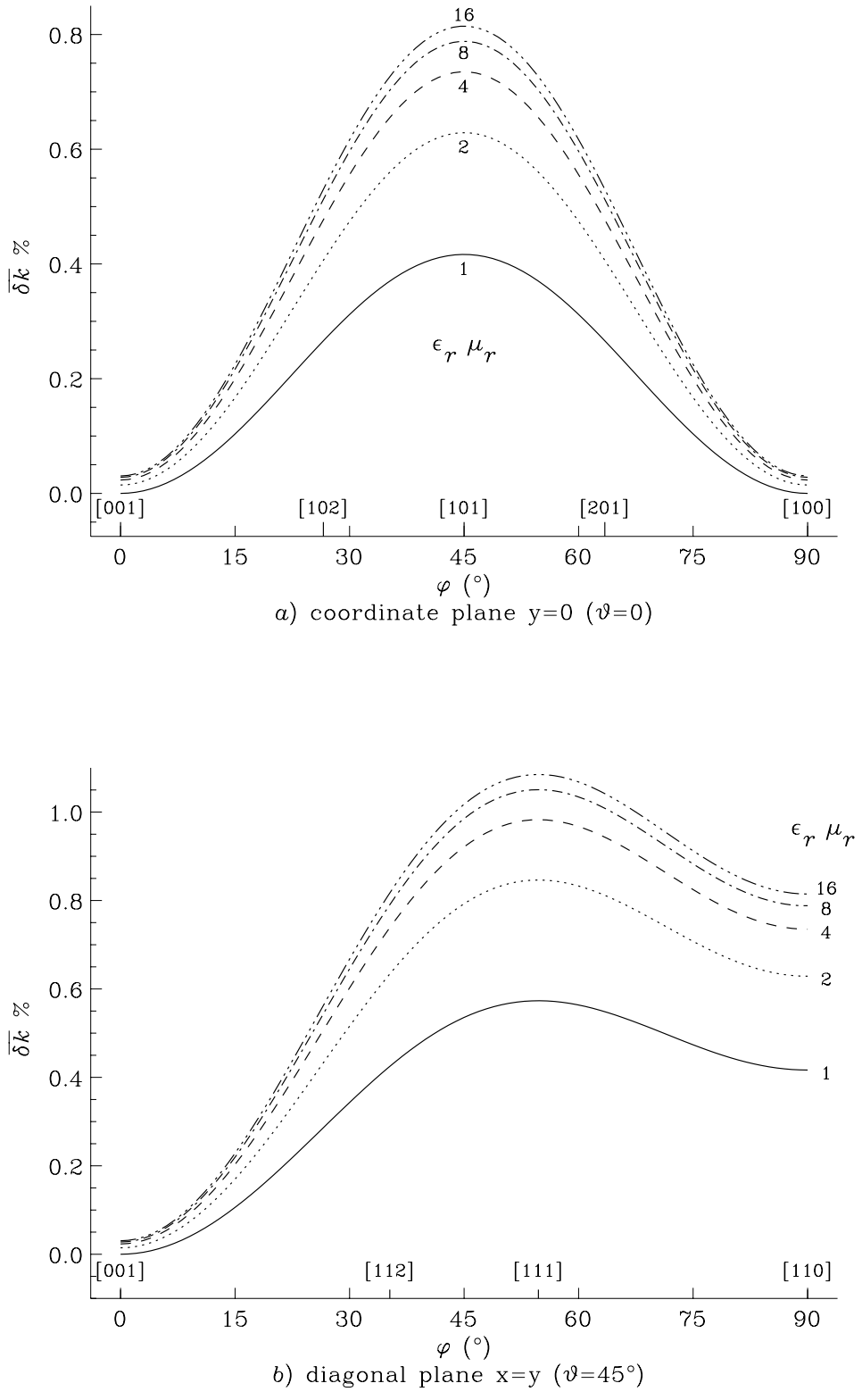

Figure 9.5 *Percentage propagation errors in the ASCN ($w = w_u$ and $\Delta l/\lambda = 0.1$)*

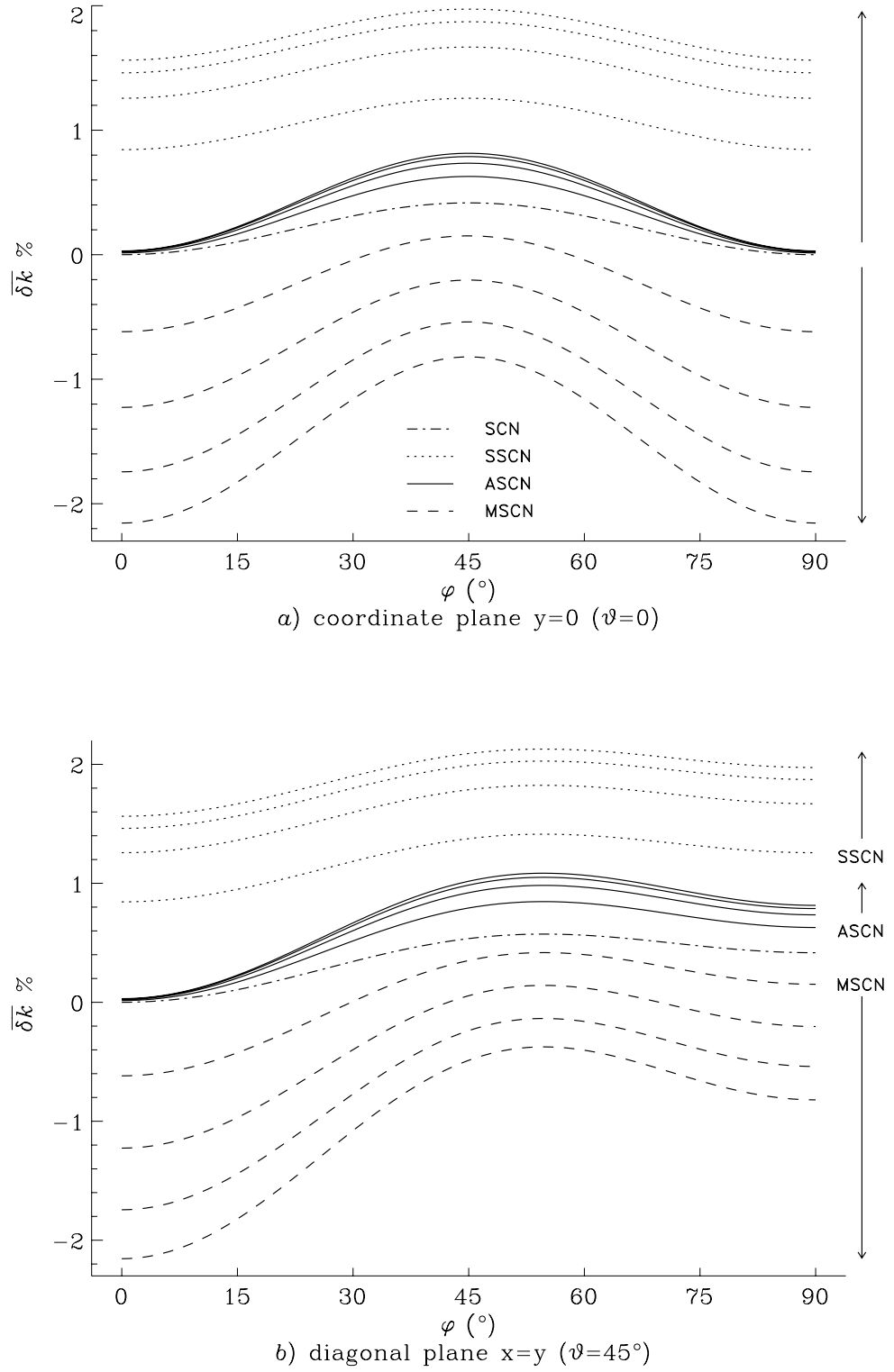

Figure 9.6 *Comparison of propagation errors in the ASCN (solid lines), the SSCN (dotted lines) and the MSCN (broken lines) for* $\varepsilon_r\mu_r \in \{2, 4, 8, 16\}$ *and* $\Delta l/\lambda = 0.1$. *The direction of the increase in* $\varepsilon_r\mu_r$ *is denoted by arrows*

The propagation characteristics of the ASCN are therefore found to be more advantageous than those of all previous nodes. In addition to the existence of the same propagation solution for any ratio μ_r/ε_r and the independence of the wave impedance for $\varepsilon_r\mu_r = const$, already found in the SSCN and the MSCN, this node produces unilateral dispersion (found only in the SSCN) and has an error range less than half that of the SSCN and the MSCN. The cost of this superior propagation behaviour of the ASCN is the presence of six stubs and a more complicated scattering procedure.

Numerical characteristics of the ASCN can be further compared to those of other nodes by using the figures of merit introduced in Chapter 8 and summarized for other nodes in Table 8.2. Note that, due to an equivalence between the MSCN and the stub-loaded SCN in Case 2, the characteristics of the MSCN can be taken as identical to those presented in Table 8.2 for the stub-loaded SCN in Case 2.

The maximum normalized propagation error in the ASCN, obtained for a very high $\varepsilon_r\mu_r = 200$, is found to be 1.11%. Since the dispersion in the ASCN is unilateral, this number actually represents the total error range $\overline{\delta k}_t$, as defined earlier in Chapter 8. It can be seen from Table 8.2, that the corresponding error ranges for the HSCN and the SSCN are 1.62% and 2.22%. Considering that the ASCN uses $N = 18$ node ports, the factor $\overline{\delta k}_{t,18}$ which relates the accuracy with the memory requirements, defined by (8.11), is in case of the ASCN $\overline{\delta k}_t = \overline{\delta k}_{t,18} = 1.11$, which is still better than the factors for the SSCN and the HSCN which are found from Table 8.2 as $\overline{\delta k}_{t,18} = 1.69\%$ for the SSCN and $\overline{\delta k}_{t,18} = 1.43\%$ for the HSCN. This shows that even though the ASCN uses 18 locations per node, its performance, taking into account both storage and accuracy, is still better than nodes with fewer stubs.

However, the scattering procedure in the ASCN demands 18 multiplicative (MUL) and 54 additive (ADD) operations per node per time step, which is higher than in the HSCN and the SSCN where respectively 12 and 6 MUL operations and 48 ADD operations are required. Accordingly, the theoretical performance index P_t appearing in Table 8.2 was found to be $P_t = 2.45$ for the ASCN, which puts the ASCN before the HSCN ($P_t = 2.38$) but behind the SSCN ($P_t = 3.23$). This is merely due to the fact that in the ASCN as many as 3 times more MUL operations per node are required than in the SSCN.

All these quantitative factors should be, however, used with caution, as they are obtained in an ideal case, assuming a homogeneous mesh filled with the same type of nodes, which is rare in practical problems. In view of the ever increasing num-

ber of available TLM nodes, these factors do never-the-less provide a preliminary guidance of what can be expected from each scheme. However, a definitive comparison of different schemes can only be achieved by performing TLM simulations of practical problems.

9.4 Numerical results

The dispersion relations for the TLM nodes investigated in this thesis apply for an infinite space with a homogeneous medium. By using a simulation procedure explained before for other nodes, the solution to the dispersion relation for the newly derived ASCN given by (9.25) and the curves plotted in Figures 9.4 and 9.5 can be verified for the example of homogeneous cubic resonators filled with different media. However, in real problems, nodes with stubs and varied link line impedance are used in order to model local increases in the medium parameters, i.e. for modelling inhomogeneous problems. Hence, further investigation is needed to quantify dispersion behaviour in these cases.

The interface between two materials is modelled differently by the various condensed node schemes. In the stub-loaded SCN TLM mesh, where the link line impedance is constant irrespective of the medium, pulses pass the interface without an immediate reflection, which contradicts conventional wave propagation, where a reflection does occur at the interface between different materials. In other nodes, where the impedance of link lines generally differs at the interface discontinuity, a two port junction is used to model reflection and transmission of pulses, thus introducing spurious reflections. In the case of the MSCN, where the link line impedances are always matched to the intrinsic impedance of medium, it is expected that scattering at the interface describes more accurately the physical condition.

A full investigation into the effect of interface discontinuities in the TLM method has not yet been described in the literature. However, these effects have been investigated empirically [58] by studying frequency errors in inhomogeneous resonators. A similar approach is used here in order to test the performance of different nodes and to estimate the influence of spurious reflections on propagation behaviour. The two square resonators depicted in Figure 9.7, partly filled with a medium with materials parameters: Case 1) $\varepsilon_r = 4$, $\mu_r = 1$ and Case 2) $\varepsilon_r = \mu_r = 2$ are studied in the simulations. Note that the stub-loaded SCN and the HSCN are identical in Case 1, while the stub-loaded SCN and the MSCN are identical in Case 2.

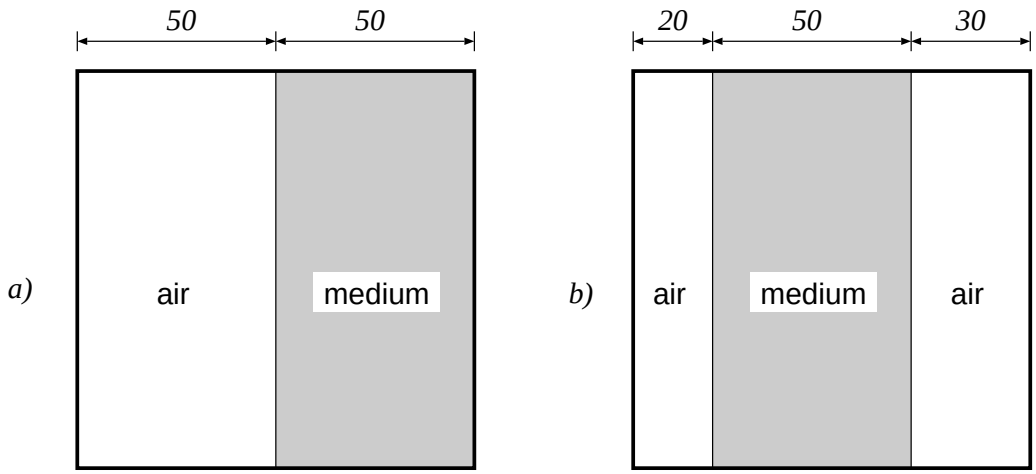

Figure 9.7 *Schematic of inhomogeneous resonators (dimensions are in mm)*

The resonant frequencies of TE modes **10, 20, 30, 11, 21** and **31** are calculated for each case using TLM simulations with different nodes on a mesh with node spacing $\Delta l = 1$cm. The relative propagation error normalized to the benchmark discretization of $\Delta l/\lambda = 0.1$ is calculated using (8.8) and (8.9) as:

$$\overline{\delta k} = \frac{(f_0 - f)}{f}\left(\frac{0.1}{\Delta l/\lambda}\right)^2 = \frac{(f_0 - f)}{f}\left(\frac{0.1c}{\Delta l f_0\sqrt{\varepsilon_r\mu_r}}\right)^2 \tag{9.29}$$

where f is the modelled frequency, c is speed of light and f_0 is the reference frequency obtained by performing calculations on a very fine mesh. Note that the normalization is done with respect to the wavelength in the material. The results for the two resonators are presented in Tables 9.1 and 9.2.

It can be seen from Tables 9.1 and 9.2 that generally, the ASCN and the HSCN are the most accurate of all nodes, as predicted from the dispersion analysis. However some discrepancies can be noted, most probably due to the spurious reflections at the interfaces. The spurious reflections can be studied by comparing the results for resonator b (with two interfaces medium-air) with the results for resonator a. In all nodes the accuracy in modelling the two resonators differs greatly, expect in the MSCN where accuracy is generally the same (most noticeable in Case 2). This indicates that in problems with multiple interfaces the MSCN might provide greater accuracy. In the SSCN, the propagation error for resonator b is always shifted in the positive direction compared to that for resonator a. In the ASCN, it is shifted mainly in the negative direction. Note that for the ASCN, the errors for the mode **10** are negative, which is not expected from the dispersion relation for uniform problems, but was probably introduced due to spurious reflections at interfaces. The positive error in the ASCN for the mode **20** in resonator a becomes

TE mode →		10	20	30	11	21	31
Case 1: $\varepsilon_r = 4$, $\mu_r = 1$							
f_0 [GHz] →		0.9116	2.0863	2.9980	1.2523	2.3176	3.2314
SCN & HSCN		-0.22	-0.55	-0.25	+0.03	-0.35	-0.20
MSCN	$\overline{\delta k}$	-0.90	-0.90	-0.58	-0.15	-0.63	-0.40
SSCN	[%]	+1.48	+0.75	+0.64	+1.77	+1.11	+0.62
ASCN		-0.34	+0.19	+0.05	+0.32	+0.31	+0.22
Case 2: $\varepsilon_r = 2$, $\mu_r = 2$							
f_0 [GHz] →		0.9993	1.9987	2.9980	1.3476	2.2845	3.1883
SCN & MSCN		-0.82	-0.80	-0.78	-0.19	-0.50	-0.57
HSCN	$\overline{\delta k}$	-0.11	-0.53	-0.35	+0.03	-0.29	-0.28
SSCN	[%]	+1.46	+0.57	+0.86	+1.73	+0.92	+0.80
ASCN		-0.38	+0.23	+0.07	+0.25	+0.31	+0.24

Table 9.1 *Normalized percentage propagation error in resonator (a)*

TE mode →		10	20	30	11	21	31
Case 1: $\varepsilon_r = 4$, $\mu_r = 1$							
f_0 [GHz] →		0.8066	1.8316	2.9980	1.1346	2.0305	3.1452
SCN & HSCN		+0.28	-0.21	-0.43	+0.25	-0.05	-0.33
MSCN	$\overline{\delta k}$	-0.74	-0.91	-0.93	+0.02	-0.50	-0.75
SSCN	[%]	+2.22	+1.49	+1.11	+2.14	+1.68	+1.27
ASCN		-1.00	-0.33	+0.08	+0.14	-0.01	+0.17
Case 2: $\varepsilon_r = 2$, $\mu_r = 2$							
f_0 [GHz] →		0.9993	1.9987	2.9980	1.2868	2.2094	3.1778
SCN & MSCN		-0.83	-0.80	-0.78	-0.09	-0.48	-0.61
HSCN	$\overline{\delta k}$	+0.07	-0.14	-0.36	+0.18	-0.01	-0.25
SSCN	[%]	+2.00	+1.42	+0.97	+2.04	+1.62	+1.14
ASCN		-0.81	-0.34	+0.07	+0.13	-0.08	+0.14

Table 9.2 *Normalized percentage propagation error in resonator (b)*

negative in resonator b, which can be explained by the presence of the additional interface in resonator a.

The dependence of the error on the wave impedance for constant $\varepsilon_r \mu_r$, predicted for the stub-loaded SCN, can be observed by comparing results obtained for different filling materials in Cases 1 and 2. It is evident from Tables 9.1 and 9.2 that in all other nodes, the errors in the two cases do not differ significantly, which is in agreement with the theory (Chapter 8). It is also interesting to note that for

different propagation modes in the axial direction (**10, 20, 30**) all nodes, except perhaps the MSCN, exhibit significant variations in errors. Clearly, this requires further investigation but it would appear from these preliminary results that the lower order modes are influenced more by the spurious reflections at interfaces. It is evident from Tables 9.1 and 9.2 that in the SSCN and the ASCN, the normalized propagation errors for the **30** mode are generally smaller than for the **10** mode.

9.5 Conclusion

In this chapter, new TLM condensed nodes with improved dispersion characteristics were developed from the unified formulation of the general symmetrical condensed node. The derivation of the link line and stub parameters, the scattering properties, implementation issues and the full propagation analysis for these nodes were described in detail. The new adaptable SCN (ASCN) is unique in the sense that its dispersion behaviour can be controlled by a weighting factor.

A comparative study of the new and previously developed TLM condensed nodes for the uniform mesh was performed by calculating the normalized propagation errors in inhomogeneous resonators with different geometry and filling materials. Generally, it was found that the HSCN and the ASCN exhibit the best accuracy. The influence of spurious reflections occurring at the interfaces between materials was studied, and it was found that the node with a matched impedance condition (MSCN) is the least affected. It was also noticed in modelling inhomogeneous problems that, for the configurations studied, the normalized frequency errors in a given direction are generally smaller for the higher harmonics, especially in the SSCN and the ASCN. Some irregularities in the results obtained were observed and these need further investigation.

In general, the study conducted in this chapter has shown that a combination of link and stub parameters in the condensed nodes leads to an improved accuracy, because the individual contributions to the propagation error by stubs and link lines are in opposition. It is noticeable, that the two nodes which use both stubs and different link link impedances, namely the HSCN and the ASCN, show the best accuracy. The weighting factor used in the present implementation of the ASCN was chosen to secure unilateral dispersion in the case of propagation in a homogeneous medium. However, bilateral dispersion in modelling inhomogeneous media was caused by spurious reflection at interfaces. Hence, a future study may be able to determine an optimal weighting factor for modelling inhomogeneous problems.

Chapter 10 Discussion and conclusions

10.1 Introduction

The objectives of this thesis were to theoretically establish the existing formulations of the TLM method and to explore possibilities for the development of new, advanced nodes for modelling general non-uniform media in three-dimensional (3D) space. Due to its suitability for efficient modelling of wave propagation in 3D space, the symmetrical condensed node (SCN) [9] was chosen as the starting point for new developments.

The SCN contains six interconnected transmission lines with the same characteristic impedance. The twelve voltage pulses travelling on these lines represent, by an established analogy, the field components propagating in 3D space. The basic version of the SCN can be applied for modelling only homogeneous materials on a uniform mesh, while its modification is necessary to allow for the modelling of general inhomogeneous problems and for using cells with arbitrary aspect ratios, i.e. a graded mesh.

The modifications which can be applied to the 12-port SCN are stub-loading and changing of the link line characteristic impedances. Originally, it was proposed by Johns [9] that link lines should have a constant characteristic impedance equal to the intrinsic impedance of the background medium in the whole mesh, in order to ensure time synchronism, whilst open- and short-circuit stubs could be added to make up for any local increase in the dielectric permeability and magnetic permittivity. This approach is sound and intuitively satisfying. However, the stub-loaded SCN uses six extra memory locations in order to store voltage pulses associated with stubs, thus becoming considerably less efficient compared to the basic 12-port version. The scattering procedure for this node is also more complicated and requires more arithmetic operations than the 12-port version [38]. Probably the biggest drawback of the stub-loaded SCN is that the maximum time step which is allowed in a graded mesh is in some cases prohibitively small [6]. The time step

is, in fact, dependent on the ratio of the biggest to the smallest node dimension. Hence when highly asymmetric grading is introduced into the mesh, a TLM simulation may need to run for a very large number of time steps in order to make up for their small values.

To overcome these problems, Scaramuzza and Lowery [19, 32] have developed a hybrid version of the SCN (HSCN), where the condition for the equal link line impedances was relaxed. In this development, only open circuit stubs were used and three sets of the characteristic link line impedances were allowed. Since there are only three stubs, this node is computationally more efficient compared to the traditional stub-loaded SCN, but far more importantly, this node can operate in graded meshes at a considerable higher time step than the stub-loaded node [31, 32]. A complementary version of the HSCN, with short-circuit stubs only, but otherwise similar characteristics, was also recently developed and implemented [20].

Obviously, the successful development and implementation of the HSCN have opened several questions: Whether stubs can be removed from the node all together? What would be the efficiency and propagation characteristics of such a node? Could it be possible to develop other nodes with different combinations of stubs and link lines? Could the TLM method with these new nodes be derived directly from an established field theory? In order to answer these questions, a systematic approach was adopted and described in this thesis, as summarized below.

10.2 Review of new developments described in the thesis

10.2.1 Theoretical foundation

By studying the development of the existing TLM nodes, it was noticed that the most common approach to the calculation of the node parameters is based on equalizing the total capacitance and inductance contributed by the link lines and stubs to that of the block of modelled medium [6]. This approach was generalized in Chapter 2 through the *general TLM constitutive relations* which define parameters of a TLM node with arbitrary configuration, modelling general anisotropic media. It was shown that this formulation is valid for all the existing 3D time-domain nodes, as well as for the two-dimensional and frequency-domain nodes. The unified formulation of the TLM parameters for a three-dimensional time-domain scheme contains six degrees of freedoms, hence additional constraints

must be imposed to derive a particular scheme. These requirements were clearly identified in Chapter 2 for the existing stub-loaded and hybrid nodes. Another interesting conclusion drawn from Chapter 2 was that the parameters of link lines and stubs must be identical for any of the three basic structure used in 3D TLM modelling, namely the expanded node, the asymmetrical condensed node and the symmetrical condensed node. This means that the calculation of parameters performed for one structure can be readily used for others, with minor alterations in modelling boundaries and material interfaces.

In order to derive a TLM node, apart from the calculation of its link and stub parameters, its scattering properties must also be determined. The scattering for the SCN cannot be determined from an equivalent electric circuit, hence the imposition of unitary conditions on the scattering matrix was traditionally used [9]. To avoid the complexity of such a derivation, an elegant approach, based on established physical principles, was presented in Chapter 3. This approach allows a simple formulation of scattering for a very general condensed node with up to twelve different characteristic impedance of link lines and up to twelve stubs and lossy elements.

In Chapter 4, a bijective one-to-one mapping between field components and voltage pulses was introduced to derive the GSCN directly from Maxwell's equations by using central differencing and central averaging. In this way, a direct correspondence between the TLM method based on the GSCN and a finite-difference scheme was established, thus offering a rigorous theoretical foundation for any new TLM node derivable from the GSCN. Also, by analysing the approximations used in the derivation of the GSCN it was found that TLM based on the GSCN is second order accurate, regardless of the modelled medium and mesh grading.

10.2.2 Symmetrical super-condensed node

A theoretical foundation of the general symmetrical condensed node established in Part One, provided all the necessary conditions for the development of a stubless node in Chapter 5, referred to as the symmetrical super-condensed node. The detailed derivation of the parameters of this node for isotropic as well as anisotropic media was performed in Chapter 5, together with a complete description of the implementation procedure. Apart from the reduced memory storage, it was shown that the SSCN allows for a higher time step in graded meshes and with anisotropic media, compared to the previous nodes. The numerical examples presented in Chapter 5 demonstrated the validity and versatility of the new node and showed

possible ways of 'smart grading' in order to achieve more accurate results.

In order to assess computational features of the new SSCN, the efficient implementation of scattering procedure was discussed in Chapter 6. The optimal algorithms for general nodes, as well as the stub-loaded and the hybrid nodes were first described, followed by a detailed explanation of the scattering procedure in the SSCN. It was shown that only six multiplicative operations per node per time step are required in the SSCN modelling arbitrary lossless media, which is half the number required for the stub-loaded or the hybrid nodes. A new efficient scattering algorithm for the 12-port SCN was also described, which requires only 6 multiplicative and 24 additive and subtractive operations per node per time step.

10.2.3 Dispersion analysis

Since it had been shown in Part Two that the SSCN exhibits superior computational characteristics compared to the previous nodes, in terms of memory storage, computer run-time and allowable maximum time step, a further study was undertaken to determine its propagation properties. A difficulty encountered at this stage was that a comprehensive dispersion analysis for previous nodes was not available, hence a detailed study of the TLM general dispersion relation was first undertaken.

An analytical expansion of the general dispersion relation was performed in Chapter 7 in order to facilitate the study of available condensed nodes. The derivation of the algebraic form dispersion relations proved to be a complex mathematical process and closed-form solutions were only possible in the case of the 12-port SCN and the SSCN. However, the implicit polynomial forms of the dispersion relations for the stub-loaded SCN and the HSCN, derived in Chapter 7, were found to be sufficient for an exact analytical study of propagation errors performed in Chapter 8.

The dispersion analysis performed in Chapter 7 showed that in all nodes, in addition to the physical solution of the dispersion, there are also unphysical solutions which do not converge to the linear dispersion relations of Maxwell's equations. The high-frequency unphysical solutions can be eliminated by applying appropriate low-pass filtering, but there are also low-frequency unphysical solutions with high wave numbers which, if excited, propagate together with physical solutions. However, simulation results from modelling homogeneous resonators, presented in Chapter 8, showed excellent agreement with those predicted from the physical

solutions, thus indicating that most of the spurious modes are evanescent and do not influence the field solution significantly [54].

A quantitative analysis of the physical solutions was performed for the presently available nodes in Chapter 8. The errors for propagation in arbitrary directions were calculated for a benchmark discretization ratio of $\Delta l/\lambda = 0.1$ and visualized in three-dimensional space. A systematic comparison of numerical errors in different schemes was performed for uniform and graded meshes. It was found that the HSCN and the stub-loaded SCN exhibit two solutions for different orthogonal wave polarizations, which is at variance with the solutions of Maxwell's equations. In addition, dispersion in the stub-loaded SCN is further dependent on the ratio ε_r/μ_r for a constant $\varepsilon_r\mu_r$ and both nodes show bilateral dispersion. These features were not found in the SSCN, which behaves, in terms of dispersion characteristics, similarly to the 12-port SCN: it produces the same solution for the two wave polarizations, the dispersion is unilateral and independent of the wave impedance. However, the range of propagation errors in the SSCN is higher than in the HSCN and from that viewpoint, the HSCN is more accurate. Various figures of merits were introduced in Chapter 8 to relate the memory and run-time requirement with accuracy, which showed that, in general, an optimal TLM scheme is problem dependent. The results obtained in this chapter were further explored to find ways for minimizing and eliminating dispersion errors. It was demonstrated that this can be achieved by using 'smart grading' and 'flattening of dispersion'. The error trends noticed in this chapter were exploited in the final part of the thesis to derive new, optimized nodes.

10.2.4 Further developments

The possibility of deriving new nodes with a combination of the link and stub parameters which would exhibit improved dispersion characteristics was explored in Chapter 9. The theoretical foundation of the GSCN from Part One was combined with the results of dispersion analysis from Part Three to provide the means for the development of new, optimized nodes.

First, a matched impedance SCN (MSCN) node, similar to the traditional stub-loaded SCN, was derived, but with dispersion characteristics independent of wave polarization and wave impedance. The error trends in the MSCN were further compared to those in the SSCN to conclude that errors caused by stub-loading in the MSCN are in opposition to errors caused by altering link line impedances in the SSCN. This was used to formulate a new class of condensed nodes, referred

to as the adaptable condensed nodes (ASCN), whose dispersion behaviour was between those of the SSCN and the MSCN. The special feature of the ASCN is that a weighting factor appears in its formulation, which can be used to customize (adapt) the dispersion characteristics of the node. Several forms of the weighting factors were explored, and one which ensures unilateral dispersion was chosen for further study. Numerical simulations of inhomogeneous cubic resonators were performed to compare the performances of the new and previously derived nodes. Some irregularities were noticed due to spurious reflection present at material interfaces, which were not accounted for in the traditional dispersion analysis. Generally, it was found that the nodes which use a combination of link and stub parameters, namely the HSCN and the ASCN, offer the best accuracy, as predicted by the dispersion analysis.

10.3 Suggestions for further research

Suggestions for further research can be summarized as follows:

- Optimization of the TLM method should be primary task for a further study. Clearly, the analytical tools established in this thesis for the developments and characterization of new nodes could be further exploited. A problem-dependent, 'smart' TLM node, with adjustable propagation characteristics, could be developed, but more investigations are needed to quantify spurious reflections on material interfaces.
- The results from the dispersion analysis showed that errors are minimized if all nodes in the mesh operates at their maximum time step, hence, a 'smart grading' can reduce dispersion effects greatly. Since grading in traditional TLM meshes is *structured*, i.e. connectivity between the cells is preserved, more emphasis could be placed on the implementation of the available nodes in *multiple grid* meshes [74].
- Several separate techniques, developed for modelling fine features in TLM, such as thin conducting elements (wires, panels, slots) [75, 76], which are necessary in many studies, for example, in electromagnetic compatibility (EMC) [77], could also be included in the implementation of new nodes.
- The unified formulation of TLM nodes, presented in Chapter 2, should be generalized further to accommodate modelling of the anisotropic media described by non-diagonal tensors. Also, the unified formulation should be verified by applying it to the recently derived new FD-TLM nodes [78].

- The unbalanced nodes, with differing link line characteristic impedance with respect to the node centre, should be investigated more closely. Thus far, a proper derivation of these nodes directly from Maxwell's equations has not been possible, indicating that they could be used only to model special features [23].
- More investigation is needed into spurious modes supported by the TLM condensed node meshes. At this stage, it is not clear to which extent they influence overall accuracy of physical solutions. Contradicting results can be found in recent publications [79, 80] and this should be clearly explained in a further study.

10.4 Overall conclusions

The main original contributions from this thesis may be summarized as follows:

- The TLM method based on the SCN was generalized to allow for link lines with different characteristic impedances and up to six stubs. A formulation for calculating the parameters of a general symmetrical condensed node (GSCN) was presented. The scattering properties of the general node were derived both from an equivalent network model and directly from Maxwell's equations, thus establishing a rigorous theoretical foundation for all nodes derivable from the GSCN. A unified formulation of parameter calculations for other TLM schemes was also described.
- Novel nodes were derived from the formulation of the GSCN, namely, the symmetrical super-condensed node (SSCN), the matched impedance SCN (MSCN) and the adaptable SCN (ASCN). The implementation and numerical characteristics of these nodes were described in detail. It was shown that these nodes possess advantageous computational and/or propagation properties compared to traditional nodes.
- A detailed mathematical analysis of the general TLM dispersion relation was pursued. Algebraic forms of the dispersion relations for the previously and newly developed nodes were derived using a systematic approach. A detailed comparison of the propagation errors of the presently available nodes was performed, including an extensive study of the impact on accuracy of stub-loading, changing of link line impedances, time step and mesh grading.

To conclude, the development and characterization of advanced nodes for the TLM method was successfully completed.

References

[1] M. N. O. Sadiku. *Numerical Techniques in Electromagnetics*. CRC Press, 1992.

[2] T. Itoh. *Numerical Techniques for Microwave and Millimeter-Wave Passive Structures*. John Wiley & Sons, New York, 1989.

[3] S. Cornbleet. *Microwave and Geometrical Optics*. Academic Press, London, 1994.

[4] K. S. Kunz and R. J. Luebbers. *The Finite Difference Time Domain Method for Electromagnetics*. CRC Press, 1993.

[5] W. J. R. Hoefer. The transmission-line matrix (TLM) method. In T. Itoh, editor, *Numerical Techniques for Microwave and Millimeter-Wave Passive Structures*, chapter 8. John Wiley & Sons, New York, 1989.

[6] C. Christopoulos. *The Transmission-Line Modelling (TLM) Method*. Series on Electromagnetic Wave Theory. IEEE/OUP Press, 1995.

[7] P. B. Johns and R. L. Beurle. Numerical solution of 2-dimensional scattering problems using a transmission-line matrix. *Proc. IEE*, 118(9):1203–1208, Sept. 1971.

[8] W. J. R. Hoefer and R. Vahldieck. Welcome address. In *First International Workshop on Transmission Line Matrix (TLM) Modelling - Theory and Applications*. University of Victoria, BC, Canada, August 1-3 1995.

[9] P. B. Johns. A symmetrical condensed node for the TLM method. *IEEE Trans.*, MTT-35(4):370–377, April 1987.

[10] D. P. Johns, R. Scaramuzza, and A. J. Wlodarczyk. 'Micro-Stripes' – microwave design tool based on 3D-TLM. In *First International Workshop on TLM*, pages 169–177, University of Victoria, BC, Canada, August 1-3 1995.

[11] S. Akhtarzad and P. B. Johns. Generalised elements for TLM method of numerical analysis. *Proc. IEE*, 122(12):1349–1352, Dec. 1975.

[12] W. J. R. Hoefer and P. P. M. So. *The Electromagnetic Wave Simulator*. John Willey and Sons, NY, 1991.

[13] S. Akhtarzad and P. B. Johns. The solution of Maxwell's equations in three space dimensions and time by the TLM method of numerical analysis. *Proc. IEE*, 122(12):1344–1348, Dec. 1975.

[14] W. J. R. Hoefer. The transmission-line matrix method – theory and applications. *IEEE Trans.*, MTT-33(10):882–893, Oct. 1985.

[15] K. S. Yee. Numerical solution of initial boundary value problem involving Maxwell's equations in isotropic media. *IEEE Trans. Antennas Propagat.*, AP-14(3):302–307, May 1966.

[16] A. Amer. *The Condensed Node TLM Method and its Application to Transmission in Power Systems*. PhD thesis, University of Nottingham, UK, 1980.

[17] P. Saguet and E. Pic. Utilisation d'un nouveau type de noeud dans la méthode TLM en 3 dimensions. *Electronics Letters*, 18(11):478–480, May 1982.

[18] D. A. Al-Mukhtar and J. E. Sitch. Transmission-line matrix method with irregularly graded space. *IEE Proc., part H*, 128(6):299–305, Dec. 1981.

[19] R. A. Scaramuzza and A. J. Lowery. Hybrid symmetrical condensed node for TLM method. *Electronics Letters*, 26(23):1947–1949, Nov. 1990.

[20] P. Berrini and K. Wu. A pair of hybrid symmetrical condensed TLM nodes. *IEEE Microwave and Guided Wave Letters*, 4(7):244–246, July 1994.

[21] D. P. Johns, A. J. Wlodarczyk, A. Mallik, and C. Christopoulos. New TLM technique for steady-state field solution in three dimensions. *Electronics Letters*, 28(18):1692–1694, Aug. 1992.

[22] H. Jin and R. Vahldieck. The frequency-domain transmission line matrix method – a new concept. *IEEE Trans. Microwave Theory Tech.*, 40(12):2207–2118, Dec. 1992.

[23] F. J. German. Infinitesimally adjustable boundaries in symmetrical condensed node TLM simulations. In *9th Annual Rev. of Prog. in Applied Comp. in EM*, pages 483–490, NPS Monterey, CA, USA, 1993.

[24] P. Naylor and R. A. Desai. New three dimensional symmetrical condensed lossy node for solution of electromagnetic wave problems by TLM. *Electronics Letters*, 26(7):492–493, March 1990.

[25] F. J. German, G. K. Gothard, and L. S. Riggs. Modelling of materials with electric and magnetic losses with the symmetrical condensed TLM method. *Electronics Letters*, 26(16):1307–1308, Aug. 1990.

[26] D. P. Johns and C. Christopoulos. Lossy dielectric and thin lossy film models for 3-D steady state TLM. *Electronics Letters*, 29(4):348–349, Feb. 1993.

[27] P. B. Johns. Use of condensed and symmetrical TLM nodes in computer-aided electromagnetic design. *IEE Proc.,Pt.H*, 133(5):368–374, Oct. 1986.

[28] D. D. Ward. *A Three-Dimensional Model of the Lightning Return Stroke.* PhD thesis, University of Nottingham, UK, 1991.

[29] S. Wright. *The Application of Transmission-Line Modelling Implicit and Hybrid Algorithms to Electromagnetic Problems.* PhD thesis, University of Nottingham, UK, 1988.

[30] R. H. Voelker and R. J. Lomax. A finite-difference transmission-line matrix method incorporating a non-linear device model. *IEEE Trans. Microwave Theory Tech.*, 38:302–312, 1990.

[31] R. A. Scaramuzza and C. Christopoulos. Development in transmission line modelling and its application in EM field simulation. In *Int. Symp. on EM Fields in Electrical Engineering*, pages 65–68, Southampton, UK, 18-20 Sept. 1991.

[32] R. A. Scaramuzza. *Simulation of Conductive Environments Using Transmission Line Modelling.* PhD thesis, University of Nottingham, UK, 1993.

[33] W. J. R. Hoefer and P. Sautier. Characteristics of the general rectangular 2-D TLM network. *Int. Journ. of Num. Modelling*, 7(2):127–139, March 1994.

[34] D. Johns and C. Christopoulos. New frequency-domain TLM method for the numerical solution of steady-state electromagnetic problems. *IEE Proc.Sci.Meas.Technol.*, 141(4):310–316, July 1994.

[35] D. P. Johns. An improved node for frequency-domain TLM – the 'Distributed Node'. *Electronics Letters*, 30(6):500–502, March 1994.

[36] P. Berrini and K. Wu. A new frequency domain symmetrical condensed TLM node. *IEEE Microwave and Guided Wave Letters*, 4(6):180–182, June 1994.

[37] P. Naylor and R. Ait-Saidi. Simple method for determining 3-D TLM nodal scattering in nonscalar problems. *Electronics Letters*, 28(25):2353–2354, Dec. 1992.

[38] J. L. Herring and C. Christopoulos. The application of different meshing techniques to EMC problems. In *9th Annual Rev. of Prog. in Applied Comp. in EM*, pages 755–762, NPS Monterey, CA, USA, 1993.

[39] J. L. Herring. *Developments in the Transmission-Line Modelling Method for Electromagnetic Compatibility Studies*. PhD thesis, University of Nottingham, UK, 1993.

[40] J. S. Nielsen and W. J. R. Hoefer. Generalized dispersion analysis and spurious modes of 2-D and 3-D TLM formulations. *IEEE Trans. Microwave Theory Tech.*, 41(8):1375–1384, Aug. 1993.

[41] R. E. Collin. *Foundations for Microwave Engineering*. McGraw-Hill, 2nd edition, 1992.

[42] H. Jin and R. Vahldieck. Direct derivations of TLM symmetrical condensed node and hybrid symmetrical condensed node from Maxwell's equations using centered differencing and averaging. *IEEE Trans. Microwave Theory Tech.*, 42(12, part 2):2554–2561, Dec. 1994.

[43] Z. Chen, M. N. Ney, and W. J. R. Hoefer. A new finite-difference time-domain formulation and its equivalence with the TLM symmetrical condensed node. *IEEE Trans. Microwave Theory Tech.*, 39(12):2160–2169, Dec. 1991.

[44] M. Krumpholz and P. Russer. A field theoretical derivation of TLM. *IEEE Trans. Microwave Theory Tech.*, 42(9):1660–1668, Sept. 1994.

[45] L. S. Griffiths. *Introduction to the Theory of Equations*, chapter 2, pages 25–32. John Wiley & Sons, New York, 1946.

[46] D. Stanlin, A. Morgenthaler, and J. A. Kong. *Electromagnetic Waves*. Prentice Hall, 1994.

[47] G. E. Mariki and C. Yeh. Dynamic three–dimensional TLM analysis of microstriplines on anisotropic substrate. *IEEE Trans.*, MTT-33(9):789–799, Sept. 1985.

[48] C. Bulutay and S. Prasad. Analysis of millimeter waveguides on anisotropic substrates using the three-dimensional transmission-line matrix method. *IEEE Trans. Microwave Theory Tech.*, 41(6/7):1119–1125, June 1993.

[49] Q. Zhang and W. J. R. Hoefer. Characteristics of 3-D distributed node TLM mesh with cells of arbitrary aspect ratio. *IEEE Trans. Microwave Theory Tech.*, 42(12, part 2):2365–2370, Dec. 1994.

[50] C. Tong and Y. Fujino. An efficient algorithm for transmission line matrix analysis of electromagnetic problems using the symmetrical condensed node. *IEEE Trans. Microwave Theory Tech.*, 39:1420–1424, 1991.

[51] C. R. Brewitt-Taylor and P. B. Johns. On the construction and numerical solution of transmission-line and lumped networks models of Maxwell's equations. *Int. J. Numer. Meth. Eng.*, 19:13–30, 1980.

[52] J. S. Nielsen and W. J. R. Hoefer. A complete dispersion analysis of the condensed node TLM mesh. *IEEE Trans. Magnetics*, 27(5):3982–3985, Sept. 1991.

[53] J. S. Nielsen and W. J. R. Hoefer. Effect of dispersion in the 3-D condensed node TLM mesh. In *IEEE MTT-S Digest*, pages 853–855, 1992.

[54] J. S. Nielsen. *TLM Analysis of Microwave and Millimetre Wave Structures with Embedded Nonlinear Devices*. PhD thesis, University of Ottawa, Canada, 1992.

[55] J. S. Nielsen. Spurious modes of the TLM-condensed node formulation. *IEEE Microwave and Guided Wave Letters*, 1(8):201–203, Aug. 1991.

[56] M. Celuch-Marcysiak. Towards better understanding of the SCN TLM method for inhomogeneous problems. In *2nd Intl. Workshop on Discrete Time Domain Modelling of Electromagnetic Fields and Networks*, Berlin, Germany, Oct. 1993.

[57] D. P. Johns and C. Christopoulos. Dispersion of time-domain and frequency domain formulations of the symmetrical condensed TLM node. In *2nd Intl. Conf. on Computation in Electromagnetics*, pages 295–298, Nottingham, UK, April 1994. IEE Conf. publ. 384.

[58] M. Celuch-Marcysiak and W. K. Gwarek. On the effect of bilateral dispersion in inhomogeneous symmetrical condensed node modelling. *IEEE Trans. Microwave Theory Tech.*, 42(6):1069–1073, June 1994.

[59] J. A. Morente, G. Gimenez, A. Porti, and M. Khalladi. Dispersion analysis for a TLM mesh of symmetrical condensed nodes with stubs. *IEEE Trans. Microwave Theory Tech.*, 43(2):452–456, Feb. 1995.

[60] P. Berini and K. Wu. A comprehensive study of numerical anisotropy and dispersion in 3-D TLM meshes. *IEEE Trans. Microwave Theory Tech.*, 43(5):1173–1181, May 1995.

[61] M. Krumpholz and P. Russer. A generalized method for the calculation of TLM dispersion relations. In *Proc. 23rd EMC*, pages 288–290, Madrid, Sept. 1993.

[62] M. Krumpholz and P. Russer. On the dispersion in TLM and FDTD. *IEEE Trans. Microwave Theory Tech.*, 42(7):1275–1279, July 1994.

[63] C. Huber, M. Krumpholz, and P. Russer. Dispersion in anisotropic media modelled by three-dimensional TLM. *IEEE Trans. Microwave Theory Tech.*, 43(8):1923–1934, Aug. 1995.

[64] J. Heading. *Matrix Theory for Physicists*, chapter 2, pages 53–54. Longmans, London, 1963.

[65] P. P. M. So and W. J. R. Hoefer. A new look at the 3D condensed node TLM scattering. In *IEEE Intl. Microwave Symp. Dig.*, pages 1443–1446, Atlanta, Ga, June 1993.

[66] M. Krumpholz. Dispersion characteristics of two- and three-dimensional TLM schemes. In *First International Workshop on TLM*, pages 27–36, University of Victoria, BC, Canada, August 1-3 1995.

[67] P. Russer and B. Bader. The alternating transmission line matrix ATLM scheme. In *IEEE MTT-S*, pages 19–22, Orlando, Florida, May 16-20 1995.

[68] P. Russer. On the field theoretical foundation of the transmission line matrix method. In *First International Workshop on TLM*, pages 3–12, University of Victoria, BC, Canada, August 1-3 1995.

[69] R. Weigel S. Lindenmeier, B. Isele and P. Russer. On the suppression of spurios modes in stub-loaded 3D-symmetrical condensed TLM-nodes. In *First International Workshop on TLM*, pages 41–44, University of Victoria, BC, Canada, August 1-3 1995.

[70] F. R. Gantmacher. *The Theory of Matrices*, chapter 4, pages 87–89. Chelsea Publishing Company, New York, 1959.

[71] Z. Chen. Modelling of absorbing boundary conditions with TLM. In *First International Workshop on TLM*, pages 63–72, University of Victoria, BC, Canada, August 1-3 1995.

[72] Q. Zhang and W. J. R. Hoefer. Modelling of inhomogeneous dielectric layers using TLM cubiod condensed node. In *IEEE AP-S Symposium Digest*, pages 774–777, June 1995.

[73] Q. Zhang and W. J. R. Hoefer. Analysis of 3-D planar structures by TLM cubiod condensed node. In *First International Workshop on TLM*, pages 243–246, University of Victoria, BC, Canada, August 1-3 1995.

[74] J. L. Herring and C. Christopoulos. Solving electromagnetic field problems using a multiple grid transmission-line modelling method. *IEEE Trans. Antennas Propagat.*, 42(12):1654–1658, Dec. 1994.

[75] D. P. Johns, A. Mallik, and A. Wlodarczyk. TLM enhancement for EMC studies. In *IEEE Proc. 1992 Regional Symposium on Electromagnetic Compatibility*, page 3.3.3, Israel, Nov. 1992.

[76] J. A. Porti, J.A. Morente, M. Khalladi, and A. Gallego. Comparison of thin-wire models for TLM method. *Electronics Letters*, 28(20):1910–1911, Sept. 1992.

[77] C. Christopoulos. *Principles and Techniques of Electromagnetic Compatibility.* CRC Press, 1995.

[78] R. Vahldieck, H. Jin, and J. Huang. Frequency-domain TLM modelling of waveguide discontinuities. In *First International Workshop on TLM*, pages 205–214, University of Victoria, BC, Canada, August 1-3 1995.

[79] M. Krumpholz, B. Bader, and P. Russer. On the theory of discrete TLM Green's functions in three-dimensional TLM. *IEEE Trans. Microwave Theory Tech.*, 43(7):1472–1483, July 1995.

[80] C. Eswarappa and W. J. R. Hoefer. Radar cross-section of metallic and dielectric cubes computed with TLM. In *First International Workshop on TLM*, pages 165–168, University of Victoria, BC, Canada, August 1-3 1995.

Author's publications

During the course of the work, leading to the preparation of this thesis, the author has published the following papers:

1. V. Trenkic, C. Christopoulos, and J. G. P. Binner. The application of the transmission-line modelling (TLM) method in combined thermal and electromagnetic problems. In R. W. Lewis, editor, *Numerical Methods in Thermal Problems – Proceedings of the 8th International Conference*, volume VIII, part 2, pages 1263–1274, Swansea, Wales, July 1993.

2. V. Trenkic, C. Christopoulos, and T. M. Benson. Simple and elegant formulation of scattering in TLM nodes. *Electronics Letters*, 29(18):1651–1652, Sept. 1993.

3. V. Trenkic, C. Christopoulos, and T. M. Benson. New developments in the numerical simulation of RF and microwave circuits using the TLM method. In B. Milovanovic, editor, *1st Conference in Modern Satellite and Cable Systems (TELSIKS '93)*, pages 6.1–6.6, Nis, Yugoslavia, Oct. 1993.

4.* V. Trenkic, C. Christopoulos, and T. M. Benson. New symmetrical super-condensed node for the TLM method. *Electronics Letters*, 30(4):329–330, Feb. 1994.

5. C. Flockhart, V. Trenkic, and C. Christopoulos. The simulation of coupled electromagnetic and thermal problems in microwave heating. In *2nd International Conference on Computation in Electromagnetics*, pages 267–270, Nottingham, UK, April 1994.

6. V. Trenkic, C. Christopoulos, and T. M. Benson. Generally graded TLM mesh using the symmetrical super-condensed node. *Electronics Letters*, 30(10):795–797, May 1994.

*This paper was awarded the IEE Electronics Letters Premium

7. V. Trenkic, C. Christopoulos, and T. M. Benson. A graded symmetrical super-condensed node for the TLM method. In *IEEE AP-S International Symposium*, pages 1106–1109, Seattle, Washington, USA, June 1994.

8. V. Trenkic, A. P. Duffy, T. M. Benson, and C. Christopoulos. Numerical simulation of penetration and coupling using the TLM method. In *International Symposium on Electromagnetic Compatibility*, pages 321–326, Roma, Italy, Sept. 1994.

9. V. Trenkic, C. Christopoulos, and T. M. Benson. Numerical simulation of polymers and other materials for electronic shielding applications. In *Polymer Technologies for Electronics (POLYMAT '94)*, pages 384–387, London, UK, Sept. 1994.

10. C. Christopoulos, V. Trenkic, and T. M. Benson. Prediction of shielding effectiveness by numerical simulation. In *Workshop on Shielding Effectiveness, EEC COST Action 243*, Budapest, Hungary, Nov. 1994.

11. V. Trenkic, C. Christopoulos, and T. M. Benson. Dispersion analysis of TLM symmetrical super-condensed node. *Electronics Letters*, 30(25):2151–2153, Dec. 1994.

12. V. Trenkic, C. Christopoulos, and T. M. Benson. New developments in the numerical simulation of RF and microwave circuits using the TLM method. *Facta Universitatis (Nis), Series Electronics and Energetics*, 1:87–95, 1995.

13. V. Trenkic, T. M. Benson, and C. Christopoulos. Dispersion analysis of a TLM mesh using a new scattering matrix formulation. *IEEE Microwave and Guided Wave Letters*, 5(3):79–80, March 1995.

14. V. Trenkic, C. Christopoulos, and T. M. Benson. Dispersion of TLM condensed nodes in media with arbitrary electromagnetic properties. In *IEEE Microwave Symposium*, volume 2, pages 373–376, Orlando, Florida, USA, May 1995.

15. V. Trenkic, C. Christopoulos, and T. M. Benson. Theory of the symmetrical super-condensed node for the TLM method. *IEEE Transactions on Microwave Theory and Techniques*, 43(6):1342–1348, June 1995.

16. V. Trenkic, C. Christopoulos, and T. M. Benson. Minimization and elimination of dispersion in electromagnetic simulations by selection of node aspect ratio and time step in the TLM super-condensed node. In *PIERS*, Seattle, Washington, USA, July 1995.

17. V. Trenkic, C. Christopoulos, and T. M. Benson. A unified approach to the derivation of TLM node parameters. In *First International Workshop on Transmission Line Matrix (TLM) Modelling - Theory and Applications*, pages 23–26, Victoria, BC, Canada, Aug. 1995.

18. V. Trenkic, C. Christopoulos, and T. M. Benson. 'Det(I-TPS)=0' - a package for visualizing TLM dispersion relations. In *First International Workshop on Transmission Line Matrix (TLM) Modelling - Theory and Applications*, pages 37–40, Victoria, BC, Canada, Aug. 1995.

19. V. Trenkic, C. Christopoulos, and T. M. Benson. Efficient computational algorithms for TLM. In *First International Workshop on Transmission Line Matrix (TLM) Modelling - Theory and Applications*, pages 77–80, Victoria, BC, Canada, Aug. 1995.

20. V. Trenkic, C. Christopoulos, and T. M. Benson. On the time step in hybrid symmetrical condensed TLM nodes. *IEEE Transactions on Microwave Theory and Techniques*, 43(9):2172–2174, Sept. 1995.

21. V. Trenkic, C. Christopoulos, and T. M. Benson. The application of the super-condensed TLM node to propagation problems in inhomogeneous, anisotropic materials. In *ISEF*, pages 69–72, Salonika, Greece, Sept. 1995.

22. V. Trenkic, C. Christopoulos, and T. M. Benson. Simulation of the shielding effectiveness of cabinets used in communication equipment. In *2nd Conference in Modern Satellite and Cable Systems (TELSIKS '95)*, Nis, Yugoslavia, Oct. 1995.